Quantitative approaches to understanding signaling regulation of 3D cell migration

by

Aaron Samuel Meyer

B.S., University of California, Los Angeles (2009)

Submitted to the Department of Biological Engineering
in partial fulfillment of the requirements for the degree of

Doctor of Philosophy in Biological Engineering

at the

MASSACHUSETTS INSTITUTE OF TECHNOLOGY

June 2014

Signature redacted

Author .....
Department of Biological Engineering
April 8, 2014

Signature redacted

Certified by .....
Douglas A. Lauffenburger
Professor of Biological Engineering, Chemical Engineering, and Biology
Thesis Supervisor

Signature redacted

Certified by .....
Frank B. Gertler
Professor of Biology
Thesis Supervisor

Signature redacted

Accepted by .....
Forest M. White
Chairman, Graduate Program Committee

Quantitative approaches to understanding signaling regulation of 3D cell migration

by

Aaron Samuel Meyer

Submitted to the Department of Biological Engineering
on April 8, 2014, in partial fulfillment of the
requirements for the degree of
Doctor of Philosophy in Biological Engineering

Abstract

For many cancers, dissemination of tumor cells to form metastases is not only a hallmark of the disease but an essential step to mortality. Migration and dissemination are complex, multistep processes, and study of their regulation has been challenging. Metastases need only be driven by a rare subpopulation of tumor cells, and a portion of dissemination is necessarily interaction with the cell's environment and thus cell extrinsic. Experimentally, there is additional uncertainty as exactly how to best assess migration outside of the complex *in vivo* environment.

To develop a systems perspective of invasive disease, we first examine some of the experimental models used to study cell migration. We then apply this knowledge to examine regulation by proteases of endometrial cell invasion, and the pro-migratory effects of receptor crosstalk in breast carcinoma cells. Finally, extending from clear limitations in our knowledge of signaling regulation specifically within the invasive subpopulation of cells, we develop a model of ligand-mediated signaling for a receptor often expressed specifically during the process of dissemination. In total, this thesis extends systems biology techniques to the study of cell migration within the extracellular environment, with focus on that subpopulation of cells most directly implicated in the formation of metastatic disease.

Thesis Supervisor: Douglas A. Lauffenburger
Title: Professor of Biological Engineering, Chemical Engineering, and Biology

Thesis Supervisor: Frank B. Gertler
Title: Professor of Biology

Acknowledgments

The past years at MIT have been an incredible opportunity to meet some amazing people.

Foremost, I must thank my advisers, Frank Gertler and Douglas Lauffenburger, for their uniquely flexible support and advice throughout this project. My committee members, Forest White and Alan Wells, have kept me on my toes and continually offered invaluable advice for the development of these projects. My labmate and collaborator, Miles Miller, led development of the second project, provided instrumental help with completion of the third, and has been a great partner for inspiring discussions. I am indebted to Shannon Hughes for setting me on my feet as a new graduate student and for critical insights in the migration work presented here. My labmates in the Lauffenburger and Gertler laboratories have been unconditionally helpful and a joy to work with; some of those who have helped with specific elements of these projects (in no particular order) are Brian Joughin, Joel Wagner, Dave Clarke, Hyung-Do Kim, Edgar Sanchez, Shelly Peyton, Elma Kurtagic, Sarah Schrier, Allison Claas, Michael Beste, Caroline Chopko, and Douglas Jones.

I thank my classmates of BE '09 who provided high jinks and camaraderie through our first years, and have remained good friends and at times important scientific help since. Outside MIT, I thank friends from Boston—Mike Bowles, Ryan Nistler, Jayson Vucovich, Chris Sanders, Jeffrey Russo, Jeff Brailsford, Scott Carlson, Ariana Breckner—and from California—David Quiros, Stacey Shiigi, Sergey Boyarskiy, Kenneth Hurst, Arthur Zey, David Chu, Jessica Piffero, Robin Jones, and Allison Cross—for the adventures, distractions, treks, favors, and surprises that have made so many cherished moments over the past years.

I would like to thank my parents Mary Lou and Dennis, and my brother Travis, for their unconditional love and support as I've ventured across the country. Lastly but most critically, this work would not be the same without Charles Liles, who keeps be sane, happy and loved.

This doctoral thesis has been examined by a Committee of the Department of Biological Engineering as follows:

Professor Forest M. White .....
Chairman, Thesis Committee
Professor of Biological Engineering

Professor Douglas A. Lauffenburger .....
Thesis Supervisor
Professor of Biological Engineering

Professor Frank B. Gertler .....
Thesis Supervisor
Professor of Biology

Professor Alan Wells .....
Member, Thesis Committee
Professor of Pathology

Contents

List of Figures

List of Tables

List of Terms

AXL AXL receptor tyrosine kinase. Uniprot ID: P30530.

c-Cbl E3 ubiquitin-protein ligase CBL. Uniprot ID: P22681.

CTC Circulating tumor cell.

DSS Dioctyl sodium sulfosuccinate.

ECM Extracellular matrix.

EMT Epithelial to mesenchymal transition. A developmental dedifferentiation process which endows epithelial cells with the ability to migrate.

EPHA1 Ephrin (EPH) type-A receptor 1. Uniprot ID: P21709.

FGFR1 Fibroblast growth factor receptor 1. Uniprot ID: P11362.

Gas6 Growth arrest-specific 6, a TAM receptor ligand. Uniprot ID: Q14393.

GSK3 Glycogen synthase kinase 3.

HER2 Epidermal growth factor receptor 2. Uniprot ID: P04626.

IGF1R Insulin-like growth factor receptor. Uniprot ID: P08069.

INSR Insulin receptor. Uniprot ID: P06213.

JNK c-Jun N-terminal kinase.

MerTK MerTK receptor tyrosine kinase. Uniprot ID: Q12866.

MET Hepatocyte growth factor receptor. Uniprot ID: P08581.

MT1-MMP MMP14. Uniprot ID: P50281.

MT2-MMP MMP15. Uniprot ID: P51511.

PDGFR Platelet-derived growth factor receptor..

PIP3 Phosphatidylinositol (3,4,5)-triphosphate.

RTK Receptor tyrosine kinase.

STAT3 Signal transducer and activator of transcription 3.

TAM Tyro3, AXL, MerTK.

Tyro3 Tyro3 receptor tyrosine kinase. Uniprot ID: Q06418.

Chapter 1

Introduction: Resistance & metastasis are intrinsically linked

Improved understanding of the molecular events driving carcinogenesis has led to drugs specifically targeting these signals. In cancers with a more limited set of genetic abnormalities, such as chronic myelogenous leukemia, these treatments have frequently shown complete disease response, vastly improving upon conventional cytotoxic therapies [1]. In the most common malignancies however, success of these treatments has been more limited. Targeted therapies have shown striking initial responses, and outlier cases of extensive survival gains, but resistance and recurrence soon follow. Recurrent tumors and metastases are often quite distinct in phenotype and therapeutic response. While many new targets have been developed, second-line treatments have shown a similar or worse pattern of response, and a sufficient understanding of resistance to design treatments that reliably result in stable disease has not developed.

These more "challenging" cancers are often carcinomas. Tumor cell dissemination is usually a requisite process for carcinoma-associated mortality, and thus an especially important hallmark of these cancers [2]. In order to establish a distant tumor, cells must obtain some capacity to migrate, enter the blood or lymph, escape to the surrounding tissue, survive, and then resume the growth process [3]. Large-scale changes must occur prior to and during metastasis since epithelial cells do not retain the capacity to move [4]. However, despite considerable effort to understand metastasis, drugs targeting the process have remained elusive.

Metastatic spread and resistance show striking similarities. Resistance often correlates with the metastatic potential of a cancer, and tumor spread has been used as a predictor of eventual drug response [5]. Processes such as epithelial to mesenchymal transition (EMT) that endow epithelial cells with the ability to move have similarly been implicated in resistance. After conventional treatments the remaining cells frequently show features suggesting enhanced metastatic potential [6]. These similarities between each problem are not coincidental. Tumor resistance and metastasis each provide common challenges in their study, such as the importance of rare cells poorly represented by the tumor average, and transient states of transformation. Sometimes, directly causal links underlie these similarities, such as shared molecular mechanisms, or the unique microenvironment of a metastasis providing bypass signaling. There is considerable value understanding some of the recent developments in metastatic dissemination and resistance of carcinomas, framing them from the perspective of their commonalities, and thus targeting of both.

Rare cells drive disease progression

Both tumor cell acquired resistance and dissemination highlight the importance of rare, outlier cells, the behavior of which may not be captured by assay of the bulk tumor. Since the majority of a tumor does not migrate and invade away from the primary tumor mass, and disseminating cells are phenotypically distinct, this feature clearly

highlights the challenges as to exactly which population of cells to study.

In carcinomas, evidence has accumulated that tumor cells take advantage of developmental transformations to acquire the ability to invade, such as EMT driven by overexpression of Twist1 [4]. However, examination of the role of this process has been confusing due to an expectation that this process proceed within all tumor cells similarly. An outstanding question regarding the relevance of EMT has been why, despite seemingly strong evidence implicating EMT-regulators as modulators of metastasis, are primary tumors and metastases markedly epithelial in phenotype [7], and can gene expression in the primary tumor can predict dissemination [8]. In a detailed study, Tsai and colleagues have documented that EMT is an essential step to metastatic dissemination, but that transience of the state is equally essential such that the mesenchymal state is always present in only a minority population within tumors [9]. By examining each step of the metastatic cascade, the authors pinpointed that EMT promotes local invasion, intravasation, and extravasation, but that cells locked in the mesenchymal state cannot then proliferate within their new environment. Even in the experimental model of stable EMT induction, the rare metastases observed were of epithelial state, suggesting these tumors absolutely require a means around the effects of Twist1-upregulation and highlighting the importance of EMT transience. In breast cancer, a large set of cell lines display mesenchymal traits and have thus had their relevance questioned [10]. These findings perhaps suggest these lines are in fact an effective model for this subpopulation.

Studies of circulating tumor cells have largely corroborated the significance of this transient mesenchymal state. The abundance of CTCs, and mesenchymal markers within that subpopulation, can be a strong prognostic marker of tumor progression and survival [11, 12]. A murine model of pancreatic cancer, through purification of CTCs and single-molecule RNA sequencing, identified upregulated Wnt2 signaling with respect to matched solid tumors, and targeting Wnt2 or inhibition of TAK1 kinase blocked metastasis [13]. In humans, studies of CTCs have revealed a more complex picture, in which the mesenchymal state is abundant but shows dynamic changes. CTCs from patients with advanced prostate and breast cancer display both epithelial and mesenchymal markers, and each population changes dynamically in abundance in response to treatment [14, 15]. However, the predominance of mesenchymal CTCs strongly corresponds to tumor progression. Thus, epithelial-state CTCs may still not be significant to metastatic spread, though the circulatory environment may be able to dynamically transform these cells [15, 16]. Further complicating matters, not only can the overall phenotypic state of CTCs change, but genetic changes can be dynamically selected for within the population and within the primary tumor [17, 18].

Given the relevance of this subpopulation, how might we target these cells? Though CTC-specific targeting has been attempted, better experimental models of *in vivo* CTC state are likely to be critical to successful development of such drugs [19]. Fairly metastasis-specific results upon certain interventions certainly suggest that specific targeting of this subpopulation may be effective. For example, the dependence receptor DCC or inhibition of the AXL receptor shows little influence on the primary tumor but potently suppresses metastasis [20, 21]. CTC-targeted therapies will likely show best effectiveness only in combination with epithelial-targeted therapies to eradicate the primary tumor. Stem cells within a developmental context would suggest that simply targeting this subpopulation would be sufficient to ablate tumors, but cancers do not seem to retain the same hierarchical lineage forms of development [22]. Targeting localization of CTCs to the circulatory system is effective in reducing continued tumorigenic spread, but does not address those cells disseminated into the tissue, which may remain in an indolent state for considerable time [23, 24]. Given the ability of cancer cells to dynamically transition between distinct states, modeling that takes into account these processes will likely be necessary for maximal therapeutic benefit. This was recently attempted, taking into account differential sensitivities to radiotherapy, in a murine model of glioblastoma [25]. However, such modeling efforts will need to take into account a wider array of therapeutic options and patient-specific tumor composition for maximal efficacy.

Many pathway routes to similar phenotypes

Common to recent developments in cancer resistance and metastatic spread is the concept of pathway redundancy. In tumor cell dissemination this has become most prevalent with increasing use of *in vitro* migration assays which better mimic the tumor environment [26]. Just examining tumor spread from the primary mass, cells can utilize lamellipodial or blebbing migration modes, or means which do not rely on canonical polarization [27, 28]. Tumor cells may invade as a collective mass, allowing for diversification of migration roles, or invade as single cells fully competent in traversing tissue on their own [29, 30], and can dynamically change their mode of invasion in response to treatment [31, 32]. Cells may direct themselves through the matrix, or may rely on either signals or matrix degradation from tumor-infiltrating immune cells [33–35]. Extracellular matrix remodeling can be performed by tumor cells themselves, or promoted through cancer-associated fibroblasts [36, 37]. While EGF is perhaps the most studied chemotactic ligand for carcinoma cells, an overwhelming number of other growth factors and cytokines, such as RANKL or CCL18 from infiltrating immune cells, have been identified as promoting tumor cell dissemination [34, 38, 39].

Similarly, while initial study of resistance mechanisms focused on acquired changes in the molecular target, focus has broadened to identify common and widespread redundancy in cell signaling as a most problematic source of resistance to targeted agents [40, 41]. Because of this redundancy, overexpression or dysregulation of many different cell signaling molecules can lead to therapeutic resistance [42]. These can take the form of simpler redundancy, such as multitude of RTKs compensating for one another in terms of the requisite resistance signaling [43], or more complex redundancy from entirely distinct sources of survival signaling such as GTPases [44]. As one would expect given redundancy in the exact kinases which drive survival signaling, overall network response can often predict therapeutic response better than overexpression of single proteins [45]. With an improved understanding of overall network response, network-level sensitivities are more easily identifiable, as was demonstrated for HER2/3 inhibition compared to combined Mek/Akt inhibition [46].

Much of the research into resistance to date has focused on elucidation of resistance mechanisms, likely with the thought that very few would exist. However, with an ever-expanding literature of pathway redundancies, lengthening the list of resistance mechanisms is unlikely to help therapeutic development. This is an area where cancer cell resistance can likely learn a great deal from study of migration phenotypes. A great deal of work has elucidated the basic principles of cell migration, which provides a framework for understanding novel findings at higher levels, such as which matrix geometries give rise to particular types of migration [47]. With that understanding, it might then be easier to elucidate the many routes to resistance [48]. Optimism that even moderate accounting for pathway redundancy may provide considerable improvements in patient survival is justified [49].

Relevance of *in vitro* models

In recent years, many observations have called into question the relevance of simple experimental models for assessing metastatic potential [50]. Tumor cell dissemination necessarily depends on environmental interactions, many of which are missed by assessing motility on simple planar or porous surfaces. *In vitro* models also lack communication with other tumor-associated cell types and tissue structure, making it difficult to study metastasis-promoting effects such as vascularization and endothelial interaction [51]. Certain forms of cell invasion, such as with lobopodia or as tubular structures, lack any sort of 2D analog [27, 52].

Resistance similarly depends on environmental interactions, and thus can be difficult to assess outside the *in vivo* microenvironment. For example, many oncogenes can contribute to breast tumor progression when in an unstructured or fibrotic ECM environment, but do not result in outgrowth of single cells when formed in proper acini [53]. Drug responses within proper tissue structures can be quite distinct as well [54]. Paracrine cues rely on the presence and proper activation of a variety of other cell types that cannot be feasibly combined within *in vitro* systems, and the extracellular matrix can further influence presentation of autocrine and paracrine cues. Recently, periostin was identified as an essential matrix factor, secreted by normal fibroblasts, which recruits

Wnt ligands and thus promotes metastatic colonization of disseminated cancer stem cells [55]. New engineered scaffolds can improve the complexity of *in vitro* models, but it is difficult to know *a priori* which features of the *in vivo* environment need translation [56, 57]

These observations are not to say resistance and metastatic potential are always best evaluated within the *in vivo* environment. The immense complexity of *in vivo* models often confound mechanistic interpretation of results. Thus, there is a need to build up from simplicity, while tackling the complex *in vivo* environment. Experimental models are necessary to provide proper controlled manipulation, and many measurement techniques are simply not possible using *in vivo* systems. *In vitro* study of specific processes which contribute to invasion and metastasis, rather than migration overall, has been effective in improving translation to *in vivo* models. For example, many studies have looked at the pathways which regulate actin turnover at the leading edge of cells [58]. Actin polymerization-based translocation translates well to mesenchymal migration within 3D collagen matrices, and is often the rate-limiting step [33, 59, 60]. Invadopodia have well-developed methods of assessment *in vitro*, and their activity seems to translate well to *in vivo* models of cancer cell metastasis [61, 62]. This separation of scales will likely be necessary for study of resistance as well.

Migration can causally provide resistance

One very clear source of similarities between resistance to targeted therapies and metastatic dissemination is by causal relationships between the two. As a very simple example, metastasis to the brain confers resistance to many therapies that cannot effectively cross the blood brain barrier [63]. These effects generally arise as a characteristic of the local metastatic environment, differential selection of cells within a diverse population, or shared molecular mechanism.

The invasion process necessarily relocates cells to diverse environments, some of which can provide resistance to therapies. Leukemia cell infiltration to the bone marrow provides protection against antibody-based therapies, where the cells are able to coax the resident cells to be protective [64]. Immune clearance of these cells requires additional modulation of the environment with cytotoxic agents or cytokines. Disseminated breast carcinoma cells often lie dormant adjacent to the vasculature, not only in a distinct environment from the primary tumor, but receiving signals such as thrombospondin-1 which induce dormancy and thus resistance to therapies which rely on selective killing of dividing cells [65].

Molecular mechanisms that promote metastasis simultaneously can provide survival signaling. A recently identified example of this is signaling through P-Rex1. Unsurprisingly as a Rac-GEF, P-Rex1 promotes invasion and metastatic dissemination particularly within melanoma, in a Rac-dependent manner [66]. As a link from PIP3 dependent signaling to MAPK activation, the protein can simultaneously provide PI3K-dependent Erk activation and thus bypass resistance of canonical Erk activation, shifting the requirement of RTK activation from dual activation of two pathways to just activation of PIP3 synthesis [67, 68]. Within the extracellular milieu, matrix metalloproteinases such as MT1-MMP and MT2-MMP degrade extracellular matrix and thus physically enable invasion of tumor cells, but simultaneously protect against collagen-mediated apoptosis [69, 70]. Cell invasion through the matrix environment can cause both rewiring and crosslinking of extracellular matrix, often essential for cell invasion within extracellular matrix, but also driving differential integrin activation and resistance [54, 71]. More globally, EMT leads to diverse regulatory changes within a cell. One part of this in ErbB3-positive breast carcinoma cells is a switch to PI3K activation mediated by alternative RTKs [72]. These bypass signals result in qualitatively distinct survival dependencies for disseminated cells, and thus resistance from the perspective of therapies designed by assessment of bulk tumor response.

More subtly, dissemination of tumor cells can enable sampling and selection within a heterogeneous population of cells. This can allow tumor cells of distinct phenotypes that otherwise might not have survived find a distinctly suitable environment compared to the average tumor cell. Thus, differences in adhesion between bulk and disseminated tumor cells for example may not only reflect differences in invasive capacity but differences in

most suitable environment, enhancing diversity in the tumor cell population [73]. For example, bone metastases are skewed toward Src-driven survival cues due to the high prevalence of CXCL12 and IGF1 in the microenvironment, and thus require distinct therapeutic targeting [74]. In total, these effects, through reprogramming or differential selection, all result in metastatic dissemination giving rise to therapeutic resistance.

TAM receptors as a framework for studying resistance & metastasis

TAM receptors are a family of RTKs, represented by AXL, Tyro3, and MerTK, distinguished by their ectodomain comprised of two immunoglobulin domains and two fibronectin domains [75]. Gas6 and protein S are the only known ligands for the TAM receptors [76], and while Gas6 has measurable binding to all three receptors, protein S binds only Tyro3 and MerTK [77]. Protein S has a lower affinity even for the receptors with measurable binding, but is found in much higher concentrations, particularly in the blood, and has been validated as a relevant ligand *in vivo* [78]. Both ligands contain two C-terminal sex-hormone binding domains (SHBD) responsible for receptor binding. On the N-terminal end of the proteins, linked by four EGF-like domains, a Gla domain is gamma-carboxylated in a vitamin K-dependent process to gain capacity to bind phosphatidylserine. Ligands bind in a mirrored two ligand-two receptor complex in which there are no receptor-receptor or ligand-ligand contacts [79, 80]. Many of the phenotypes observed upon genetic manipulation of the receptors or ligands relate to processes signaled by presentation of phosphatidylserine on the outer leaflet of cells. Indeed, the first homologous receptors appear in the genomes of prevertebrate urochordates (family *Cionidae*), and have a Gla domain (present only in the TAM ligands) directly linked to a transmembrane protein kinase domain, suggesting a conserved role for kinase signaling associated with phosphatidylserine exposure [81].

TAM receptors, and especially AXL, have attracted considerable interest in the past decade as a potential therapeutic target in a wide range of cancers. In solid tumors, mutations and overexpression in the bulk tumor are uncommon. However, overexpression of the receptors has generally coincided with metastatic capacity, invasiveness *in vitro*, and resistance to targeted therapies. Consistent with this observation, AXL expression was identified as driven by EMT [21, 85] and, while therapeutic inhibitors of AXL have had less effectiveness in preclinical models on the primary tumor, they have shown promising results in combination with other targeted therapies or standard therapies and in blocking metastasis. Even in disseminated cancers, targeting the distinct population of AXL-expressing cells while simultaneously targeting the bulk tumor with standard treatments shows promise in considerably improving patient survival. MerTK and Tyro3 have also been observed as overexpressed and therapeutic targets in acute myeloid leukemia, glioblastoma, melanoma, thyroid cancers, and lung adenocarcinoma, though with a simpler pattern of uniform overexpression compared to AXL [86–88].

Therapeutic targeting of the TAM receptors was initially motivated in part by relatively mild effects upon knocking out expression [75]. However, further study has uncovered important function of the receptors in diverse processes, and cautions against overly broad therapeutic targeting but suggests further promise for TAM-targeted cancer therapy. The most studied effects of TAM-ablation have been in the immune system, where signaling from the receptors couples clearance of cell debris to regulation of the innate immune system [89]. One of the striking phenotypes of the triple knockout mice is a broad accumulation of apoptotic cell debris throughout various tissues. This has been tracked to defects in phagocytosis of this debris by macrophages in most tissues (termed efferocytosis), with the strongest effects in the single receptor knockouts observed upon ablation of MerTK [90, 91]. In addition to efferocytosis, signaling from TAM receptors acts as a negative feedback mechanism to the innate immune response [92]. Consistent with this, upon ablation of TAM receptor expression, one effect upon additional insult is development of autoimmune disorders, though it is unclear whether this due to accumulation of cross-presented auto-antigen, ablation of this negative regulation, or a combination of both [93]. Protein S from T cells was recently identified as an important means to downregulate the innate immune response after T cell activation, and TAM signaling in NK cells through c-Cbl blocks clearance of tumor cells [82, 83]. Many viruses are in fact coated by host phosphatidylserine-exposed membranes, which utilize this signaling

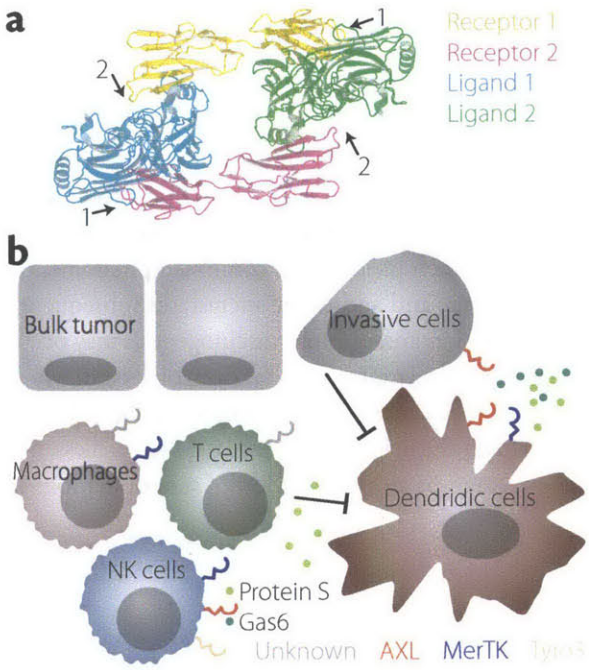

Figure 1.1: Overview of TAM signaling in cancer. a) Ligand binds TAM receptors in a mirrored two ligand-two receptor complex in which there are no receptor-receptor or ligand-ligand contacts [79, 80]. Two binding sites exist on each receptor and ligand (1 and 2), of highly asymmetric affinity for AXL-Gas6 [79]. b) TAM signaling within the tumor environment. In many tumors, the invasive subset of cells displays overexpression of AXL (red). TAM receptor activation within dendritic cells also potently inhibits the innate immune response through AXL and MerTK (blue). T cell release of protein S further dampens the immune response, and TAM signaling in NK cells blocks tumor cell clearance [82, 83] Macrophages, T cells, and NK cells all express a complement of TAM receptors, which likely further influence the tumor immune response [84].

to delay an immune response [94]. As a result of these effects, modulation of immune signaling could improve or impair therapeutic benefits of TAM-targeted therapies. Indeed, ablation of AXL and MerTK increases susceptibility to DSS-induced colitis on one hand, while having potent tumor-extrinsic anti-metastatic effects in murine models of breast cancer, melanoma and colon cancer on the other [84, 95].

Effects of TAM receptors outside of the immune system are pleiotropic. Some effects, such as retinal degeneration and infertility in older animals, are linked to clearance of phosphatidylserine-exposing debris [78, 96]. Activation may additionally provide survival cues for a variety of cell types [97]. Results from cancer studies have suggested MerTK signaling modulates vascularization, though the extent to which this occurs outside cancer is unclear. The most widespread expression of TAM receptors in the adult is within the brain, though effects upon inhibiting this signaling have only been identified very recently. MerTK has been identified as important for synapse elimination by astrocytes, TAM receptors seem to be important for adult neurogenesis, and autoimmunity causes inflammatory brain damage in triple knockout mice [98–100]. However, a clear picture of the exact processes disrupted in the brain has not yet emerged.

For these reasons, TAM receptors represent a uniquely interesting context in which to investigate how we might develop fundamentally new approaches to cancer therapy. These receptors highlight the importance of rare cells etiologically important to tumor progression, since their preliminary effectiveness has been specific to metastasis. At the same time, the importance of host signaling will limit design of therapies, but also presents new possibilities for modulating immune response which may not suffer from the characteristic acquired resistance limitations of previous targeted therapies.

Conclusion

Targeting tumor metastasis mechanisms has come under justifiable scrutiny due to observations of occult disseminated tumor cells in many carcinoma types. If tumors, at time of diagnosis, are already distributed throughout the body, what good is there in preventing further dissemination? Better screening technologies may still move the time of diagnosis to before tumor dissemination, particularly in pancreatic cancer in which a long latency exists in carcinogenesis [101]. It should be clear from these discussed links between tumor resistance and dissemination that value exists in studying each process as a combined phenomenon, particularly as resistant and disseminating cells may often be the same, and additional metastases subsequently give rise to increased tumor heterogeneity [102]. Indeed, dissemination and original carcinogenesis may occur simultaneously due to significant overlap in the molecular drivers. In melanoma this has been observed, where the majority of pro-invasion drivers are oncogenes [103]. In pancreatic cancer, certain genetic backgrounds may require pro-invasion genes for survival outside stable disease within the original tumor [102]. Regardless, both processes stress the need to move beyond study of the tumor average, as clonal selection of subpopulations implicate all outliers in disease progression [104].

Chapter 2

Growth Factor-Induced Breast Carcinoma Cell Migration in 3D Collagen is Predicted by 2D Protrusion but not Motility

Abstract

Growth factor-induced migration is a critical step in the dissemination and metastasis of solid tumors. Although differences in properties characterizing cell migration on two-dimensional (2D) substrata versus within three-dimensional (3D) matrices have been noted for particular growth factor stimuli, the 2D approach remains in more common use as an efficient surrogate, especially for high-throughput experiments. We therefore were motivated to investigate which migration properties measured in various 2D assays might be reflective of 3D migratory behavioral responses. We used human triple-negative breast cancer lines stimulated by a panel of receptor tyrosine kinase ligands relevant to mammary carcinoma progression. Whereas 2D migration properties did not correlate well with 3D behavior across multiple growth factors, we found that increased membrane protrusion elicited by growth factor stimulation did relate robustly to enhanced 3D migration properties of the MDA-MB-231 and MDA-MB-157 lines. Interestingly, we observed this to be a more reliable relationship than cognate receptor expression or activation levels across these and two additional mammary tumor lines.

Introduction

In most all solid cancers, dissemination of cells and establishment of distant metastases is an essential step in disease mortality [2]. Dissemination of carcinomas occurs by invasion across a basement membrane layer and migration through interstitial matrix to blood or lymph vessels. Efficient migration in this context requires coordinate regulation of cytoskeletal protrusion, adhesion, proteolysis and contraction [105, 106], each of which is modulated by paracrine and autocrine growth factor cues.

Cell migration has principally been studied as translocation across rigid two-dimensional substrata. Despite the relevance of migration within extracellular matrix (ECM) to tumor progression [107], and known qualitative and quantitative differences in cell movement between 2D and 3D environments [50, 108, 109], analysis of cells embedded within ECM remains relatively uncommon due to technical difficulty and incompatibility with most biochemical analyses. Functional genomic screening techniques have been employed to identify regulators of cell migration in planar contexts [110, 111] and analogous efforts used to identify small molecule drug targets [112] or ascertain dependence on key signaling pathways [113]. The physiological relevance of results obtained from such high-throughput efforts is related directly to the degree that cellular responses measured in 2D systems correlate to those within ECM environments. Determining whether in fact any metrics easily obtained from 2D

assays correlate robustly with 3D migration behavior across a broad range of treatment conditions is therefore critical.

We herein address this challenge for the important case of breast carcinoma cell migration. Through quantitative analysis of motility across multiple triple negative (ER-/PR-/HER2 normal) breast carcinoma cell lines moving in 3D within collagen I matrix, we evaluate the predictive value of measurements such as receptor expression, and motility surrogates such as cell translocation in 2D. We fail to observe correlation between growth factor-induced motility responses on either stiff or compliant ECM in a 2D context and those within 3D ECM. While cognate receptor expression can weakly predict the relative motility responses across cell lines, it fails to quantitatively predict motility enhancement due to growth factor stimulation. By examination of individual migration-related biophysical processes, we identify that acute lamellipodial protrusion dynamics of cells in response to growth factor cues can predict motility within 3D ECM. These findings have broad consequence in the assessment of motility responses *in vitro*, both for high-throughput studies and for deeper investigation of how growth factor-elicited signaling network activities govern migration behavior.

Results and Discussion

Systematic quantification of migration

To address multicomponent responses to growth factor stimulation, we performed a battery of quantitative single cell migration assays using multiple human breast tumor cell lines and assay geometries (Fig. 2.1A & 2.1B; see Materials and Methods). Cells were fluorescently labeled to facilitate image analysis, and their displacement was tracked via live-cell microscopy over the course of 16 hours in the presence or absence of seven growth factor cues relevant to the tumor microenvironment [2, 119–129] (Fig. 2.1C, 2.2A & 2.2B). Semi-automatic centroid tracking was used to extract multiple parameters that describe the migration phenotype of each cell. Each individual cell track provides five distinctly quantifiable properties (Fig. 2.1D): (1) a root mean squared (RMS) speed of each time interval; (2) the variance of that speed; (3) a total speed calculated as the total path length normalized by the time of the experiment; (4) a net speed or the net displacement normalized by the duration of the experiment; and (5) a "random motility coefficient" calculated by fitting to a random walk model [105, 106, 130]. The migration parameters were independent of position within the gel, nor were cells biased in their direction of migration, indicating homogenous physical characteristics [131, 132] and that the growth factors had distributed fairly uniformly throughout the gels before the observation period. Of ten breast carcinoma cell lines investigated across clinical markers and subtypes, five were observed to migrate robustly (Table 2.1). Vimentin expression and subtype classification distinguished cells that did or did not migrate in 3D.

Initial analysis of the full dataset by multidimensional reduction techniques illustrated that speed (RMS speed, total speed) and persistence (net speed, random motility) broadly cluster into two groups (Fig. 2.2C). This multidimensional scaling seeks to preserve distance as a description of relative difference between each motility metric, and indicates cell speed and persistence are distinct parameters to describe migration captured by the assay. Using unsupervised clustering techniques, cell lines (Fig. 2.3A), and dimensionalities or ECM in 2D (Fig. 2.3B) were found to be separable. Weaker clustering among speed- or persistence-related motility metrics from identical cell lines or geometries was obtained, consistent with single cell-based clustering (Fig. 2.2C). In some cases distinguishable responses were observed when analyzing different quantiles of the single-cell migration metrics (Fig. 2.2D), resulting in different response profiles (Fig. 2.3). Analysis of "outlier" cell populations is particularly important in invasive disease, as bulk population responses may not reflect disease etiology [12, 50, 108, 109, 133–135]. One important advantage of our large single-cell migration parameter dataset is the ability to quantify differences in responses within distinct cell subpopulations across assay conditions.

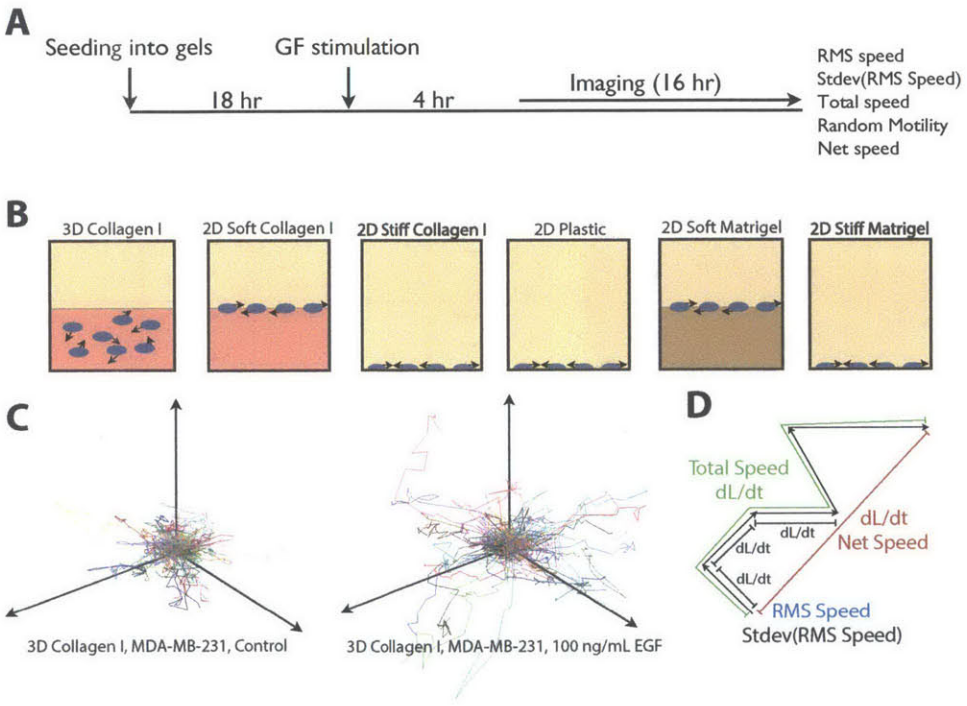

Figure 2.1: Schematic of the migration assays. Cells were seeded on or in matrix, or on plastic (B), for 18 hours before growth factor stimulation. Four hours after growth factor stimulation cells were imaged for 16 hours. Tracks of each cell were produced (C) and used to calculate five parameters summarizing the migration phenotype of each cell (D).

Cell Line	Subtype	Markers	Migratory in 3D
MDA-MB-231	Basal B	V	+
SUM-159	Basal B	N, V	+
BT-549	Basal B	N, V	+
MDA-MB-157	Basal B	V	+
SUM-1315	Basal B	V	+
BT-483	Luminal	E, ER, PR, HER2	-
T47D	Luminal	E, N, ER, PR	-
MCF7	Luminal	E, ER, PR	-
MDA-MB-453	Luminal		-
SKBR3	Luminal	HER2	-

Table 2.1: Table of cell lines tested for motility in collagen I gels. Cell lines examined in 3D. Markers column indicates which of the following clinical markers are present: E-cadherin (E), N-cadherin (N), vimentin (V), estrogen receptor (ER), progesterone receptor (PR), HER2 [10, 114–118].

Prediction of motility enhancement by receptor expression

We tested the ability of growth factor receptor expression to predict differential motility response upon stimulation, as receptor expression is widely used to define clinical breast tumor subtype. Total protein expression was measured for 3 different growth factor receptors, implicated in breast cancer invasion and metastasis [2, 136–138], in 2D for each cell line (Fig. 2.4B) and every pairwise comparison of receptor expression and motility enhancement in 3D was performed (Fig. 2.4A). With 24 comparisons ($4 \times C(4,2)$) at least 17 trials must correspond between receptor expression and motility for this relationship to be considered significantly predictive (p

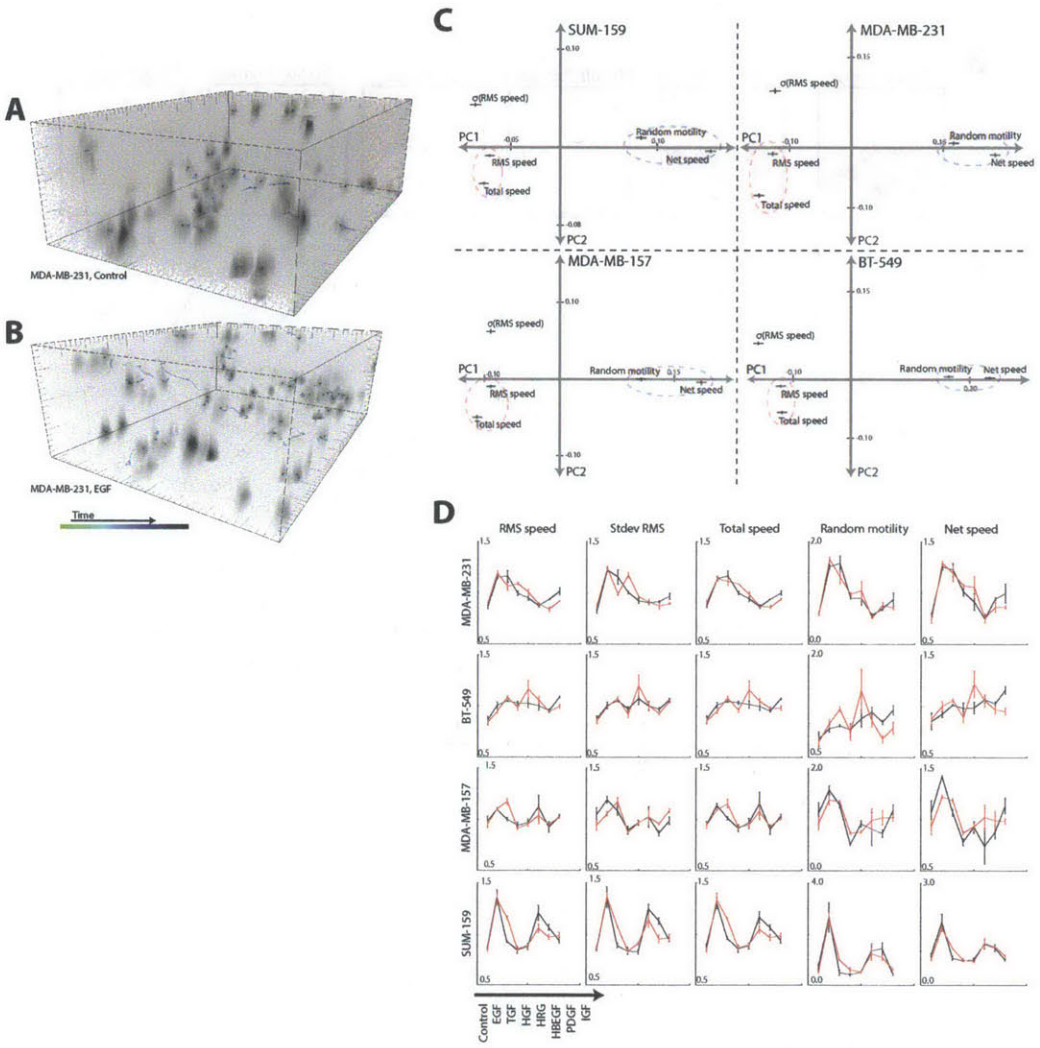

Figure 2.2: Fluorescence contrast images of cells migrating within collagen I gels. Tracks were produced using Bitplane Imaris and show the migration of MDA-MB-231 cells over 16 hrs with (bottom) or without (top) stimulation with 100 ng mL^{-1} EGF 4 hrs before imaging. Stacks consist of 70 slices measured 0.665 by 0.665 mm taken 3 μm apart. Shown is the maximal 45d perspective projection, with darker colors indicating higher fluorescence intensity. Fig. 2.1C is a wind-rose plot of these conditions. C) Pairwise distances between each metric were calculated using the inverse Spearman rank correlation across individual cells, and condensed by multidimensional scaling. This method seeks to preserve the distances between each motility metric while representing all distances in two dimensions. Two dimensions (PC1 and PC2) captured >99% of the distance quantities. Speed- and persistence-related metrics are circled in red and blue, respectively. Error bars are SEM. D) Plots for each motility metric across growth factor conditions are shown. Black and red lines indicate the median and 90th percentile responses, respectively. Each independent experiment was mean centered across growth factor conditions. The mean and SEM of all experiments (N ≥ 3) is shown.

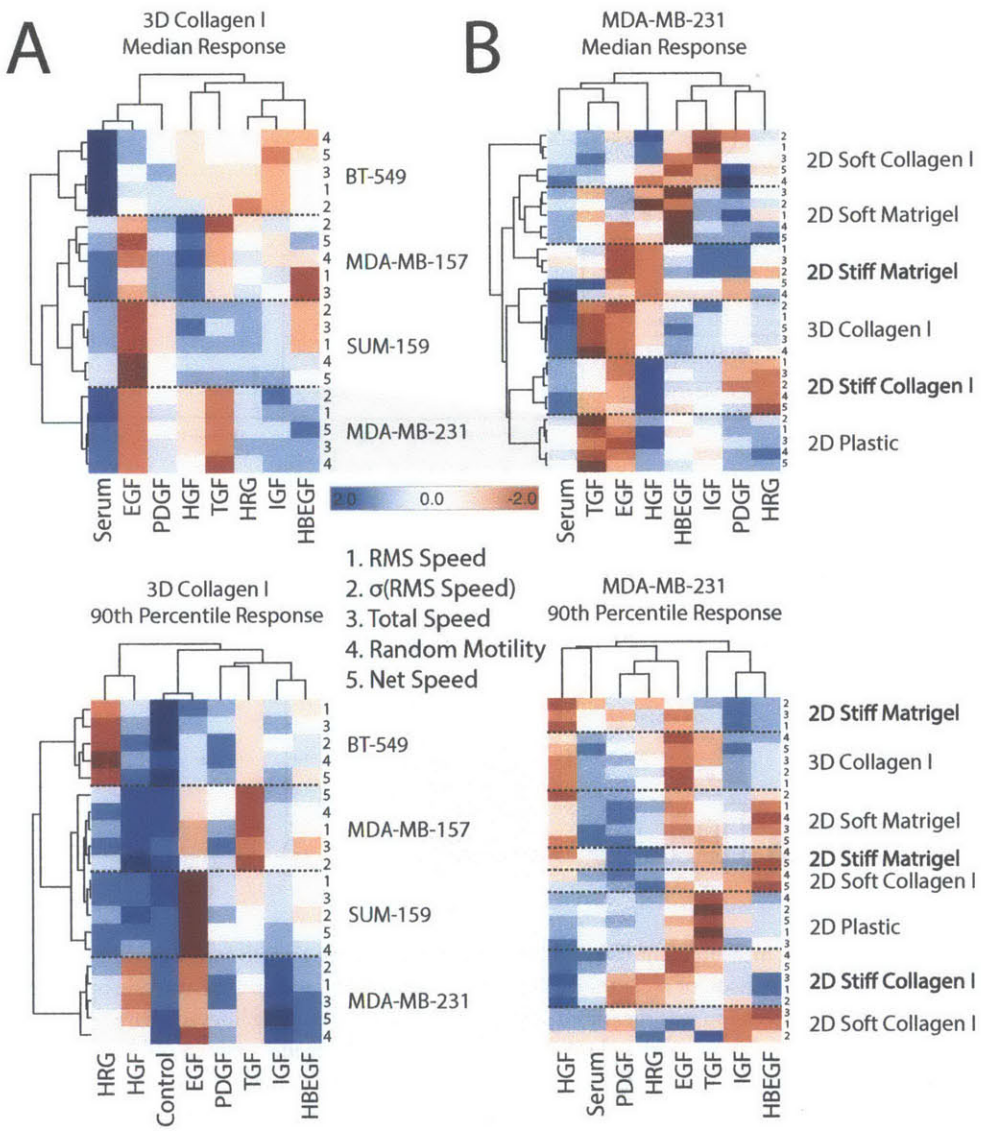

Figure 2.3: Large-scale quantification of migration responses enables systems analysis of migration. Shown are mean-centered motility responses across eight growth factor conditions and four cell lines within collagen I gels (A) or MDA-MB-231 cells across different 2D and 3D motility assays (B, see 2.1B). Each profile and growth factor is clustered by rank correlation and average linkage. Both the median (top) and 90th quantile (bottom) responses are shown, as well as each migration metric (indicated by numbers).

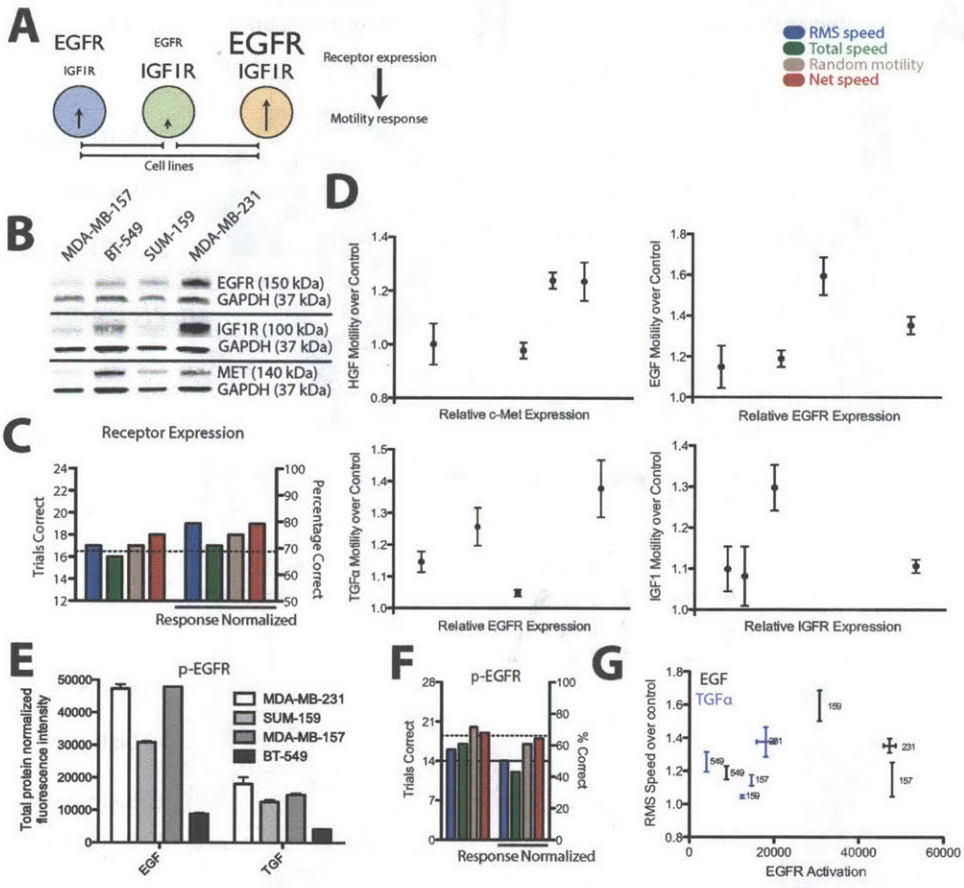

Figure 2.4: Cognate receptor measurement is weakly informative of relative growth factor motility enhancement. A) Illustration of the pairwise comparison of receptor measurement and motility enhancement made between each cell line. B) EGFR, IGF1R and c-Met expression was measured across four cell lines. Dividing lines indicate separate gels. C) Every pairwise comparison of receptor expression and motility enhancement was made between cell lines for each metric of motility. Additionally, the motility enhancement for each cell line across all growth factor conditions was used to normalize for differences in the ability of each cell line to globally respond by migrating. The left and right y-axes indicate the number and percent of correct comparisons, respectively. Significance was tested by use of the binomial distribution (dotted line, $p < 0.05$). D) Plots of RMS speed enhancement upon receptor stimulation versus relative receptor expression. Error bars indicate SEM. E) EGFR pan-pY measurement in cells stimulated with either EGF or TGFα for 5 minutes. Error bars indicate range of duplicate measurements. F) Similar pairwise comparison analysis using measurement of p-EGFR to predict migration response. G) Plot of RMS speed enhancement upon EGFR stimulation versus EGFR pan-pY measurement. Vertical error bars indicate SEM, horizontal error bars indicate measurement range.

< 0.05). The analysis revealed a weak but significant association for 3 of 4 motility properties, with 15-18 correct associations (Fig. 2.4C). Normalizing the measured properties for each cell line across the range of growth factor treatment conditions by variance, which may potentially account for differences among cell lines in their intrinsic motility capabilities, slightly improved the predictive capacity of receptor expression to 16–20 correct associations (Fig. 2.4C). As receptor activation might have improved predictive capacity over expression, we additionally tested the ability of EGFR pan-pY measurements to predict EGF and TGFα motility enhancement (Fig. 2.4E). Both stimulations may be directly compared in this case, resulting in 28 (C(8,2)) comparisons. Receptor activation, although distinct from expression, was not a better predictor of motility enhancement (Fig. 2.4F).

Receptor expression levels thus predicted growth factor-elicited motility enhancement to a small degree that barely reached statistical significance. While this provides support that receptor expression can account for some of the variation observed among cell lines and presumably among tumors, it is manifest that receptor expression or activation levels do not readily explain disparities in relative or absolute growth factor-enhanced migration responses (Fig. 2.4D and 2.4G). Therefore, while expression measurements across many samples may indicate etiologically important changes, measurement of receptor expression alone within tumor cells will likely not be sufficient to identify the particular growth factor cues driving invasion and metastasis in the context of myriad heterogeneities among various samples.

Growth factor motility responses are distinct in 2D and 3D

Migration across a planar substratum has been the principal means for quantitative studies of responses to compound and genetic manipulations intended to inhibit metastasis [105, 106, 110, 111]. Dissimilarities in unstimulated migration between 2D and 3D have been noted [50, 108, 131]. However, while migration *in vivo* is driven by autocrine and paracrine growth factor cues, the effects of growth factor stimulation have not been compared in different dimensional contexts. It is conceivable that growth factor motility responses may be similar in distinct dimensional contexts if various migration-related processes (e.g. protrusion, proteolysis, and retraction) are similarly modulated by growth factor cues.

To study the contributions of dimensional and matrix context on cell migration in vitro systematically, we performed all pairwise comparisons of growth factor enhanced cell motility metrics in MDA-MB-231 cells (Fig. 2.5A). A stronger correlation exists between different motility metrics within a single dimensional or matrix type, reflected by analysis for significant correlations (Fig. 2.5B; $p < 0.05$), which only exist within, and not across, dimensionalities. This is consistent with observed differences in EGF-stimulated migration response in 2D versus 3D [33, 50, 108, 109].

Here, we systematically demonstrate for the first time that growth factor enhanced motility is distinct between dimensional contexts. This difference holds serious implications for studies investigating migration in general, and in particular for analyzing intracellular signaling events that promote migration.

Early protrusion is a better surrogate for measurement of 3D migration response

Next, we sought to identify biophysical processes that may better reflect growth factor enhanced 3D motility. Within seconds following growth factor stimulation, cells respond through actin polymerization and lamellipodia protrusion, which can be measured in 2D as an area change [38, 110, 111]. We hypothesized that initial 2D protrusion may reflect eventual motility enhancement in 3D, particularly as 2D protrusion enhancement correlates with metastatic capacity and migration metrics in vivo in one case [33, 112, 139].

Acute changes in the area of MDA-MB-231 cells after growth factor stimulation were quantified (Fig. 2.6A). This "profile" of growth factor response (the 50^{th}, 90^{th} or 95^{th} quantile area change across growth factors) was then compared to that of each motility metric in differing dimensional contexts. We found that lamellipodial protrusion correlates positively with 3D migration (Fig. 2.6B). Upon comparison to all 2D motility assays and lamellipodial protrusion, 3D migration correlated better with the acute membrane protrusion response than with any 2D migration measurements (Fig. 2.6C). The generality of the link between migration in 3D and early

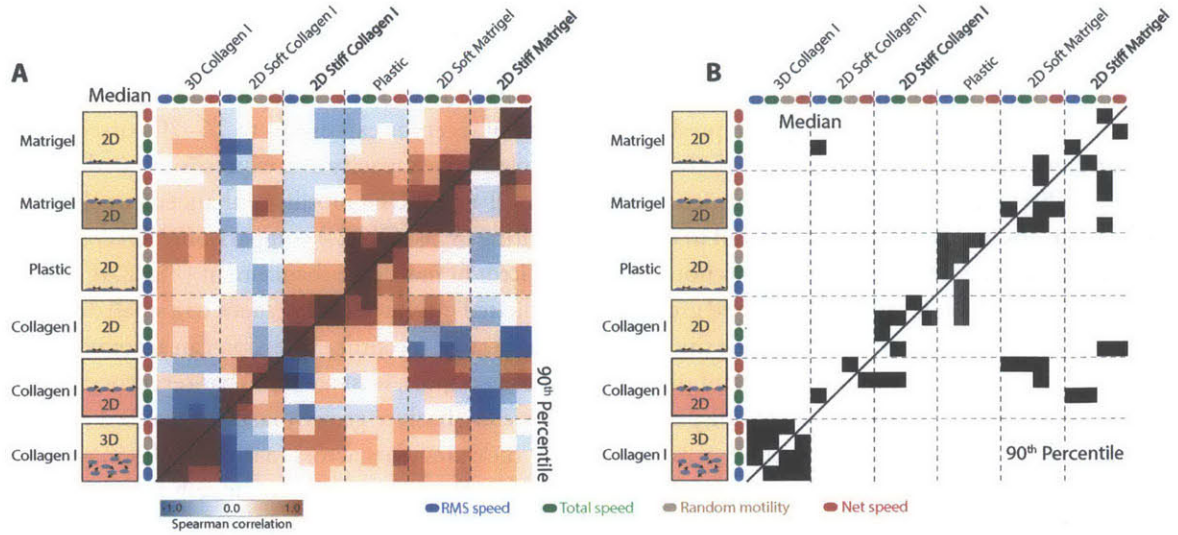

Figure 2.5: Motility enhancement in 2D and 3D in MDA-MB-231 is broadly distinct. A) All Spearman pairwise correlation coefficients between each motility metric in each 2D and 3D migration assay across growth factor stimuli. The upper and lower diagonals show coefficients corresponding to the median and 90th percentile response profiles respectively. B) Significant correlations ($p < 0.05$) are indicated in black. Correlations are observed along the diagonal between motility metrics, but not between different migration assays and 3D migration.

protrusion was tested independently by measuring protrusion across all growth factor conditions in MDA-MB-157 cells (Fig. 2.6A). Significant association between 3D migration and lamellipodial protrusion was once again observed despite differences in the growth factor responses between the two cell lines (Fig. 2.6D, 2.3A). This test is especially stringent, as it requires similarity across growth factors that promote different intracellular signaling responses [113, 140].

In order to more stringently test our observed link between initial protrusion and eventual migration in 3D, as well as to evaluate whether protrusion plays a specific causal role in 3D migration or is simply an auspicious measure of signaling, we selected three drugs which disrupt cytoskeletal elements to test whether 2D migration or protrusion would better predict eventual 3D migration. Notably, drugs which block migration in both 2D and 3D would not address our prediction, since we wish to assess the ability of protrusion to specifically evaluate 3D migratory capacity. Nocodazole and blebbistatin were selected for their documented distinct effects in 2D and 3D contexts [108], while cytochalasin D was chosen for its ability at low doses to block localization of Enah to the barbed ends of actin filaments [130, 141]. MDA-MB-231 cells were treated with the three drugs with or without EGF stimulation on stiff collagen in 2D (Fig. 2.6E and 2.7A) or in 3D collagen gels (Fig. 2.6F and 2.7B). In parallel, initial protrusion was evaluated as before (Fig. 2.6G). While, in general, 2D migration was not affected by any of the drug treatments, 3D migration was significantly reduced. These reductions corresponded well to a reduced protrusion response.

Our results ought not be taken to imply that modulation of membrane protrusion dynamics be considered to necessarily be the sole, or even predominant, mechanism of motility enhancement in response to growth factor stimuli. Evidence exists for modulation of other processes, such as contraction and proteolysis, to occur downstream of membrane protrusion. Focal proteolysis in 3D collagen gels has been suggested to be driven by pericellular constriction resulting from pseudopodial protrusion, promoting integrin and membrane-associated protease clustering [30, 132]. Whether by functional or phenomenological means, protrusion frequency and matrix deformation correlate significantly in 3D collagen [12, 50, 133–135]. Importantly, the correlation between acute actin polymerization responses and longer-term 3D migration response offers a window of opportunity for studying the interacellular signaling pathways important for driving 3D migration. The tractability of biochem-

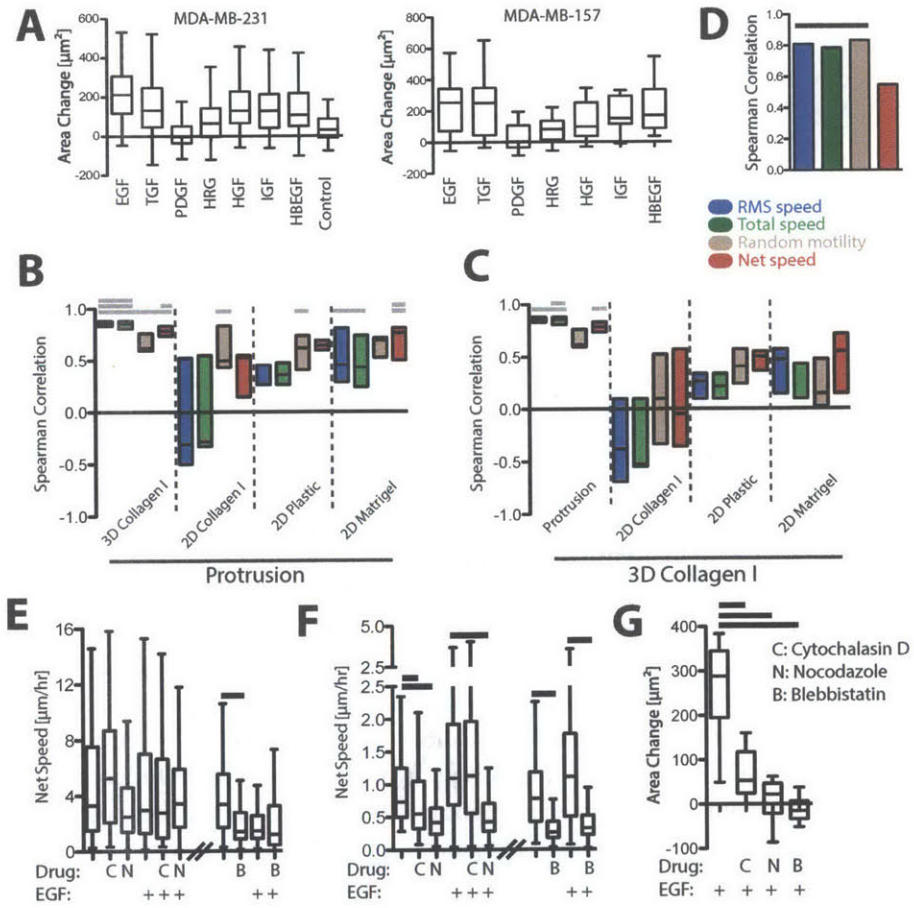

Figure 2.6: Protrusion correlates specifically with 3D motility enhancement. A) MDA-MB-231 and MDA-MB-157 cells were stimulated with each growth factor condition and the fold change in cell area calculated by manual tracing of DIC images (MDA-MB-231, N=60-138; MDA-MB-157, N=15-25). B) Rank correlation coefficients were calculated for MDA-MB-231 between the median, 90th percentile, and 95th percentile protrusion responses, and the migration responses across different metrics of migration and assays. Each box is bounded by the highest and lowest correlation calculated, with a line indicating the median correlation calculated. Bars above indicate the number of quantiles for which the correlation is significant (Storey correction, $q < 0.05$, 0.75 false positive). C) Similar analysis shows correlations between 3D motility, and protrusion or different 2D motility assays ($q < 0.05$, 0.2 false positive). D) Protrusion and 3D motility also correlate in MDA-MB-157 cells ($p < 0.05$). E) Net displacement of MDA-MB-231 cells treated with three cytoskeleton-related inhibitors with or without EGF stimulation on stiff collagen matrix. Bars above indicate significant differences with respect to the no inhibitor control ($p < 0.05$). F) Net displacement of cells treated similarly within 3D collagen gels. G) Protrusion in response to EGF stimulation for cells treated with each cytoskeletal drug.

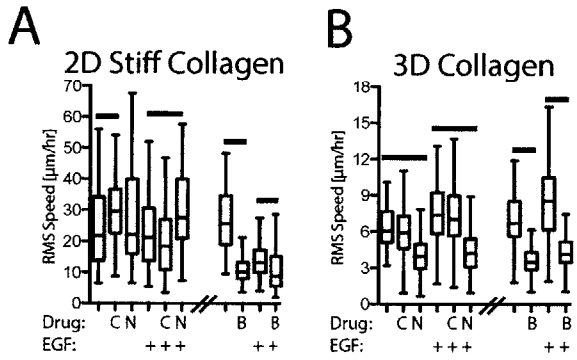

Figure 2.7: MDA-MB-231 cells show differing sensitivity to cytoskeletal perturbation in 2D and 3D. A) RMS speed of cells treated with three cytoskeleton-related inhibitors with or without EGF stimulation on stiff collagen matrix. Bars above indicate significant differences with respect to the no inhibitor control ($p < 0.05$). B) RMS speed of cells treated similarly within 3D collagen gels.

ical analysis from a plate of sparsely seeded cells with enough physical space for robust membrane protrusion is significant versus collection of cells or real-time analysis of signaling events within cells in a 3D matrix.

As migration within 3D was only observed with cells of one clinical subtype (ER-, PR-, HER2 normal), our observation of correspondence between short-term protrusion and migration in 3D remains to be tested for cells of other clinical subtypes and lineages. However, while bulk tumors may not be represented by the cell lines of mesenchymal phenotype, metastasis-relevant subpopulations may show a distinct expression signature [32]. Our results urge consideration of protrusion measurement, at least over measurement of 2D motility, as an indicator of 3D migration-relevant response.

A detailed mechanistic picture describing the modulation of multiple essential processes involved in interstitial migration remains to be constructed, with careful consideration of intricate forms of crosstalk between these processes an important key. Here, we have presented a systematic deconstruction of migration behaviors across an especially invasive and lethal subtype of breast cancer. Our findings point towards the initial steps in actin polymerization as an important regulator of invasive potential in these cells. Our contribution offers an improved basis for rational experimental design and pinpoint the timescale that may be most relevant for quantification. As migration in vivo may occur via directed paracrine cues from tumor-associated cell populations, high-throughput analyses of migration responses to growth factor cues are likely to reveal effective targets of metastatic suppression.

Methods

Antibody Reagents, Growth Factors and Inhibitors Antibodies against EGFR, IGF1R, Met, and GAPDH were purchased from Cell Signaling Technologies. EGF, PDGF-BB, and TGFα were purchased from Invitrogen. IGF1, HGF, HBEGF, and HRGβ1 were purchased from Peptrotech. EGF and IGF1 were used at 100 ng mL^{-1}, HRGβ1 at 80 ng mL^{-1}, and all others at 50 ng mL^{-1} for all experiments. (S)-(-)-Blebbistatin, cytochalasin D and nocodazole were purchased from Santa Cruz Biotechnology and used at 50 μM, 25 nM and 10 μM, respectively.

Cell Culture MDA-MB-231, BT-549 and MDA-MB-157 cells were cultured in high-glucose Dulbecco's modified eagle medium supplemented with 10% fetal bovine serum and 1% penicillin-streptomycin. SUM-159 cells were cultured in Ham's F12 media supplemented with 5 μg mL^{-1} insulin (Lonza), 1 μg mL^{-1} hydrocortisone (BD), 5% FBS and 1% penicillin-streptomycin.

MDA-MB-231, A549, BT-549, A172 and U87 cells were obtained from ATCC. Anna Starzinski-Powitz (University of Frankfurt) generously provided 12Z cells by way of Steve Palmer (EMD Serono).

Migration Analysis For 3D migration assessment, cells were labeled with CMPTX (Invitrogen) for 20 min and mixed with 2.2 mg mL^{-1} pH-neutralized, acid-extracted collagen I (BD) with Dulbecco's modified eagle medium at 500,000 cells/mL. The matrix-cell solution was placed in a glass-bottom multiwell plate (MatTek; Ashland, MA) and polymerized for 30 min at 37°C, then overlaid with full serum media overnight. Cells were stimulated four hours before imaging on an environment-controlled Nikon TE2000 microscope (Nikon Instruments; Melville, NY) with a Hamamatsu Photonics C4742-95-12ERG camera (Hamamatsu Photonics; Hamamatsu City, Japan). Image stacks of 70-3 μm slices were obtained every 60 min for 16 hrs using a 10× air objective and Metamorph (Molecular Devices; Sunnyvale, CA). Where indicated, inhibitors were added simultaneous to stimulation. To avoid artifacts due to potential gradients in stiffness near the edges of the gel, analysis fields were selected greater than 200 μm from the glass surface.

For soft 2D migration assays, 100 μL of pH-neutralized, acid-extracted 2.2 mg mL^{-1} collagen I or 100% matrigel was spread across wells of a 48-well plate and allowed to polymerize. For stiff 2D migration assays, either 100 μg mL^{-1} collagen I in 20 mM acetic acid or 0.2% matrigel in serum free medium was used to coat uncoated glass multiwall plates for 30 min (MatTek). Cells were then labeled with CMFDA (Invitrogen) for 20 min and seeded sparsely on wells with matrix or directly on tissue culture plastic. The next day cells were stimulated 4 hrs before imaging every 10 min for 16 hrs. Where indicated, inhibitors were added simultaneous to stimulation.

Cells were tracked using Bitplane Imaris. From each track, the root-mean-squared cell speed was calculated from position intervals between time points, as well as the standard deviation of the mean. Total and net speeds were calculated by dividing the total path length and net displacement by the duration of the experiment. Each track was then fit to a random walk model using the method of nonoverlapping intervals as described before to calculate the random motility coefficient [132].

Protrusion Assays Glass-bottomed dishes (MatTek) were coated with 0.2% matrigel in serum-free media for 30 min. Cells were seeded sparsely overnight, then serum starved for 4 hrs in L15 media with 0.35% bovine serum albumin. Inhibitors, when indicated, were added at the beginning of serum starvation. DIC images were acquired every 10 secs for 1 min before stimulation and 9 mins after stimulation. Cell areas were traced immediately before stimulation and 9 min post-stimulation using ImageJ.

Receptor Expression and Activation Measurement Cells were plated sparsely on 15 cm plates overnight, washed with PBS and lysed with 500 μL of RIPA buffer containing protease inhibitor (Roche) and phosphatase inhibitor cocktail (Boston Bioproducts). Equal protein was loaded for SDS-PAGE analysis using a bicinchoninic acid assay and blotted using standard techniques with antibodies against GAPDH, EGFR, IGF1R, and Met. Densitometry was performed on a LI-COR Odyssey (LI-COR Biosciences; Lincoln, NE) and normalized to GAPDH as a loading control.

For activation measurement, cells were seeded sparsely overnight and starved for 4 hrs the next day, followed by stimulation with either 100 ng/mL EGF or 50 ng/mL TGFα for 5 min. Cells were lysed using Biorad lysis buffer (Biorad) containing protease inhibitor (Roche) and phosphatase inhibitor cocktail (Boston Bioproducts). EGFR pan-pY was measured using a bead-based ELISA assay (Biorad) loaded with equal protein using a bicinchoninic acid assay. Linearity of the assay with respect to protein concentration was verified.

Numerical Analysis All analysis was performed in MatLab (Mathworks; Natick, MA). Single cell data from each experiment was imported, and each quantile of interest (50^{th}, 90^{th}, or 95^{th}) was calculated for each motility metric and condition. Each set of growth factor conditions within a given quantile was then normalized to the condition absent of growth factor stimulation (or mean centered if indicated). The mean and standard error were

then calculated from independent experiments. Comparisons of motility metrics between single growth factor conditions were performed using the Student's t-test, or the Mann-Whitney test for single cell data.

For single cell-based migration parameter clustering, Spearman correlation of the parameters for individual cells from all experiments for a single cell line in 3D ($N \geq 3$) were calculated and used to calculate pairwise distances, where perfect correlation corresponds to a distance of 0, and anti-correlation a distance of 2 ($1-\rho$). Multidimensional scaling in two dimensions captured >99% of the distance quantities for all cell lines. The first principle component captured 90-95% of the distance quantities, while the second principle component captured 5-10%. Standard error was calculated by jackknife, during which each cell was removed separately, and each time both the distances and scaling repeated [142]. For clustering of quantile-level migration metrics, each growth factor profile was mean-centered and averaged across experimental replicates. Clustering of profiles and growth factors was performed by rank correlation and average linkage.

Receptor expression and motility enhancement comparison was tested for significance using the binomial distribution. Where indicated, motility enhancement was variance normalized between cell lines by log transformation (so as to center fold-change values around zero) and division by the standard deviation across growth factor conditions.

Growth factor profiles were compared by calculating the Spearman correlation, and significance by permutation. Where many comparisons were performed, multiple hypothesis testing was performed as indicated. When comparing migration in 2D and 3D contexts, multiple hypothesis correction was not performed as Type I error is not a concern. When comparing protrusion and 3D migration results, identical quantiles of single cell data were always used.

Chapter 3

ADAM-10 and -17 regulate endometriotic cell migration via concerted ligand and receptor shedding feedback on kinase signaling

Abstract

A Disintegrin and Metalloproteinases (ADAMs) are the principal enzymes for shedding receptor tyrosine kinase (RTK) ectodomains and ligands from the cell surface. Multiple layers of activity regulation, feedback, and catalytic promiscuity impede our understanding of context-dependent ADAM "sheddase" function and our ability to predictably target that function in disease. This study uses combined measurement and computational modeling to examine how various growth factor environments influence sheddase activity and cell migration in the invasive disease of endometriosis. We find that ADAM-10 and -17 dynamically integrate numerous signaling pathways to direct cell motility. Data-driven modeling reveals that induced cell migration is a quantitative function of positive feedback through EGF-ligand release and negative feedback through RTK shedding. Although sheddase inhibition prevents autocrine ligand shedding and resultant EGFR transactivation, it also leads to an accumulation of phosphorylated receptors (HER2, HER4, & MET) on the cell surface, which subsequently enhances Jnk/p38 signaling. Jnk/p38 inhibition reduces cell migration by blocking sheddase activity while additionally preventing the compensatory signaling from accumulated RTKs. In contrast, Mek inhibition reduces ADAM-10 and -17 activities but fails to inhibit compensatory signaling from accumulated RTKs, which actually enhances cell motility in some contexts. Thus, here we present a sheddase-based mechanism of rapidly acquired resistance to Mek inhibition through reduced RTK shedding that can be overcome with rationally directed combination inhibitor treatment. We investigate the clinical relevance of these findings using targeted proteomics of peritoneal fluid from endometriosis patients and find growth-factor driven ADAM-10 activity and MET shedding are jointly dysregulated with disease.

Introduction

A Disintegrin and Metalloproteinases (ADAMs), especially ADAM-10 and -17, are the principal mediators of proteolytic ectodomain shedding on the cell surface [143]. ADAMs and the closely related matrix metalloproteinases (MMPs) work together as "sheddases" to cleave hundreds of diverse transmembrane substrates including growth factor ligands, receptor tyrosine kinases (RTKs), adhesion molecules, and even proteases themselves from the cell surface. Unfortunately, little is known regarding how such a broad palette of proteolytic activity integrates to modulate behaviors such as cellular motility. Furthermore, extensive cross-talk and complexity among signaling networks, proteases, and their substrates make understanding sheddase regulation on a component-by-

component basis challenging [144]. Therapeutics have targeted sheddases and their substrates for the treatment of invasive diseases such as cancer, yet many of these inhibitors have failed in clinical trials [145]. Therefore, a need exists for understanding how the balance of sheddase-mediated degradation integrates multiple layers of signaling networks to coordinately influence cell behavior in various disease contexts.

Here we study how sheddase activity contributes to cell migration in the invasive disease of endometriosis, defined by the presence of endometrial-like tissue residing outside the uterus. Up to 10% of adult females and 40% of infertile women have the disease, which also exhibits co-morbidity with several cancers [146, 147]. Endometriosis currently has no cure: hormonal therapies merely manage the disease with significant side-effects, and surgery provides only temporary relief for many, with recurrence rates as great as 40% within 5 years post-operation [148]. Like cancer, endometriosis is associated with aberrant cell invasion into ectopic organ sites, and endometriotic tissues often exhibit dysregulated molecular pathways commonly perturbed in other invasive diseases. Mitogenic and inflammatory phospho-signaling (for example, p-Erk1/2, p-Akt, & p-P38), receptor tyrosine kinases (RTKs, including epidermal growth factor receptor, EGFR), and metalloproteinases have all been clinically associated with endometriosis [149, 150], and consequently represent attractive therapeutic strategies [151–153].

Many challenges in developing targeted therapeutics stem from network-level complexities such as compensatory feedback, and recent work has demonstrated how critical such mechanisms are to achieving therapeutic success, especially in cancer [154, 155]. Computational models of systems-level biochemical networks have shown promise as tools to understand how multiple enzymatic reactions integrate to impact overall biological behavior, often with the goal of aiding the design of personalized or combination therapies [156, 157]. Considering its complex role in disease, sheddase regulation represents an ideal application of such network-level approaches. In this work, we apply the "cue-signal-response" (CSR) paradigm [156, 157] to examine how disease-implicated growth-factor "cues" interact with experimentally monitored phospho-protein and protease networks (collectively referred to as "signals"), ultimately to influence cellular migration "response." Computational modeling elucidates quantitative and predictive relationships among multiple layers of experimental data and offers testable hypotheses of context-dependent behavior and signaling feedback. We find ADAM-10 and -17 to be critical regulators of motility that are dynamically controlled through several signaling pathways, thereby affecting cell-behavior through both positive feedback from EGF-ligand release and negative feedback from MET, HER2, and HER4 RTK shedding. We find kinase inhibition generally reduces ADAM-10 and -17 activities, reduces subsequent RTK shedding, and consequently allows the accumulated RTKs to enhance downstream c-Jun N-terminal kinase (Jnk) and P38 signaling. Thus, here we demonstrate an ADAM-10 and -17 based mechanism of rapidly acquired resistance to kinase inhibition through reduced RTK shedding that can be overcome with combination therapy. Targeted proteomic analysis of clinical samples from endometriosis patients indeed confirms growth-factor driven ADAM-10 activity and consequent MET shedding are dysregulated with disease. Overall, our results have wide implications for designing combination therapies and identifying context-dependent personalized therapeutic strategies for both kinase and protease inhibitors.

Results

Overview of cue-signal-response (CSR) study design. We use a CSR approach to understand the signaling-regulated impacts of sheddase activity on cell migration from a multivariate, network-level perspective (Fig. 3.1A). First, we stimulate the immortalized 12Z cell line, a commonly studied in vitro disease model established from an endometriotic biopsy [158], with a panel of growth factor "cues" (see Table A.1 for references of clinical associations): epidermal growth factor (EGF), transforming growth factor alpha (TGFα), neuregulin beta-1 (NRG1β), hepatocyte growth factor (HGF), insulin-like growth factor 1 (IGF1), and platelet-derived growth factor-bb (PDGFbb). Post-stimulation, we quantitatively monitor an array of downstream molecular features, or "signals" (Fig. 3.1B-C). Nearly all "signals" in the CSR dataset are clinically associated with en-

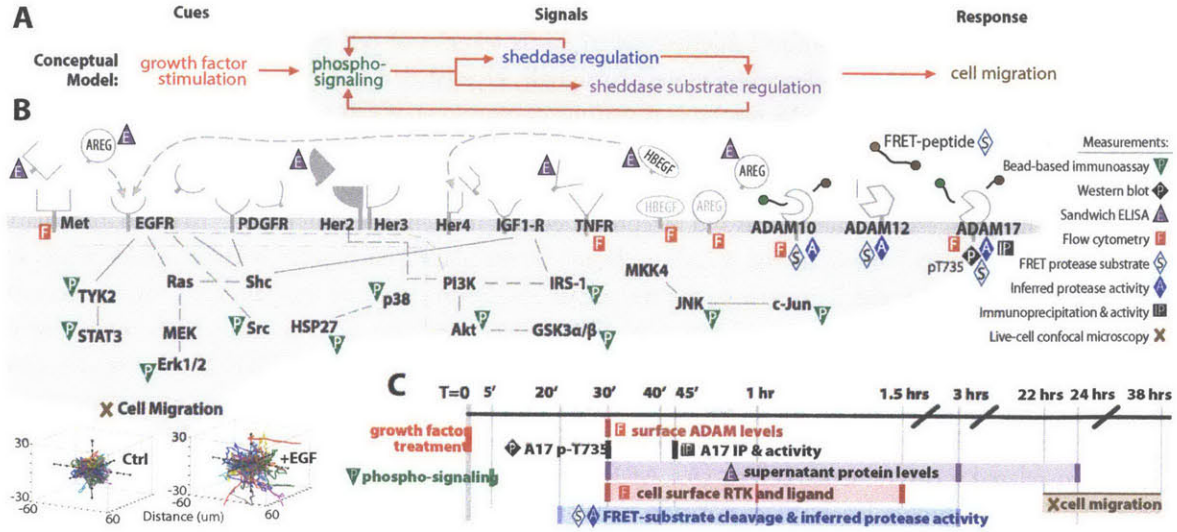

Figure 3.1: Cue-signal-response (CSR) study design. (A) CSR overview: we stimulate endometriotic cells with a panel of growth factor "cues," record multiple downstream "signals" comprising measurements of phospho-signaling, sheddase regulation, and sheddase substrate regulation, and use computational modeling to map these observations onto cell migration "responses." (B) Overview of "signals" and "responses" included in the CSR dataset. All receptors shown were directly measured and/or stimulated. (C) Experimental timeline of CSR study. Dark colored lines denote measurement time-points. At bottom left, cell migration is depicted as single-cell tracks, where initial cell positions were centered for visualization.

dometriosis (see Table A.1 for unabbreviated names and clinical evidence). To assess intracellular signaling, 5 min post-stimulation we measured levels of 11 key phospho-proteins using bead-based sandwich immunoassays (Fig. A.1).

We performed multiple measurements of key ADAM sheddases, themselves, following growth-factor stimulation. To directly assess ADAM-17 activity, we immunoprecipitated the enzyme from whole-cell lysate, incubated the bound protein with a FRET-substrate, and recorded cleavage rates by fluorimetry (Fig. A.2A). However, this approach disrupts protein complexes observed in the live-cell context. Therefore, we co-administered seven soluble FRET-based polypeptide substrates with growth factor treatments to assess regulation of general catalytic activity of proteases in live cells. Cleavage rates of these substrates were assessed by live-cell fluorimetry for several hours (Fig. A.2B-C). However, the FRET-substrates are by nature non-specific. We therefore used Proteolytic Activity Matrix Analysis (PrAMA) as an inference algorithm to estimate the effective concentrations of catalytically active ADAM-10, -12, and -17, based on FRET-substrate cleavage rates and prior knowledge of enzyme-substrate specificities [159] (Fig. A.2D-E). Additionally, we quantified ADAM-10 and -17 surface levels to assess protease trafficking (Fig. A.3A-H), and monitored levels of ADAM-17-pT735, which is thought to impact activity [160] (Fig. A.3I).

We investigated regulation of membrane-bound substrates by quantifying their cell-surface trafficking and proteolysis. To measure short-term shedding of heparin-binding-EGF (HBEGF, an EGF-ligand), we transgenically over-expressed it with a Myc-tagged ectodomain and a GFP-tagged c-terminus [161]. Immunostaining enabled quantification of intact HBEGF on the cell surface relative to total levels. These measurements were averaged over three time-points (30, 60, and 90 min.; Fig. A.4). For more highly expressed membrane-bound substrates (compared to HBEGF), we measured endogenous levels of surface-bound MET (also known as hepatocyte growth factor receptor), TNFR1 (tumor necrosis factor receptor 1), and amphiregulin (AREG, an EGF-ligand), averaged over three time points post-stimulation (30, 60, and 90 min.; Fig. A.5A). We also monitored supernatant levels of endogenous substrate at multiple times using enzyme-linked immunoassays (ELISAs), al-

though not all analytes were detectable at early time-points (Fig. A.5B-G).

Finally, we used time-lapse confocal microscopy to assess features of cell migration as "responses" to the growth-factor cues and previously-described molecular signals. Dye-labeled 12Z cultures suspended in collagen-I gels were individually tracked for 16 hours, and various descriptions of cell movement including total path length, net displacement, and the "random motility coefficient" derived from a thermodynamic-based model of the persistent-random-walk were calculated as metrics of single-cell motility for each condition [59] (Fig. A.6).

CSR modeling suggests parallel ligand and receptor shedding influence cell migration. To glean information from the full CSR dataset (shown in Fig. 3.2A), we began by calculating correlation between pairs of measurements as they varied across the 7 growth-factor treatment conditions. Significant pair-wise correlations were then graphically mapped in an unsupervised manner. This "correlation-network" encouragingly reflects several features of known biology (Fig. A.7A). For example, the greatest correlation among all phospho-signaling measurements lies between Jnk and its known substrate c-Jun (Fig. A.7B). ADAM-10 catalytic activity, as inferred by PrAMA, correlated very closely with supernatant accumulation of a known substrate, MET. Among the most negatively correlated measurements, cell-surface AREG was strongly anti-correlated with supernatant accumulation of AREG. At a higher level, the correlation-network suggests modularity among the data, where highly interconnected phospho-signaling events link to early (30 min – 3 hr) protease activity measurements primarily through ADAM-17 phosphorylation. These early markers of protease activity then correlate with supernatant accumulation of ligands and receptors by 24 hrs, which in turn are highly correlative with features of cell migration (Fig. A.7). Of all measurements in the CSR dataset, 3D cell migration features correlated most closely with ligand and receptor shedding. We tested if ligand/receptor shedding was affected by whether cells were cultured on 2D tissue culture plastic or in 3D collagen-I matrices. For those species included in the CSR dataset, we found significant agreement between results from these two cell culture models (Fig. A.8A), further suggesting that ligand/receptor shedding measurements made in 2D cultures sufficiently reflect shedding and migration behaviors observed in 3D cultures.

We performed principal components analysis (PCA) to describe measurements from the CSR dataset in terms of key axes of co-variance, or principal components (PCs), as they varied across the growth factor treatments. The scores/loadings plot describes where each of the growth factor treatments and measurement variables fall along the first two PCs, which capture 40% and 25% of the total data variance, respectively (Fig. 3.2B; shown fully labeled in Fig. A.8B). Similar to results from the correlation-network, modularity can also be observed in the PCA scores/loadings plot. The lower right quadrant is largely populated with phospho-protein levels and short-term metrics of substrate shedding, and these are anti-correlated with surface levels of endogenous substrate (AREG and Myc-HBEGF) in the top-left quadrant. The top right quadrant associates with persistent migratory behavior, and is populated with ADAM-10 and -17 activities (inferred by PrAMA), along with levels of supernatant ligands/receptors at 24 hr. Direct comparison of correlations between CSR dataset measurements and the "random motility coefficient" echo the PCA results: supernatant ligand/receptor at 24 hr. represent by far the most correlative indicators of cell migration, led by AREG and MET as the top two features (Fig. 3.2C).

Taken together, these results suggest that growth-factor stimulation directly regulates the effective concentration of catalytically active sheddases, which then leads to similar (although not identical) patterns of shedding across multiple endogenous and FRET-based substrates. Furthermore, these patterns of substrate proteolysis correlate extremely well with cell migration, suggesting that sheddases significantly influence motility.

Joint AREG and MET shedding predict cell migration. Although individual shed analytes significantly correlate with features of cellular motility, single-variable relationships between shedding and motility fail to accurately predict motile responses under untested conditions in a sufficiently quantitative manner, with a prediction accuracy of $Q2<50\%$. Consequently, we implemented partial least squares regression (PLSR) as a statistical method to distill the effects of multiple shedding events into key axes of control (PCs, as with PCA), that quantitatively combine to describe overall migration behavior. More specifically, we used an optimization algorithm to build a reduced PLSR model that optimally selects the minimal set of descriptor variables from the CSR dataset that predict migration with high accuracy. To improve model accuracy, we included additional measurements,

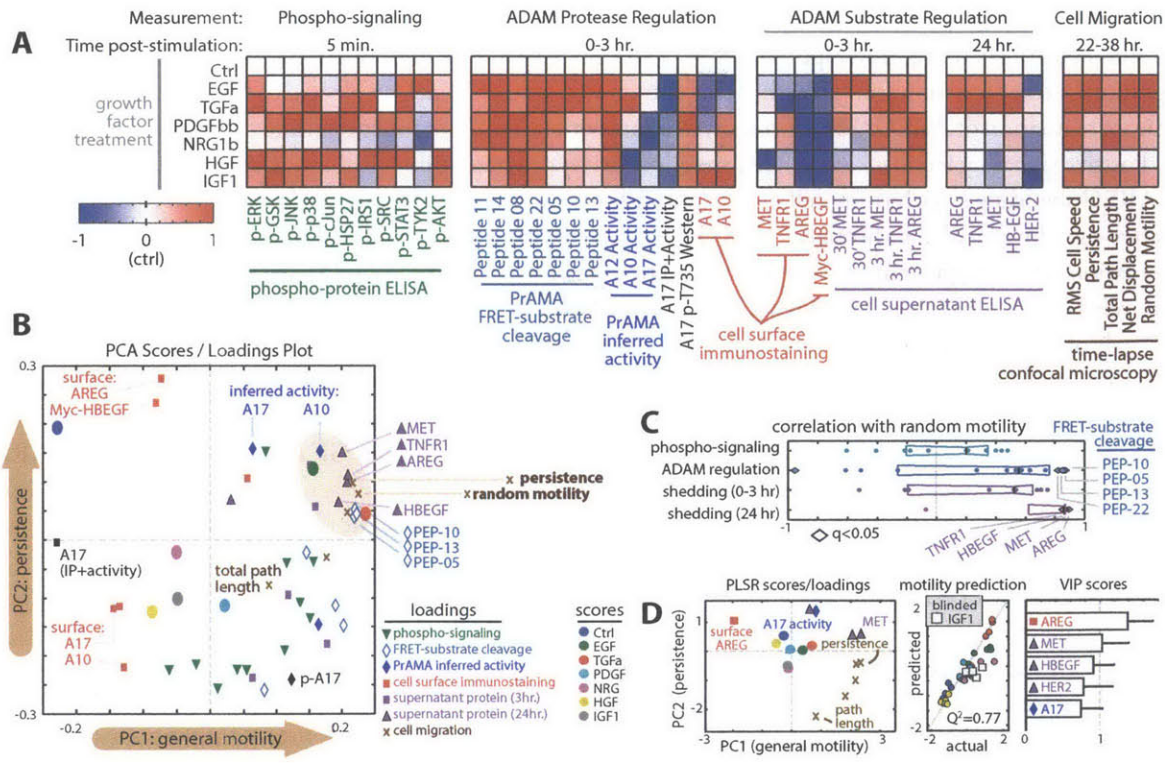

Figure 3.2: CSR modeling suggests dual ligand/receptor shedding influences cell migration. (A) Heat-maps depict CSR dataset, at time-points described in Fig. 3.1C. Data were normalized by control-centering and scaling max abs. value to 1. (B) PCA presents an unsupervised description of co-variation within the CSR dataset values in A. The brown ellipse denotes measurements most associated with persistent cell migration. (C) AREG and MET shedding by 24 hrs post-stimulation most closely correlate with random motility, among all measurements in the CSR dataset (q-value denotes multiple-hypothesis-corrected p-value). Box-and-whisker bars show the 1st – 3rd quartiles. (D) The reduced PLSR model describes features of cell migration as a function of select variables from the CSR dataset. The scores/loadings plot (left) describes co-variance among the descriptor variables and migration features. Cross-validation prediction accuracy (Q2=77%) was determined with IGF1 measurements blinded from the optimization routine (center plot). Model descriptors were ranked by importance according to VIP score (right plot). Error bars denote SEM.

made in the presence of a broad-spectrum metalloproteinase inhibitor (BB94) and an EGFR blocking antibody (mab225), to determine the dependency of shed analyte accumulation on sheddase activity and EGFR endocytosis of autocrine ligand (data shown in Fig. A.5). Among all measurements in the "expanded" CSR dataset, metrics of AREG and MET shedding were the two most important variables chosen by the algorithm (Fig. 3.2D; fully labeled scores/loadings in Fig. A.8C). Although patterns of MET and AREG shedding closely correlate with each other, PLSR model accuracy significantly improves when both are included together, suggesting subtle underlying mechanisms of substrate-specificity. Indeed, PLSR accuracy relies upon multiple principal components for accurate prediction accuracy (Fig. A.8D), implying multiple axes of substrate shedding regulation.

In addition to supernatant ligand/receptor accumulation, we also measured accumulation of MMPs and tissue inhibitor of metalloproteinases (TIMPs) across the panel of growth factor treatments (Fig. A.9A). The aims here were to investigate enzymes more associated with extracellular matrix degradation, and to examine their ability to predict cell migration compared to ligand/receptor levels. In comparison to ligand/receptor shedding, however, MMP/TIMP levels generally did not significantly correlate with or help in prediction of cell migration (Fig. A.9B-C). This indicates that, at least with respect to growth factor stimulation, cell motility is principally regulated outside modulation of MMP/TIMP expression.

Overall, the correlation-network modeling, PCA results, and PLSR models all suggest that concomitant ligand and receptor shedding, and especially AREG and MET shedding, are key determinants of endometriotic cell migration in response to various growth factor cues. Based on this model, we elected to further experimentally investigate regulation of AREG/MET proteolysis along with its resultant functional and therapeutic consequences.

Positive signaling feedback via AREG shedding drives cell migration. CSR modeling results predicted a role for AREG shedding in governing cell migration, and we next sought to investigate its potential role in mediating positive signaling feedback through EGFR. Experiments with BB94 demonstrated that AREG supernatant accumulation is metalloproteinase-dependent, and treatment with mab225 provided evidence that soluble AREG is actively being endocytosed via EGFR in an autocrine manner (Fig. 3.3A). Interestingly, we found that saturating levels of TGFα, which is known to exhibit higher binding affinity to EGFR compared to AREG [162] and likely inhibits AREG-EGFR binding, stimulates even greater AREG supernatant accumulation. This result suggested a positive feedback loop similar to those described previously [163], whereby EGFR signaling promotes AREG shedding, in turn enhancing further EGFR signaling. Stimuli beside EGF-ligands also stimulated AREG shedding, including the inflammatory cytokine TNFα (Fig. 3.3A), which transactivates EGFR in an EGF-ligand dependent manner (Fig. 3.3B). Furthermore, TNFα stimulation enhanced the effect of mab225 treatment in reducing cellular migration (Fig. 3.3C-D).

With evidence of AREG-mediated EGFR transactivation, we examined whether growth factor stimulation sensitized cell motility to EGFR kinase inhibition. For this and all subsequent cell migration experiments, we employed a migration endpoint assay (Fig. A.11). Briefly, cells were seeded under collagen-I gels and exposed to bath application of growth factors after 1 hr. treatment with inhibitors. We quantified cellular migration into gels 24 hr. later (Fig. 3.3E). Although EGFR kinase inhibition using gefitinib (an EGFR inhibitor) and lapatinib (a dual EGFR/HER2 inhibitor) was ineffective at reducing cellular motility under basal conditions, nearly every tested growth factor sensitized cells to kinase inhibition (Fig. 3.3F-G & A.10). We compared AREG shedding to gefitinib sensitivity across the growth-factor treatments and found significant correlation (Fig. 3.3G). AREG shedding is particularly enhanced with IGF1 treatment, and IGF1 sensitized cells most to gefitinib compared to other non-ErbB growth factors. Examination of p-EGFR in IGF1 treated cells confirmed EGFR-transactivation (Fig. 3.3G). Treatment with an anti-AREG decoy antibody effectively reduced both basal and IGF1-induced cellular motility, confirming a specific role for AREG among other potential EGF-ligands (Fig. 3.3H). In sum, this data provides further evidence for the role of AREG-mediated positive signaling feedback in endometriosis cell migration.

EGFR autocrine signaling regulates ADAM-10 and -17 catalytic activities. We next examined how AREG shedding itself is regulated by ADAM proteases, particularly in the context of EGFR signaling feedback. Direct examination of ADAM-10 and -17 catalytic activity in live-cells using PrAMA revealed that the positive feedback via EGFR activity occurs at least in part through direct regulation of ADAM-10 and -17 catalytic activity (Fig. 3.4A). EGF and TGFα treatment led to an increase in FRET-substrate proteolysis, while mab225 treatment led to a decrease (Fig. A.11A). These effects were also seen with endogenous sheddase substrates (besides AREG). For example, mab225 treatment led to an increase in surface TNFR1 and a decrease in its supernatant accumulation (Fig. A.11B-C). However, the exact mechanisms of protease regulation remain unknown. Although EGF stimulation led to decreased ADAM-17 dimerization (Fig. A.3J-K) and increased ADAM-17 pT735 (Fig. 3.2A), mab225 treatment did not elicit changes in ADAM-17 dimerization (Fig. A.11D-E), ADAM-17 activity as measured after immunoprecipitation (Fig. A.11F), ADAM-17-pT735 (Fig. A.11G), or ADAM-17 surface levels (Fig. A.11H). Nonetheless, PrAMA results combined with decreased endogenous substrate shedding suggest decreasing ADAM-10 and -17 catalytic activities in response to mab225 treatment. Given these complex results, we decided to perform additional computational modeling to formulate testable hypotheses as to how proteases may regulate substrate shedding in response to various signaling cues.

AREG shedding is controlled by ADAM-10 and -17 in a context-dependent manner. We constructed reduced PLSR models to describe endogenous substrate shedding as a function of phospho-proteins, protease surface-levels, and protease activity (including PrAMA and the IP+activity assay). PLSR results decomposed

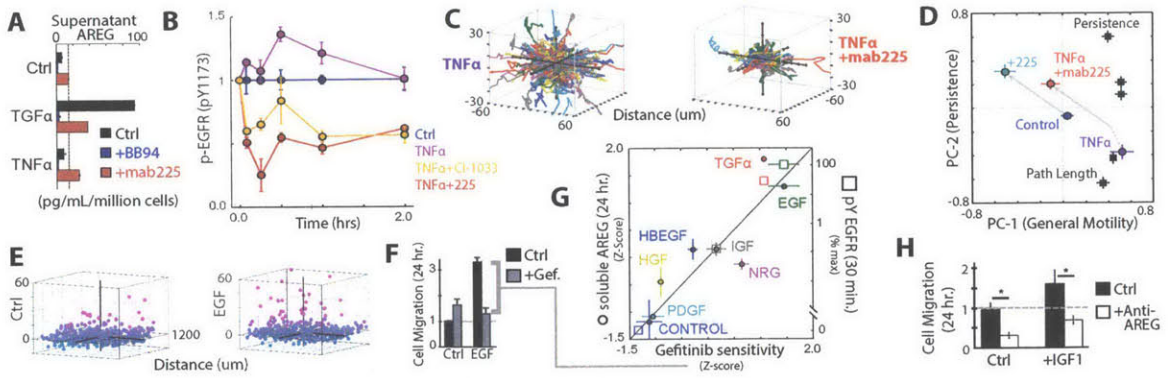

Figure 3.3: EGFR transactivation through AREG shedding sensitizes 12Z to EGFR inhibition. (A) AREG levels reveal induced shedding and autocrine uptake via EGFR (24 hr. post-treatment; ELISA; see Fig. A.5G for details). (B-D) TNFα stimulates EGFR pY1173 (B; bead immunoassay) and motility (C-D) in an EGFR-ligand dependent manner. In D, cellular-motility was described using PCA of time-lapse microscopy measurements 22-38 hr. post-stimulation (shown as single-cell tracks in C., where initial cell positions were centered for visualization). Scores (circles) and loadings (squares) are plotted. (E) 12Z nuclei positions demonstrate EGF-stimulated migration into collagen-I gels as a function of distance from the plate-bottom, shown quantified in (F). Treatment with gefitinib blocks the effect of EGF added 1 hr. later. (G) Supernatant AREG (left axis; ELISA) and p-EGFR levels (right axis; bead immunoassay) correlate with the gefinitib efficacy in reducing cell migration. (H) Anti-AREG decoy Ab treatment inhibits basal and IGF1-stimulated cell migration in the endpoint assay. (*$p<0.05$; single-tailed Student's t-test). All error bars denote SEM.

substrate proteolysis along two PCs, with PC-1 describing overall shedding and PC-2 distinguishing ligands vs. receptors (Fig. A.12A-B). Interestingly, the PLSR results suggested a concerted role for both ADAM-10 and -17, where each protease exhibits more-or-less influence depending on the growth-factor context (Fig. A.12C-D). Indeed, knockdown of either ADAM-10 or -17 reduces shedding of all the substrates tested (Fig. A.12E). One particular hypothesis from the PLSR modeling is that EGF and TGFα stimulation drive ADAM-10 activity more than ADAM-17 activity. These results were primary determined by observations that (a) EGF and TGFα lead to decreased activity measured in the ADAM-17 IP+activity assay, (b) EGF and TGFα stimulate downregulation of ADAM-17 surface levels, and (c) PrAMA infers that EGF and TGFα stimulate significantly more ADAM-10 activity than ADAM-17 activity (Fig. 3.2A). Consequently, although AREG is predominantly thought of as an ADAM-17 substrate [164], PLSR results suggest that EGF-stimulated AREG shedding may actually be occurring via ADAM-10. Using recombinant ADAM-10 prodomain as a specific inhibitor, we found ADAM-10 inhibition to cause increased AREG surface levels under EGF-stimulated, but not basal, treatment conditions (Fig. 3.4B). Furthermore, ADAM-10 inhibition only decreased supernatant AREG accumulation after EGF stimulation (Fig. 3.4C). siRNA knockdown of ADAM-10 showed a greater inhibitory effect on AREG supernatant accumulation in EGF-stimulated cells (Fig. 3.4D). In contrast, ADAM-17 knockdown equally reduced AREG shedding under basal and EGF-stimulated conditions (Fig. 3.4D). Direct examination of specific ADAM activities in the siRNA-treated cells using PrAMA suggests that ADAM-10 does not impact ADAM-17 activity, further supporting a specific role for ADAM-10 in shedding AREG (Fig. 3.4E). Finally, western blots show metalloproteinase-dependent, EGF-stimulated cleavage of pro-AREG in cell lysates (Fig. A.13A-C), and digestion of immunoprecipitated pro-AREG with recombinant ADAM-10 and -17 demonstrated that both enzymes are capable of acting upon AREG and generating cleavage products similar to those seen in the EGF-stimulated lysate (Fig. A.13D-F). Overall, these results provide evidence for EGF-stimulated ADAM-10 activity and a context-dependent dual role for ADAM-10 and -17 in regulating substrate shedding.

ADAM-10 inhibition reduces cellular migration. Consistent with the CSR modeling results showing the importance of ADAM-10 activity (as inferred using PrAMA) for cell motility, we found that ADAM-10 knockdown substantially decreased basal motility (Fig. 3.4F). Additionally, a specific ADAM-10 inhibitor

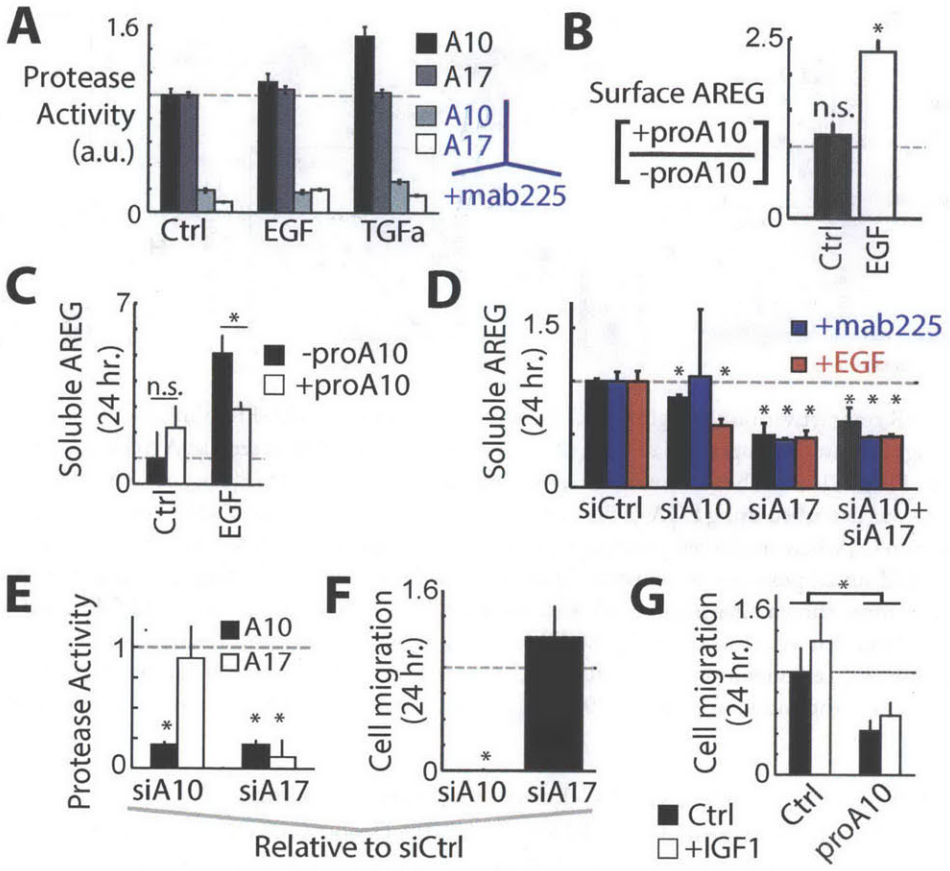

Figure 3.4: Both ADAM-10 and -17 contribute to AREG shedding. (A) PrAMA indicates mab225 treatment reduces ADAM activities. Following 30 min. of mab225 treatment, FRET-substrates and growth factors were simultaneously added to serum-starved 12Z cultures, and protease activities were recorded by fluorimetry for 3 hr. post-stimulation. (B) ADAM-10 inhibition only increases surface AREG under EGF-stimulation, quantified by immunostaining following 24 hr. treatment with proADAM10 and EGF. (C) proADAM10 treatment significantly reduces levels of supernatant AREG in the presence of EGF (ELISA). (D) Both ADAM-10 and -17 siRNA treatment reduce supernatant AREG levels (ELISA). (E) ADAM-17 knockdown reduces basal ADAM-10 activity, but not vice-versa (PrAMA). (F) ADAM-10 knockdown blocks cell migration in the endpoint assay. (G) proADAM10 treatment inhibits basal and IGF1-stimulated cell migration in the endpoint assay. All error bars denote S.E., * $p<0.05$, Student's t-test.

(proADAM10) significantly reduced basal and IGF1-stimulated cell motility (Fig. 3.4G). In contrast, ADAM-17 knockdown did not show an effect on basal cell motility (Fig. 3.4F), possibly due in part to previously reported adhesion-related protein functions [111, 164, 165]. Notably, however, ADAM-17 activity (as inferred using PrAMA) did not significantly correlate with cell motility in a positive manner in the CSR dataset, and ADAM-17 IP+activity results significantly anti-correlated with features of cell migration. Taken together, these data demonstrate that ADAM-10 influences cellular migration, owing at least in part to its role in mediating AREG shedding and autocrine EGFR signaling.

Negative signaling feedback via RTK shedding reduces Jnk/p38 signaling. In addition to positive signaling feedback from AREG, CSR modeling suggested the shedding of RTKs (principally MET) also plays a role in governing cell migration. We hypothesized that RTK shedding functions as a mechanism of negative signaling feedback by attenuating receptor phospho-signaling. Indeed, direct protease inhibition using BB94 led to increased full-length p-HER2 & p-HER4 (Fig. 3.5A), total & p-MET (Fig. 3.5B), and p-p38 & p-cJun (Fig. 3.5C). Supernatant MET, HER2, and HER4 correspondingly decreased (Fig. A.1 & A.14A). We also found that BB94-

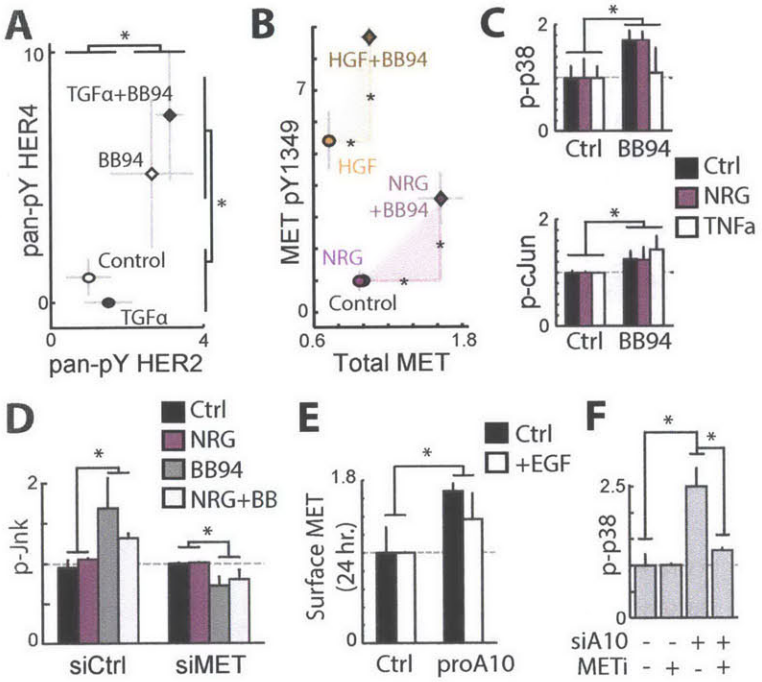

Figure 3.5: ADAMs mediate negative signaling feedback via RTK shedding. (A) Full length p-HER2 and p-HER4 levels increase with 1.5 hrs BB94 treatment (bead immunoassay). Subsequent 30 min TGFα-treatment didn't alter BB94 effects. (B) 1.5 hrs BB94 treatment followed by 30 min treatments with NRG1β and HGF lead to higher total, full-length MET (x-axis) and MET pTyr1349 (y-axis) (western blot; see Fig. A.14B for images). (C) BB94 increases p-cJun and p-p38 (bead immunoassay). Cells were stimulated with NRG1β and TNFα for 30 min. following 1.5 hrs BB94 treatment. (D) BB94 increases p-Jnk levels in a MET-dependent manner. Following siRNA knockdown of MET, cells were treated with BB94 for 1.5 hrs and stimulated with NRG1β for 30 min. (bead immunoassay). (E) 24 hrs proA10 treatment increases surface MET levels, ± co-treatment with EGF, detected by immunostaining. (F) ADAM-10 knockdown increases basal p-P38 levels in a MET-dependent manner, using 1.5 hrs treatment with the MET inhibitor foretinib (bead immunoassay). All error bars denote SEM, *p<0.05, Student's t-test.

induced p-Jnk elevation could be blocked with MET knockdown, further suggesting that enhanced signaling was due to accumulation of MET on the cell surface (Fig. 3.5D). Experiments confirmed that protease-inhibition effects were related to ADAM-10, the principal MET sheddase. Specific inhibition of ADAM-10 led to an accumulation of cell-surface MET (Fig. 3.5E), and we found ADAM-10 knockdown led to an increase in p-P38 that could be blocked using the MET inhibitor foretinib (Fig. 3.5F). Overall, these results demonstrate that ADAM-10 mediated RTK shedding functions as a negative signaling feedback mechanism, and that direct inhibition of sheddase activity leads to the accumulation of HER2, HER4, and MET, along with enhanced signaling through p38/Jnk/cJun signaling pathways.

Indirect sheddase downregulation via kinase inhibition mediates drug resistance. Given evidence that sheddase activity can be activated by multiple signaling pathways, we next interrogated the effects of various kinase inhibitors on protease activity. In general, treatment with various Mek, Jnk, p38, and PI3K inhibitors broadly reduced the accumulation of both receptor and ligand sheddase substrates in cellular supernatant (Fig. 3.6A). The Mek inhibitor U0126 was also found to reduce supernatant TNFR1 levels within 30 min. of treatment (Fig. A.15A), and multiple kinase inhibitors led to increased surface TNFR1 levels after 1 hr of treatment (Fig. A.15B). We found U0126 treatment to elicit no change in ADAM-17 dimerization (SI-16C), phosphorylation (Fig. A.15D), surface levels (Fig. A.15E-F), or ADAM-10 surface levels (Fig. A.15G), and the ADAM-17 IP + activity assay only showed a slight decrease with U0126 treatment (Fig. A.15H). In contrast, live-cell measurements using PrAMA indicated a substantial reduction in ADAM-10 and -17 catalytic activities with ki-

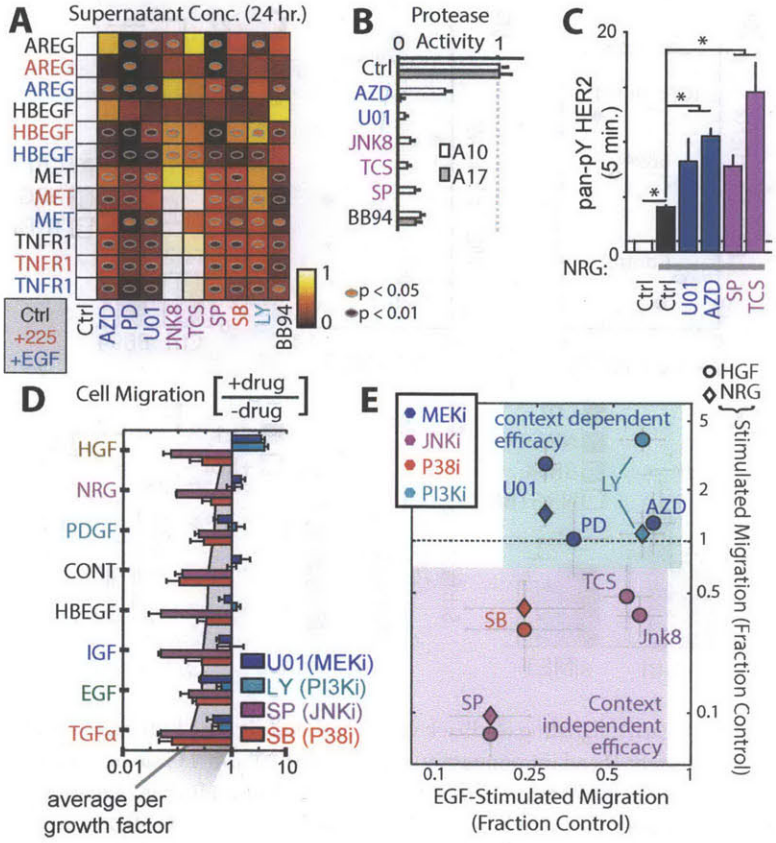

Figure 3.6: Decreased ADAM activity via kinase inhibition mediates drug resistance. (A) 24 hr. treatments with kinase inhibitors that target Mek (blue), Jnk (magenta), p38 (red), and PI3K (cyan) lead to reduced supernatant levels of ligands and RTKs (ELISA). Cells were also co-treated with EGF or mab225. (B) PrAMA-inferred sheddase activities decrease in response to 4 hrs Mek and Jnk inhibitor treatment. (C) NRG1β-induced p-HER2 increases following a 1.5 hr pre-treatment with Mek and Jnk inhibitors (bead immunoassay). (D) Mek and PI3K inhibitor efficacies depend on growth factor context, while Jnk and p38 inhibitors do not (24 hr. endpoint migration assay). (E) Data from D were combined with experiments using additional Jnk and Mek inhibitors, and results are plotted to highlight differences in inhibitor efficacy under EGF- vs. HGF/NRG1β- stimulated conditions. All error bars denote S.E., *p<0.05, Student's t-test.

nase inhibition (Fig. 3.6B). Based on these results, we hypothesized that indirect sheddase inhibition secondary to kinase inhibition could lead to compensatory signaling from reduced RTK shedding. Indeed, we found that pre-treatment with Mek or Jnk inhibitors increased full-length p-HER2 levels following NRG1β stimulation (Fig. 3.6C).

We next tested whether kinase inhibitors, and their indirect effects on RTK shedding, would have an impact on cellular migration in response to various growth factor stimuli (Fig. 3.6D). Results show two distinct patterns of inhibitor efficacy: p38 and Jnk inhibitors strongly reduced 12Z motility under all growth factor treatment conditions, while in contrast, Mek and PI3K inhibitors demonstrated context-dependent efficacy (Fig. 3.6D). While Mek and PI3K inhibitors effectively reduced EGF and TGFα stimulated motility, they actually enhanced motile responses to NRG1β and HGF. We further tested context-dependency using alternative Mek and Jnk inhibitors, and found results to be consistent (Fig. 3.6E & A.15I). To explain these differences, we measured NRG1β-stimulated p-p38 levels after 1 hr pre-treatment with Jnk or Mek inhibitors. Results indicated that compared to Jnk inhibition, Mek inhibition was unsuccessful in reducing p-p38 (Fig. A.15J). Overall, these data suggest that compensatory signaling through unshed RTKs, primarily through p38 and Jnk signaling pathways,

can lead to Mek inhibitor resistance. Moreover, this compensatory signaling can become amplified in the presence of ligands that stimulate ADAM-substrate RTKs (such as NRG1β and HGF).

Combined MET-Mek inhibition blocks motility across multiple growth factor contexts. Given our evidence that protease inhibition can enhance MET signaling and that Mek inhibitor resistance in part arises from reduced sheddase activity, we hypothesized that Mek insensitivity in the presence of HGF and NRG1β is mediated by enhanced MET signaling. Using foretinib as an inhibitor of MET (and several other ADAM substrate RTKs, including VEGFR-2), we found that combination Mek/MET inhibition was more effective than either inhibitor alone, under multiple growth-factor contexts (Fig. 3.7A-B). Combination Mek/MET inhibition reduced basal p-Jnk levels more than either inhibitor alone (Fig. 3.7C). U0126 treatment only blocked NRG1β-stimulated migration when combined with MET siRNA treatment (Fig. 3.7D). Individual effects from MET siRNA and U0126 were not significant in this experiment. Overall, these results confirm the importance of alternative MET signaling in the context of Mek inhibition and reduced MET shedding.

Clinical samples suggest dysregulated ErbB-signaling and ADAM-10 activity with disease. Finally, to test for relevance of our *in vitro* findings to *in vivo* pathophysiology in human patients, we analyzed surgically obtained peritoneal fluid (PF) from patients with and without endometriosis. PF comprises a heterogeneous mixture of leukocytes, cell debris, and soluble proteins that interact with endometriotic lesions. We analyzed clarified PF samples using a targeted proteomics approach that utilized roughly the same reagents employed in 12Z supernatant profiling experiments, assessing total protein levels using sandwich immunoassays and comparing these to previously reported proteolytic ADAM and MMP activities from the same patient samples [166] (Fig. 3.8A). Due to the large number of highly correlated measurements in each patient sample, we decomposed the data into an interpretable set of PCs using PCA. The first and third PCs best capture differences between control and disease PF samples (Fig. 3.8B; fully labeled in Fig. A.16A). Interestingly, disease samples fall into two distinct clusters in PC-space, with one cluster defined by relatively high levels of ADAM-10 activity and high concentrations of ADAM-10 substrates including EGF, AREG, HER2, and HER4. In agreement with our in vitro finding that AREG is a substrate of ADAM-10 (Fig. 3.4), we observed significant correlation between ADAM-10 activity and concentrations of HER2 and AREG in the PF samples (Fig. A.16B). In contrast to the high ADAM-10 cluster of disease samples, the second cluster of disease samples exhibits relatively low ADAM-10 activity, higher levels of ADAM-10 inhibitors (TIMPs), and higher levels of ADAM-9 activity. Of note, ADAM-9 is not inhibited by TIMPs [167]. The control samples form a non-overlapping cluster between the two disease clusters. Although the sample size is small (n = 7 disease samples), PCA results suggest multiple disease states in endometriosis that are defined principally by dysregulation of ADAM-10 activity and corresponding changes in ADAM-10 substrate accumulation.

We then used supervised PLS-DA to classify patient samples as falling into one of the three patient clusters based on a minimal number of protein measurements. PLS-DA shows that combined measurement of ADAM-9 activity and three ADAM-10 substrates (HER2, AREG, and HBEGF) can sufficiently classify patients with high (>95%) accuracy (Fig. A.16C-D). We also used PLS-DA to classify patient samples into just two groups, disease and control, and observed that combined measurements of MMP-2 activity along with MET and TIMP1 levels sufficiently classify samples as either disease or control with high (>95%) accuracy (Fig. A.16E-F). We analyzed the simple ratio of MET to TIMP1 levels for a more interpretable result, and observed a significant increase with disease (Fig. 3.8C). To identify the likely cellular source of increased MET shedding in the PF samples, we analyzed various cell populations from healthy and endometriotic patients, including eutopic endometrial fibroblasts and peritoneal fluid mononuclear cells (PFMCs). Compared to 12Z, PFMCs shed only 10% the relative levels of MET (Fig. A.17A). In contrast, endometrial fibroblasts, which generally express significant MET [168], shed similar levels of MET as 12Z (Fig. A.17B). Experiments with primary endometrial fibroblasts demonstrate that EGF stimulates dual EGF-ligand and MET shedding in other relevant endometrial cell populations (Fig. A.17B-C). Therefore, both endometriotic lesions and endometrial fibroblasts represent significant sources of total MET observed in the peritoneal fluid, particularly in those patients with elevated ErbB ligand present. Consequently, the ratio of MET to TIMP1 may be a good surrogate marker of ADAM-10 activity on endometrial and en-

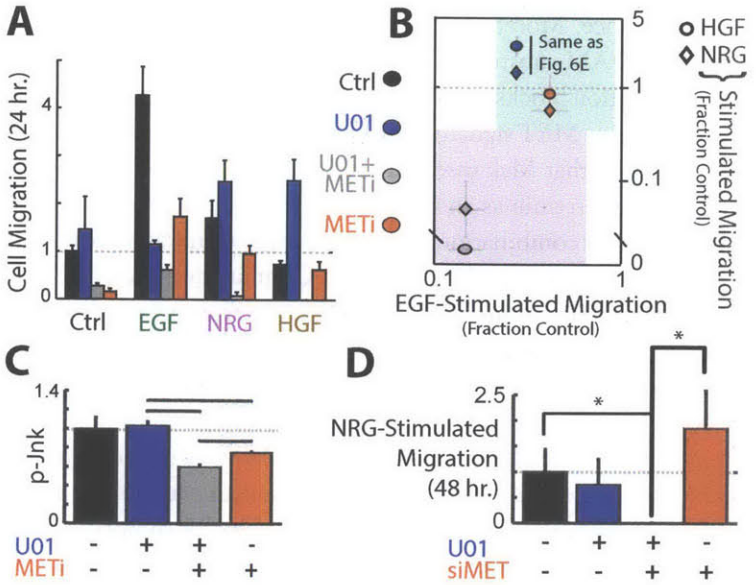

Figure 3.7: Combination MET and Mek inhibition overcomes sheddase-mediated drug resistance. (A-B) 1 hr. pre-treatments with Mek (U0126) and MET (foretinib) inhibitors reduce 12Z migratory response to growth factor stimulation in the endpoint migration assay. Combination treatment exhibits enhanced efficacy. (C) 1 hr combination MET/Mek inhibition using foretinib and U0126 leads to reduced p-Jnk (bead immunoassay). (D) Combination MET knockdown and Mek inhibitor (U0126) synergistically block NRG1β-stimulated cell migration in the endpoint migration assay. Neither MET-knockdown nor U0126 treatment had a significant effect individually. All error bars denote S.E., *p<0.05, Student's t-test.

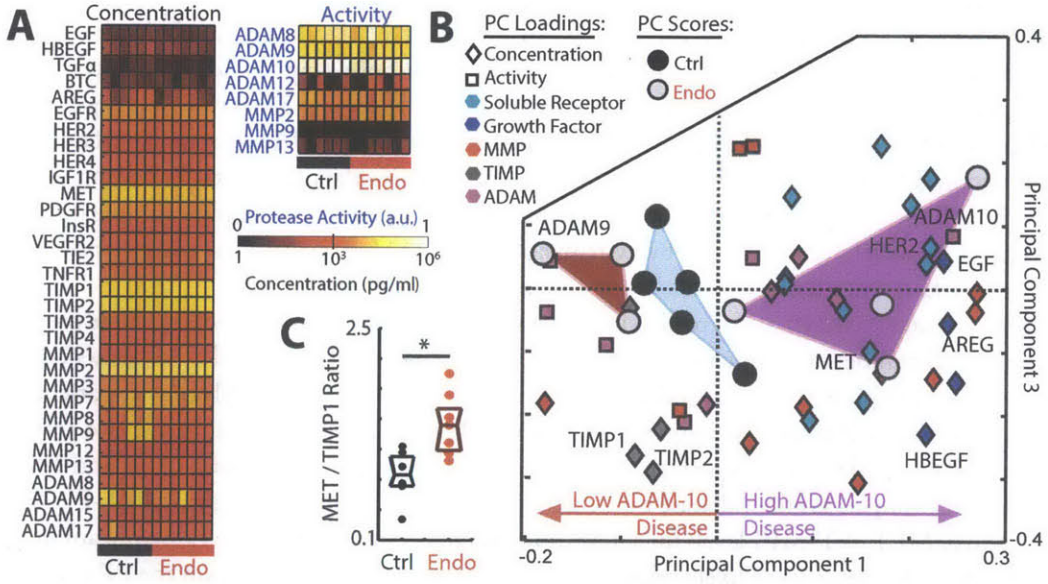

Figure 3.8: Clinical PF samples suggest dysregulated ErbB-driven ADAM-10 activity. (A) PF samples from patients with and without endometriosis were profiled for protein levels (bead immunoassay) and protease activities (PrAMA). (B) PCA scores and loading plot decomposes patient samples along principal components of co-variation, and separates samples into three non-overlapping clusters in an unsupervised manner (fully labeled in Fig. A.16A). (C) The ratio of MET to TIMP1 increases with disease (*p=0.014, Wilcoxon rank-sum).

dometriotic tissue. Overall, these results suggest that joint dysregulation of ADAM-10 activity, ErbB-signaling, and corresponding RTK shedding play an important role in disease progression.

Discussion

Understanding systematic regulation of ectodomain shedding has been challenging to accomplish on a component-by-component basis for multiple reasons. The web of protease-substrate interactions involves significant overlap and cross-talk: proteases (a) degrade potentially hundreds of often shared substrates [169]; (b) interact with and regulate each other through direct proteolysis [170]; and (c) respond to and modulate signaling pathways [160]. These multiple layers of complexity compel quantitative and multivariate approaches, and here we employ integrative experimental/computational methodologies to understand how ADAM-sheddases interact with signaling networks to direct overall cellular behavior.

Network-level insights into sheddase regulation of cell migration. In this work we combine quantitative experimental measurements with network-inference methods to build computational models of signaling-mediated protease regulation and motility. The CSR approach successfully identifies canonical biochemical interactions, for example between Jnk and c-Jun (Fig. A.7), while simultaneously providing unique insight into mechanisms of sheddase regulation. Shedding is generally considered a function of both protease catalytic activity and substrate availability, yet the balance of protease and substrate regulation remains unclear [161]. Here we directly assess proteolytic activity in a relatively "substrate-independent" manner using PrAMA, and find close correlation between proteolysis of both soluble FRET-peptides and multiple endogenous membrane-bound ligands and receptors. Moreover, these measurements best described cell migration among all other measurements in the CSR dataset, including phospho-signaling responses proximal to the growth-factor receptors that were being stimulated. Overall, these results (a) provide evidence for significant regulation of the sheddases themselves, (b) clearly underscore how joint ligand and RTK shedding are concomitantly controlled, and (c) suggest a prominent role for ectodomain shedding in governing cell migration.

Although we found strong correlations among multiple substrate shedding reactions, we also identified ample evidence that broad patterns of sheddase activity are governed by more than just a single regulatory pathway. This could be seen, for example, by the marked differences in surface level changes among the various ligands and receptors, as they varied across the growth factor treatments (Fig. 3.2B). Reflecting this observation, predictive modeling of substrate shedding and motility required multiple descriptors and PCs to achieve sufficient accuracy. Furthermore, CSR modeling results emphasize that sheddase-regulation is a dynamic process. For example, PCA and correlation-network results pointed to modularity within the CSR dataset, characterized by early phospho-signaling events linked to ectodomain shedding primarily through ADAM-17 phosphorylation (Fig. A.7). Although complex, the network-inference results nevertheless converge upon AREG and MET as key regulators of cell migration, where they are defined as central components in predictive models of motility (Fig. 3.2D).

Based on computational modeling results, we investigated a mechanism of shedding defined by the coordinated, context-specific action of both ADAM-10 and -17. Multiple computational and experimental results suggested that EGF and TGFα primarily stimulate ADAM-10 activity (Fig. 3.4A) and lead to the downregulation of ADAM-17 surface levels within 30 min. of treatment (Fig. A.3). Surprisingly, these results also suggested that EGF-induced AREG shedding may be occurring through the activity of ADAM-10, even though AREG has traditionally been considered an ADAM-17 substrate. We confirmed that ADAM-10 had the potential to cleave AREG using recombinant protease (Fig. A.13D-F), and also found that ADAM-10 inhibition affected AREG shedding to a much greater degree under EGF-treatment conditions (Fig. 3.4B-E). Furthermore, siRNA knockdown of ADAM-10 and -17 confirm the dual dependency of multiple other substrates on both ADAM-10 and -17 activities, in agreement with previous work [171]. Overall, these results demonstrate how sheddases dynamically interact with multiple signaling pathways to govern overlapping ectodomain shedding events, and

emphasize the difficulty in selectively manipulating the proteolysis of specific substrates through kinase and protease inhibitors.

Implications of RTK ectodomain shedding in modulating drug response. Although sheddase involvement in ErbB-ligand shedding makes them compelling drug targets in ErbB-driven disease, the biological consequences of ADAM-10 and -17 mediated RTK shedding continue to be poorly understood. In HER2+ breast cancer, ADAM-10 inhibition reduces HER2 shedding, which generally has been described as beneficially limiting the accumulation of the membrane-bound HER2 fragment (p95HER2) that remains after ectodomain proteolysis [172]. However, it remains unclear how p95HER2 activity compares to full-length HER2, especially after ligand stimulation. Furthermore, soluble HER2 ectodomain has been shown to inhibit signaling [173]. For other RTKs including HER4 and MET, shedding likely reduces RTK signaling at the cell surface [174, 175]. TIMP1 inhibition of MET shedding in breast cancer enhances MET signaling and increases liver metastasis [176]. In this work we demonstrate that cellular motility is an integrative process that depends not just on AREG shedding, but also on the combined and quantitative effect of multiple proteolytic reactions, including RTK shedding. We find that ADAM-10 and -17 mediated receptor shedding downregulates HER2, HER4, and MET signaling (Fig. 3.5). Reduced sheddase activity and RTK cleavage, either through metalloproteinase inhibition (Fig. 3.5) or indirectly through signaling pathway inhibition (Fig. 3.6), leads to accumulation of intact RTKs on the cell surface. RTK accumulation potentiates the signaling response to HGF and NRG1β, and causes enhanced RTK phosphorylation (Fig. 3.5B, 3.6C) and downstream activation of Jnk and p38 (Fig. 3.5C-F). Consequently, Mek and PI3K inhibitors actually enhance the motile response of endometriotic cells to NRG1β and HGF treatment by inhibiting RTK shedding while failing to block the compensatory p38 and Jnk activity that results from signaling of accumulated RTKs (Fig. 3.6D-E). Previous studies implicate Jnk and p38 in endometriosis [177, 178], and our results show that Jnk and p38 inhibitors effectively reduce ADAM-activity while also blocking the compensatory signaling and motility regardless of the growth factor environment (Fig. 3.6D-E; Fig. A.15J). Overall, these results have significant implications for the design of combination therapies involving the numerous signaling pathways that affect ADAM activity, and complement previous studies that stress the importance of Jnk/p38 pathways in cell migration [179].

The emergence of secondary resistance to targeted kinase inhibition represents a major obstacle in developing successful therapeutics, and in this work we identify a novel sheddase-mediated mechanism of rapidly acquired inhibitor resistance that has potential applications for a variety of kinase and protease inhibitor therapies. In the context of breast cancer, secondary resistance to Mek inhibitors has been well documented and arises from upregulation of RTKs that are known sheddase substrates, including PDGFRb, MET, and Axl [180]. Furthermore, the presence of growth factors that activate known ADAM-substrate RTKs, for example MET, facilitates the emergence of resistant populations [154]. Consistent with these results, here we present that Mek inhibitor resistance arises through multiple upregulated RTKs, many of which have been implicated in other reports including MET and HER2. In this work we demonstrate that sheddases play a role in the acute upregulation of receptor levels, and this is particularly relevant in the presence of growth factors that have been previously implicated as pro-survival and pro-migration microenvironmental cues [43, 119, 154]. In endometriosis, kinase inhibitors are in the earlier stages of testing and acquired inhibitor resistance is not yet a clear problem. Nonetheless, we demonstrate that the logic of combination therapies can be successful in our in vitro model for overcoming compensatory signaling pathways that arise secondarily from inhibitor treatment.

Clinical evidence of dysregulated sheddase activity and therapeutic implications. Analysis of clinical samples from endometriosis patients helped demonstrate the relevance and inherent overlap of sheddase-mediated proteolysis and RTK signaling dysregulation in disease progression. Although many previous studies have examined ErbB-signaling and metalloproteinase levels individually (Table A.1), here we present a multivariate analysis of systemic interaction between ErbB-ligands, RTK shedding, and metalloproteinase dysregulation. Furthermore, we use measurements from a recently developed microfluidic device to analyze protease activity directly and relate these observations to corresponding protease substrate levels observed in the same patient sample [166]. Clinical results confirm many of the observations made *in vitro*, for example demonstrating significant correlation

between ADAM-10 activity and accumulation of known ADAM-10 substrates such as HER2, EGF, and AREG (Fig. A.16). This clinical correlation supports *in vitro* evidence that AREG shedding is sustained through a positive feedback loop involving ADAM-10 activity, EGFR signaling, and multiple cell types including endometriotic epithelium (12Z), endometrial fibroblasts, and PFMCs (Fig. A.17). Furthermore, this positive feedback loop drives persistent cellular migration and enhances cellular sensitivity to various kinase inhibitors in vitro. Interestingly, we find that disease PF samples comprise two distinct clusters defined in large part by the balance between ADAM-9 and ADAM-10 activities (Fig. 3.8B). ADAM-10 is a known ADAM-9 substrate, and ADAM-9 has been observed to downregulate ADAM-10 activity on the cell surface [170]. Common among both clusters of disease samples, however, was the observation that the ratio of MET shedding to TIMP1 concentration increased with endometriosis, thereby confirming the relevance of MET signaling in designing therapeutic strategies that may impact ADAM-10 activity (Fig. 3.8C). Previous work has shown TIMP1 to inhibit the establishment of endometriosis in a mouse model, and these effects were primarily assumed to be MMP-related [181]. However, in this work we demonstrate the critical role of ADAM-10 in mediating in vitro cellular migration, and our clinical evidence associates TIMP1 with ADAM-10 activity via its relation with MET shedding.

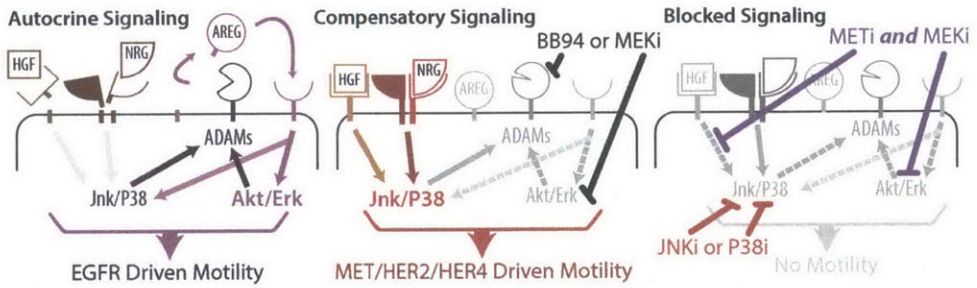

Figure 3.9: Ectodomain shedding exerts pro- and anti- migratory effects depending on context. Left: EGFR drives motility in an Erk/Akt dependent manner. High sheddase activity leads to HER2, HER4, and MET shedding along with concomitant positive feedback via AREG release. Center: Suppression of sheddase activity directly or indirectly via Mek inhibition confers reduced RTK shedding and enhanced response to NRG and HGF through Jnk and p38. Right: p38, Jnk, or combination Mek/MET inhibition blocks motility.

Conclusions We have presented an integrative paradigm for analyzing how complex networks of protease activities work in concert with signaling pathways to influence overall cell response to various disease-relevant environments and therapeutic interventions. In the future, we anticipate that this approach may be useful to explore other facets of sheddase regulation (such as osmotic stress), cell phenotypes (including proliferation and apoptosis), and sheddase-related diseases (such as breast cancer). In this work, we found that ADAM-10 and -17 tune cellular signaling by concomitantly shedding ligand and receptor ectodomains from the cell surface, and we demonstrate here how this competing signaling feedback determines context-dependent cell migration and drug response (Fig. 3.9).

Full appreciation of the many competing roles of sheddase activity be will essential for understanding their function in development and disease, and has wide implications for designing therapeutic strategies in a broad range of pathologies.

Chapter 4

AXL Diversifies EGFR Signaling and Mitigates Response to EGFR-Targeted Therapeutics in Triple Negative Breast Carcinoma Cells

Abstract

The relationship between drug resistance, changes in signaling, and emergence of an invasive phenotype is well-appreciated but the underlying mechanisms are not well understood. Using machine-learning analysis applied to the Cancer Cell Line Encyclopedia database, we identified that expression of AXL, the gene that encodes the epithelial-to-mesenchymal transition (EMT)-associated receptor tyrosine kinase (RTK) as exceptionally predictive of lack of response to ErbB family receptor-targeted inhibitors. Activation of EGFR transactivated AXL, and this ligand-independent AXL activity diversified EGFR-induced signaling into additional downstream pathways beyond those triggered by EGFR alone. AXL-mediated signaling diversification was required for EGF-elicited motility responses in AXL-positive TNBC cells. Using crosslinking coimmunoprecipitation assays, we determined that AXL associated with EGFR, other ErbB receptor family members, MET, and PDGFR, but not IGF1R or INSR. From these AXL interaction data, we predicted AXL-mediated signaling synergy for additional RTKs and validated these predictions in cells. This alternative mechanism of receptor activation limits the utility of ligand blocking therapies and indicates against therapy withdrawal after acquired resistance. Further, subadditive interaction between EGFR- and AXL-targeted inhibitors across all AXL-positive TNBC cell lines may indicate that increased abundance of EGFR is principally a means to transactivation-mediated signaling.

Introduction

Receptor tyrosine kinases (RTK) are widely abundant and dysregulated in cancers, and have been the focus of targeted therapies for several decades [182]. While inhibitors targeting RTK signaling have shown clinical benefit in certain malignancies, the utility of such drugs is unfortunately limited because of primary (innate) or secondary (acquired) resistance that renders therapeutics against seemingly appropriate targets surprisingly ineffective [183]. Often, striking initial benefits of such treatments are ultimately futile as a result of quickly developed resistance and disease progression. Recently, activation of alternative RTKs as an important resistance process has been identified [43, 184], although underlying mechanisms are not well understood. Amplification of the targeted signal can also confer resistance, particularly *in vivo* where access to the tumor site by therapeutics may be limited [41, 185].

Another process involved in RTK inhibitor resistance is epithelial-mesenchymal transition (EMT), a global program that endows epithelial cells with the ability to migrate and invade surrounding tissue [186, 187]. In

multiple cancers exhibiting initial response to targeted therapeutics, development of secondary resistance correlates with metastatic potential, invasiveness, and mesenchymal-like traits [6, 11, 182, 188–192]. Certain transcriptional, post-transcriptional, and post-translational changes that confer differences in growth factor signaling, migratory capacity, and resistance have been reported [183, 187, 193–195]. However, the global nature of the EMT program indicates that integrative studies combined with multivariate, systems approaches will be required to elucidate how these diverse changes contribute to disease progression [43, 140, 184].

AXL, the gene which encodes the TAM (TYRO3, AXL, MERTK) receptor tyrosine kinase family member AXL, is widely overexpressed in cancers and is predictive of poor patient outcome [21, 41, 185, 196–203]. Its expression is induced by the EMT program [21, 42, 186, 187, 189, 204–206], and activation of AXL has been linked to resistance to ErbB-targeted therapies [189, 204, 207]. Although AXL can be activated by binding its ligand, Gas6, it often appears to be activated in an alternative ligand-independent manner [207–211]. Given the prospect for AXL signaling as a potential explanation for EMT-related ineffectiveness of RTK-directed therapeutics, we examined its contribution to RTK-targeted drug resistance and investigated the potential underlying mechanism.

Using machine learning techniques and multivariate signaling network analysis in concert with public databases and our own targeted experiments, we identified AXL expression as an exceptionally strong predictor of resistance to ErbB inhibitors. We discovered that triple negative breast cancer (TNBC) cell lines that had similarly high abundance of both EGFR and AXL were more sensitive to AXL inhibition than to EGFR inhibition. Resistance of these cell lines to EGFR inhibitors with respect to viability was accompanied by EGFR activation-induced transactivation of AXL in a manner which amplified a subset of downstream signals that are important to invasive motility but are not activated vigorously by EGFR itself. Exploring the mechanism for this resistance-related signaling diversification, we found a correlation between the AXL-mediated lack of response to RTK-targeted drugs and the physical association of AXL with those particular RTKs as characterized by cross-linking co-immunoprecipitation. Indeed, we were able to successfully predict novel AXL transactivation in RTK/ligand pairs by considering expression and association proclivity. Taken together, our findings offer new insights concerning RTK signaling crosstalk involving AXL through a transactivation mechanism.

Results

Classification of tumor cell lines identifies AXL as an exceptionally strong predictive marker of resistance to ErbB-targeted drugs

Because activation of alternative receptors is a widespread means of resistance to RTK-targeted inhibitors [43, 184], we used the Cancer Cell Line Encyclopedia (CCLE), a publicly available dataset of expression and drug response [212] to examine whether combinatorial expression of multiple RTKs may be related to lack of response to particular RTK-directed drugs. Although straightforward inspection of univariate correlation between expression and drug response is a common approach for hypothesis generation, such an analysis is confounded by broad-ranging expression correlations between genes, particularly genes encoding proteins targeted by the inhibitor. The expression of a single gene may therefore correlate with drug resistance simply through its correlation with expression of the drug target. Pairwise comparison indicated that RTK expression is either significantly correlated or anti-correlated as often as not (51% of RTK pairs at $p < 0.05$ significance; Fig. 4.1A & 4.2A). Therefore, we instead used all possible drug target-RTK gene pairs as bivariate predictors in a support vector machine (SVM)-based classification scheme [213] to identify genes whose expression in combination with that of the gene encoding the target RTK synergistically improves prediction of drug response. Briefly, SVM methods aim to find a discriminating threshold based on "inputs" (in this case receptor gene expression) that predict an "output" (in this case sensitivity to drug). By examining whether a set of inputs can discriminate sensitive or resistant cells accurately, we formed hypotheses as to whether a particular receptor may play a causal role in drug resistance. As an initial control, the expression of genes encoding the targets of each drug were used on their own to

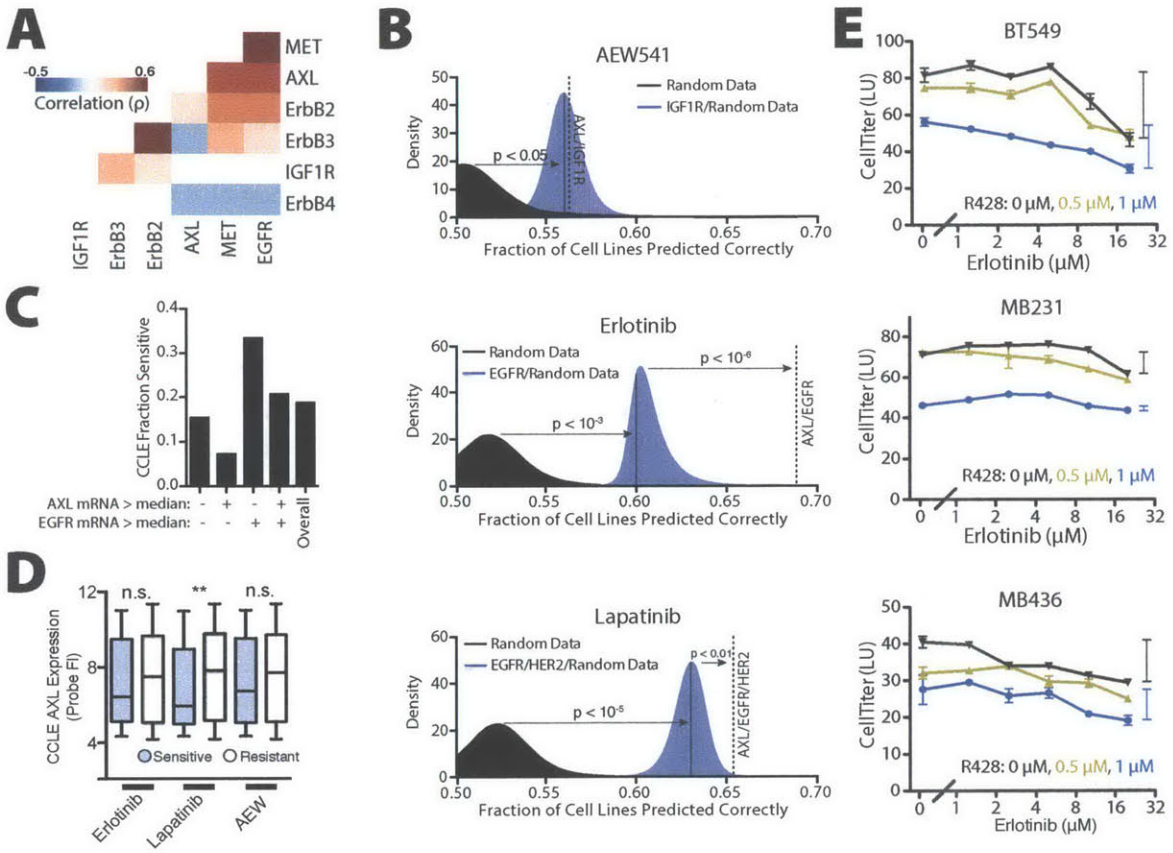

Figure 4.1: Support vector classification to identify mechanisms of drug resistance. (A) Spearman correlations of expression for a subset of receptor tyrosine kinases. Only statistically significant correlations are shown ($p < 0.01$). (B) Classification of cell lines as resistant or sensitive to AEW541, erlotinib, and lapatinib on the basis of RTK expression. Shown is the classification accuracy using randomized expression data (black), a model considering the expression of the gene encoding the drug target receptor (blue), or a model considering the expression of both the gene encoding the drug target receptor and that of AXL (dotted line). (C) The fraction of cell lines that are sensitive to erlotinib after separation according to those which exhibit greater or less than median expression of EGFR or AXL. (D) AXL expression probe values for resistant and sensitive cell lines to each drug (**$p < 0.01$, Kruskal-Wallis test, $N = 91–396$ cell lines per grouping). (E) Dose response curves for R428 and erlotinib in three triple negative breast carcinoma cell lines that have abundant EGFR and AXL. Bars on the side indicate the range of viability between the highest and lowest erlotinib dose, to illustrate subadditivity ($p < 10^{-6}$, BT549; $p < 0.05$, MB436; $p < 0.01$, MB231 by Loewe's synergy analysis; see Methods) between erlotinib and R428. Data are means ± SEM from three independent biological measurements.

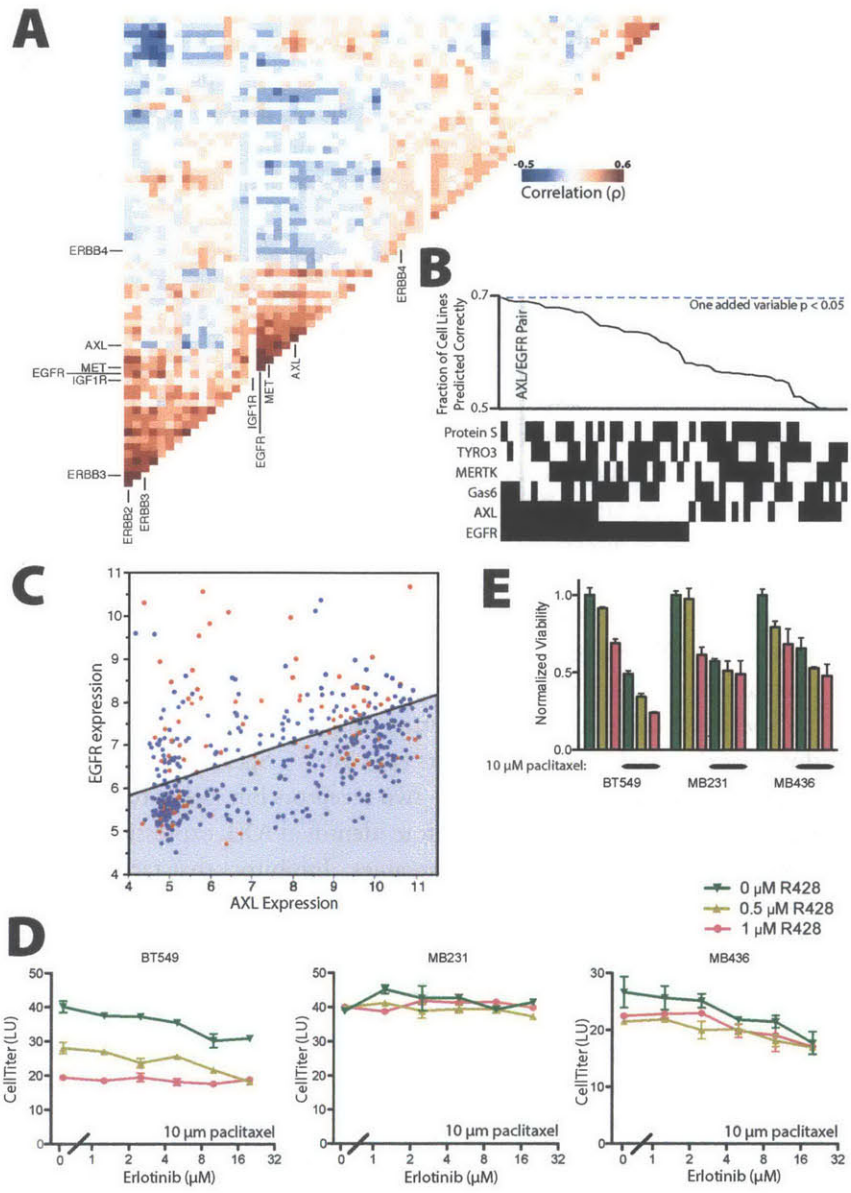

Figure 4.2: Support vector classification to identify mechanisms of drug resistance. (A) Spearman correlations for all pairs of GO-annotated receptor tyrosine kinases across all cell lines within the CCLE. Receptors were ordered by hierarchical clustering using Spearman correlation as a distance metric and average linkage. Roughly three or four clusters emerge consisting of RTKs with highly correlated expression. Only significant correlations ($p < 0.01$) are shown. (B) Model performance for prediction of erlotinib using all receptors from and ligands of the TAM family. The vertical bar indicates the AXL and EGFR model, and the horizontal line indicates the $p < 0.05$ threshold for AXL, EGFR, and one added input. The Protein S, Gas6, AXL, and EGFR model does equally well to the threshold indicated, but adds two inputs and thus requires higher performance to be significant. (C) Classifier for erlotinib sensitivity based on AXL and EGFR expression. Blue dots indicate resistant cell lines, and red dots indicate sensitive cell lines. The blue region indicates the region for which the classifier predicts cells to be resistant. Axes are RMA-normalized probe values. (D) Dose response surfaces for R428 and erlotinib co-treated with 10 μM paclitaxel in three TNBC cell lines that have high expression of EGFR and AXL. (E) Viability measurements for varying amounts of R428 with or without paclitaxel. Error bars indicate standard error of biological triplicates.

predict sensitivity. To calculate significance for later comparisons, this expression measurement was combined with a random vector and the distribution of all such trials is shown (blue area, Fig. 4.1B). This random vector additionally accounts for model performance simply due to changes in the number of input variables. A more permissive control was created by using solely the random data vectors in repeated trials (black area, Fig. 4.1B). Completely randomized data did not necessarily predict half of the cell lines correctly, as a result of asymmetry in the number of cell lines in each class (resistant or sensitive). Not surprisingly, expression of the gene that encodes the inhibitor-targeted RTK was always among the strongest independent predictors of drug response and was significantly more predictive than only random inputs.

Given that drug sensitivity can be reduced by redundancy among RTKs, we tested whether a model that considered the expression of the gene encoding the targeted RTK along with the expression of a gene encoding another RTK was better at predicting drug response than the model considering the drug-target RTK alone. The predicted response to the ErbB-targeted drugs lapatinib and erlotinib was significantly improved by considering AXL expression, whereas the prediction of response to the IGF1R-targeted drug AEW541 was not substantially improved (Fig. 4.1B). The expression of genes that encode TAM ligands (such as Gas6 and Protein S) or other TAM receptors (TYRO3, MERTK) all failed to generate synergistic prediction improvement when combined with that of the drug-target RTK alone, with that of AXL, or with that of the drug-target RTK and AXL (Fig. 4.2B). With respect to directionality, the classifier for sensitivity to the EGFR inhibitor erlotinib using AXL and EGFR expression (Fig. 4.2C) yields the prediction that EGFR expression indicates increased sensitivity while AXL expression indicates increased resistance (Fig. 4.1C). In contrast, univariate analysis predicted no relationship between AXL expression and erlotinib sensitivity (Fig. 4.1D). Methods depending only on AXL expression likely do not capture a relationship because AXL and EGFR are themselves correlated in expression ($p < 10^{-32}$; Spearman correlation), convoluting simpler analyses as we argued above. Interestingly, this correlation additionally exists within clinical tumors ($p < 10^{-17}$, Spearman correlation), however our aim is not to ascribe significance to correlation between the two receptors but rather to point out this convoluting factor in univariate analyses [214]. Our modeling therefore identified AXL expression as a common marker for resistance to ErbB-targeted, but not IGFR-targeted, therapies. Inhibitors that target MET and PDGFR, for which sensitivity data is available, target multiple receptor families, therefore a meaningful analysis could not be readily performed. Although AXL expression showed the highest significance in this analysis, that of EPHA1 and FGFR1 also exhibited similarly high significance (Table 4.1); expression of these genes has been implicated similarly in resistance to ErbB-targeted therapies in breast carcinoma [43, 215].

Although AXL has been shown previously to confer secondary resistance to lapatinib and erlotinib in other cancer subtypes, including HER2-positive breast cancer and non-small cell lung cancers [204, 207], we focused on a role for AXL in modulating the response of TNBC cells to EGFR-targeted drugs. Despite high abundance and activation of EGFR in TNBC, EGFR inhibitors have not been efficacious on their own, so discerning explanations for the lack of sensitivity could be important both for understanding basic aspects of EGFR signaling and for potentially improving therapeutic strategies. Because TNBC typically express both EGFR and AXL endogenously, our model would indeed predict AXL-related resistance to erlotinib in these cells. Extrapolating from the observation that inclusion of AXL expression improved the predictive capacity of the model, we additionally reasoned that simultaneous inhibition of AXL and EGFR would result in synergistic cytotoxicity in TNBC and that these cells would be more sensitive to AXL inhibitors than to EGFR inhibitors. We treated three such cell lines with erlotinib and R428, a specific inhibitor of AXL, and confirmed that they are resistant to EGFR inhibition and sensitive to AXL inhibition (Fig. 4.1E). Additionally, treatment with R428, but not erlotinib, showed synergistic cytotoxicity with paclitaxel in a subset of cells (Fig. 4.2, D & E), consistent with previously reported findings that targeted RTK inhibition can operate synergistically with DNA-damaging agents [156, 216]. However, we were surprised to observe a subadditive interaction between the EGFR- and AXL-targeted inhibitors in dual-treated cells (Fig. 4.1E). Although these results validate the prediction of erlotinib resistance in these cells, validation of AXL as the mechanism of resistance would typically be expected to show synergy in the combined effects of erlotinib and R428. Because subadditive interactions can indicate shared pathway com-

Receptor	Erlotinib Synergy	Lapatinib Synergy
AXL	$p < 0.001$	$p < 0.001$
EPHA1	$p < 0.001$	$p < 0.001$
FGFR1	$p < 0.001$	$p < 0.001$
MST1R	$p < 0.05$	$p < 0.05$
EPHA2	$p < 0.05$	$p < 0.05$
ERBB3	$p < 0.05$	$p < 0.05$

Table 4.1: RTK genes significantly associated with both erlotinib and lapatinib resistance. Significance was calculated by randomized controls. EPHA2, EPH type-A receptor 2; MSTR1, macrophage stimulating kinase 1 receptor; ERBB3, ErbB receptor 3.

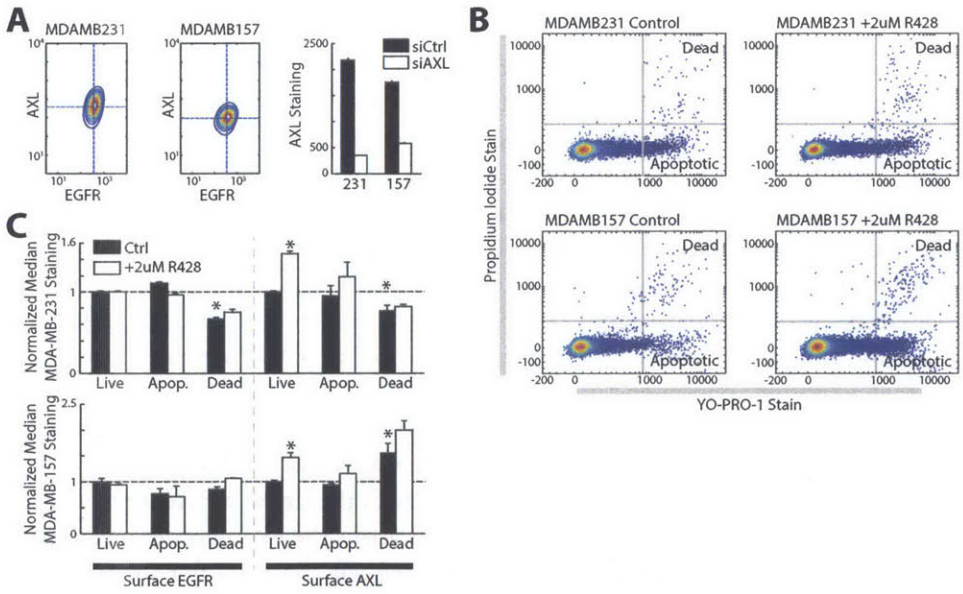

Figure 4.3: Single-cell EGFR and AXL expression with R428 treatment. (A) Live-cell immunostaining of cell lines under basal conditions to measure surface EGFR and AXL abundance. Colors and lines indicate population distribution, with warmer colors denoting higher density. Dashed lines denote median expression across the population. AXL live-cell immunostaining specificity was confirmed by AXL siRNA treatment. (B) Measurement of apoptosis and cell death in response to R428 treatment. 20,000 cells are shown within each plot. (C) EGFR and AXL surface abundance measured by live-cell immunostaining for each of the subpopulations shown in (B), following 24 hour treatment with 2 μM R428 (*$p<0.05$, Student's test comparison to live untreated cells from biological triplicates).

ponents, we wondered whether inhibition of one receptor might decrease the activity of the other. A second possibility, in which two distinct cell populations exist—one in which both AXL and EGFR are expressed and is sensitive to both drugs, and another in which neither is expressed and which is resistant to both drugs—would similarly explain our observations but not constitute drug antagonism. However, single-cell analysis revealed neither distinct populations of cells nor changes in receptor expression upon drug treatment (Fig. 4.3).

AXL knockdown impairs EGFR signaling

To test our model, we first probed whether AXL and other RTKs outside the ErbB family are activated upon EGF stimulation. Using MDA-MB-231 cells, we measured pan-phosphotyrosine (pan-pY) abundance on immunoprecipitated receptors and found that MET and AXL were phosphorylated after cells were treated with EGF (Fig. 4.4A). In contrast, we did not observe phosphorylation of EGFR upon activation of AXL with an activating antibody, demonstrating that, although activation of EGFR can induce the transactivation of AXL, the reverse does not transpire (Fig. 4.5A).

Because the expression of AXL, but not that of the gene encoding its ligand Gas6, predicted resistance to ErbB inhibitors (Fig. 4.2B), and because previous studies have verified Gas6-independent resistance effects of AXL signaling [207], we hypothesized that AXL may also modulate signaling responses elicited by activation of other RTKs. To test this, we transfected MDA-MB-231 cells with an siRNA pool targeting AXL (Fig. 4.4B) and then stimulated cells with EGF, TGFα, or HGF and measured the phosphorylation of 11 downstream phosphosites. The surface and total (Fig. 4.4C) abundance of other receptors were unchanged by AXL knockdown, and the phosphorylated (Fig. 4.5B) abundance was unchanged by treatment with R428. However, nearly all downstream phosphosites were affected by AXL knockdown, either in control or growth factor-stimulated cells (Fig. 4.4D & Table 4.2), indicating that AXL-dependent signaling effects are global in nature, and emphasizing the importance of multivariate analysis because of the limited utility of focusing on a single signaling pathway. Similar effects on the phosphorylation of two proteins were observed in cells treated with the AXL-specific inhibitor R428 (Fig. 4.5C), indicating that these effects depend on the kinase activity of AXL. Western blotting for a subset of phosphosites quantitatively matched our ELISA measurements (Fig. 4.5D). Attempting to directly stimulate AXL with Gas6 did not elicit a substantial signaling response, and these signaling consequences were small compared with EGF-elicited, AXL-dependent signaling effects (Fig. 4.5E). This observation is similar to results in other studies of Gas6-elicited signaling in MDA-MB-231 [217]. Why different cell lines display markedly distinct receptor activation patterns to Gas6 remains a question for future studies [217–219].

To investigate the crosstalk between AXL and EGFR (as well as MET) signaling further, we next examined the ratio of fold-activation (phosphorylation) of various signaling proteins in the absence versus presence of AXL (Fig. 4.6A). The unstimulated conditions represented signaling network activity presumably arising from constitutive autocrine processes. This analysis revealed more widespread AXL-dependent effects in EGF- or TGFα-stimulated cells compared with HGF-stimulated cells, with the largest difference in activation observed for GSK3 and Akt. Further, the relative magnitude of effects across the phosphosites investigated were correlated between EGF- or TGFα-stimulated cells and unstimulated cells, but were not correlated between HGF-stimulated and unstimulated cells (Fig. 4.6A, inset). These results suggest that AXL may mediate similar autocrine and EGFR-stimulated signaling pathways in TNBC cells, whereas HGF yields a distinct downstream AXL-mediated signature.

We then performed principle component (PC) analysis to gain insight concerning the network-level variation in signaling across these treatment conditions (Fig. 4.6B). Principle component 1 (PC1) was found to correspond to EGF-induced signaling, and PC2 to HGF-elicited signaling, with TGFα having an intermediate effect. Knockdown of AXL moved cells negatively along PC1 and reduced the magnitude of the effect of EGF stimulation. Examination of the loadings plot revealed separation between phosphosites only mildly affected by knockdown [for example, phosphorylation of STAT3 and JNK] and those strongly affected (such as the phosphorylation of Akt and GSK3), with the rest scattered at intermediate locations (Fig. 4.6C). Thus, EGF/TGFα

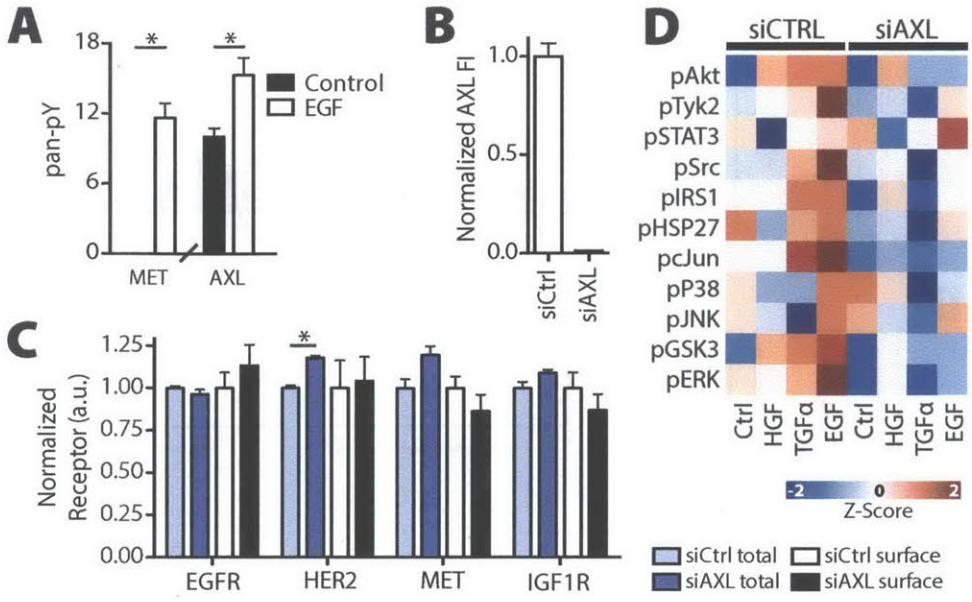

Figure 4.4: EGF stimulation transactivates AXL and MET. (A) ELISA-based pan-phospho-tyrosine (pan-pY) measurement of alternative receptors after EGF stimulation in MDA-MB-231 (*$p < 0.05$, Student's test). (B) AXL knockdown, measured by ELISA. (C) Total and surface amounts of alternative receptors in AXL-silenced MDA-MB-231 cells (*$p < 0.05$, Student's test). Data are means ± SEM of three biological measurements. (D) Downstream signaling assessed by kinase phosphorylation in MDA-MB-231 cells 5 min after stimulation with EGF, TGFα, or HGF in the presence or absence (siAXL) of AXL. Each phosphosite was mean centered and variance normalized.

	Unstim	EGF	TGFα	HGF	Paired
pErk		•	•		•
pGSK3	•	•	•	•	•
pJNK					
pP38					
pcJun		•	•		•
pHSP27	•				
pIRS1			•		•
pSrc					
pSTAT3					
pTyk2					•
pAkt	•				

Table 4.2: Single phosphosite or condition analysis provides an incomplete perspective of the signaling effects upon AXL knockdown. The difference in the phosphorylation of ERK, GSK3, (and so on, left) in unstimulated or stimulated conditions (top) in the presence or absence of AXL was assessed for significance using a Student's test. Data is presented in Fig. 4.4D. Paired comparisons were made by a signed rank test. (*$p < 0.05$).

induce ErbB-mediated downstream signaling that is qualitatively similar to basal signaling but is distinct from MET-mediated signaling, and this baseline-like signaling is disrupted by AXL knockdown. The difference between HGF and EGF, TGFα, or baseline signaling is likely a result of the absence of signaling from EGFR, HER2, or AXL in the former case, because MET is presumably transactivated also in the EGF- or TGFα-stimulated cases. An appealing interpretation is that autocrine EGFR ligand activity is constitutive and transactivates AXL.

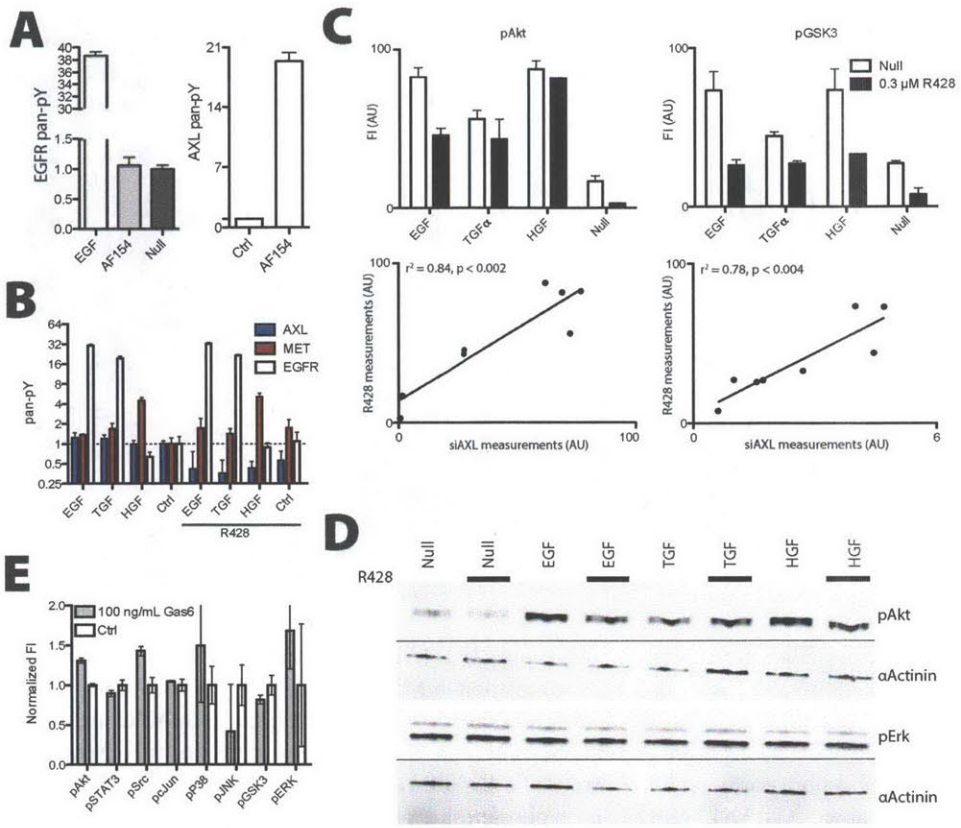

Figure 4.5: RTK crosstalk occurs in triple negative breast carcinoma cells. (A) Measurement of receptor activation after treatment with an activating antibody for the AXL receptor. (B) Receptor activation measurement for conditions corresponding to those of downstream analysis. (C) Top, ELISA of the phosphorylation of Akt and GSK3 in MDA-MB-231 cells untreated (null) or after treatment with the indicated growth factor, with or without 0.3 μM R428 treatment. Bottom, comparison of the measurements in MDA-MB-231 cells treated with 0.3 μM R428 or AXL siRNA. Pearson correlation values and significance is shown. Error bars indicate standard error of biological triplicate measurements. (D) Western blot validation of a subset of phosphosite measurements. Results are qualitatively identical to those performed by ELISA in Fig. 4.4D. (E) Downstream signaling measured after 5 min treatment with 100 ng mL^{-1} Gas6.

AXL amplifies signaling in the EGFR-associated pathway but does not sensitize EGFR to its ligand

Because receptor activation can be quantitatively characterized in terms of ligand concentration-related sensitivity and maximal activation at saturation, we investigated how AXL influences the dose-response of EGFR to EGF. We stimulated MDA-MB-231 cells with a range of concentrations of EGF and measured the pan-pY on EGFR and the phosphorylation of Akt (Fig. 4.7, A & B). Phosphorylation of Akt was chosen for measurement as a critical downstream signal that was strongly influenced by AXL knockdown, though not to imply that all transactivation-mediated effects are regulated through Akt alone (Fig. 4.6C). Phosphorylation of EGFR was unaffected by AXL knockdown except at very high (above saturating) EGF concentrations (Fig. 4.7A), likely as a result of altered trafficking or cellular processes induced at such non-physiological amounts of stimulation. Other receptor-proximal components, the adaptor protein SHC and the CDC2 kinase, exhibited similar phosphorylation after stimulation at the EGF dose used in the signaling studies here (Fig. 4.8). In contrast, AXL knockdown affected the phosphorylation of Akt in response to all doses of EGF by a shift in magnitude ("vertically") rather than in sensitivity ("horizontally") (Fig. 4.7B). To deconvolve these concomitant changes in the phosphorylation of EGFR and Akt, we plotted the abundance of phosphorylated Akt as a function of phosphorylated EGFR

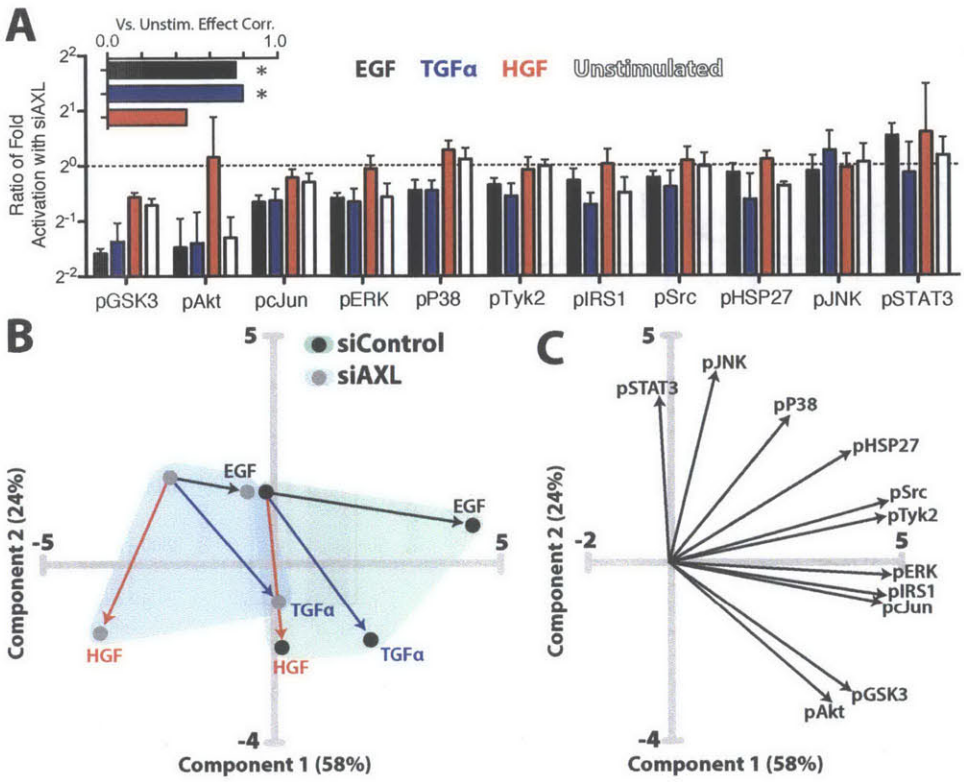

Figure 4.6: AXL knockdown attenuates downstream signaling in MDA-MB-231. (A) Ratios of fold activation after treatment with growth factor in AXL knockdown cells relative to wild-type cells: ([siAXL GF]/[siAXL Unstim]) ÷ ([siControl GF]/[siControl Unstim]). The unstimulated bar indicates the ratio of unstimulated abundance: [siAXL Unstim]/[siControl Unstim]. Inset shows the Spearman correlation across all phosphosites between the unstimulated and stimulated ratios (*$p < 0.05$). (B) Principle components analysis score plot of signaling data after AXL knockdown. Line colors indicate stimulation conditions denoted in (A). (C) Loadings plot of signaling data after AXL knockdown.

Model	AIC	AIC L	AICc	AICc L
1	277	10^{-4}	277	0.0005
2	266	**0.58**	269	**1.0**
3	305	10^{-17}	307	10^{-16}
4	279	10^{-5}	284	10^{-6}
5	268	**0.10**	273	0.025
6	274	0.0002	277	0.0004
7	302	10^{-16}	305	10^{-15}
8	265	**1.0**	270	**0.25**

Table 4.3: Relative model goodness of fits based on the Akaike information criterion (AIC). Models were compared using the corrected and uncorrected Akaike information criterion denoted AICc and AIC, respectively [220]. AICc more strongly penalizes model size when comparing models with different numbers of fit parameters. Likelihoods (L) in bold are greater than 0.05 and so those models are not significantly eliminated. Model numbers correspond to the equation numbers given in the Methods. Models 2 and 8 cannot be distinguished in their goodness of fit, but have similar biological conclusions.

in cells treated with either control siRNA or AXL siRNA (Fig. 4.7C). This revealed a uniform downward shift across all stimulation amounts in the absence of AXL, indicating a consistent fold-change in the magnitude of signal transduction. Each curve could be well-described to first approximation by a Hill function, with com-

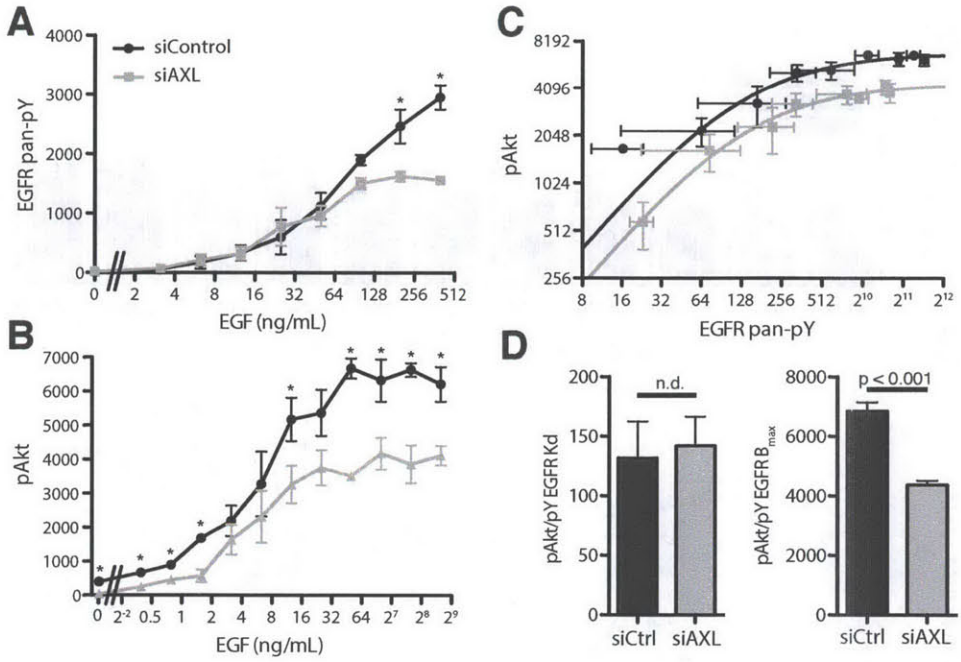

Figure 4.7: AXL amplifies the EGFR signaling response. (A) ELISA of pan-pY EGFR in wild-type (siControl) or AXL-silenced (siAXL) MDA-MB-231 after 5 min treatment with varying EGF amounts. Data are means ± SEM, $p < 0.05$, Student's test, N = 3. (B) The phosphorylation of Akt in response to a range of EGF doses. Data are means ± SEM, $p < 0.05$, Student's test, N = 3. (C) ELISA for the abundance of pan-phospho-tyrosine on EGFR versus the phosphorylation of Akt in MDA-MB-231 cells. Lines show a Hill regression to each set of data with standard error of biological triplicate measurements. (D) Hill regression of each plot shows similar Kd values, but significantly different maximal activation (F-test). Error bars indicate standard error of the fit.

parable Kd (threshold of half-maximal activation) but dramatically different maximal activation (Fig. 4.7D). To identify the level at which this regulation may occur, we fit these data to alternative models of signal transduction from the receptor layer (see Methods). The data were best explained by a model in which basal and stimulated AXL activity exists, the latter in proportion to EGFR activation and in which transduction of both signals occurs through separately saturable processes (Table 4.3). This model is consistent with our biochemical observations (Fig. 4.4A). The effect of baseline activation of AXL can be observed from the plot of phosphorylated Akt as a function of pan-pY EGFR, where at low EGFR activation in the presence of AXL the phosphorylation of Akt was higher than a simple Hill regression would suggest (Fig. 4.7C). Biologically, this indicates that the components downstream of the receptor are saturated by maximal EGFR activation and that, at least with respect to phosphorylated Akt, the transactivation of AXL increases the effective amount of RTK signaling and amplifies the signaling consequence of stimulation.

Multi-pathway signaling correctly predicts AXL knockdown inhibition of EGF-stimulated protrusion

We next asked how the broad effects on signaling which resulted from AXL knockdown might influence the migration behavior of cells. We elected to use acute membrane protrusion as a surrogate measurement of 3-dimensional (3D) migratory capacity on the basis of our previous findings that this assay corresponds well to growth factor-stimulated invasive motility within extracellular matrix [59]. Protrusion measurements from wild-type MDA-MB-231 cells were used to train a family of partial least-squares regression models for how protrusion activity depends on multiple phosphoproteomic signals. Minimal models that use only three signals were exam-

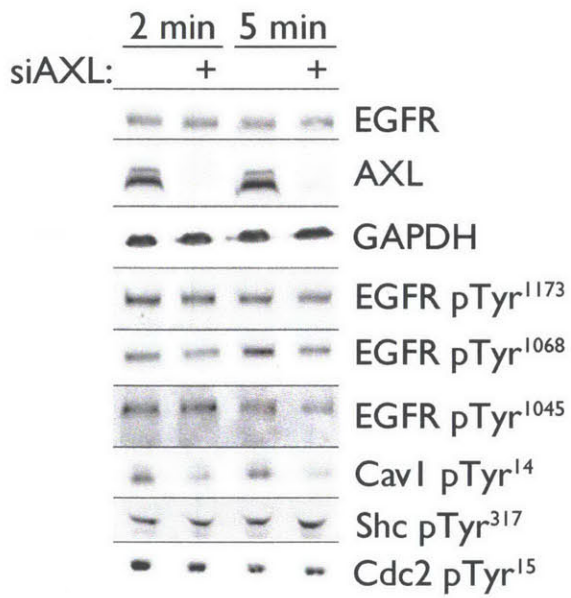

Figure 4.8: Receptor activation is similar in AXL knockdown cells. Cells were starved for 4 hrs and stimulated with 100 ng mL^{-1} EGF for the time indicated. Only the phosphorylation of caveolin at Tyr14 was substantially changed by AXL knockdown. Blots are representative of two experiments.

ined in order to ascertain the most vital pathway predictors for growth factor-induced motility. We identified models that fit the data by cross-validation ($Q2 > 0.6$), and found that these were enriched in inclusion of GSK3, STAT3, and Akt as the key predictor signals (Fig. 4.10A). These models involved similar weights for the predictor signals in both principle components, demonstrating consistency across the ensemble of top-fitting models in their multi-pathway signaling-to-protrusion relationships (Fig. 4.9A).

This ensemble of models was then used to predict wild-type MDA-MB-231 protrusion by cross-validation and to a priori predict protrusion modulation by AXL knockdown (Fig. 4.9B). EGF-stimulated protrusion was predicted to be the most substantially attenuated response after AXL knockdown, whereas HGF-stimulated protrusion was predicted to remain essentially unaffected. These predictions were indeed correct in MDA-MB-231 cells transfected with AXL siRNA: HGF-elicited protrusion was not significantly affected, whereas EGF-elicited protrusion was significantly reduced (Fig. 4.9C). Treatment with R428 confirmed that EGF-stimulated protrusion depended on AXL-mediated signaling in another TNBC line, MDA-MB-157, but that it did not in two other breast cancer cell lines, MCF7 and T47D, which lack AXL expression (Fig. 4.9D). The effect of R428 phenocopied that of AXL siRNA treatment in terms of the protrusion response to EGF in MDA-MB-231 cells (Fig. 4.9, C & D). TGFα-stimulated protrusion was also reduced in MDA-MB-231 cells by R428 treatment, although to a lesser degree, which was in accord with our model predictions (Fig. 4.10B). These results indicate that along with amplification of EGFR-induced downstream signaling, the transactivation of AXL additionally activates a qualitatively distinct set of signals that are important for cell migration in response to stimuli. Moreover, our three-pathway partial least-squares regression model successfully captured the integrated effects of these signals on this phenotypic response.

AXL is in proximity to ErbB and MET, but not IGF1R or IR.

We investigated whether the transactivation of AXL (and MET) by EGFR might involve physico-chemical proximity of these RTKs. Because of technical limitations in capability for distinguishing receptor co-localization by other methods (Fig. 4.12A-B), we employed a technique in which immunoprecipitation of cross-linked recep-

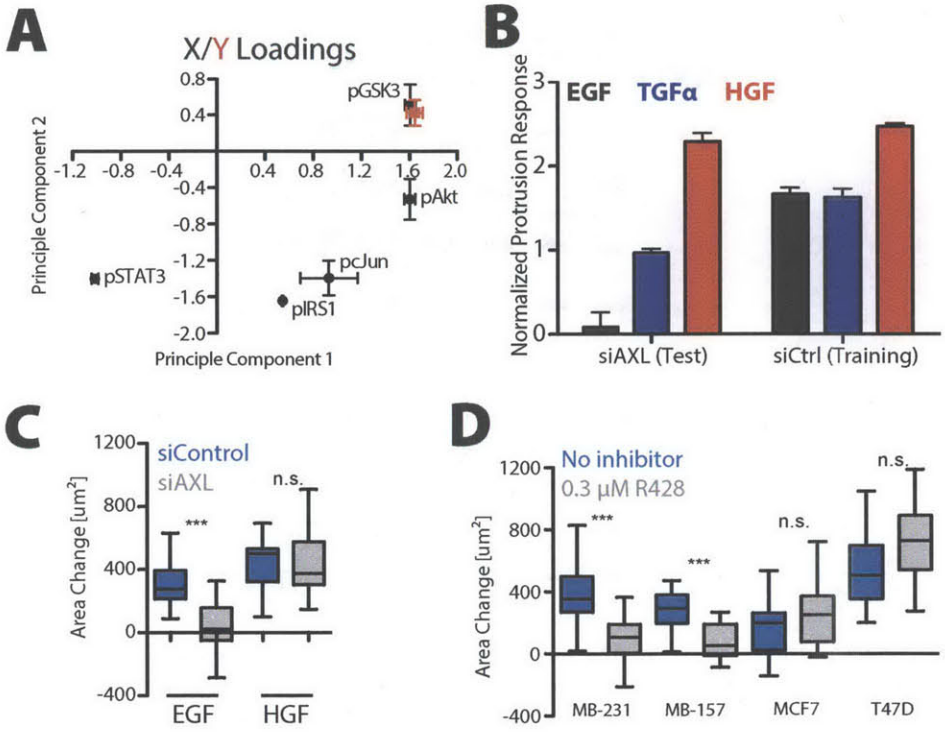

Figure 4.9: AXL signaling is required for EGF-elicited protrusion. (A) Mean loadings of the reduced partial least squares regression (PLSR) models. The red point corresponds to the projection of the phenotype. Error bars indicate the standard error for the family of reduced models. (B) Protrusion predictions from reduced PLSR models for wild-type (by cross validation) and AXL knockdown (by prediction) cells. Error bars indicate the standard error of prediction across the family of reduced models. (C) EGF-elicited protrusion response of MDA-MB-231 cells upon AXL knockdown (***$p < 0.001$, Mann-Whitney test, N = 13–25 from three independent experiments). (D) EGF-elicited protrusion responses with or without 0.3 μM R428 (***$p < 0.001$, Mann-Whitney test, N = 17–35 from three independent experiments). MDA-MB-231 and MDA-MB-157 cells express AXL, whereas MCF7 and T47D cells do not.

tors from lysate was performed in a multiplexed fashion on barcoded fluorescent beads. The degree of AXL cross-linking with each of various other RTKs was quantified using an AXL antibody (Fig. 4.11A). Across multiple cells lines we observed a significant degree of AXL cross-linking with ErbB receptors, MET, and PDGFR, but not with INSR or IGF1R (Fig. 4.11B & 4.12C). The amount of AXL cross-linking was roughly proportional to the abundance of that particular RTK—with the exception of INSR and IGF1R, neither of which garnered cross-linked AXL to a measureable extent (Fig. 4.11C). We confirmed cross-linking results with reciprocal IP assays in MDA-MB-231, in which we observed the association of AXL with EGFR but not with IGF1R (Fig. 4.12D).

On the basis of these data, we sought a quantitative framework to understand the respective amounts of complexing observed between AXL and each RTK across different cell lines. According to fundamental stoichiometric considerations, the amount of AXL observed in complex with a particular RTK in a particular cell line should be approximately the product of the RTK abundance in that cell line, with proportionality described by coefficients comprising (a) the cross-linking and protein loading efficiency, and (b) the antibody immunoprecipitation efficiencies and extent of co-localization. With measurements of RTK abundance and the amount cross-linked to AXL, we determined the remaining parameters (see Methods) to provide a way to account for differences in receptor expression when interpreting cross-linking data (Fig. 4.12D). With this quantitative formulation, we could then calculate whether the parameter characterizing AXL/RTK colocalization deviated significantly from 0 for each RTK (Fig. 4.11D). Significant deviation from 0 indicates colocalization. Despite IGF1R and INSR being substantively abundant in various cell lines, the calculated likelihood that they localized with AXL

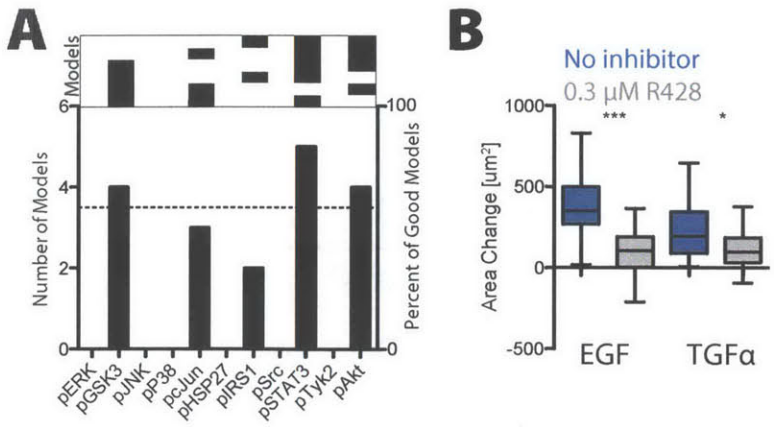

Figure 4.10: AXL signaling is required for EGF elicited protrusion. (A) Variable enrichment upon PLSR model reduction. Each sufficiently predictive model ($Q2 > 0.6$) of the wild-type protrusion measurements is shown (top). Bars indicate the frequency with which variables are included in the six selected reduced models. The dotted line indicates the threshold of significant enrichment ($p < 0.05$, hypergeometric test). (B) MDA-MB-231 cells treated with EGF or TGFα and R428. ***$p < 0.001$, *$p < 0.05$, Mann-Whitney test. Single cells were pooled from three independent experiments; N=30-36.

was not significant. Although this parameter includes the efficiency of immunoprecipitating IGF1R or INSR, we verified that these two receptors were detected with similar efficiency both by direct ELISA of the same cell lysates and by quantification of a recombinant standard. We additionally confirmed cross-linked immunoprecipitation between AXL and EGFR to the exclusion of IGF1R by reciprocal immunoprecipitation in MDA-MB-231 (Fig. 4.12E). Our quantitative analysis framework ruled out the possibility that merely low abundance of IGF1R and INSR was a trivial explanation for the absence of significant colocalization. We therefore conclude that AXL is colocalized with ErbB, MET, and PDGFR, but not with IGF1R or INSR.

The amount of EGFR-AXL complex was much greater in MDA-MB-231 than in other cell lines, likely as a result of the differences in abundance of EGFR (Fig. 4.11C). MCF7 cells transfected with AXL and treated with EGF showed no synergistic response characteristic of receptor transactivation, consistent with the relatively little EGF-elicited signaling overall (Fig. 4.14A). We therefore considered whether we could predict the importance of AXL transactivation induced by activation of RTKs other than EGFR. MDA-MB-453 cells have large amounts of HER2 and HER3 in complex with AXL, so our notion would predict that AXL signaling might contribute to a heregulin (HRG)-stimulated response in these cells. We learned by direct test, using AXL transfection and HRG treatment, that this is in fact observed (Fig. 4.13A & 4.14B). We analogously predicted that the relative degree of synergistic HRG-induced signaling should be similar to the difference in signaling between EGF, TGFα, HGF, HRG, HBEGF and IGF, if the effect of clustering can be resolved from single RTK-specific effects. In other words, phosphorylation sites that show synergistic activation should be relatively less stimulated by IGF stimulation because IGF1R does not display comparable AXL colocalization. Indeed, the magnitude of synergy induced by HRG and AXL signaling correlated significantly with colocalized RTK-specific signaling (Fig. 4.13B & 4.14C). This indicates that RTK/AXL colocalization can predict RTK-mediated AXL transactivation, and that this transactivation leads to similar downstream signaling not obtained through activation of IGF1R or INSR.

Discussion

Differential expression between two sets of cells or tumors is often used as evidence for the functional significance of particular genes but ignores the intricate correlation present between genes that can lead to spurious

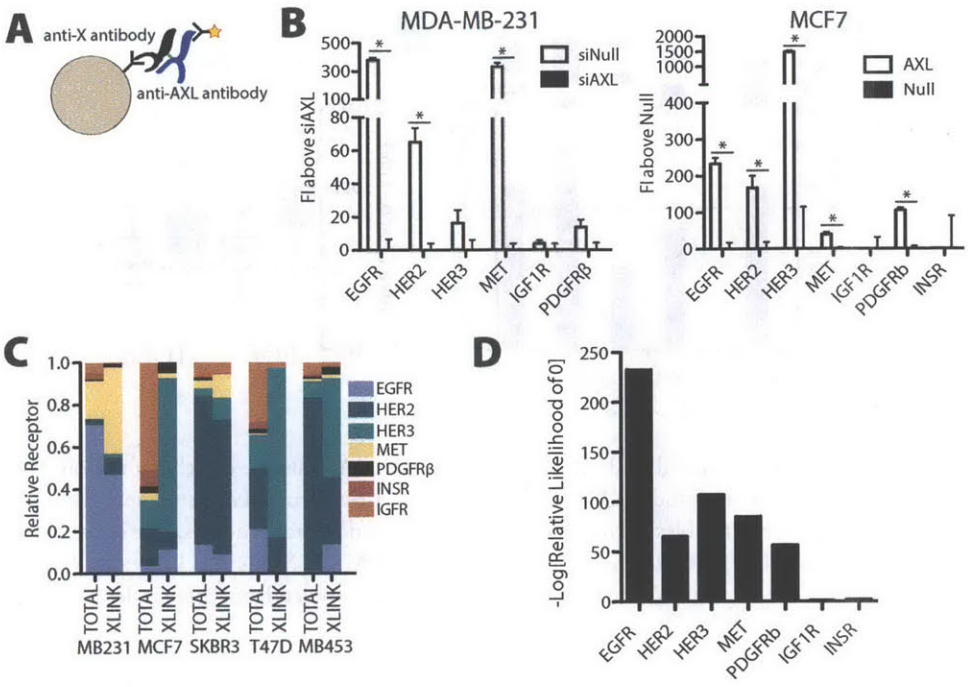

Figure 4.11: AXL colocalizes with ErbB receptors and MET. (A) Illustration of the multivariate cross-linking-mediated co-immunoprecipitation procedure adopted. After ethylene glycolbis(succinimidylsuccinate) cross-linking, cells are lysed and incubated with identifiable beads targeting non-AXL RTKs, then with an antibody for AXL to quantify the amount of receptor co-IP. (B) Quantification of AXL in complex with the indicated receptor in MDA-MB-231 and MCF7 cells. To account for possible antibody crosstalk, samples were always compared to those with AXL modulated either by siRNA-mediated knockdown (siAXL) or exogenous expression (AXL) in MDA-MB-231 or MCF7 cells, respectively. Data are means ± SEM from 6 technical replicates, across biological duplicates; $p < 0.05$, Student's test. (C) Summary of the relative amount of the indicated receptor found in AXL-linked complexes assessed by direct ELISA (TOTAL) or cross-receptor measurement (XLINK) from each cell line in cross-linked lysates. (D) Relative likelihood of each parameter being 0 (no complex occurring with AXL) for each receptor across all five cell lines.

associations in targeted studies. We interrogated a large publicly available dataset derived from cancer cell lines to examine the role of receptor expression in resistance to RTK-targeted therapeutics, and find that AXL expression synergizes with expression of the gene encoding the targeted receptor when predicting resistance to erlotinib and lapatinib. However, as a result of coexpression of AXL and EGFR, this relationship could not be clearly identified by univariate analyses. Although activation of AXL has been implicated in resistance to ErbB inhibitors in both lung cancer and HER2-positive breast cancer [204, 207], our analysis suggests that AXL expression may be a common marker of EGFR inhibitor resistance in TNBC, and possibly in other subtypes of breast carcinoma (Fig. 4.1B). Using dedicated experimental tumor cell cultures, we discovered a synergistic interaction between ErbB and AXL signaling in which AXL transactivation mediated by associated EGFR amplified the response of a subset of downstream elements, quantitatively shifting emphasis of the downstream network across multiple pathways. This diversification contributed in a critical manner to the migration and efficient proliferation of TNBC cells in response to EGF (Fig. 4.1E & 4.9D). Moreover, we found that this transactivation appeared to result from physical clustering interactions, which are quantitatively restricted to certain RTKs depending on a combination of intrinsic "affinity" and expression (Fig. 4.11C-D). We also predicted additional RTK/ligand contexts in which AXL synergistically amplified downstream signaling (Fig. 4.13).

Context-dependent physical interaction between EGFR and AXL has recently been appreciated [221]. Our data indicate that ErbB, MET, and AXL receptors exist in local clusters on the plasma membrane, though do

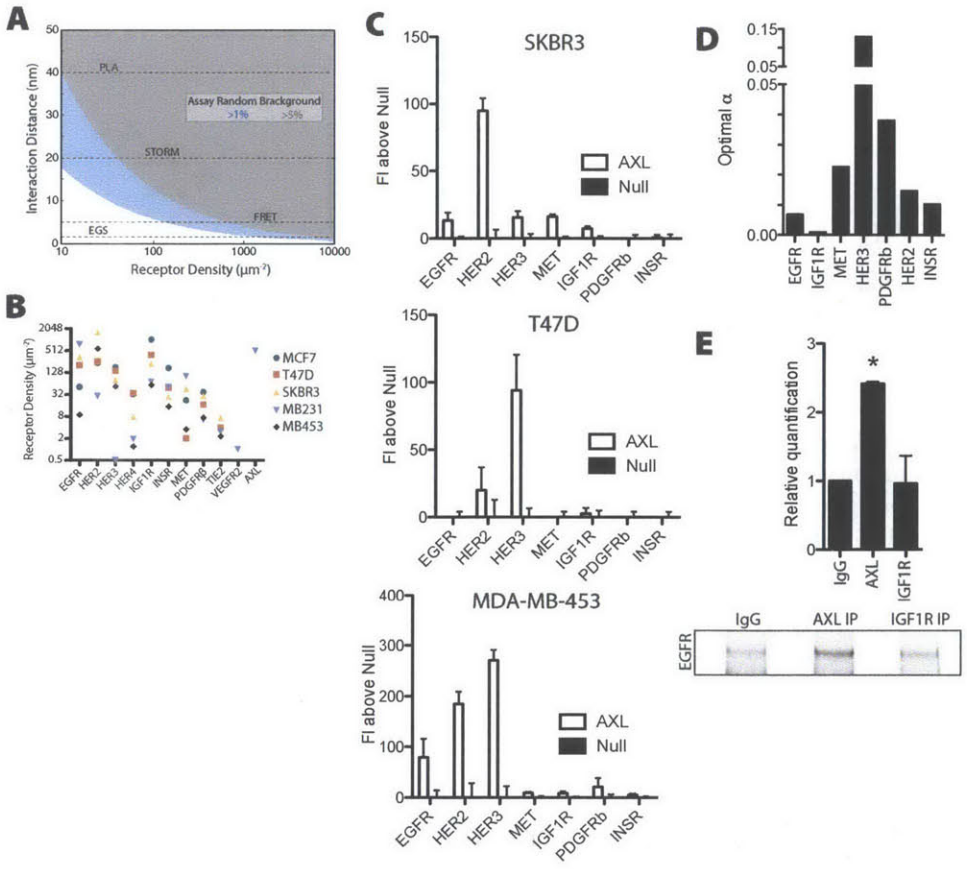

Figure 4.12: A multivariate chemical cross-linking approach to study receptor co-localization. (A) A random receptor distribution model eliminates antibody-based in situ methods as means to study co-clustering of surface receptors at high expression. Each colored region indicates a threshold of background for a particular assay with characteristic distance and receptor density. (B) Absolute quantification of receptor expression identifies which receptors can be analyzed using various methods. Details of receptor density quantification are given in the Methods. Points not shown are below the limit of detection ($< 2\ \mu m^{-2}$ for every receptor). (C) Quantification of AXL cross-linking in three luminal, HER2+ breast carcinoma cell lines. For each, increased expression of AXL is compared to cells which do not express AXL (biological duplicate, N=6 technical replicates). (D) Optimal α_i parameters for the data across seven RTKs. (E) Reciprocal co-immunoprecipitation of EGFR with AXL or IGF1R. A blot of the immunoprecipitation is shown (bottom) along with quantification of duplicate experiments (top, $^*p < 0.02$, Student's test).

not distinguish between distinctly bound complexes and diffusional proximity. As IGF1R and INSR are the only receptors examined here not found in complex with AXL, and IGF1R seems to be qualitatively distinct in its inability to provide compensatory resistance, we expect this clustering may be important to the signaling that confers resistance [43]. Clustering may arise as a consequence of mutual interactions with the extracellular matrix, weak lipid interactions, or shared scaffold interactions. Our observations along with previous reports are consistent with the phenomenon that clustering leads to subsequent activation-dependent enhancement of interactions after stimulation [221], with striking correlation between the receptors that are activated in trans and their localization on the cell surface [211]. Future work is needed to perturb this clustering specifically and examine the extent to which such clustering is required for resistance, transactivation, and diversification of receptor signaling. If clustering is required for these effects, drugs targeting the interaction mechanism may be efficacious in counteracting this signal diversification, thereby bolstering RTK-targeted therapy effectiveness.

These results carry clinical significance in the design of therapies targeting AXL and MET signaling, par-

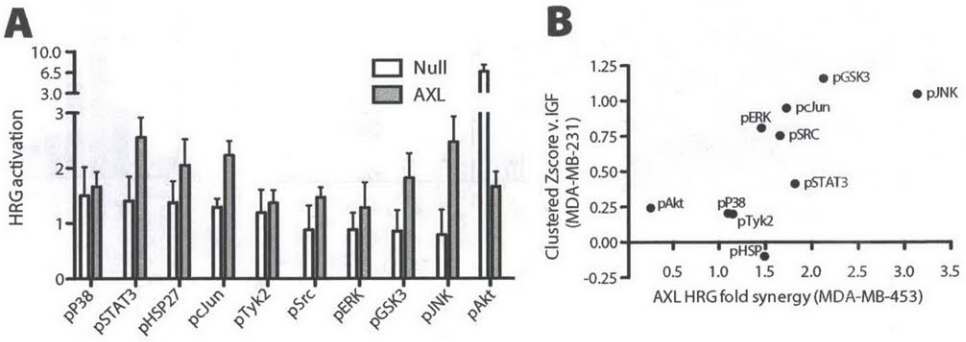

Figure 4.13: Cross-linking predicts HRG-AXL crosstalk in MDA-MB-453. (A) Fold activation of downstream signaling after HRG stimulation in cells with or without exogenous AXL expression. (B) For the effect of clustered receptors in MDA-MB-231, the signaling measurement of IGF-stimulated cells was zscore-normalized to the mean measurement of EGF-, TGFα-, HGF-, HRG-, and HBEGF-stimulated cells. For synergy in MDA-MB-453 cells, the ratio of fold activation after HRG treatment in cells overexpressing AXL to that in cells that do not express AXL. MDA-MB-453 cells do not normally express AXL. $p = 0.027$, Spearman correlation.

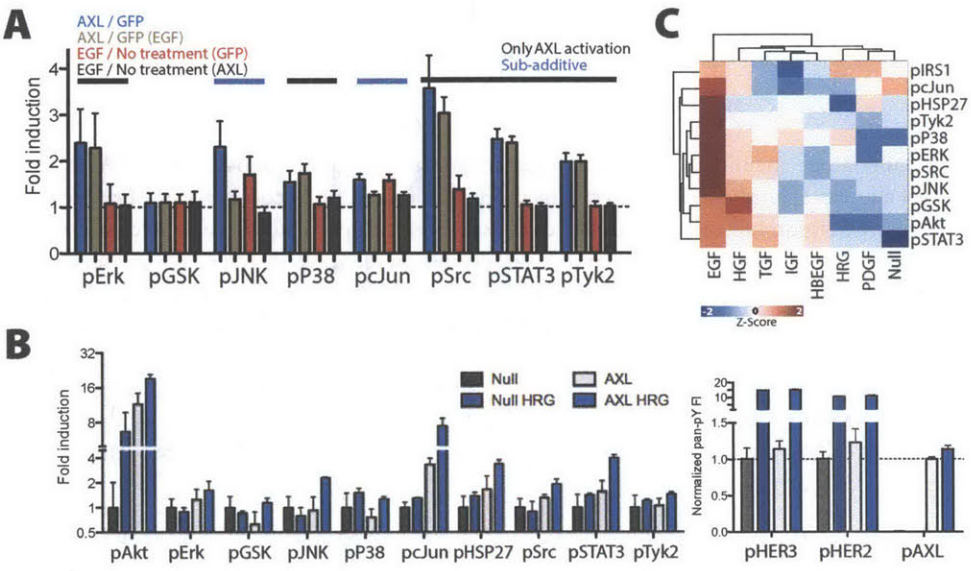

Figure 4.14: Cross-linking can predict receptor transactivation pairs. (A) Ratio of kinase phosphorylation after 5 min treatment of MCF7 cells with EGF, with or without exogenous AXL expression. Each bar indicates the ratio of two treatment conditions, with the standard error propagated from the error of each individual measurement from biological triplicates. Synergistic signaling response would correspond to a greater black than red bar for a given phosphosite. (B) Phosphorylation of indicated kinases (left) or receptors (right) in MDA-MB-453 cells that were untreated (Null), treated with HRG for 5 min, or transfected with exogenous AXL and either untreated or treated with HRG. Error bars indicate standard error of biological triplicate measurements. (C) Phosphorylation of indicated kinases treated with different growth factors for 5 min for use in Fig. 4.13B. Each measurement was mean centered and variance normalized across conditions.

ticularly within TNBC. Subadditive cytotoxicity after dual treatment with AXL and EGFR inhibitors suggests that the TNBC cells investigated here may be more reliant on AXL or MET for downstream signaling than EGFR itself, and that the effects of increased EGFR abundance may be in large part manifest by activation of AXL or MET. If dispensable for survival, EGFR is still important for directing metastatic dissemination, and our results suggest that transactivation may be important for promoting such an invasive response [139]. Activation by alternative receptors indicates that treatments blocking ligand binding to AXL and MET, an area of active investigation [222–225], may not be effective in blocking signaling from these receptors, and that inhibitors of their kinase activity or treatments that reduce receptor abundance may be more effective [223, 226]. Transactivation-mediated signaling may additionally be a means of secondary resistance to MET or AXL ligand-blocking treatments. In other carcinomas, EMT and the expression of AXL and c-MET have been identified as a mechanism of secondary resistance to ErbB targeted therapies [204, 207]. Crosstalk in these cells, particularly after ErbB-targeted treatment is halted due to RTK-mediated secondary resistance, may provide qualitatively distinct signaling through new receptors, though in response to the original activating ligand. Consequently, upon withdrawal of treatment, cells could respond to the original ligand with a more invasive or aggressive phenotype as a result of the dynamic network rewiring that created resistance [227–229]. Finally, given the striking similarities in signaling and resistance profiles of AXL and MET, as well as the observation that MET can drive AXL expression [230], inhibition of both receptors simultaneously in drug design may be desirable.

Our work more broadly raises the implication that modulation of RTK expression may not simply dictate response to stimulation by a receptor's cognate ligand, but that particular receptor pairs can communicate in a directional manner. Thus, cancer therapies targeting ligand interaction may be circumvented by activation in trans, and quantitative changes in inhibitor resistance may take place by amplification of signaling through other receptors. Future work is needed to gauge the extent and exact molecular mechanism of interfamily transactivation, the mechanisms of pre-clustering, as well as the exact signals that are sufficient for therapeutic resistance through activation of alternative receptors.

Methods

Antibody reagents, growth factors, and inhibitors EGF, PDGF-BB and TGFα were purchased from Invitrogen. HGF, IGF1, HBEGF and HRG were purchased from Peprotech. Unless otherwise indicated, EGF and Gas6 (R&D Systems) were used at 100 ng mL^{-1}. TGFα, PDGF-BB, HBEGF and HGF were used at 50 ng mL^{-1}. HRG was used at 80 ng mL^{-1}. AF154 (R&D Systems) was used at 900 ng/mL. Biotinylated AXL detection, capture and activating antibodies were purchased from R&D Systems. EGFR, GAPDH, EGFR pTyr1173, EGFR pTyr1068, EGFR pTyr1045, SHC pTyr317, Cdc2 pTyr15, ERK pThr202/pTyr204, Akt pS473, and α-Actinin were used for Western blotting and purchased from Cell Signaling. AXL (Santa Cruz) and Cav1 pTyr14 (Sigma) were also used for Western blotting.

R428 was purchased from Synkinase. AXL SMARTpool ON-TARGETplus siRNA, nontargeting SMARTpool ON-TARGETplus siRNA and Dharmafect 4 was purchased from Thermo Scientific. Lipofectamine 2000 was purchased from Invitrogen.

ELISA-based signaling measurements were performed according to the manufacturer's instructions (Biorad). In all cases, pERK is ERK1/2 (pThr185/pTyr187, pThr202/pTyr204), pGSK3 is GSK3α/β pSer21/pSer9, pJNK is JNK pThr183/pTyr185, pP38 is P38 pThr180/pTyr182, pcJun is c-Jun pSer63, pHSP27 is HSP27 pSer78, pIRS1 is IRS1 pSer636/pSer639, pSrc is Src pY416, pSTAT3 is STAT3 pTyr705, pTyk2 is Tyk2 pTyr1054/pTyr1055, and pAkt is Akt pSer473.

Lysis was performed using 50 mM Tris-HCl pH 7.5, 10% glycerol, 150 mM NaCl, and 1% NP40, with cOmplete protease (Roche) and phosphatase (Boston Bioproducts) inhibitors added before use.

Cell culture MDA-MB-231, MDA-MB-157, T47D, MDA-MB-453, SKBR3 and MCF7 cells were cultured in high-glucose DME supplemented with 10% FBS and 1% penicillin-streptomycin. For knockdown, 5×10^5 MDA-MB-231 cells in a 10 cm plate were transfected with 125 pmol of nontargeting siRNA or siRNA targeting AXL using Dharmafect 4 according to the manufacturer's instructions. All further analysis was performed 48 hours after siRNA transfection. For AXL overexpression, untagged AXL in pIRESpuro2 was transfected using Lipofectamine according to the manufacturer's instructions, and further experiments were performed 12 hours later.

Signaling analysis Cells were seeded sparsely in 6-well plates overnight and serum starved for 4 hrs in DME media with 0.35% bovine serum albumin and 1% penicillin-streptomycin. Following starvation, cells were stimulated with EGF, TGFα, or HGF for 5 min and lysed. Protein concentration was measured using BCA. When used, inhibitors were added upon serum starvation.

Protrusion measurement Glass-bottomed dishes (MatTek) were coated with 0.2% Matrigel in serum-free media for 30 min. Cells were seeded sparsely overnight and serum starved for 4 hours in L15 media with 0.35% bovine serum albumin. Inhibitors, when indicated, were added at the beginning of serum starvation and present in the stimulatory bolus. DIC images were acquired every 10 s for 1 min before stimulation and 9 min after stimulation. Cell areas were traced immediately before stimulation and 9 min after stimulation using ImageJ (National Institutes of Health). Single-cell information was aggregated from at least three independent experiments.

Receptor cross-linking For MDA-MB-231, 5×10^5 cells in 10 cm dishes were transfected with either siRNA targeting AXL or a nontargeting control, and the next day the cells were plated at identical densities. Two days post-transfection, cells were starved 4 hours and cross-linked using 1 mM EGS for 30 min at 4°C. For MCF7, SKBR3, T47D, and MDA-MB-453, 50% confluent 15 cm plates were transfected with 20 μg of AXL in the IRESpuro2 vector. The next day, cells were starved 4 hours and cross-linked using 1 mM EGS for 30 min at 4°C. Cells were lysed and normalized by total protein. Measurement of cross-linking was performed by modification of a kit for total RTK measurement (Novagen). Briefly, lysates were diluted two-fold in assay buffer and incubated with capture beads for RTKs other than AXL overnight. The lysates were then cleared, and the beads were washed with wash buffer and then incubated with a biotinylated antibody for AXL for 1 hour. After washing again, the beads were incubated with streptavidin-conjugated phycoerythrin for 30 min, and then quantified using a Bio-Plex 200 (Bio-Rad Laboratories).

Support Vector Classification Cell lines were classified according to their published drug response and expression, measured as cell viability using CellTiter Glo after 72 hrs [212]. Microarray expression measurements were processed by the robust multi-array average (RMA) method as described in the original publication. A cell line was considered resistant to the selected drug if its IC50 was reported to be above 8 μM. This cutoff was selected somewhat arbitrarily as it was the maximum dose tested; however other cutoffs produced identical results. This method of classification largely agreed with classification based on activity areas and EC50 values. Cell lines without corresponding drug and expression measurements were thrown out.

As an initial control (blue region, Fig. 4.1B), the targets of each drug were used on their own to predict sensitivity. The drug target was always among the strongest independent predictors of drug response. To calculate significance for later comparisons, this expression measurement was combined with a pseudorandom vector generated using the randn function, and the process was repeated 10^4–10^8 times, depending upon the significance stringency being tested.

Another control (black region, Fig. 4.1B) was created by only use of the random data vector in repeated trials. Prediction with the drug target was always significantly higher than with only random data. Thus, with these controls, expression of another RTK was considered to be predictive of drug sensitivity if a model of the RTK with the drug target was above the 95th quantile of the blue and black lines.

Classification was performed using the `svmtrain` function in MatLab, using a linear kernel and quadratic programming optimization method. A quadratic kernel or other optimization methods led to qualitatively identical results. The probes corresponding to AXL and EGFR expression were `558_at` and `1956_at`, respectively.

Synergy significance The Loewe interaction model was used to evaluate synergy or antagonism [231]:

$$1 = \frac{D_1}{IC_{50,1}\left(\frac{E}{E_{con}-E}\right)^{\frac{1}{m_1}}} + \frac{D_2}{IC_{50,2}\left(\frac{E}{E_{con}-E}\right)^{\frac{1}{m_2}}} + \frac{\alpha D_1 D_2}{IC_{50,1}IC_{50,2}\left(\frac{E}{E_{con}-E}\right)^{\frac{1}{2m_1}+\frac{1}{2m_2}}}$$

where D_1 and D_2 are the concentrations of the first and second drugs respectively, $IC_{50,11}$ and $IC_{50,2}$ are respectively the IC_{50} values of each drug, and m_1 and m_2 are a shape parameter for each drug respectively. E_{con} is the viability of untreated cells, and E the viability of cells for the respective drug concentrations. Viability data was normalized such that the maximum measurement was scaled to 1, and E_{con} was set to be 1. Lastly, α is the Loewe synergy parameter, which is negative for antagonism, positive for synergy, and zero for additive effects. Because of the lack of analytical expression for E, the value of E was calculated using lsqnonlin by solving for the value that minimizes:

$$\underset{E\in[0,1]}{\text{argmin}} \left| \frac{D_1}{IC_{50,1}\left(\frac{E}{E_{con}-E}\right)^{\frac{1}{m_1}}} + \frac{D_2}{IC_{50,2}\left(\frac{E}{E_{con}-E}\right)^{\frac{1}{m_2}}} + \frac{\alpha D_1 D_2}{IC_{50,1}IC_{50,2}\left(\frac{E}{E_{con}-E}\right)^{\frac{1}{2m_1}+\frac{1}{2m_2}}} - 1 \right|$$

Fitting was performed using the nlinfit function within Matlab with initial parameters identified by inspection of the single drug data. Optimization was unconstrained, but IC_{50} values were in all cases significantly positive and all m values significantly negative as verification of effective fitting. Confidence intervals presented were calculated from the empirically derived Jacobian using the `nlparci` function. Significance was separately verified by jackknife [142].

Partial least squares regression & principle components analysis Replicate measurements were averaged, and each signaling variable was mean centered and variance normalized before further analysis. Principle components analysis was performed using singular value decomposition within the pca function. The first two components explained 83% of the variance.

For reduced partial least squares modeling, the output variable was assembled from mean protrusion measurements for each growth factor, and the unstimulated condition set to 0. Model reduction was performed by training models using all possible combinations of three input variable sets. Three variables were chosen, as it was the smallest model size with sufficient well-trained models to ensure robust variable enrichment. Model reduction with larger reduced models produced qualitatively similar results. Each individual reduced model was then used concomitantly, and the results shown by displaying the average and standard error of loadings values and predictions. As a result of variation in baseline signaling, predictions for knockdown cells were taken to be the prediction for the knockdown and stimulated condition minus the prediction of the knockdown and unstimulated condition.

Amplification modeling Each model was fit using the `nlinfit` function within MatLab (Mathworks). To ensure robustness with respect to initial parameter selection, fitting was performed 100 times with randomly selected initial parameters within the range of feasible values. ξ is 0 with AXL knocked down and 1 with AXL present. [pEGFR] and [pAkt] are from measurements of pan-pY EGFR and pAkt across a dose range of EGF. Models were compared using the corrected and uncorrected Akaike information criterion denoted AICc and AIC, respectively [220].

To fit data to a model in which activation of AXL is in proportion to EGFR activation, and signaling integration is receptor-proximal, equation 1 was used:

$$[\text{pAkt}] = \frac{B_{\max}([\text{pEGFR}] + \alpha\,[\text{pEGFR}]\,\xi)}{\text{K}_\text{D} + ([\text{pEGFR}] + \alpha\,[\text{pEGFR}]\,\xi)} + B_0$$

For a model in which amplification of Akt activation with respect to a set amount of EGFR activity, and AXL only affects this proportional relationship, equation 2 was used:

$$[\text{pAkt}] = \frac{B_{\max}(1 + \alpha\xi)\,[\text{pEGFR}]}{\text{K}_\text{D} + [\text{pEGFR}]} + B_0$$

For a model in which no signaling effect from AXL exists, equation 3 was used:

$$[\text{pAkt}] = \frac{B_{\max}\,[\text{pEGFR}]}{\text{K}_\text{D} + [\text{pEGFR}]} + B_0$$

For a model in which some baseline activation of AXL is possible in addition to proportional activation, and signaling integration is receptor-proximal, equation 4 was used:

$$[\text{pAkt}] = \frac{B_{\max}([\text{pEGFR}] + \alpha\,[\text{pEGFR}]\,\xi + \xi\beta)}{\text{K}_\text{D} + ([\text{pEGFR}] + \alpha\,[\text{pEGFR}]\,\xi + \xi\beta)} + B_0$$

For a model in which Akt activated by AXL and activated by EGFR is simply summed, with proportional activation of AXL, equation 5 was used:

$$[\text{pAkt}] = \frac{B_{\max,1}\,[\text{pEGFR}]}{K_{D,1} + [\text{pEGFR}]} + \frac{\xi B_{\max,2}\,[\text{pEGFR}]}{K_{D,2} + [\text{pEGFR}]} + B_0$$

For a model in which no signaling effect from AXL through EGFR pathway exists, but there is simply a baseline effect of AXL presence, equation 6 was used:

$$[\text{pAkt}] = \frac{B_{\max}\,[\text{pEGFR}]}{K_D + [\text{pEGFR}]} + \xi\beta + B_0$$

For a model with only baseline activation of AXL, and signaling integration is receptor-proximal, equation 7 was used:

$$[\text{pAkt}] = \frac{B_{\max}([\text{pEGFR}] + \alpha\xi)}{K_D + ([\text{pEGFR}] + \alpha\xi)} + B_0$$

For a model with Akt activated by AXL and activated by EGFR is simply summed, with proportional and baseline activation of AXL, equation 8 was used:

$$[\text{pAkt}] = \frac{B_{\max,1}\,[\text{pEGFR}]}{K_{D,1} + [\text{pEGFR}]} + \frac{\xi B_{\max,2}([\text{pEGFR}] + \beta)}{K_{D,2} + ([\text{pEGFR}] + \beta)}$$

Total receptor quantification Total receptor amounts were measured using a bead based ELISA (Novagen). For quantification of AXL and MER, established ELISA antibodies and standards (R&D Systems) were used. The capture antibody was conjugated to unconjugated beads (Bio-Rad) and used in a multiplexed fashion with the other targets. Linearity of the assay was validated during measurement by dilution series of both the lysates and standards.

Each cell line was seeded sparsely, and the next day starved 4 hours and lysed. Receptor measurements were

normalized to total protein content to provide a receptor mass fraction (i.e. fg receptor per mg cell lysate). This mass fraction was used in all subsequent modeling. For receptor density calculations, a sub-confluent plate of cells was trypsinized, the number of cells counted and lysed, and total protein quantified. This provided the conversion, for each cell line, from mg of lysate to number of cells. Combined with the known mass of each receptor, a value could then be converted to number of receptors per cell. Finally, a receptor density was calculated by using the surface area of a HeLa cell (1600 μm^2, BNID 103718, [232]).

Assay selection To determine which methods might be suitable for studying such complexes on the cell surface, we developed a simple statistical model to describe the background one might expect given particular receptor expression, a characteristic distance for a particular assay, and random distribution of receptors on the surface of a cell. The background of an assay that gives signal when two receptors are within a particular distance has a background of one minus the probability of co-localization occurring by chance, given by a Poisson distribution: $B = 1 - p(0|\lambda) = e^{-\lambda}$. The average number of receptors at a density of n found within a characteristic distance of R is given as $\lambda = n\pi R^2$. Integrating these, the background B of an assay with a characteristic distance of R and with a mean receptor density of n is $B = 1 - e^{-n\pi R^2}$ and for a given amount of acceptable background, the maximal characteristic radius is:

$$R = \sqrt{\frac{-\ln(1-B)}{n\pi}}$$

Cross-linking distance modeling T_{ij} is the amount of receptor i in cell line j. β_j encompasses variation in the efficiency of cross-linking and protein loading from experiment to experiment. α_i encompasses variation in the efficiency of antibodies for each receptor, and the amount of cross-linking between AXL and receptor i. Therefore, the amount of cross linking X_{ij} from AXL to receptor i within experiment and cell line j is modeled as $X_{ij} = \alpha_i \beta_j T_{ij}$ where $i \in [1, 7], j \in [1, 4]$. The likelihood of each observation was calculated using the distance between the amount of cross-linking predicted by a particular model and that observed, as well as the standard error for each measurement (all cross-linking measurements were performed with 4–6 technical replicates).

Constrained optimization was performed with $\alpha_i \in [0, 1]$ and $\beta_j \in [0, 1]$ using fmincon within MatLab. To assess confidence in robust cross-linking, individual α_i parameters were constrained as 0 and optimization was again performed. The difference in likelihood was used for assessment of cross-linking. For the globally optimal solution, initial parameters were randomly assigned repeatedly to avoid local minima. For constrained solutions, the global optimum without constraint was used as the initial parameter state.

Receptor cross-linking immunoprecipitation Three confluent 15 cm plates of MDA-MB-231 cells were cross-linked with 1 mM EGS for 30 min at 4°C and then lysed. The lysate was clarified by centrifugation at 16,100×g for 15 min, and then pre-cleared for 30 min with agarose resin. Lysate was then incubated with protein A/G agarose and either an IgG control, AXL, or IGF1R antibody overnight at 4°C. The next day, the resin was washed 6 times with lysis buffer and then incubated with 2M hydroxylamine·HCl in PBS pH 8.5 for 6 hours at 37°C. The resin was then removed and the supernatant run on a reducing gel.

FACS analysis Cells were treated with 2 μM R428 in full-serum media. 24 hours later, cells were trypsinized, stained and immediately analyzed by flow cytometry. Dual staining was performed using mab225 and AF154 (R&D Systems) for 1 hour on ice. Staining for each receptor was performed separately when in conjunction with live/dead analysis. YO-PRO-1 and propidium iodide were used according to manufacturer's guidelines (Invitrogen).

Chapter 5

The AXL Receptor is a Ligand Spatial Heterogeneity Sensor

Abstract

The AXL receptor is a TAM (Tyro3, AXL, MerTK) receptor tyrosine kinase (RTK) important in blood clotting, viral infection, innate immune response and cell clearance, deregulated in many human carcinomas [92, 207, 233–235]. While the immediate cognate ligand-receptor complex (Gas6-AXL) structure is known, studies examining ligand-mediated signaling often provide paradoxical results [79, 94]. Therefore, a detailed, mechanistic picture of AXL activation, and thus quantitative understanding of the nature and contexts of ligand-mediated signaling, has not been previously undertaken. Employing quantitative biochemistry and deterministic modeling we show that AXL operates to sense local spatial heterogeneity in ligand concentration, due to an unusual dichotomy between ligand-dependent and ligand-independent signaling. We experimentally validate diverse model predictions concerning this behavior. The results demonstrate that AXL functions distinctly from other RTK families, and this surprising insight will be vital for the design of AXL-targeted therapeutic intervention.

Introduction

Genetic studies perturbing expression of with TAM receptors or their ligands have identified roles for the proteins in diverse physiological processes. Since identification of Gas6 as a ligand for AXL, it has been observed to activate AXL signaling in a variety of cell types [97, 236–240]. At the same time, conflicting results have prevented assembly of a unified understanding for the stimulation contexts which activate the receptor. This prevents effective manipulation of receptor activity and thus study of its effects. Upon overexpression, AXL has been observed to be constitutively active and poorly responsive to ligand stimulation [79, 94, 208]. Blocking ligand expression is not always sufficient to block AXL-mediated resistance in cancer cell lines, even when blocking receptor activation is sufficient [207]. Recombinant ligand has been insufficient to mimick paracrine signaling but the mechanisms of how ligand might be presented differently are unknown [241]. Viral envolopes can synergistically activate TAM receptors when stimulated with a constant amount of ligand [94]. Many of these effects are thought to arise through simultaneous interaction of TAM ligands with phosphatidylserine-containing objects, though conflicting interpretations exist as to how this interaction effects receptor activation [242–244].

Results & Discussion

To better understand ligand-induced AXL signaling, we assembled a kinetic differential equation model of receptor-ligand binding, dimerization, and activation, incorporating current structural understanding of TAM

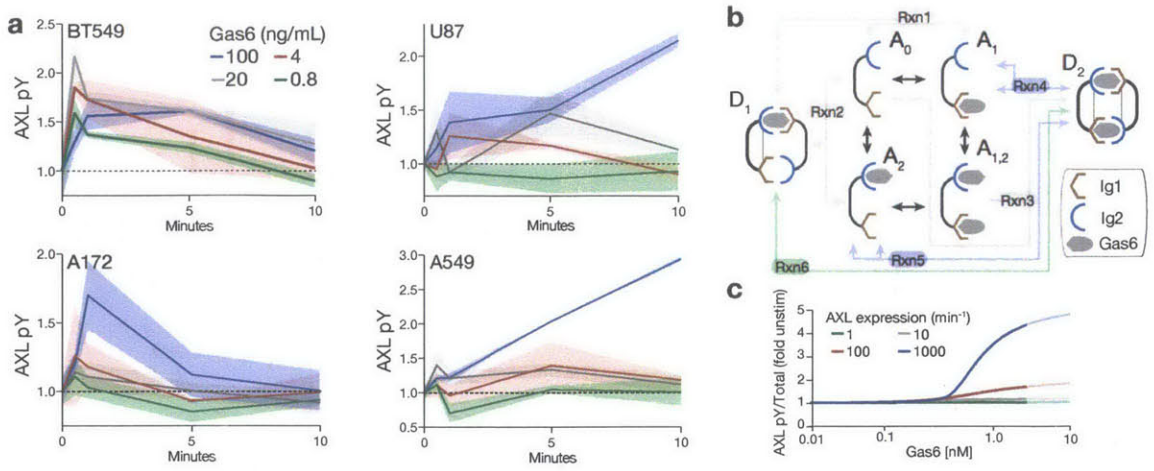

Figure 5.1: a) ELISA-based pan-phosphotyrosine measurement of AXL upon treatment with indicated concentrations of Gas6. Shaded areas indicate standard error of triplicate measurements. b) Diagram of the AXL signaling model. Trafficking is not shown. Binding reactions occur identically with internalized and surface species. c) Predicted steady-state (T = 240 min) AXL phosphorylation at varying abundances of AXL and Gas6.

ligand binding (Fig. 5.1b & Methods). TAM receptors are similar to growth hormone receptor in that ligand bridges two receptors with asymmetric affinity for each, though with the added complexity of two ligands, instead of one, bridging two receptors in a mirrored arrangement [79, 245]. Receptor trafficking was extrapolated from knowledge of other receptor tyrosine kinase families [246, 247]. For initial parameter estimation, we stimulated four carcinoma cell lines harboring varying levels of AXL expression with increasing concentrations of Gas6 and measured receptor phosphorylation time-courses (< 10 min) (Fig. 5.1a). We separately measured receptor phosphorylation and total abundance at 4 hours (Fig. 5.2a). Measurement of total TAM receptor expression confirmed that the vast majority of TAM receptor present in the cell lines used is AXL (Fig. 5.2b). These represent the first quantitative, dynamic measurements of TAM signaling, and the most comprehensive analysis of TAM ligand-elicited signaling, to our knowledge.

Depending on the AXL expression level and Gas6 concentration, Gas6-elicited AXL phosphorylation displayed either a transient peak (< 5 min) that rapidly returned to near-baseline levels or a monotonic increase in phosphorylation at high doses with relatively little response to lower doses of ligand (Fig. 5.1a). These dynamics of response are strikingly distinct from ErbB and other RTK signaling examined to date, which occurs relatively rapidly and with a simple relationship with respect to ligand concentration [140, 248, 249]. We confirmed using an activating antibody for AXL that these interesting responses are a feature of ectodomain regulation, as stimulation with the antibody produced a rapid and strong phosphorylation response (Fig. 5.2c).

We next interrogated our best-fit model to probe the dynamic capacity of ligand-mediated AXL signaling. AXL shows a surprisingly limited range of ligand-mediated response both in our experimental measurements and in predictions from our model (Fig. 5.1a & 5.2a); for instance, steady-state receptor phosphorylation displays only five-fold activation above unstimulated conditions (Fig. 5.1c). By evaluating the model across a broad range of Gas6 concentrations and AXL expression levels, we ascertained that within 5 and 10 minutes AXL exhibits at most a 2.5- and 4.5-fold increase in phosphorylation (Fig. 5.2d). This model prediction raises a fundamental question concerning the nature of information transduced by TAM receptors. Many other RTK families such as ErbB receptors conceptually perform as sensors of ligand concentration as they display characteristics of a sensor such as fast switching and a monotonic input-output relationship on short timescales. AXL activation, though, is strongly limited by the kinetics of binding (Fig. 5.1a & 5.2c), displays a relatively small range in activation across order of magnitude changes in ligand concentration, and under certain regimes displays exclusively transient signaling (Fig. 5.1a).

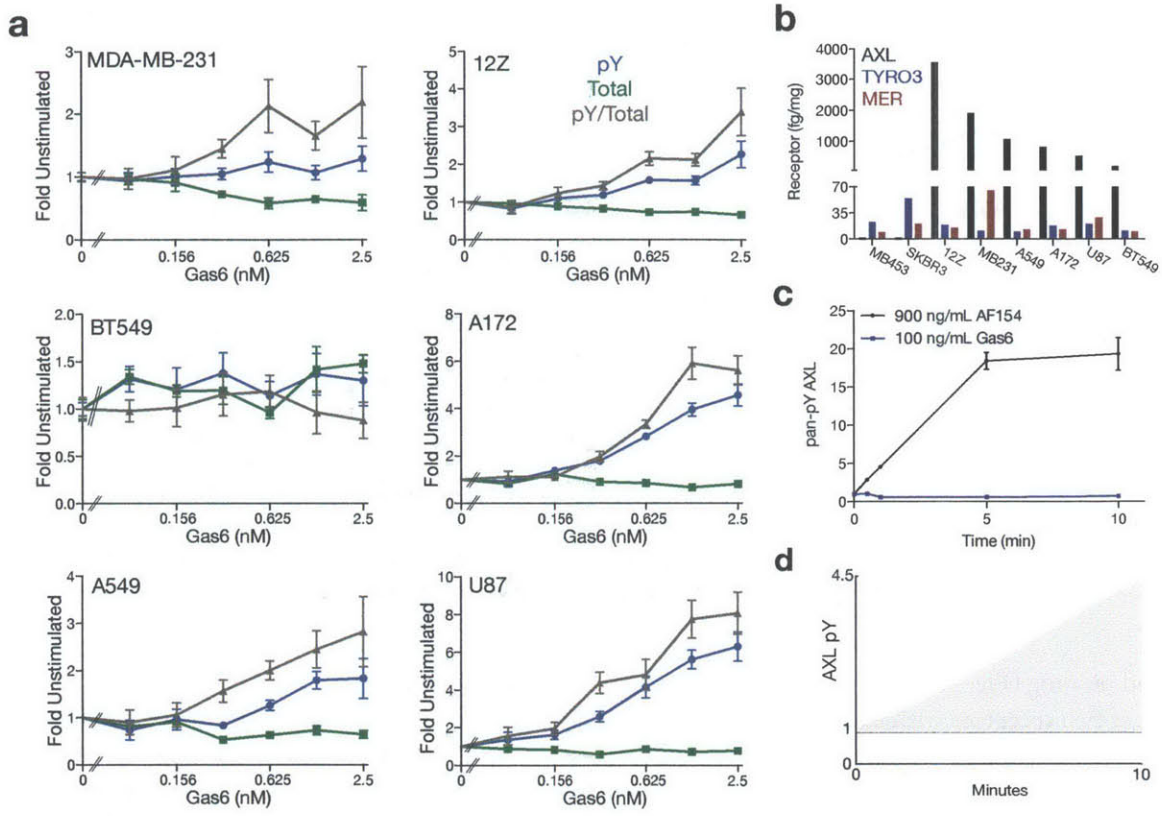

Figure 5.2: a) Measurement of AXL phosphorylation and abundance across varying doses of Gas6 in six cell lines. b) Absolute receptor quantification of TAM family members in starved cells by ELISA. c) Measurement of AXL phosphorylation in MDA-MB-231 in response to an activating antibody or Gas6. Phosphorylation measurement was normalized to total AXL abundance. d) Model range over time of AXL pan-pY for all reasonable autocrine ligand, simulated ligand, and receptor expression levels. Error bars indicate standard error of measurements in triplicate.

The phenotypes observed in TAM knockout mice suggest that physiological signaling principally involves ligand engagement once immobilized on phosphatidylserine-presenting surfaces [89]. Therefore, we extended our model to account for spatial heterogeneity and diffusion of ligand and receptor, via a finite difference framework (Fig. 5.3a). In contrast to the homogeneous model, local stimulation was now predicted to cause stronger and sustained receptor phosphorylation (Fig. 5.3b) and in fact greater total receptor phosphorylation (Fig. 5.3c). We determined by investigating the components of the model that this increase corresponded to a decrease in abundance of A_1 (receptor with Gas6 bound only at the high affinity site) and increase in D_2 (the full two-Gas6/two-AXL dimer) (Fig. 5.3d). This indicates greater occupancy of the low affinity site while reducing formation of $A_{1,2}$ (receptor with Gas6 bound at both sites) which can only dimerize with A_0 (completely unbound receptor). Impaired endocytosis of immobilized Gas6-bound AXL could not similarly increase receptor phosphorylation response (Fig. 5.4c). To test this prediction experimentally, we employed phosphatidylserine-mediated ligand-immobilization similar to that occurring within the in vivo environment to compare local and bulk stimulation quantitatively [250]. We incubated cells with identical concentrations of Gas6 in presence or absence of phosphatidylserine-containing vesicles to restrict ligand engagement. Despite bulk stimulation with a Gas6 concentration that produced no measurable change in bulk receptor phosphorylation (Fig. 5.1a), the presence of vesicles induced a small amount of receptor phosphorylation that strongly synergized when both factors were present (Fig. 5.3e & 5.3f). To test our hypothesis in an orthogonal manner, we coated polystyrene beads with Gas6 and incubated them with MDA-MB-231 cells, which displayed little response to bulk Gas6 stimulation

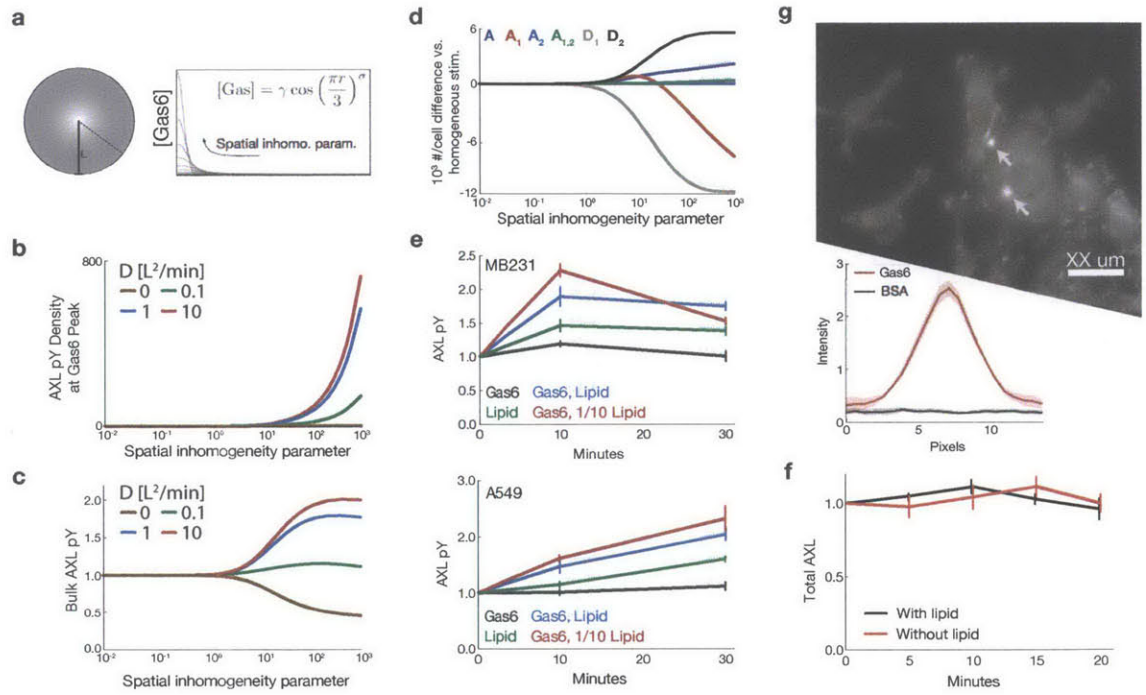

Figure 5.3: Spatially inhomogenous stimulation leads to robust AXL activation. a) Schematic of the finite differencing model. Diffusion was allowed within a radially symmetric region of interest. Total Gas6 amount was held constant while varying spatial profiles of concentration. b) Modeling output for AXL pan-pY density at the peak point of Gas6 at 30 min with respect to varied Gas6 concentration profiles. Autocrine Gas6 levels and AXL expression were set to A549 levels. c) Modeling output for bulk AXL pan-pY under identical conditions. d) Modeling output of species abundance at 30 min under identical conditions. Internalized and surface species were considered together. e) Measurements of AXL pan-pY in MDA-MB-231 (top) and A549 (bottom) upon stimulation with phosphatidylserine containing vesicles in the presence of 0.25 nM Gas6. 1× and 1/10× lipid concentrations correspond to 100 $\mu g\,mL^{-1}$ and 10 $\mu g\,mL^{-1}$ of lipid, respectively. f) Measurement of total AXL abundance in A549 cells upon stimulation with 0.25 nM Gas6, with or without vesicles. g) Pan-pY immunofluorescence (top) of MDA-MB-231 cells starved and stimulated with polystyrene beads coated with BSA or Gas6, and quantification of the immunofluorescence (bottom, N > 10). Cells were stimulated for 30 min prior to fixation. Error bars indicate the standard error of triplicate measurements, unless indicated otherwise.

(Fig. 5.2c). We observed substantive spots of phosphotyrosine staining in a Gas6-dependent manner, consistent with localized activation by bead-immobilized Gas6 (Fig. 5.3g). This mechanism of robust AXL activation is vital to the normal physiological role of AXL as a marker for phagocytic uptake of cellular debris and promotion of clotting [251]. A yet unexplained phenomenon is how ubiquitous Gas6, in the blood particularly, can produce transient signaling upon clotting [251–253]. While aggregation of receptor has been proposed our model shows that, while a greater local concentration of receptor may be important, this synergy is specific to ligand engagement and actively regulated [94, 254]. Whereas other RTK ligands can provide chemotactic cues, this system importantly allows for autocrine production of ligand—without signal generation by itself—to sense phagocytic targets.

A striking feature of our model is the requirement that AXL should have weak signaling capacity when not engaged in the ligand-bound signaling dimer D2 (Table 5.1 and Fig. 5.4a). To test this, we deleted each extracellular domain from AXL individually in turn, expressed each form of the receptor in MDA-MB-453 cells that lack AXL expression (Fig. 5.2b), and blotted for either total or phosphorylated receptor (Fig. 5.6a). Since ligand engagement requires binding to the Ig1 domain of one receptor and Ig2 domain of another, Ig1 or Ig2 domain deletion should entirely block ligand-dependent phosphorylation [79]. These deletions in fact maintained some receptor phosphorylation (Fig. 5.5a, 5.6a & 5.6b), indicating ligand-engagement is not strictly required for phos-

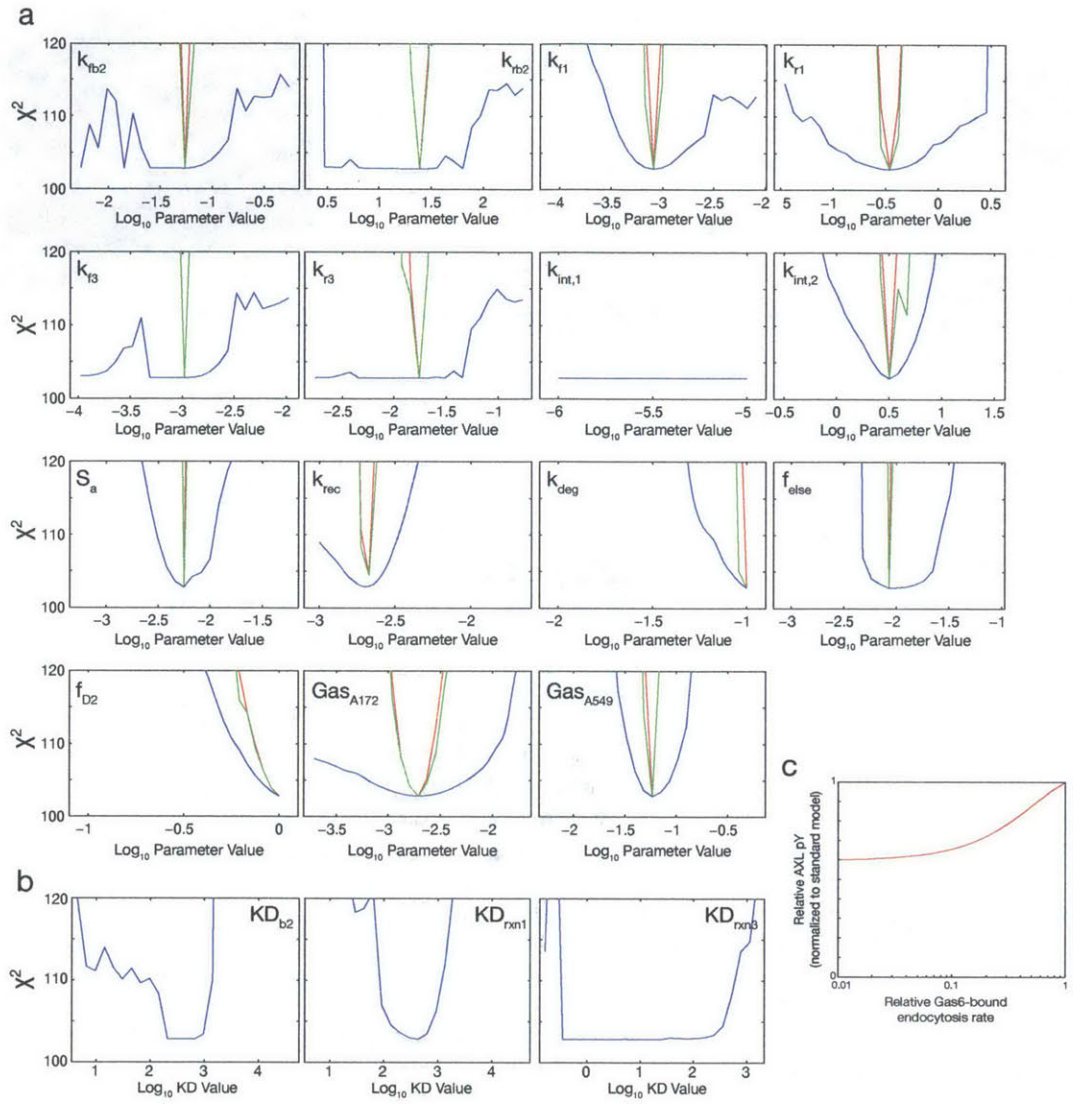

Figure 5.4: The kinetic model is partly identifiable and inhibited endocytosis cannot account for phosphatidylserine effect. A) Sensitivity analysis for individual parameters. The red, green and blue lines indicate the goodness-of-fit upon parameter scanning, local optimization and global optimization respectively. B) Sensitivity analysis for combination parameters. Unlike in original model fitting, the affinity for Ig2 is not constrained within 10-1000 nM. C) Relative receptor phosphorylation output for a model corresponding to A549 cells stimulated with 0.25 nM with varying extents of endocytosis impairment for the Gas6-bound surface species.

phorylation of AXL. Interestingly, deletion of the Fn1 domain of the receptor largely decreased activation of AXL, suggesting this domain may have an important unknown role in activation of the receptor. Others have noted similar constitutive activation of AXL, particularly upon overexpression [79]. Our model indicates this is not an artifact of overexpression, but instead is relevant to endogenous receptor function. While we treat ligand-independent signaling as a constant factor, its potential regulation, such as in trans from other RTK families, is an outstanding question [233].

Finally, we sought to test some further predictions of prospective importance for therapeutic manipulation of AXL signaling. Two interventions that have been proposed for targeting AXL activity are blocking the accumulation of Gas6 within the tumor microenvironment or disrupting gamma-carboxylation of Gas6 [222, 223].

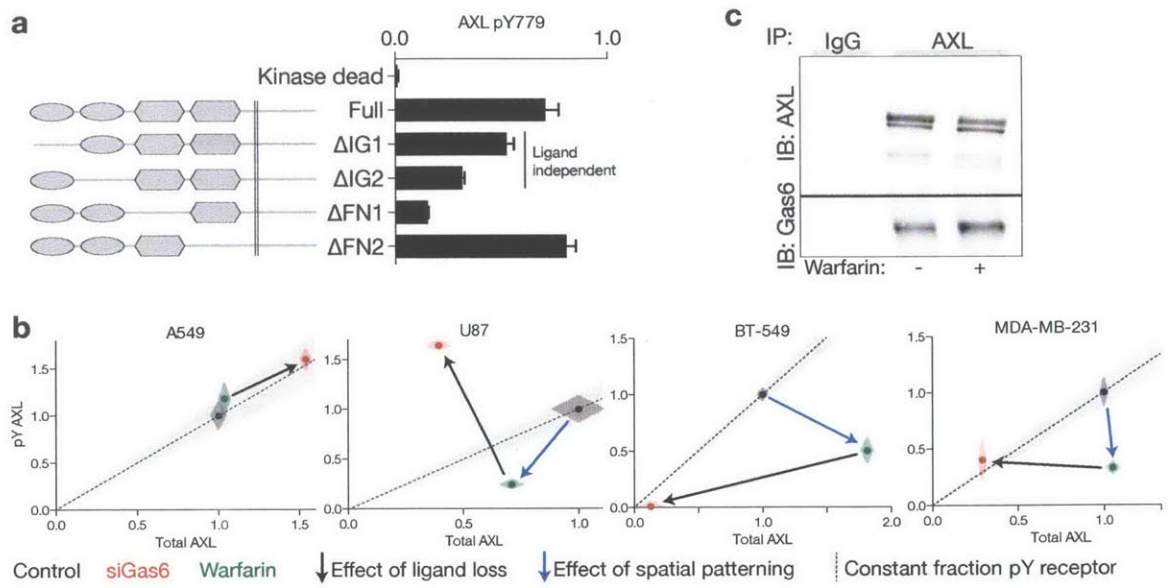

Figure 5.5: Experimental validation is consistent with ligand-independent signaling capacity and immobilization-based signal promotion. a) Activation of AXL deletion constructs in MDA-MB-453 cells, as measured by Tyr779 phosphorylation, normalized to total receptor abundance. b) AXL phosphorylation response of cell lines to Gas6 knockdown or warfarin treatment. Total and pan-pY AXL are indicated on separate axes. Shaded areas indicate standard error of triplicate measurements on each axis. c) Coimmunoprecipitation of AXL and Gas6 in MDA-MB-231 cells in the presence or absence of warfarin.

To mimic the former, we either knocked down Gas6 in AXL-overexpressing cell lines using an siRNA or treated with a blocking antibody that binds to Gas6 and blocks receptor interaction. Our model suggests that in some cells Gas6 knockdown may have little to no effect on AXL activity. While the BT549 cell line displayed a dramatic decrease in overall AXL abundance and thus phosphorylated receptor, three other tumor cell lines showed similar or greater receptor activation (Fig. 5.5b & 5.6c). With respect to gamma-carboxylation, conflicting literature exists as to whether maturation of Gas6 is required for interaction or activation of AXL [219, 241, 243, 244, 255–258]. Our model specifically predicts that modification of Gas6 need only confer differences in the localization of ligand to produce the differences in activity observed. Therefore, immature ligand may differentially activate the receptor, but should still have measurable signaling effects and should still interact with the receptor identically. The cells dependent upon gamma-carboxylation and those dependent on concentration of Gas6 need not be the same. To test this, we treated cells with warfarin, which inhibits synthesis of vitamin K, an essential component in gamma-carboxylation [219]. Three cell lines displayed significant changes in receptor phosphorylation, and consistent with our spatial modeling warfarin treatment always reduced receptor phosphorylation (Fig. 5.5b & 5.6d). Importantly, Gas6 displayed identical binding to AXL even when warfarin treatment significantly disrupted AXL activation (Fig. 5.5c).

Our combined experiment/modeling study here provides the first quantitative, mechanistic understanding of TAM signaling, and in doing so provides essential information for specific targeting of signaling dysregulation and normal function (Fig. 5.7). In a malignant context, our results suggest modulating the concentration of Gas6 within the tumor environment may be a less efficient means to blocking signaling as compared to directly targeting the receptor, and observations of Gas6 overexpression may require more nuanced interpretation. Tumor cells may take advantage of spatial ligand heterogeneity to upregulate AXL signaling, and the signaling may be directly upregulated by this mechanism through phosphatidylserine exposure after cytotoxic treatments. Fn1 domain targeting may be effective after additional functional investigation, and while true cancer cell specific

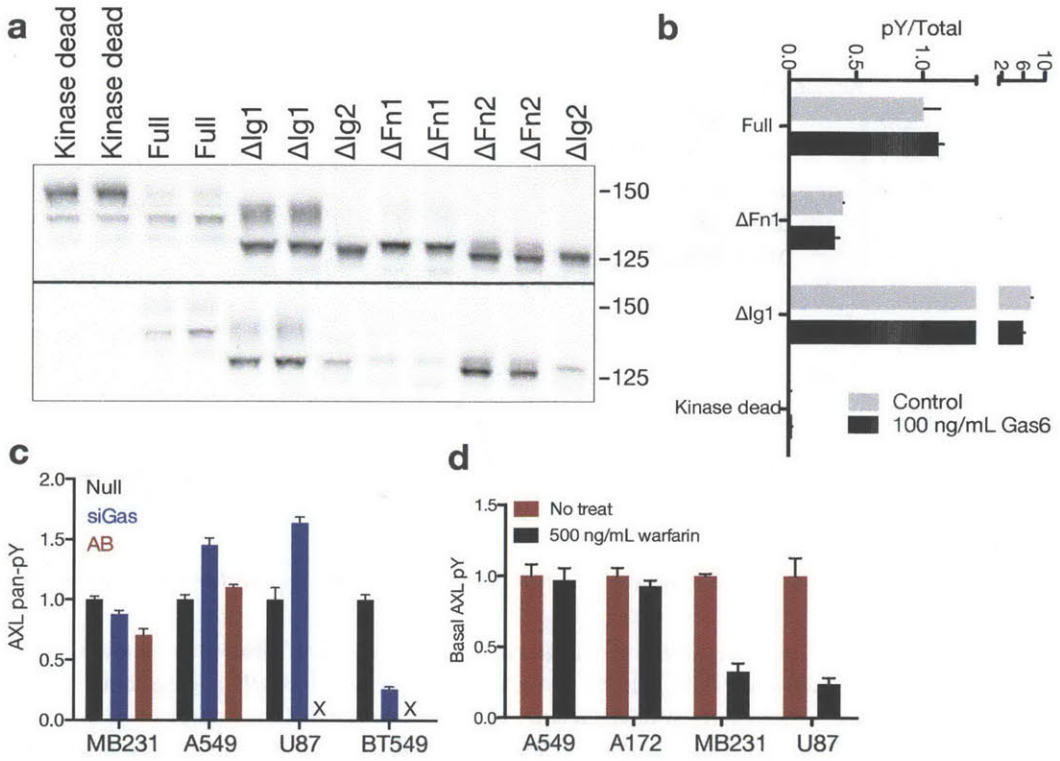

Figure 5.6: The ligand-binding domains of AXL are dispensable for receptor phosphorylation. A) Total and pY779 AXL in MDA-MB-453 cells overexpressing domain deletion mutants of the receptor. B) ELISA measurements of receptor pan-pY in MDA-MB-453 overexpressing domain deletion mutants of AXL. The capture antibody recognizes the Ig2 domain and so the mutant could not be measured. C) AXL pan-pY measurement of cells with Gas6 knocked down or blocked with an antibody against the ligand. D) AXL pan-pY measurement in cells with or without warfarin treatment. Error bars indicate the standard error of triplicate measurements.

targeting of AXL signaling is likely impossible, carefully engineered Gas6 binding manipulation may show some specificity for dysregulated signaling, important given recent reports of negative consequences for broad TAM inhibition [95]. Finally, as Gas6 is used once immobilized as a marker by the innate immune system for apoptotic clearance, manipulation of this system may hold promise in treatment of tumors that do not express TAM receptors through immune targeting for clearance [89].

Our work largely unifies current understanding of TAM signaling, and describes an unusual RTK system whereby cells sense discontinuities in ligand concentration rather than concentration itself. Kinetic modeling provides a framework for elucidation of many complex aspects of RTK signaling and integration of extant knowledge. While ligand presentation is intricately controlled within the in vivo environment, reaction-diffusion interactions have not been extensively identified [259]. Indeed, these complex effects will only be understood through detailed mechanistic modeling. Ligand concentration is only one property of the extracellular environment useful for measurement, and we anticipate future investigations will reveal similarly elegant sensing solutions designed by natural selection.

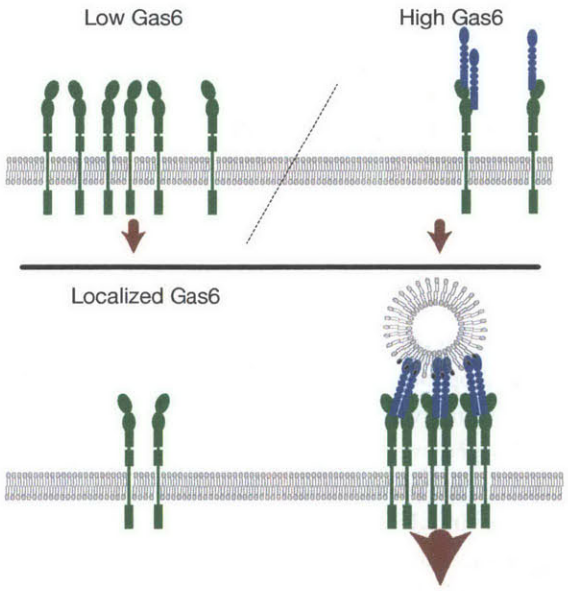

Figure 5.7: Model for efficient activation of AXL signaling. In the low Gas6 regime, sustained low signaling capacity provides a threshold for any ligand-mediated response. In the presence of a high, uniform concentration of Gas6, receptor downregulation and competitive inhibition of dimer formation prevent robust receptor activation. Only with presentation of localized Gas6 is strong receptor activation observed, driven by diffusional sampling of receptors between regions of high and low Gas6 concentration. This provides the appropriate localized signal for the functions of the receptor as a marker for phagocytosis.

Materials & Methods

Reagent preparation & cell culture MDA-MB-453, MDA-MB-231, A549, BT-549, A172 and U87 cells were obtained from ATCC. Anna Starzinski-Powitz (University of Frankfurt) generously provided 12Z cells by way of Steve Palmer (EMD Serono).

All ELISA measurements were performed in multiplexed fashion, using individually identifiable polystyrene beads (Luminex Corp). Briefly, beads were sedimented for 3 min at $10^4 \times$g then resuspended in 80 µL 100 mM NaH_2PO_4 pH 6.3. 10 µL of 50 mg mL^{-1} N-NHS and 10 µL of 50 mg mL^{-1} EDC was added, and the mixture was incubated with agitation for 20 min at room temperature. Beads were then pelleted and resuspended in 300 µL 50 mM HEPES pH 7.4 with 0.1 mg mL^{-1} of either AXL, MERTK and TYRO3 capture antibody (R&D Systems). The mixture was incubated overnight at 4°C with agitation. The next day, the beads were washed repeatedly and stored in 1% BSA in PBS. Coupling efficiency was measured using biotinylated protein G.

Receptor abundance & phosphorylation quantitation Cells were starved for 4 hr then treated and lysed in 50 mM Tris, 10% glycerol, 150 mM NaCl, 1% NP40 at pH 7.5. Protein concentration was measured by bicinchoninic acid assay. Lysates were incubated with capture beads overnight with agitation, then washed with 0.1% Tween-20 in PBS and incubated with either detection antibodies for each TAM receptor (R&D Systems) or biotinylated 4G10 for 30 min. After washing again, beads were incubated with streptavidin-phycoerythrin for 10 min then quantified using a FlexMap 3D (Luminex Corp).

Localized Gas6 stimulation Gas6 was coupled to polystyrene beads following identical methods to the capture antibodies. Coupled beads were washed six times to remove uncoupled protein. Cells were starved for 4 hr, then beads were added and allowed to settle for the indicated amount of time. 4% PFA in PHEM buffer with phosphatase inhibitor (Boston Bioproducts) was used to fix the cells for 10 min. Immunofluorescence was performed by standard methods. Imaging was performed using a CARVII spinning disk confocal microscope with a 40× objective. Stacks were imaged every 1 µm, and then processed by maximum projection.

For lipid stimulation, 5:3:2 w/w phosphatidylethanolamine:phosphatidylserine:phosphatidylcholine (Avanti Polar Lipids) was resuspended in L15 media with 0.35% BSA at 1 mg mL^{-1}, vortexed vigorously, then diluted to the indicated concentration. 20 ng mL^{-1} Gas6 was added where indicated, and the mixture was incubated with gentle shaking for 1 hr. Cells were then stimulated with the indicated mixture and lysed.

siRNA and warfarin treatment 50,000 cells were seeded in 10 cm plates. The next day, plates were transfected with 5 µL Dharmafect 4 and 125 fmol of pooled siRNA in OptiMEM. Four hours later cells were placed back in full serum media. Two days after transfection cells were starved for 4 hrs then lysed. For warfarin treated cells, warfarin was added 24 hrs prior to lysis, along with exchange of the media. Oligonucleotides against human transcripts were (5'-3'): siControl ON-TARGETplus Non-targeting Pool D-001810-10-05; siGas6 (pooled four siRNAs) ON-TARGETplus SMARTpool siRNA J-009069-09, target sequence `GUGACGAGGGCUUUGCGUA`; ON-TARGETplus SMARTpool siRNA J-009069-10, target sequence `GGAGAAGGCUUGCCGAGAU`; ON-TARGETplus SMARTpool siRNA J-009069-11, target sequence `GCGUACAAGCACAGCGACA`; ON-TARGETplus SMARTpool siRNA J-009069-12, target sequence `CGCGGGAGGUGUUCGAGAA`.

AXL mutant transfection 500,000 cells were seeded in 10 cm plates. The next day, cells were transfected with 10 µg DNA of each AXL mutant using 10 µL Lipofectamine in OptiMEM according to the manufacturer's instructions. Four hrs post-transfection growth media was added back to the cells. The next day, cells were starved 4 hrs and then lysed.

AXL mutants were blunt-end cloned into pIRESpuro2 (Clontech) from wild-type human cDNA. Mutants were verified to be the following: kinase dead, K562R; ΔIg1, P27_S128del; ΔIG2, P139_T222del; ΔFN1, Q287_G331del; ΔFN2, P336_P428del.

Homogenous Modeling The kinetics of AXL signaling were modeled using ordinary differential equations. Model layout was inferred from structural understanding of ligand binding [79], and parameter estimation was performed using PottersWheel [260]. Phosphorylation was assumed to occur fast, such that species abundance directly translated to phosphorylated receptor abundance [246, 248]. Dimerization of receptors to form the D2 species was modeled as a one step reaction, implicitly assuming the second binding after dimerization through the first interface was fast. As the local concentration of incompletely dimerized Gas6 would be in excess of 1 M in the intermediate state, we believe this is a suitable assumption. As model fitting could not be performed without some amount of ligand-independent signaling, all species besides D2 were assumed to have some partial signaling capacity. Autocrine ligand was assumed to be present at a constant concentration, with stimulated ligand adding to that concentration.

Trafficking was modeled and kinetically constrained based on understanding from other receptor tyrosine kinases [246, 247]. We first assumed that endocytosis of each species occurred at a rate proportional to the phosphorylation extent of each species. A faster phosphorylation-dependent rate and slower phosphorylation-independent rate were included, as observed with other RTK families [246]. All species with the exception of D2 were assumed to have the same sorting fraction, and D2 its own fraction. Fluid-phase uptake of ligand was assumed to not occur as its contribution has only been observed at very high extracellular concentrations. Endosomal maturation and degradation were modeled as done previously, with no sorting of ligand. The ligand compartment was assumed to comprise 2% of cellular volume, or 10 fL per cell. Receptor and ligand interactions were assumed to be identical within the endosomal compartment.

Parameter fitting was performed in Potters Wheel [260]. Chi squared goodness of fit was calculated from the standard error of each measurement using experimental replicates. At least 500 independent times, global optimization was performed from a random starting point using a cycle of simulated annealing, and trust-region optimization with random perturbation, using the default parameters of the program. Model code for the optimization is included as supplementary files. Multiple independent optimization trials were confirmed to converge on the same optimal fit. A549 and A172 measurements were used in model training, as these cell lines did not display an effect upon warfarin treatment.

Models	BIC	χ^2
Full	389.2	91.3
No ligand-dependent signaling	443.3	145.4

Table 5.1: Refinement statistics for competing, topologically distinct models. BIC: Bayesian information criterion, Chi-squared: chi-squared goodness of fit.

The model was separately implemented as an external library to MatLab 2013b in C++ using CVode [261]. This native code was confirmed to produce identical results as integration within Potters Wheel. Local sensitivity analysis was performed by varying single parameters and examining the goodness-of-fit after local optimization using the default parameters of `fmincon`. In an attempt to address parameter sensitivity more globally, single parameters were also fixed, then global optimization was performed by direct search using the default parameters of `patternsearch`.

A, A_1, A_2, and A_{12} indicate AXL in an unbound state, bound at the high affinity site, bound at the low affinity site, and bound at both sites, respectively. D_1 indicates the dimer species with one Gas6 molecule bridging receptors. D_2 indicates the full receptor-ligand complex with two Gas6 molecules dimerizing two receptors.

$$\frac{\delta A}{\delta t} = k_{rb1}A_1 + k_{rb2}A_2 + (k_{r1} + k_{r2})D_1 + k_{r3}D_2 + \nu$$

$$-(k_{f1}A_1 + k_{f2}A_2 + k_{f3}A_{12} + k_{fb1}G + k_{fb2}G)A$$

$$\frac{\delta A_1}{\delta t} = k_{fb1}GA - k_{rb1}A_1 - k_{fb2}GA_1 + k_{rb2}A_{12} - k_{f1}AA_1 + k_{r1}D_1 - 2k_{f4}A_1A_1 + 2k_{r4}D_2$$

$$\frac{\delta A_2}{\delta t} = k_{fb2}GA + k_{rb1}A_{12} + k_{r2}D_1 + 2k_{r5}D_2 - (k_{rb2} + k_{fb1}G + k_{f2}A + 2k_{f5}A_2)A_2$$

$$\frac{\delta A_{12}}{\delta t} = (k_{fb2}A_1 + k_{fb1}A_2)G - (k_{rb1} + k_{rb2} + k_{f3}A)A_{12} + k_{r3}D_2$$

$$\frac{\delta D_1}{\delta t} = k_{r6}D_2 + k_{f2}AA_2 + k_{f1}AA_1 - (k_{f6}G + k_{r2} + k_{r1})D_1$$

$$\frac{\delta D_2}{\delta t} = k_{f6}D_1G + k_{f5}A_2^2 + k_{f4}A_1^2 + k_{f3}AA_{12} - (k_{r3} + k_{r6} + k_{r5} + k_{r4})D_2$$

A subset of parameters are constrained due to detailed balance (x represents either f or r):

$$k_{x2} = k_{x1}k_{xb1}k_{xb2}^{-1} \qquad k_{x4} = k_{x3}k_{xb2}k_{xb1}^{-1} \qquad k_{x5} = k_{x3}k_{xb1}k_{xb2}^{-1} \qquad k_{x6} = k_{x3}k_{xb2}k_{x1}^{-1}$$

Trafficking is defined by:

$$\frac{\delta X}{\delta t} = -X(k_{int,1} + S_a k_{int,2}) + k_{rec}(1-f)\gamma X_i$$

$$\frac{\delta X_i}{\delta t} = \frac{X}{\gamma}(k_{int,1} + S_a k_{int,2}) - k_{rec}(1-f)X_i - k_{deg}fX_i$$

where f is f_{else} for all species except D2 and f_{D2} for D2. For D2, $S_a = 1$.

Spatial Modeling Spatial modeling was performed by finite differencing on a 2D, radially symmetric geometry of set radius, integrated using CVode [261]. The receptor diffusion coefficient was assumed to be 0.1 L^2/min, where L is the radius of the region of interest. As diffusion is the only parameter which defines the length scale of the system, other lengths are defined in terms of L. $r = L$ was set as a closed boundary, and at $r = 0$ the solution was assumed to be finite. Diffusion occurred only for the receptor with no Gas6 bound on the surface, as internalization and Gas6 binding were assumed to reduce mobility. Reactions occurred normally throughout the region of interest unless noted otherwise. The extracellular Gas6 concentration profile was fixed as:

$$[\text{Gas}] = \gamma \cos\left(\frac{\pi r}{3L}\right)^{\sigma}$$

where σ is a "spatial inhomogeneity" parameter, and γ is varied such that the average Gas6 concentration over the entire region is constant.

Spatial modeling was performed within the external MatLab library using CVode, as a MatLab implementation was prohibitively resource intensive. Integration was performed using the backward differentiation formula and Newton iteration, with the dense linear solver utilizing the LAPACK backend.

Table 5.2: Fixed and fit parameters for the spatially homogenous model.

Value	Description	Optimal Value	Allowed Range
k_{fb1}	Forward binding constant for Ig1.	$0.0006\ \text{nM}^{-1}\text{min}^{-1}$	$6 \times 10^{-4} - 6.0$
k_{rb1}	Reverse binding constant for Ig1.	$4.0 \times 10^{-5}\ \text{min}^{-1}$	$10^{-5} - 10^{5}$
k_{fb2}	Forward binding constant for Ig2.	$0.0006\ \text{nM}^{-1}\text{min}^{-1}$	$6 \times 10^{-4} - 0.6$
k_{rb2}	Reverse binding constant for Ig2.	$0.032\ \text{min}^{-1}$	$10^{-5} - 10^{5}$
k_{f1}	Forward rate for reaction 1.	94 cell / min	$10^{-5} - 10^{5}$
k_{r1}	Reverse rate for reaction 1.	$18\ \text{min}^{-1}$	$10^{-5} - 10^{5}$
k_{f3}	Forward rate for reaction 3.	27000 cell / min	$10^{-5} - 10^{5}$
k_{r3}	Reverse rate for reaction 3.	$0.0038\ \text{min}^{-1}$	$10^{-5} - 10^{5}$
$k_{int,1}$	Endocytosis rate of non-pY receptor.	$1.00 \times 10^{-6}\ \text{min}^{-1}$	$10^{-6} - 1$
$k_{int,2}$	Endocytosis rate of pY receptor.	$1.5\ \text{min}^{-1}$	$10^{-3} - 100$
f_{else}	Sorting fraction of non-D2 species.	0.0038	$10^{-5} - 1$
f_{D2}	Sorting fraction of D2.	0.66	$0.1 - 1$
k_{rec}	Rate of endosomal recycling.	$0.0022\ \text{min}^{-1}$	$10^{-3} - 0.1$
k_{deg}	Rate of degradation.	$0.10\ \text{min}^{-1}$	$10^{-4} - 0.1$
S_a	Fraction non-D2 species phosphorylated.	0.0076	$10^{-6} - 1$
E_{A172}	AXL synthesis rate in A172 cells.	$66\ \text{min}^{-1}$	$1 - 10^{5}$
G_{A172}	Autocrine Gas6 concentration in A172 cells.	0.017 nM	$10^{-6} - 100$
E_{A549}	AXL synthesis rate in A549 cells.	$550\ \text{min}^{-1}$	$1 - 10^{5}$
G_{A549}	Autocrine Gas6 concentration in A549 cells.	0.20 nM	$10^{-6} - 100$
γ	Endosome ÷ plasma membrane area	0.5	Fixed

Chapter 6

Future Directions

AXL- and RTK-targeted therapeutics

While the tools to begin understanding AXL signaling are assembled, some very basic questions remain to be addressed. On the molecular level, there is very little information about observed ligand-independent signaling [79]. This form of activated receptor may completely resemble the ligand-mediated activation state, or observed phosphorylation may come from a completely distinct set of phosphosites. Ligand-independent activation may be regulated *in trans* from other RTK families through binding of unknown other proteins, may be regulated in a higher order manner such as through receptor trafficking, or may be constitutive and not directly regulated. In cell lines that display a dependence on vitamin K for robust activation by autocrine ligand, it is unclear to what phosphatidylserine-presenting surfaces ligand binds on the cells, and whether its presentation is perhaps manipulated in many cancer cells to promote AXL signaling. Lastly, more careful examination of receptor trafficking is sure to uncover differences between ligand binding at the surface and within endosomes. An intriguing possibility, since local stimulation requires areas of both high and low ligand concentration, is that endocytosis triggers a strong reduction in phosphorylated receptor.

With a better understanding of the basic mechanics of AXL and TAM receptor function, we then need an improved understanding of the higher-level function of these receptors on the cellular scale. Through refined experiment and modeling, the spatial aspects of receptor activation could be probed more specifically. Some remaining questions are: How does the synergistic signaling that arises by local stimulation vary with the length-scale of accumulated ligand patches? What patterns of receptor activation arise with more complex geometries of ligand stimulation? What features of ligand-binding (such as asymmetric affinity within each binding site) are required for these spatial effects? Protein S/MerTK, like Gas6/AXL, shows most robust response upon local stimulation [94], but other receptor-ligand or receptor-receptor combinations may show other patterns of response to spatial/non-spatial stimulation. Even if only the magnitude of response is important to inhibition of cancer cells, these higher-order effects are very likely utilized in other TAM signaling contexts.

TAM receptors represent an intriguing therapeutic target with promising preclinical results [21, 262]. Clinical trials are ultimately necessary to evaluate TAM-targeted therapies, and have begun for broad-spectrum inhibitors. However, the role of these receptors in physiological processes suggests caution in broad inhibition of all family members [90, 93, 96, 263, 264]. Carefully engineered therapies with better specificity for cancer cells, for example, by careful engineering of the Gas6-receptor affinities, will follow a better understanding of receptor function. Manipulation of TAM signaling to influence immune targeting of cancer cells is a similarly very promising area. More generally, across many malignancies, we need a better understanding of resistance mechanisms to RTK-targeted drugs.

For our basic understanding of cell-cell communication, we need an improved understanding of the yet less-studied RTKs. Multiple receptor families exist, such as DDR, Tie, and Ephrins, for which structural information

is available, and which have been shown to mediate drug resistance, but for which little understanding of ligand-mediated activation exists on a quantitative and usable level [265–267]. This lack of understanding limits design and interpretation of experiments, potential therapies manipulating activation of these receptors, and our understanding of how the receptors perform *in vivo*. The surprising results of Chapter 5 with TAM receptors will perhaps catalyze assembly of quantitative models for other receptor families.

Finally, we need a more complete understanding of receptor activation state. While RTKs are generally thought of as "on" or "off", diversity exists in the extent and dynamics of activation for each phosphosite on the receptors, and thus in interaction with other proteins. RTKs are physical proteins, interacting with a multitude of binding partners [268]. Fundamental questions remain in this area: Are individual phosphosites pre-programmed in their response upon receptor activation, or can differences in the manner of receptor activation selectively influence the abundance of particular phosphorylation sites? If so, are receptors only "on" or "off", and communication to influence receptor activation is encoded only in the timing of ligand-mediated activation, or do distinct receptor "on" states exists? Does biology take advantage of this potential additional layer of information? This improved understanding of RTK regulation will not only help basic understanding but likely aid selective targeting of tumor-associated signaling.

Systems biology: limitations and promise

This thesis has taken advantage of a variety of modeling methods ranging from largely statistical to more mechanistic in design. Clearly, computational methods will remain essential to understanding many complex, dynamic processes within a cell. On the other hand, as we assemble models of more complex cellular processes, uncertainty often hinders confidence in any model predictions, and validation of any predictions is required. If any model prediction need be directly experimentally testable, why assemble such models in the first place? Modeling methods often serve as a consolidated representation of one's current understanding and, insofar as the model is a means to organize knowledge, a more iterative outlook for model assembly and analysis is appropriate. Iterative model assembly is likely to be more valuable to experimentalists who are familiar with the approaches possible for biological interrogation.

As an example, this was applied in Chapter 4, using PLS modeling to predict a migration response measured as protrusion. As signaling and protrusion responses were already available for growth factor conditions, this easily allowed testing inferred responses in a statistical manner. One could similarly have performed the validation knockdown manipulations, but the initial modeling gave some reasonable expectation as to the responses one might expect to observe. While the tools to do such inference are understandably designed for maximal flexibility, new tools to simplify construction of small statistical models, keeping in mind the difficulty of communicating uncertainty, would greatly aid adoption of data-driven methods by experimentalists.

For data-driven modeling methods such as PLS, while prediction is often easy, interpretation and application remains challenging. Notably, in contradistinction to most biological studies using the method, Chapter 4 used PLS to predict a new condition while avoiding assignment of causal significance for any of the inputs. Better methods of ascribing causal significance, such as evaluating model performance upon removal of key variables perhaps, should be applied more widely and be more accessible. At the same time, predictive multivariate methods may simply be the wrong methods to apply when approaching the very common problem in biology of feature selection—taking a data-driven model and identifying the most key variable for manipulation—due to poor sampling of intracellular signaling and no accounting for more complex relationships such as feedback. In these cases, network approaches with wider-sampling methods such as siRNA screens may be more appropriate but have hardly been developed [48].

More mechanistic, kinetic models offer perhaps the greatest opportunity for understanding cell signaling. Even failure of such a model can itself provide detailed information and such models can often succeed in extrapolation. However, larger biomolecular systems remain difficult to model in this manner [249]. While software

packages exist for fitting models to diverse experimental data [260], they show prohibitive performance when scaling to larger systems. This might be partially overcome by effort to develop fitting tools which compile models into performance-optimized code, or better handle parallelization [269]. Optimization must often occur globally rather than with individual modules because intermediate species cannot be measured and because there is interdependence in parameter uncertainties. Such global optimization problems present an unsolved challenge for numerical analysis, and even upon successful optimization, presentation and interpretation of often-inevitable parameter uncertainty is difficult.

Chapter 5 also presented a new challenge for the tools used in reaction-diffusion modeling. While spatial reaction-diffusion models have been widely employed in chemical engineering applications, spatial modeling of biomolecular systems often presents the added complexity of differing timescales and large parameter uncertainties. Further, biological systems can often not be reduced to well-mixed systems for study before incorporating spatial aspects and the properties of intermediate species may not be observable. For these reasons, methods to more directly train models on corresponding spatially defined manipulations and measurements would vastly accelerate the study of systems that rely on spatial organization.

Given the difficulties in extending focused modeling methods to more complex systems, and in making confident inferences with more statistical approaches, hybrid modeling methods will be an important area of expansion. While these sort of approaches have been used widely in biomedical research, particularly in organ or organ-system level pharmacokinetic modeling, model components have often been segregated by spatial or temporal scale to account for model failures, rather than designed *a priori* to take into account the distinct strengths of particular methods. As an example extending from this thesis, one might combine the kinetic model in Chapter 5 and another for the ErbB family, with measurements of a phenotypic response such as actin polymerization upon receptor activation using multilinear regression, to understand responses by cells with simultaneous expression of both receptors. As an example of combining data-driven methods, one might utilize a model of stochastic state transition between basal and luminal state for a cell line [22], combined with prediction of cell death using a homogeneous population in each state, to develop a model of drug response in the context of dynamic changes in cell state. Importantly, these efforts will depend on reliable measurement of the intermediate species that link each model for reliable parameterization.

Cancer resistance and metastasis

A critical question to consider is whether targeting metastasis can provide meaningful therapeutic benefit if tumor cells disseminate early during oncogenesis [270–272]. In cancers where this is the case, and blocking tumor cell *translocation* is unlikely to prevent metastasis formation, the clearest value in studying metastasis may be in its varied links to resistance. In carcinomas, where the normal cells of origin, tumor, and metastases all generally lack migratory capacity, the metastatic cascade highlights the need to understand more than the average tumor cell. Similarly, understanding resistance may rely on improved understanding of the entire gamut of cells within a tumor. Results with AXL-targeted therapies are perhaps a crude first example of this approach, as AXL is generally more highly expressed in mesenchymal-like derived cell lines from pleural effusions than in bulk tumor [10, 273]. Indeed, as an EMT-induced RTK, it shows some specificity for currently disseminating cells. Stronger effects of AXL-targeted therapies on metastasis than inhibition of the primary tumor perhaps suggest targeting different cell populations can be complementary [21]. Thus, even if cells are disseminated, targeting distinct populations of cells may drastically reduce the remaining tumor load by preventing transition to resistant cell states [49].

As study of cancer cell invasion and migration has transitioned to three-dimensional, representative matrix, cells have been observed to use a more varied set of mechanisms to move [26]. While a mesenchymal-mode of migration has been most extensively studied due to its prevalence in two-dimensional assays, new modes such as ones without canonical polarity have been identified [27, 28, 108, 274]. To better understand 3D migration overall, we need to understand the physical conditions under which each of these migratory modes are observed,

and when they arise *in vivo*, as the matrix environments present may limit the forms of migration observed. With this improved view of which migratory modes are relevant, experimental means of assessing migration response in controlled *in vitro* assays are necessary, similar to the analysis done in Chapter 2. Experimentally accessible means of quantifying migration will allow for discovery approaches such as screening. Migration is important for many essential processes within the body, and these approaches will need to identify targets with some tumor-specificity, which is unlikely to exist at the level of the basic migratory machinery.

More generally, we need an improved understanding of resistance on a fundamental level. The last few years of research have provided many *examples* of when resistance occurs, but an integrative understanding of resistance has not emerged. Do tumors typically become resistant to treatment by fundamentally changing the core signals they rely on for survival, or by using simpler forms of redundancy to reactivate the same signals? If the latter, modeling will be essential to identify core survival signaling. With such a model it should be possible to enumerate all possible forms of resistance and find key points of therapeutic intervention. If, on the other hand, tumor cells are fundamentally plastic and transformation adjusts essential survival signals, an improved understanding of these different states is necessary. Relatively preliminary modeling efforts have shown cancer cells show dynamic plasticity distinct from the rigid hierarchal differentiation cascades in normal development, and treatment regimes are often optimized to treat the average [22, 275]. Direct targeting of each state would very likely lead to immense improvements in efficacy. Directly targeting dedifferentiated or cancer "stem cells" is an idea that has been applied in drug development, though without much thought as to the ideal experimental model for the "stem cell" state [19].

Finally, while the first focus on dysregulated signaling in cancer centered around the MAP kinase cascade, study of some of these important subpopulations of cancer cells have revealed important roles in less understood pathways such as Wnt and Hippo [13, 276, 277]. There is little reason to expect a systems understanding of this dysregulation would contribute less to understanding the pathways than it did for the MAP kinase cascade. Perhaps most limiting are the tools for measuring activation of these other cascades, since they often do not rely on easily measured modifications. However, this should motivate efforts to more easily assess activity at key nodes within these pathways. The success of systems biology approaches should be evidence enough that simple loss of function studies will be insufficient to completely understand and target these signals. Progress in our understanding of cancer therapy will continue to require more than finding the ideal single target.

Chapter A

Appendix to Chapter 3

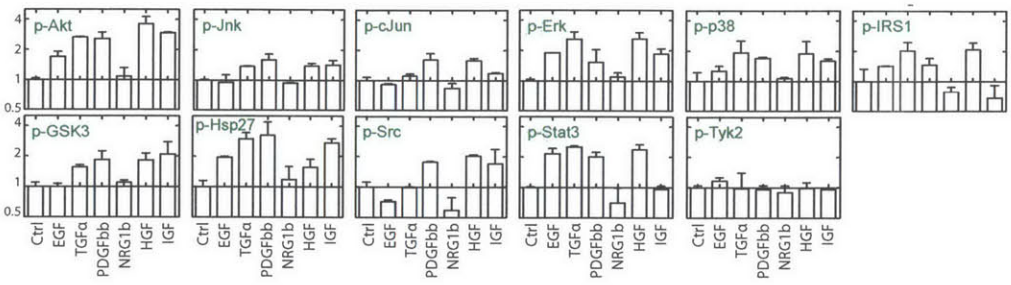

Figure A.1: CSR data: phospho-protein response to growth factor stimulation. Data shown here were incorporated directly in CSR dataset (Fig. 3.1B-C). Phospho-proteins were quantified from cells lysed 5 min post-stimulation, also shown in Fig. 3.2A (N = 2 biological reps). Error bars denote SEM.

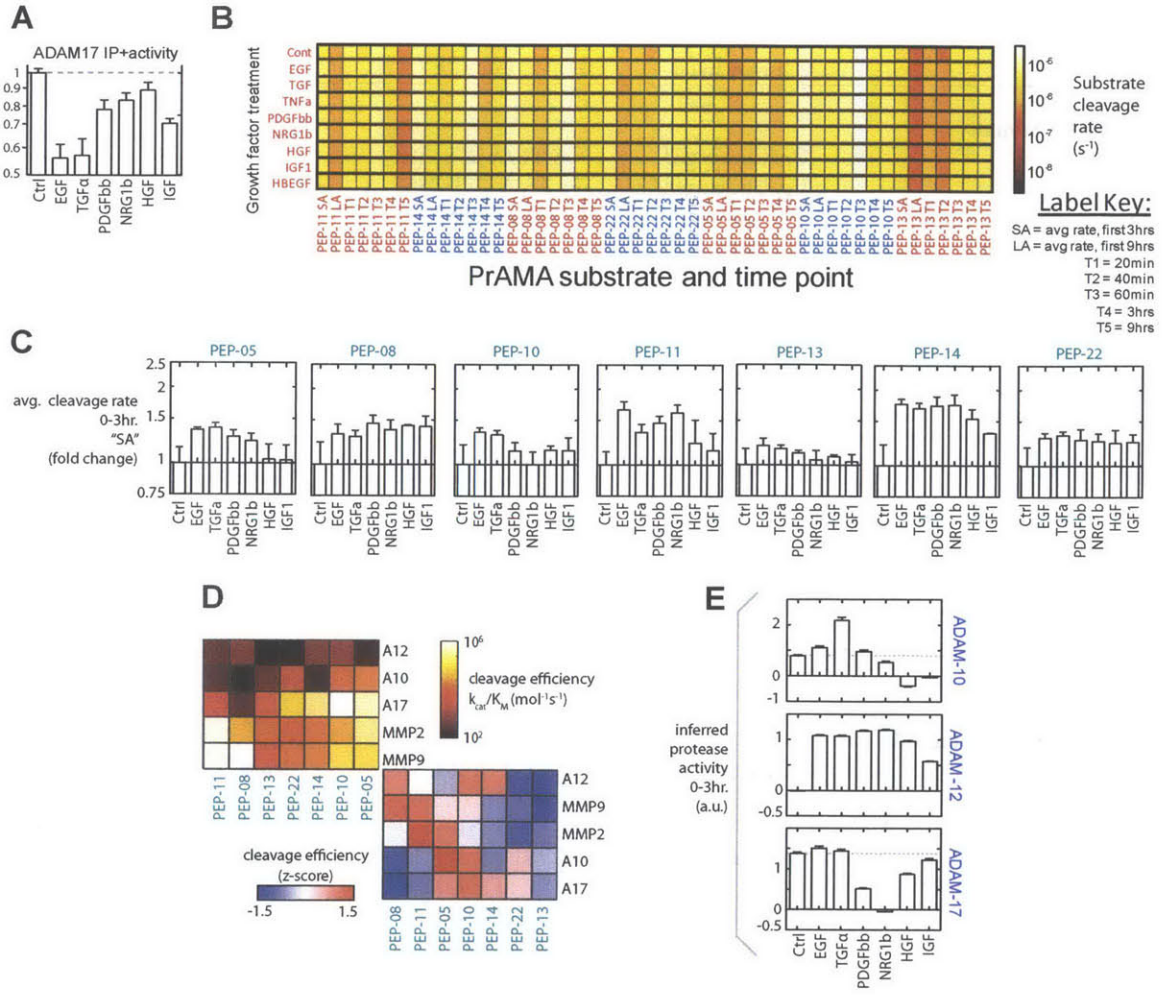

Figure A.2: CSR data: sheddase activity using FRET-substrate, PrAMA inference, and IP+activity assays. A subset of the data shown here was incorporated directly in the CSR dataset (Fig. 3.1B-C, 3.2A). (A) ADAM17 activity was quantified using the Innozyme TACE activity assay from whole-cell lysate collected 45 min. post-stimulation (also shown in Fig. 3.2A; N = 2 biological reps.). (B) Seven soluble, FRET-based synthetic polypeptide protease substrates were added concomitantly with growth factors to serum-starved 12Z cultures. Fluorescence was recorded at five time points, and cleavage kinetics were calculated from the rate of fluorescence increase for each substrate and growth factor condition (N = 4 biological reps.). The heat-map shows the cleavage rates for each time interval, as well as average kinetics across the first three hours ("SA") and across the first nine hours ("LA"). (C) Only the "SA" data were used in the integrative cue-signal-response modeling (Fig. 3.2A), and comprise the average of N = 4 biological reps. across 5 time-point readings. (D) Hierarchical biclustering of catalytic efficiencies for the panel of FRET-substrates used in *B-C*. Enzymatic efficiencies were previously reported [159], measured using purified recombinant enzymes. The top-left heat-map shows absolute catalytic efficiencies. The bottom-right heat-map shows efficiencies after each row has been mean-centered and variance-normalized, and consequently shows relative substrate efficiencies for each enzyme. Of note, PEP-05 exhibits peptide sequence similar to pro-TNFα, and known ADAM substrate, and PEP-10 is closely related. PEP-13 shares sequence similarity with the known ADAM10 substrate, CD23. E) PrAMA was used to infer specific ADAM activities from the FRET-substrate cleavage measurements shown in (C) (N = 4 reps.; data also shown in Fig. 3.2A). PrAMA algorithm parameters have been previously described [166]. All error bars indicate SEM.

Protein	Disease Trend	Evidence	Notes
Environmental Stimuli			
TNFα	Up/Unchanged	S/PF/A [278–282]	
EGF	Up/Unchanged	PF/A [283–285]	
TGFα	Up	A [285]	
NRG1β	Up*	[286]	*Ovarian cancer
PDGFbb	Unchanged	S/PF [280, 287]	
HGF	Up	PF [288]	
IGF1	Up/Unchanged	S [289–291]	
Intracellular Signaling Proteins			
p-p38	Up	T/A [153, 177, 292]	
p-Erk1/2	Up*	T [293, 294]	*Total protein unchanged
p-Jnk	Up*	T/A [295, 296]	*Endometriotic endothelium
HSP27	Up	T [297, 298]	Total protein increased
c-Jun	Up*	T [299, 300]	*RNA expression increased
p-Akt	Up	T [294, 301, 302]	Both p-Akt and tot. Akt increased
p-STAT3	Up	T [303]	
Src	N/A*	T [304, 305]	*Assoc. *in vitro* w/ MMP & PGE
IRS-2	N/A	GP [306]	Pos. assoc. with disease
Tyk2	N/A	GP [307]	Assoc. with decreased risk
Receptors & Autocrine Ligands			
EGFR	Unchanged*/Up**	T/S [149, 289, 308]	*Up w/ danazol; **Eutopic
TNFR1	Up	S/PF [290, 309]	
MET	Up*	T [310]	*Cell surface expression
HER-2	Up*/Unchanged	T/S [149, 311, 312]	*Up in endometriosis-assoc. cancer
AREG	Up	T [313]	
HBEGF	Up	T [313]	
MMPs and TIMPs			
MMP-2	Up	T/S/PF [314, 315]	
MMP-3	Up	A/T [316–318]	
MMP-7	Up	A/GP [317, 319]	
MMP-9	Up	T/PF [320–322]	
TIMP-1	Up/Down	T/S/PF [316, 322–324]	
TIMP-2	Down	T [314, 324]	
ADAMs			
ADAM-17	Up	T [324]	
ADAM-10	Up	T [325]	

Table A.1: Table of key proteins and their clinical association with endometriosis. Nearly all growth factors, kinases, cytokines, RTKs, ligands, and proteases directly measured in this work have been implicated in endometriosis by previously reported clinical data. TNFα = tumor necrosis factor alpha; Erk1/2 = extracellular related kinase 1/2; Jnk = c-Jun N-terminal kinase; HSP27 = heat-shock protein 27; STAT3 = signal transducer and activator of transcription 3; IRS-1 = insulin receptor substrate 1; Tyk2 = tyrosine kinase 2; PGE = prostaglandin E; S = serum; PF = peritoneal fluid; T = tissue, GP = genetic polymorphism; A = animal model

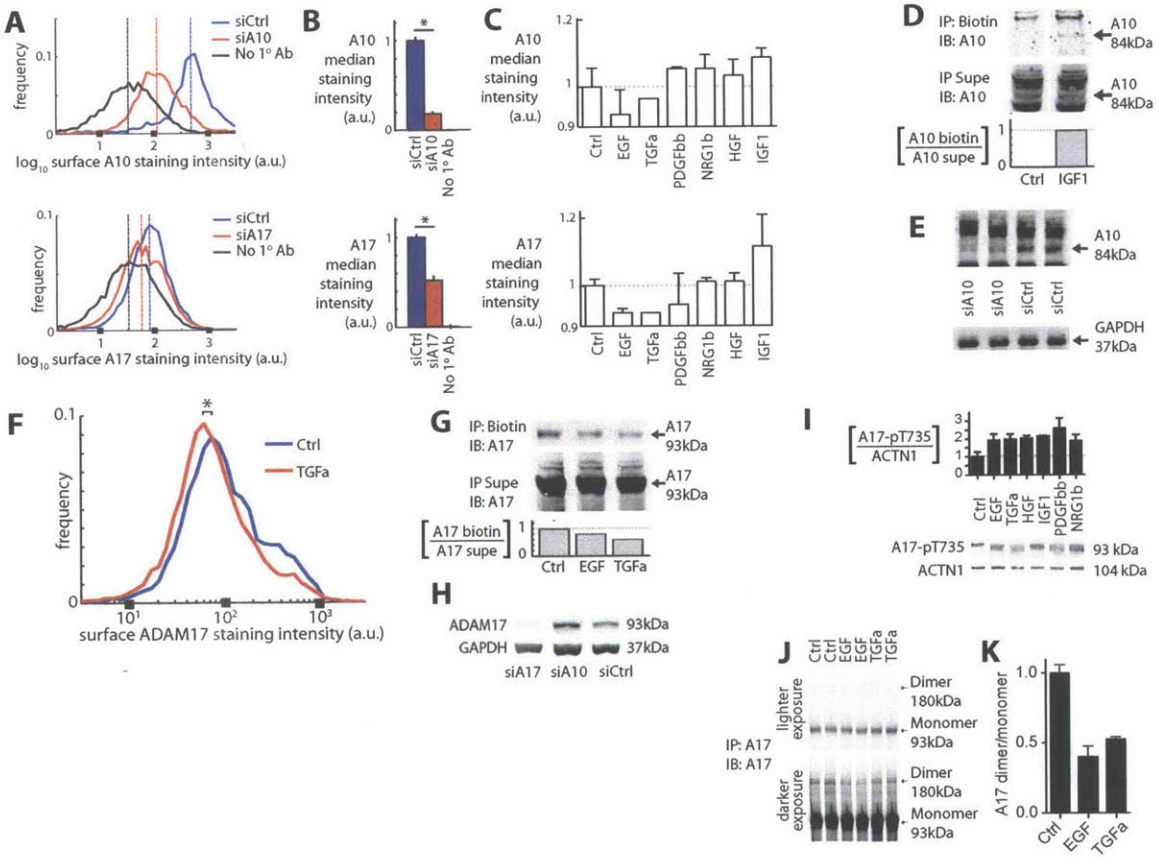

Figure A.3: (Continued on next page.)

Figure A.3: CSR data: ADAM-10 and -17 surface levels, ADAM-17-pT735, and ADAM-17 dimers. Data shown here were either incorporated directly in the CSR dataset (Fig. 3.1B-C, 3.2A), or validate those incorporated measurements. (A-B) siRNA experiments confirm Ab specificity for ADAM-10 and -17. Live-cell immunostaining and cytometric analysis show single-cell population distributions of staining intensities (A) and their corresponding averages (B), confirming Ab specificity (*$p<0.05$). Staining in the absence of a primary Ab treatment but after secondary Ab treatment ("No 1^o Ab") was used to determine background signals. (C) Staining was performed as in *A-B*, but following growth-factor stimulation. Cells were stained 30 min post-stimulation (also shown in Fig. 3.2A; n=3 reps.). (D) Western blot confirms IGF1 upregulates surface ADAM10. 30 mins post-IGF1 stimulation, cells were treated with sulfo-NHS-biotin, lysed, and incubated with streptavidin beads. Bound and unbound proteins ("IP:Biotin" and "IP Supe", respectively) were then blotted for ADAM10. The bar-plot shows surface ADAM10 quantified by densitometry. (E) Using the same Ab as in *D*, western blots of lysates from siRNA-treated cells confirm the 84 kDa band corresponds to ADAM10, exhibiting significantly decreased band intensity upon knockdown (n=2 reps., $p<0.05$). (F) Population distribution of single-cell staining intensity for ADAM17 (measured by cytometry), following treatment with TGFα. Results correspond to the bar-plot in *C* (*$p<0.05$, N = 3). (G) Western blot confirms EGF and TGFα downregulate surface ADAM17. 30 mins post-stimulation, cells were treated with sulfo-NHS-biotin, lysed, and incubated with streptavidin beads. Bound and unbound proteins ("IP:Biotin" and "IP Supe", respectively) were then blotted for ADAM17. (H) Using the same Ab as in *G*, western-blots of lysates from siRNA-treated cells confirm the 93 kDa band corresponds to ADAM17, exhibiting signficantly reduced band intensity upon knockdown (n=2 reps., $p<0.05$). (I) Representative blots showing ADAM17-pT735, and ACTN1-normalized quantitation by densitometry (also shown in Fig. 3.2A; n=3 biological reps.). Measurements were taken from whole-cell lysates 30 min. post-stimulation. (J) ADAM17 dimerization decreases following EGF and TGFα treatment. 30 min. post-stimulation, cells were treated with sulfo-EGS and lysed. Immunoprecipitated ADAM17 from lysates was blotted for ADAM17. (K) The ratio of dimer to monomer band intensity was calculated using quantification by densitometry. All error bars denote SEM, *$p<0.05$, Student's t-test.

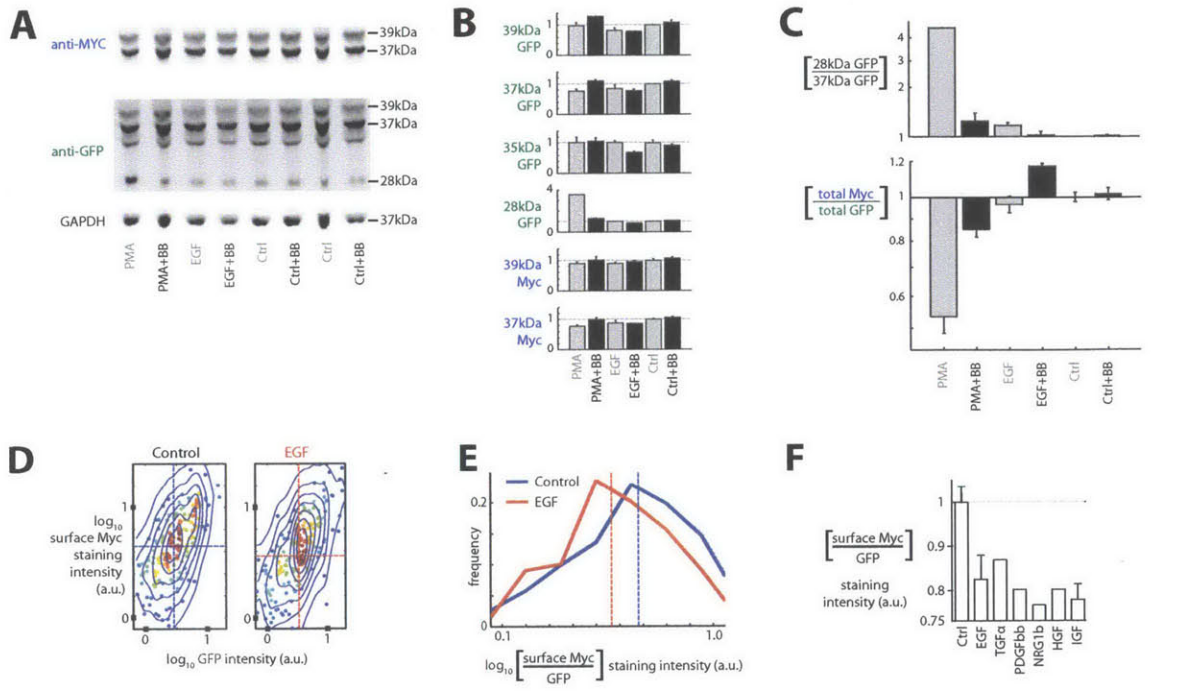

Figure A.4: CSR data: Myc-HBEGF shedding assay, validation, and results. Data shown here were either incorporated directly in the CSR dataset (Fig. 3.1B-C, 3.2A), or validate those incorporated measurements. Because HBEGF is expressed at a low level in 12Z, we transgenically over-expressed the protein in 12Z to directly measure its shedding at short time-points following growth factor stimulation. We used a retroviral construct with a GFP-tagged intracellular c-terminus and a Myc-tagged ectodomain, as described previously [326]. A) Representative western blots demonstrate modest yet statistically significant HBEGF shedding in response to 1 μM phorbol ester (PMA) and EGF stimulation, in a BB94-dependent manner. As expected based on original description of the construct [326], full-length HBEGF protein products can be detected at 39, 37 & 35 kDa by the anti-GFP Ab. The primary ADAM-mediated cleavage product is visible at 28 kDa. At the relatively lower expression levels here the 35 kDa fragment was undetectable by anti-Myc staining [326]. (B) Band intensities from *A* and another replicate were quantified by densitometry and normalized to GAPDH measurements. C) Top: The ratio of primary HBEGF cleavage product (28 kDa) and primary full-length protein (37 kDa) was calculated from *B*. Results indicate PMA and EGF significantly increase the ratio in a BB94-dependent manner. Bottom: To generate numerical values that would be reflective of cell-surface immunostaining and flow-cytometry experiments, the ratio of total Myc to total GFP staining intensity was calculated. Total Myc staining was calculated by summing band intensities at 37 kDa and 39 kDa. Total GFP staining was calculated by summing band intensities at 28, 35, 37, and 39 kDa. Results indicate PMA decreases the ratio in a BB94-dependent manner. (D) Single-cell flow-cytometry scatterplots showing GFP intesity vs. surface Myc staining intensity, 30 min following EGF stimulation. Each point represents a single-cell measurement, with warmer colors indicating higher point-density. Contour lines indicate population distribution, and dotted lines denote median intensity values. (E) Single-cell population distribution of the ratio in Myc and GFP intensities, corresponding to data in *D*. Dotted lines indicate population medians. (F) Results from *D-E*, along with measurements from the other growth-factor treatment conditions, averaged over n=9 total replicates (also shown in Fig. 3.2A). Data represent the control-normalized averages of measurements taken at 30, 60, and 90 min post-stimulation (n=3 reps. x 3 time-points per growth-factor condition). All error bars denote SEM.

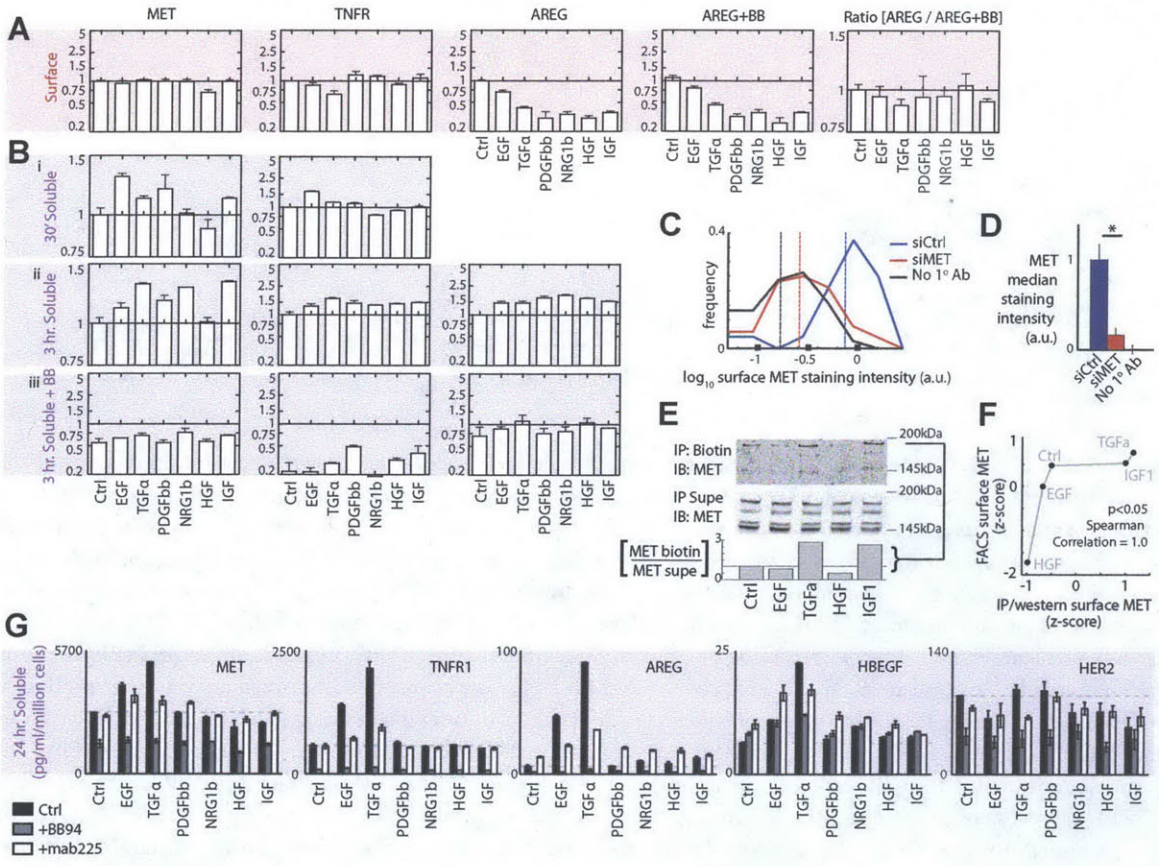

Figure A.5: (Continued on next page.)

Figure A.5: CSR data: endogenous ligand/receptor ectodomain surface and supernatant levels. Data shown here were either incorporated directly in the CSR dataset (Fig. 3.1B-C, 3.2A), or validate those incorporated measurements. (A) Results from live-cell surface immunostaining and cytometry analysis. Data represent the control-normalized averages of measurements taken at 30, 60 & 90 min post-stimulation, and the left three plots are also shown in Fig. 3.2A (n=3 biological reps. per growth-factor condition). AREG surface measurements were additionally made following 30 mins pre-treatment with 10 μM BB94. Subsequent growth factor stimulation was also in the presence of BB94 ("AREG+BB"). BB94 treatment increased AREG surface levels by an average of 12%. The ratio of surface levels [- BB94] / [+ BB94] (right-most plot) was calculated for each growth factor condition and normalized to the ratio determined under unstimulated conditions. (B) *i:* Cellular supernatant was removed from 12Z cell cultures 30 mins post-stimulation, concentrated using Amicon-ultra 3 kDa size-exclusion columns (Millipore), and analyzed by ELISA (also shown in Fig. 3.2A; n=3 biological reps.). AREG was not detectable above the sensitivity limit at this time-point. *ii–iii:* Cellular supernatant was removed from 12Z cell cultures 3 hrs post-stimulation and analyzed by ELISA (N = 3; plots from *ii* are included in Fig. 3.2A). *iii:* Cells were pre-treated 30 mins prior to growth factor stimulation with 10uM BB94, and results were normalized to the untreated control levels detected in the absence of BB94. (C-D) siRNA experiments confirm Ab specificity for MET surface levels. Live-cell immunostaining and cytometric analysis show single-cell population distributions of staining intensities (C) and their corresponding averages (D), confirming Ab specificity ($^*p<0.05$). Staining in the absence of a primary Ab treatment but after secondary Ab treatment ("No 1^o Ab") was used to determine background signals. (E) Western blotting supports flow-cytometry measurements of surface MET. 30 mins post-stimulation, cells were treated with sulfo-NHS-biotin, lysed, and incubated with streptavidin beads. Bound and unbound proteins ("IP:Biotin" and "IP Supe", respectively) were then blotted for MET. The bar-plot shows relative surface MET of the top MW band, quantified by densitometry. (F) Mean-centered and variance-normalized (that is, z-score) data from the western blot *E* (x-axis) and flow cytometry *A* (y-axis) indicate perfect rank-order correlation between the two sets of measurements. Poor linearity may be attributed to low signal in the western blot. (G) Supernatant analyte concentrations were measured 24 hrs post-stimulation from 12Z grown in the presence of either BB94 or mAb225 (n=2 reps.). All error bars denote SEM.

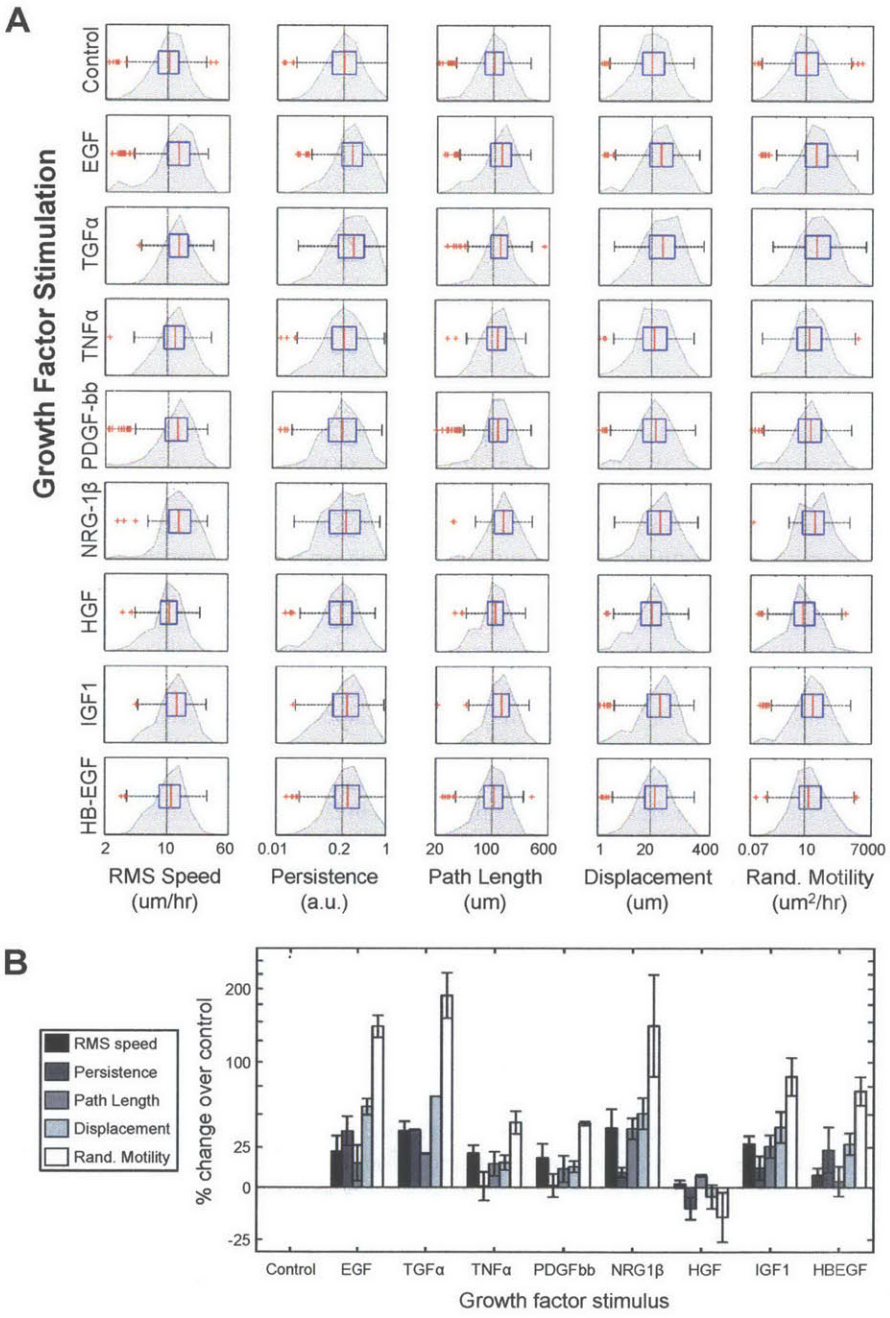

Figure A.6: CSR data: single-cell motile response of 12Z to growth factor treatment. A subset of the data shown here was incorporated directly in the CSR dataset (Fig. 3.1B-C, 3.2A). (A) Population distributions of single-cell motile response in 12Z. Various descriptive features of cellular motility were computed for individual cells based on single-cell tracking experiments using time-lapse confocal microscopy. Histograms and corresponding box-and-whisker plots show population distributions from single-cell measurements, pooled from $n \geq 2$ separate experiments, with ≥ 100 individual cells for each condition. (B) Median population statistics were calculated from the single-cell data shown at top, normalized to the control ($\pm$ SEM of experimental reps., $n \geq 2$ separate populations, with ≥ 100 cells for each condition). A subset of these data are shown in Fig. 3.2A.

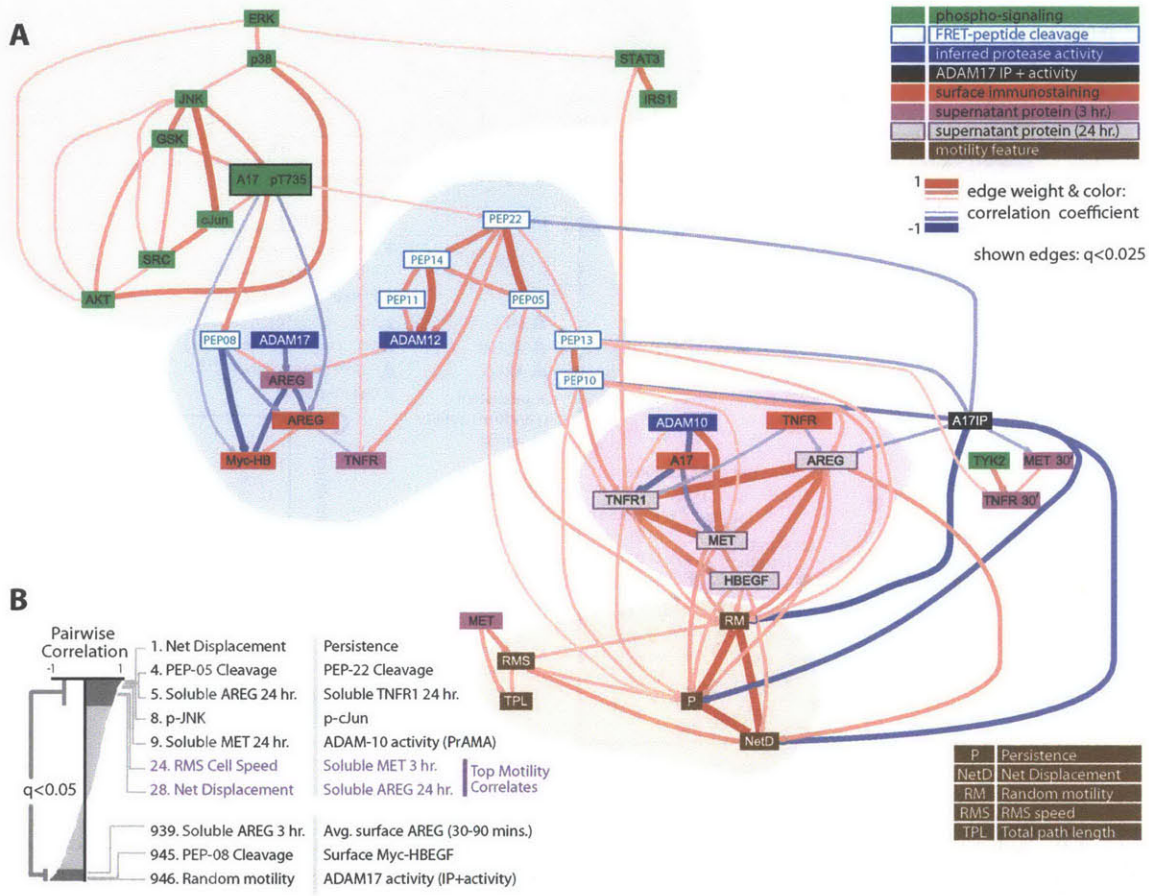

Figure A.7: Pairwise correlation within the CSR dataset. To explore regulatory relationships in the CSR dataset (Fig. 3.2A), we calculated correlation and corresponding statistical significance among all pairs of variables as they varied across the panel of growth-factor treatments. (A) The graphically representated correlation network shows significant correlation ($q<0.025$; q = multiple hypothesis corrected p-value) among pairs of measurements in the CSR dataset. Node labels and colors correspond by color to Fig. 3.2. Edge weights and color denote strength and direction of correlation. The correlation graph and spatial organization were generated in an unsupervised, automated manner using the Matlab biograph() function (Mathworks, Natick, MA). Shaded areas were manually added to emphasize modularity among the data. Highly interconnected phosho-signaling measurements (top left) link to early protease activity measurements (blue shaded area) primary through ADAM17-pT735. Early protease activity measurements then relate closely to later shedding measurements (purple shaded area), which in turn are highly correlative with features of cell migration (brown). (B) All pairwise correlation coefficients depicted in *A* were rank-ordered and shown in the waterfall plot at left. Highly significant correlative pairs are enumerated at right. Somewhat redundant pairs have been omitted from the enumerated list for clarity (for example, the second most correlative pair is very similar to the first: random motility vs. net displacement). For *A-B*, both Spearman and Pearson correlation were calculated for each pair of measurements, and the more statistically significant of the two was recorded. P-values based on correlation were calculated using either a Student's t distribution or an approximation of the exact permutation distributions, for Pearson's or Spearman's correlation, respectively. All p-values shown here have been corrected for multiple hypothesis testing using the Storey false discovery rate, and consequently are reported as q-values [327].

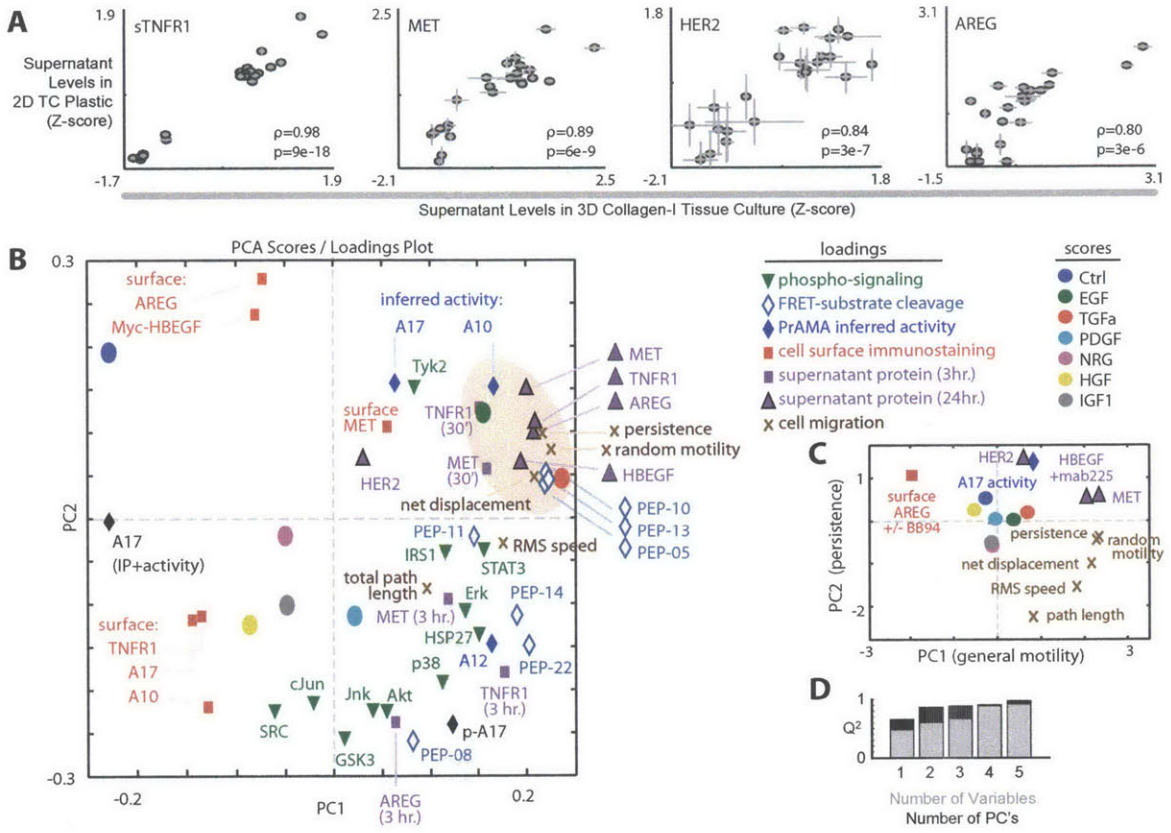

Figure A.8: Multivariate modeling relates sheddase activity to cellular motility. (A) Ligands/receptors included in the CSR dataset (Fig. 3.2A) exhibit qualitatively similar patterns of accumulation in the supernatant across growth-factor conditions, regardless of 2D or 3D culture environment. Ectodomain shedding was measured in 12Z grown on either tissue culture plastic or in 2.2 mg mL^{-1} collagen-I gels. Supernatants from both cell culture environments were collected 24 hr. post-stimulation with the panel of growth factors used in Fig. 3.2A, in the presence or absence of mab225 and BB94 (n=2 reps., ± SEM). Spearman's and Pearson's correlation coefficients were calculated for each analyte, and the greater of the two are reported as ρ. P-values based on correlation were calculated using either a Student's t distribution or an approximation of the exact permutation distributions, depending respectively on whether ρ denotes Pearson's or Spearman's correlation. In 3D culture, HBEGF was only detectable above assay sensitivity thresholds under conditions of EGF/TGFα stimulation, and therefore was not included in this analysis. (B) This fully labeled depiction of Fig. 3.2B shows the PCA scores and loadings plot of the entire CSR dataset (Fig. 3.2A-B). (C) This fully labeled depiction of Fig. 3.2D shows the PLSR scores and loadings plot of the expanded CSR dataset (predictor variables) describing motility features (response variables). The expanded CSR dataset includes measurements made in the presence of BB94 and mab225 across the panel of growth factors (see Fig. A.5). Descriptor variables were iteratively added to the PLSR model to maximize Q^2 prediction accuracy, and two of the five descriptors are not depicted in Fig. 3.2A: "Surface AREG ± BB94" denotes the BB94-dependent change in AREG surface levels, and is fully described in Fig. A.5A (right-most graph); "HBEGF+mab225" denotes the levels of supernatant HBEGF detected 24 hrs post-stimulation with growth factors, in the presence of mab225, and is fully described in Fig. A.5G. (D) Accurate prediction of motility requires multiple principal components and descriptor variables. PLSR models were constructed as in *C*, but with limits on the number of principal components (black) or descriptor variables (grey, superimposed over black bars) that were allowed to be incorporated into the model structure. Results show that the addition of a second principal component enhances PLSR accuracy by nearly 50%, indicating multiple axes of motility regulation.

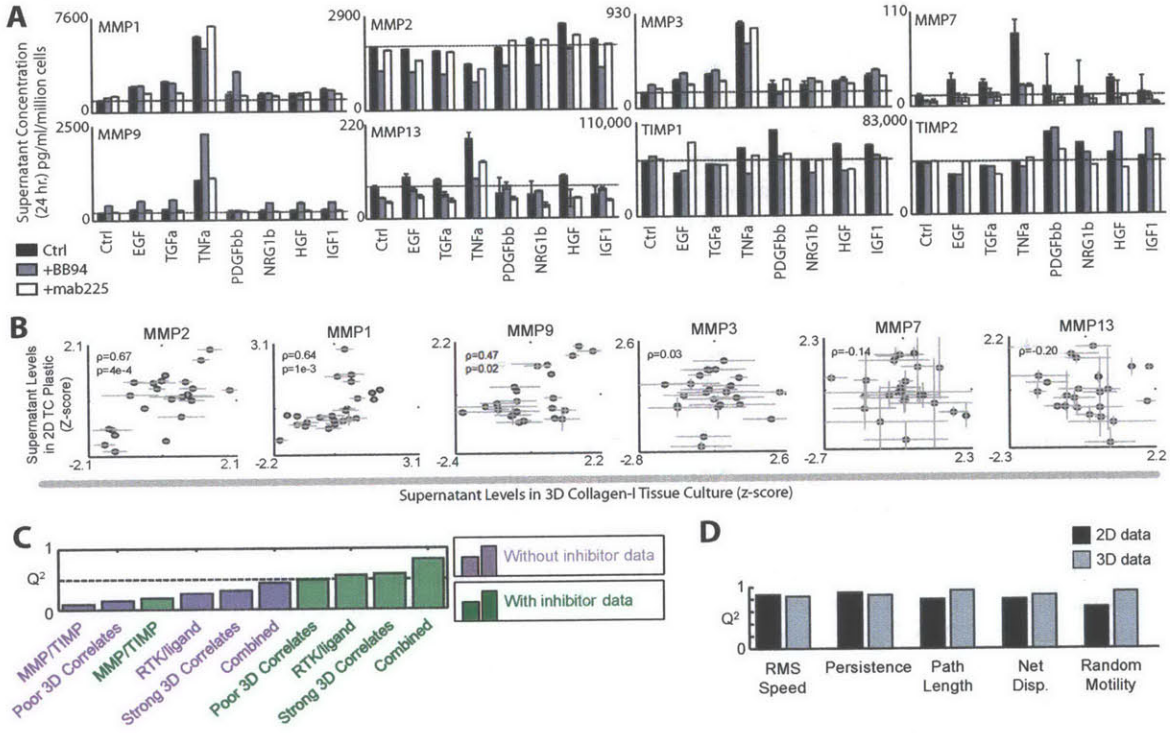

Figure A.9: (Continued on next page.)

Figure A.9: MMP/TIMP levels poorly correlate with cell migration compared to ligand and receptor shedding. (A) MMP/TIMP supernatant concentrations were measured 24 hrs post-stimulation from 12Z grown on tissue culture plastic in the presence of either BB94 or mAb225 (n=2 reps., ± S.E.). TIMPs have N = 1 replicate. (B) Compared to ligand/receptor accumulation, MMP/TIMP levels exhibit less consistent patterns of accumulation in the supernatant across growth-factor conditions, depending on 2D or 3D culture environment. Accumulation was measured in 12Z grown on either tissue culture plastic or in 2.2 mg mL^{-1} collagen-I gels. Supernatants from both cell culture environments were collected 24 hrs post-stimulation with the panel of growth factors used in Fig. 3.2A, in the presence or absence of mab225 and BB94 (N = 2, ± SEM). Spearman's and Pearson's correlation coefficients were calculated for each analyte, and the greater of the two are reported as ρ. P-values based on correlation were calculated using either a Student's t distribution or an approximation of the exact permutation distributions, depending respectively on whether ρ denotes Pearson's or Spearman's correlation. (C) PLSR models using supernatant measurements emphasize the role for autocrine ligand/RTK shedding over MMP/TIMP secretion in mediating cell migration. PLSR models were constructed to describe cell motility features using various subsets of the supernatant protein concentration data from *A* and Fig. A.5G as descriptor variables. In particular, we decomposed the data into (1) MMP/TIMP vs. RTK/ligand measurements, (2) measurements that significantly vs. insignificantly correlate across 2D and 3D tissue culture environments (using $p<0.05$ as a significance threshold; see *B* and Fig. A.8A), and (3) data including vs. excluding the additional mab225/BB94 treatment for each growth factor condition. Not surprisingly, results show that strong 3D correlate measurements are more accurate predictors of cell migration than poor 3D correlate measurements. Furthermore, results indicate that including measurements of shedding +/- mab225 and BB94 significantly enhances model prediction accuracy, suggesting that these inhibitor treatments reveal additional information regarding metalloproteinase activity and EGFR-autocrine feedback that is relevant to cell migration. Finally, results show that RTK and ligand shedding are more predictive of cell migration than MMP/TIMP secretion patterns, suggeting MMP secretion levels are a relatively poor indicator of their role in cell migration. (D) Ectodomain shedding measurements from both 2D and 3D cell cultures equally predict 3D motility. PLSR models were generated to predict cell motility using supernatant measurements collected from cells cultured on either tissue culture plastic (2D) or from cells suspended in collagen I gels (3D) (including ligand/receptor shedding; see *A* & Fig. A.8A). According to Q^2 fitting accuracy, PLSR is capable of using both 2D and 3D supernatant measurements to accurately predict 3D cellular motility. These results are concordant with observed correlation between supernatant measurements in 2D and 3D tissue culture environments (Fig. A.8A).

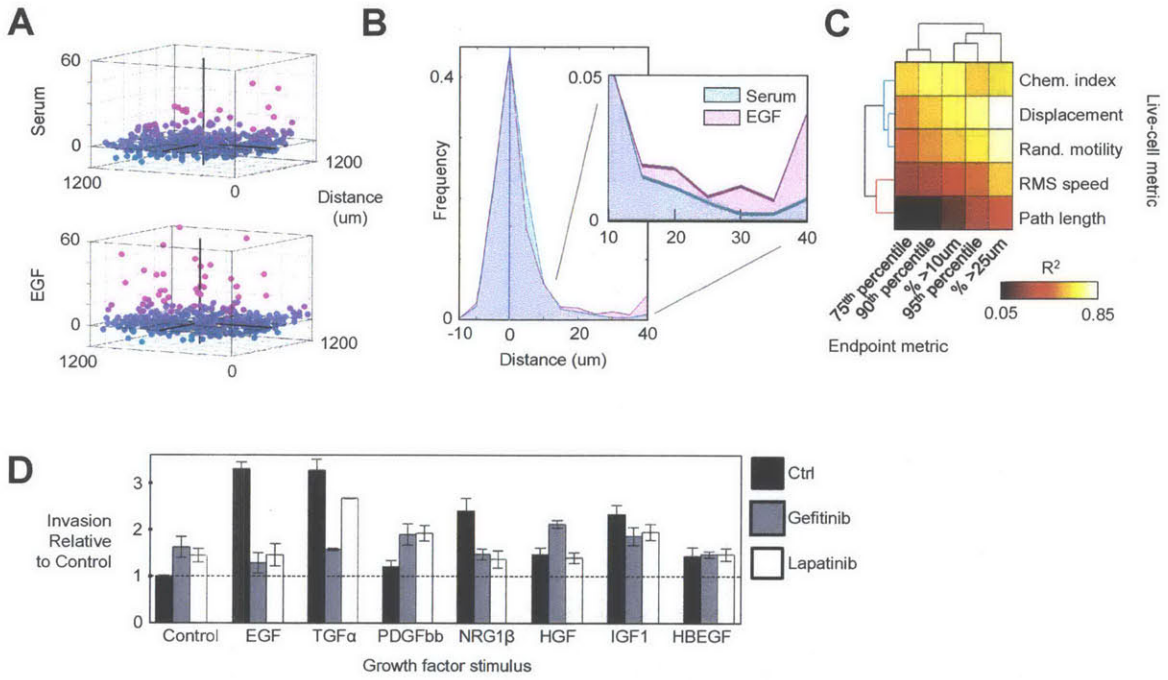

Figure A.10: An endpoint collagen-I migration assay captures inhibitor sensitivity. (A) Computationally inferred cell nuclei positions from the endpoint assay, in the presence or absence of EGF, measured 24 hrs post-stimulation (same as Fig. 3.3E). The x-y plane represents the inferred bottom of the 96-well plate. Nuclei with higher z-coordinates show warmer color. (B) Distribution of nuclei z-coordinates, corresponding to *A*. (C) Clustergram of correlations between the endpoint assay metrics and median live-cell motility data (live-cell motility data described in Fig. A.6 and Fig. 3.2A), compared across the panel of growth factors. (D) 12Z were stimulated with growth factors following a 1.5 hrs pre-treatment with the EGFR kinase inhibitor, gefitinib, or the dual EGFR/HER-2 kinase inhibitor, lapatinib. Gefitinib results correspond to Fig. 3.3F-G. The two inhibitors demonstrate similar inhibitory effects, with the exception of TGFa-stimulated motility. One possible explanation for the discrepancy may lie in differences between HER2 shedding under EGF- and TGFα- stimulated conditions (shown in Fig. A.6G): compared to EGF, TGFα stimulates significantly more HER2 shedding ($p<0.05$), and lapatinib (which inhibits HER2) is less effective under TGFα stimulation compared to EGF stimulation. Error bars denote SEM.

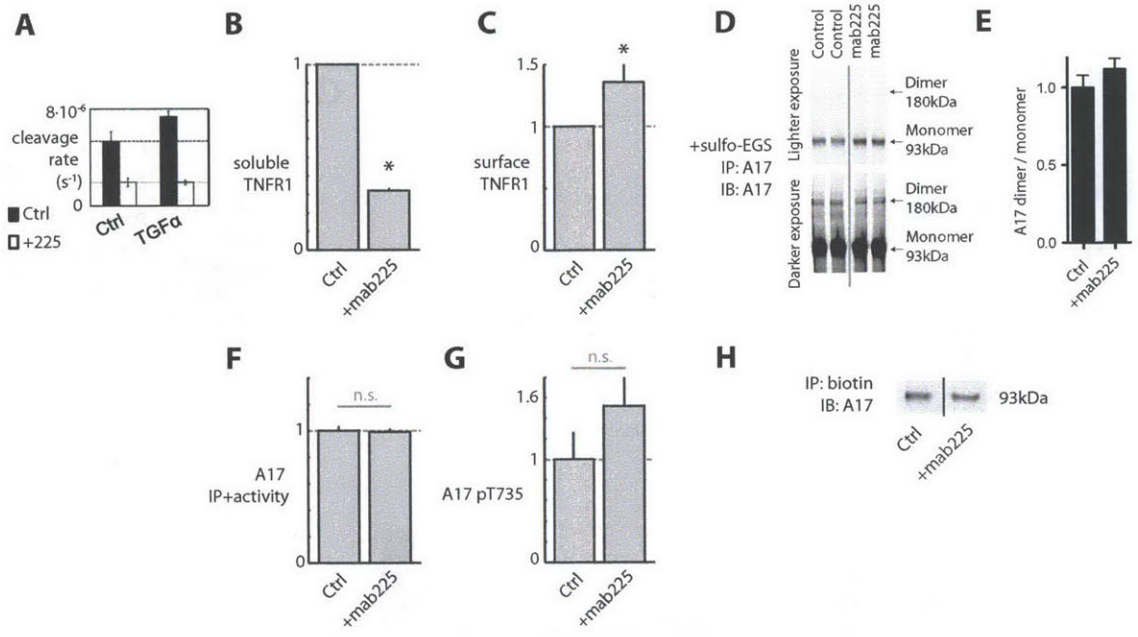

Figure A.11: mAb225 reduces ADAM substrate shedding. (A) The soluble FRET-substrate PEP-05 was applied concomitantly with TGFα to serum-starved 12Z cultures that had been pre-treated with 10 $\mu g\,mL^{-1}$ mab225 for 30 mins, and measured cleavage rates were averaged over the first 3 hrs post-stimulation (N = 4). Cleavage rates of PEP-05, which shares polypeptide sequence similarity to pro-TNFα, were significantly reduced in the presence of mab225. Results correspond to PrAMA inference results shown in Fig. 3.4A. (B) After 30 mins treatment with mab225, cellular supernatant was collected, ultra-concentrated using Amicon-ultra size-exclusion columns (Millipore), and analyzed by ELISA for TNFR1 concentration. Results show significant decrease in TNFR1 shedding with mab225 treatment (N = 3). (C) After 1 hr treatment with mab225, 12Z were surface-immunostained for TNFR1 and anlyzed by flow cytometry. Results indicate a significant increase in surface receptor with mab225 treatment (N = 2). (D) Following a 30 min. treatment with mab225, 12Z were treated with sulfo-EGS and lysed. ADAM17 was immunoprecipitated from lysate and then blotted for ADAM17. (E) The ratio of dimer-to-monomer band intensities was calculated, and showed no significant difference (N = 2). (F) ADAM17 activity was quantified using the Innozyme TACE activity assay from whole-cell lysate collected 45 min. post-treatment with mab225 (N = 2 biological reps) (G) ADAM17-pT735 was measured by western blot, quantified by densitometry, and normalized to ACTN1 loading (N = 2). Measurements were taken from whole-cell lysates 30 min. post-stimulation. (H) Surface levels of ADAM17 were unchanged by mab225 treatment. Identical numbers of cells were starved in the presence or absence of mab225 for 4 hrs, treated with sulfo-NHS-biotin, lysed, and incubated with streptavidin beads. Bound proteins were then blotted for ADAM17. All error bars denote SEM, $^*p<0.05$, Student's t-test.

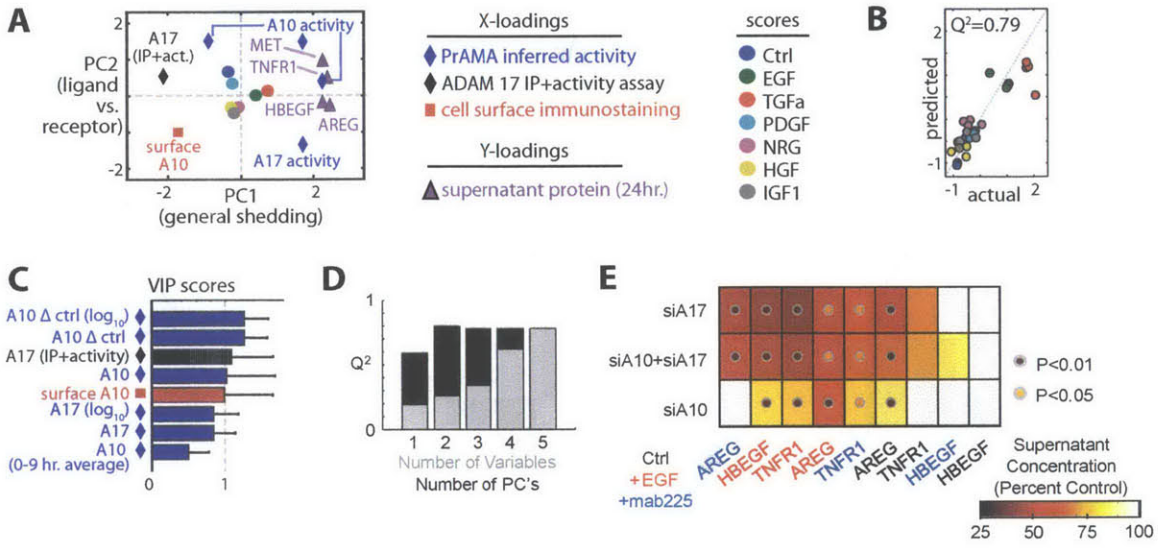

Figure A.12: Joint RTK and ligand shedding by both ADAM-10 and -17. PLSR modeling suggests joint RTK and ligand shedding by both ADAM-10 and -17. PLSR was used to build models that describe AREG, TNFR1, and MET accumulation in the supernatant as a function of phospho-signaling and measured ADAM regulation, across a panel of growth factor treatments (Fig. 3.2A). To improve model accuracy, we also included FRET-substrate cleavage and PrAMA inference results measured across each of the observed time-points (Fig. A.2B). The reduced PLSR model only includes descriptor variables that contribute to model prediction accuracy (Q^2), and the final model shown here includes 8 total descriptor variables. (A) The scores and loadings plot presents the model in terms of two principal components that chiefly capture general sheddase activity (x-axis) and ligand vs. receptor shedding preference (y-axis). (B-C) Q^2 prediction accuracy (B) and the VIP scores (C)for the reduced PLSR model shown in *A*. The PLSR model considered multiple data-transformations of the protease activity data, and included log-transformed data, fold-change normalized data, baseline-subtracted data, as well as activity measurements across multiple time-points. Multiple of these measurements (three for ADAM10, two for ADAM17) were ultimately included in the PLSR model. (D) The reduced PLSR model accuracy in *A* improves with the inclusion of multiple descriptor variables (grey bars) and/or PC's (black bars), with two PC's being sufficient to capture 90% of the covariance in the data. This result suggests two axes of regulation govern ligand/receptor shedding, which are described chiefly by ADAM-10 and -17 activities. (E) siRNA knockdown of both ADAM-10 and -17 reduces shedding of multiple endogenous substrates. siRNA knockdown results for AREG are also shown in Fig. 3.4D.

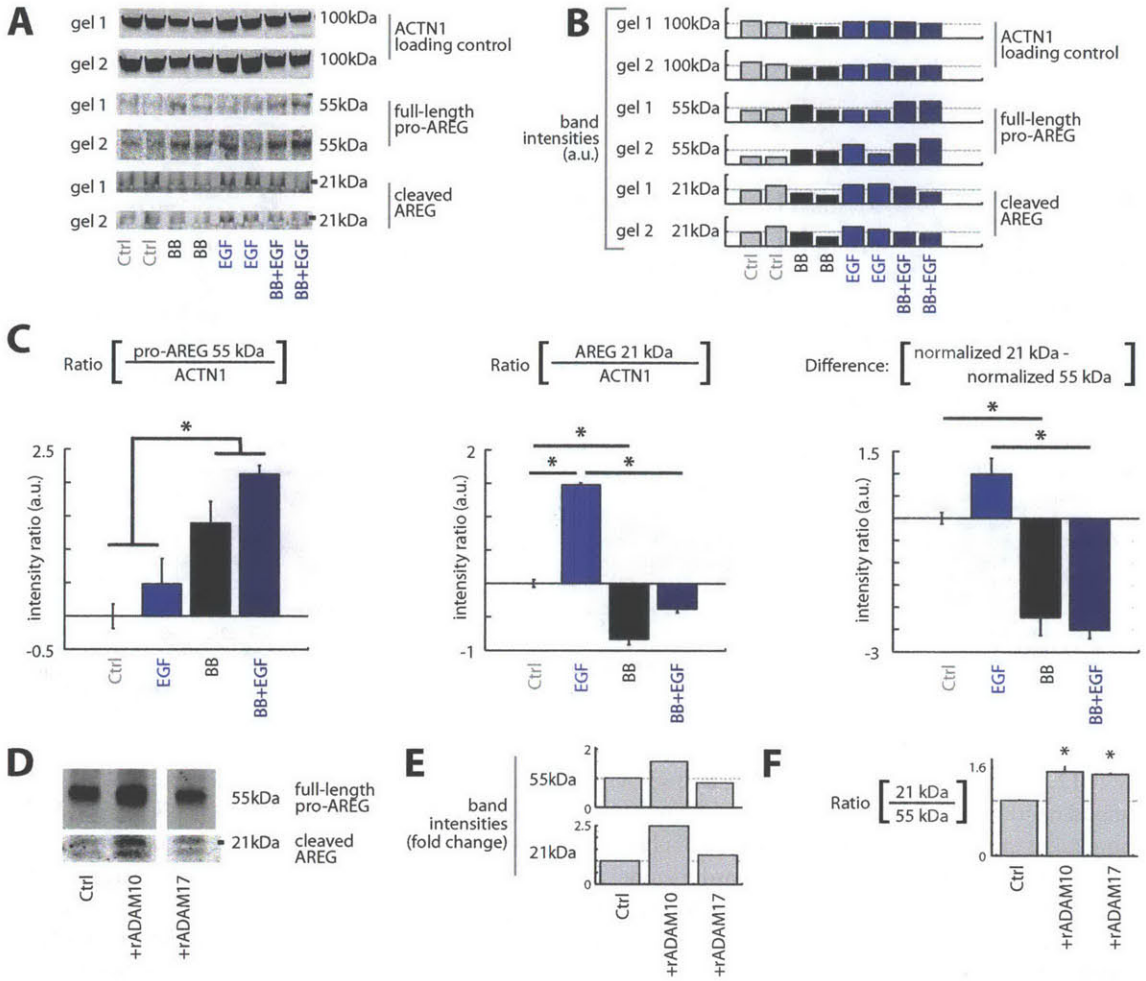

Figure A.13: Both ADAM-10 and -17 can cleave proAREG. (A-C) Detection of metalloproteinase-dependent AREG degradation in 12Z lysates. 12Z were cultured for 24 hrs following EGF and BB94 treatments, lysed, and blotted for ACTN1 and AREG. Using ectodomain antibodies from the ELISA kit, we focused on two AREG bands that had been previously reported in the literature: full length pro-AREG at roughly 55 kDa, and AREG cleavage products at roughly 21 & 19 kDa [328]. Blot images (A), densitometric quantification (B), and ACTN1-normalized averaging across N = 4 replicates (C) demonstrate that EGF treatment causes an increase in the accumulation of the 21 and 19 kDa cleavage products in a metalloproteinase-dependent manner. Furthermore, BB94 treatment leads to an accumulation of the 55 kDa fragment. No 21 kDa cleavage product was visible in blots of the cellular supernatant, which we found unsurprising considering the degree of difficulty detecting AREG even with the more sensitive ELISA format. (D-F) pro-AREG digestion with recombinant protease suggests a role for both ADAM-10 and -17. AREG was immunoprecipitated from whole-cell lysate and incubated 4 hrs on-bead with recombinant ADAM-10 and -17. The reaction was boiled in denaturing sample buffer and blotted for AREG, shown by the representative blot in *D*. Full length 55 kDa pro-AREG and the 21/19 kDa band intensities were quantified by densitometry (E), and the ratio of cleavage product to full-length protein significantly increased with both ADAM-10 and -17 digestion (N = 2). All error bars denote SEM, *$p<0.05$, Student's t-test.

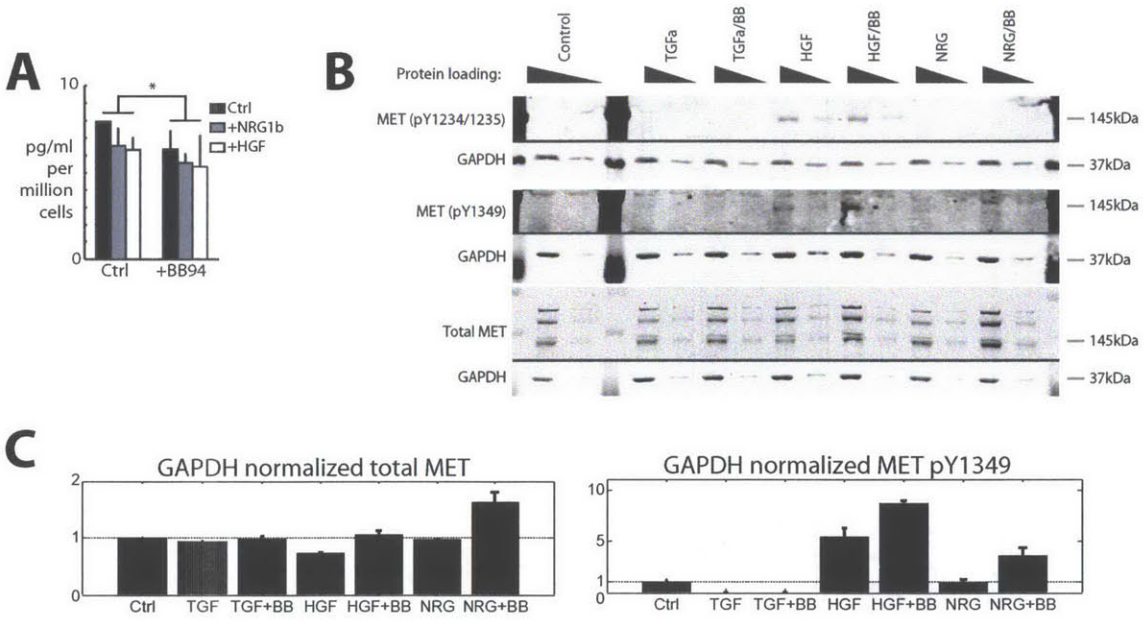

Figure A.14: Proteolytic shedding of HER4 and MET. (A) Metalloproteinase inhibition leads to a significant decrease in supernatant HER4 concentration. 12Z were stimulated with growth-factor in the presence or absence of BB94. Supernatant was collected 24 hr. later and analyzed by bead-based ELISA for HER4 concentration (N = 2 per condition; $p<0.05$, paired Student's t-test). (B-C) Metalloproteinase inhibition leads to an increase in total and pY1349 MET. (B) Representative blot images for quantification of total and phosphorylated MET. After 1.5 hr. pre-treatment with BB94 and 30 min after stimulation, cells were lysed and blotted for MET, p-MET, and GAPDH. (C) GAPDH-normalized blot quantification (N = 2, $\pm$ SEM), including data from *B*. Total MET was calculated from the sum of all molecular weight bands shown between 145-200 kDa, while pY1349 was quantified from 145 kDa band intensities. BB94 did not significantly change pY1234/34 levels, in contrast to pY1349 levels, which increased with BB94 treatment in the presence of NRG1β and HGF.

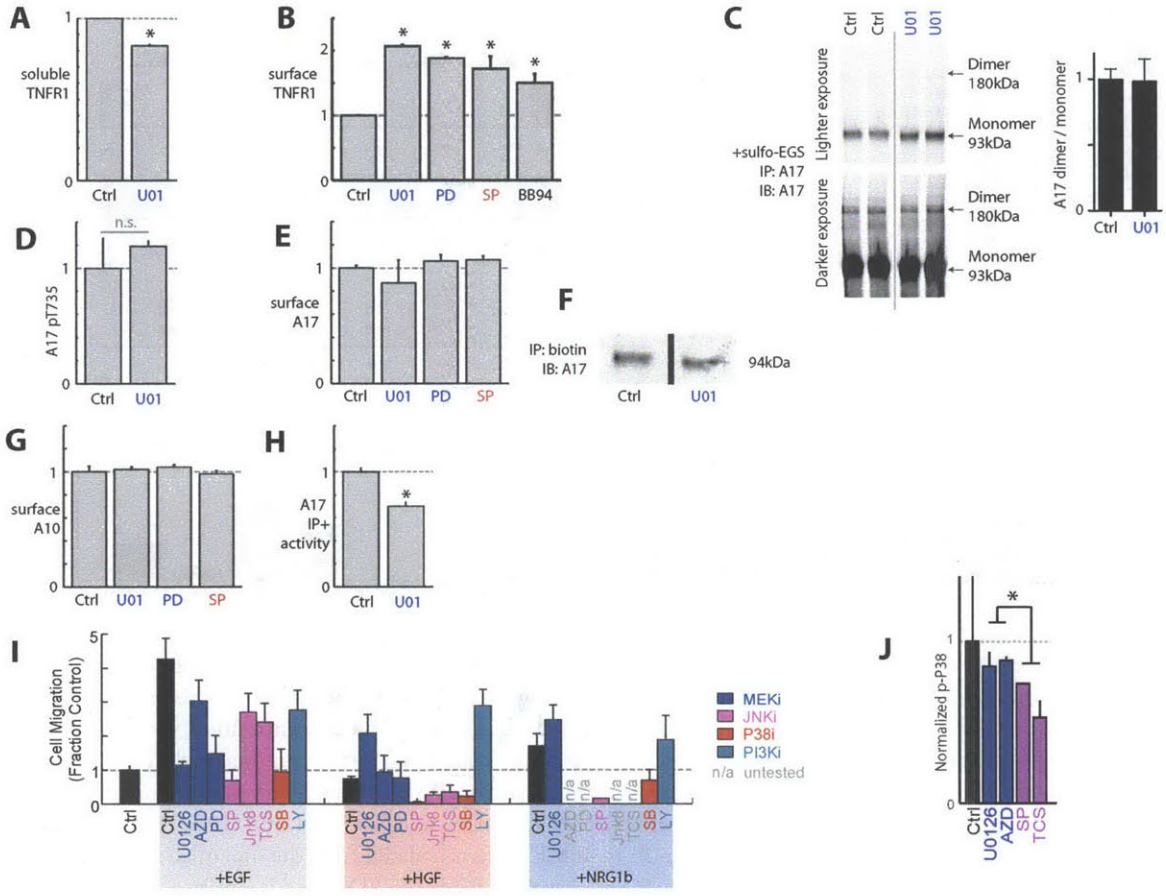

Figure A.15: (Continued on the following page.)

Figure A.15: Effects of kinase inhibition on protease activity and migratory respose to growth factor treatment. (A) U0126 treatment significantly reduces short-term (30 min) TNFR1 accumulation in cellular supernatant. After 30 min treatment with U0126, cellular supernatant was collected, ultra-concentrated using Amicon-ultra size-exclusion columns (Millipore), and analyzed by ELISA for TNFR1 concentration. Results show significant decrease in TNFR1 shedding with U0126 treatment (N = 3). (B) Inhibitor treatment increases surface TNFR1 levels. After 1 hr treatment with signaling and protease inhibitors, 12Z were surface-immunostained for TNFR1 and anlyzed by flow cytometry. Results indicate a significant increase in surface receptor with inhibitor treatment (n = 2 experimental reps.). (C) ADAM17 dimerization does not significantly change with U0126 treatment. Following a 4 hr treatment with U0126, 12Z were treated with sulfo-EGS and lysed. ADAM17 was immunoprecipitated from lysate and then blotted for ADAM17. The ratio of dimer-to-monomer band intensities was calculated, and showed no significant difference (N = 2). D) ADAM17-pT735 was measured by western blot, quantified by densitometry, and normalized to ACTN1 loading (N = 2). Measurements were taken from whole-cell lysates 30 min post-stimulation. E) Surface levels of ADAM17 were unchanged by Mek or Jnk inhibitor treatment. After 1 hr treatment with signaling inhibitors, 12Z were surface-immunostained for ADAM17 and anlyzed by flow cytometry (N = 3). F) Western blot confirms that U0126 treatment does not influence ADAM17 surface levels. Identical numbers of cells were starved in the presence or absence of U0126 for 4 hrs, treated with sulfo-NHS-biotin, lysed, and incubated with streptavidin beads. Bound proteins were then blotted for ADAM17. Control-treated band also shown in Fig. A.11H. G) Surface levels of ADAM10 were unchanged by Mek or Jnk inhibitor treatment. After 1 hr treatment with signaling inhibitors, 12Z were surface-immunostained for ADAM10 and anlyzed by flow cytometry (N = 3). H) ADAM17 activity was quantified using the Innozyme TACE activity assay from whole-cell lysate collected 45 min post-treatment with U0126 (n=2 biological reps.) I) Mek and PI3K inhibition exhibits context-dependent efficacy and most effectively reduce EGF-stimulated cell migration, whereas Jnk and p38 inhibitors effectively block EGF, HGF, and NRG1β stimulated migration. Using the endpoint cell migration assay (SI-11), cells were pre-treated with inhibitor for 1 hr., followed by growth factor stimulation, and migration was measured 24 hr. later ($n \geq 2$ reps.). Data corresponds to the scatter plot shown in Fig. 3.6E. "n/a" indicates experimental conditions were not tested. J) Jnk inhibitors are more effective than Mek inhibitors at reducing p-p38 levels. Cells were pre-treated with inhibitor for 1.5 hr, stimulated with NRG1β for 5 min, lysed, and analyzed by bead immunoassay. All error bars denote SEM., $^*p<0.05$, Student's t-test.

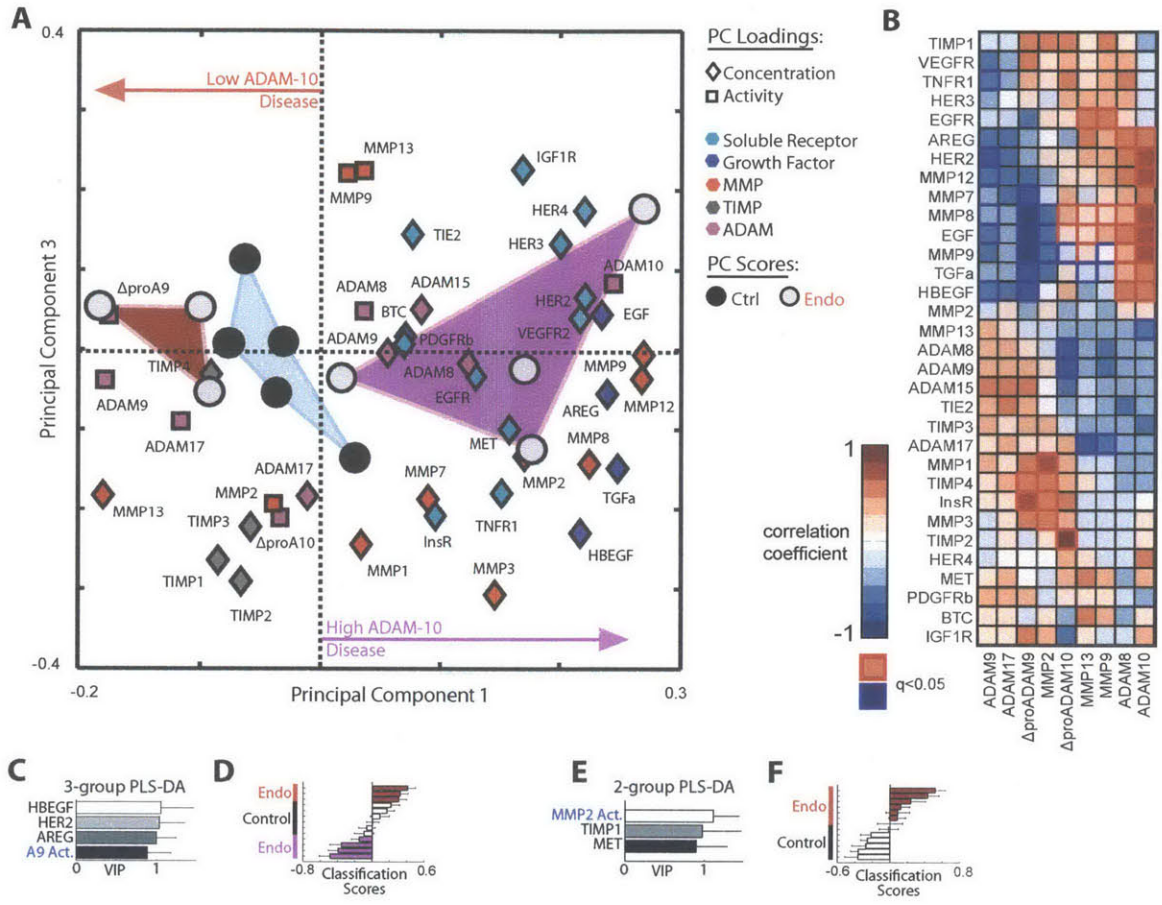

Figure A.16: Multivariate analysis of peritoneal fluid proteomics. (A) PCA decomposes the protein quantification meaurements (using ELISA) and protease activity measurements (using PrAMA) from the PF samples into key principal components (PCs) of variation. Scores and loadings for PC1 and PC3 are shown here, identical to Fig. 3.8B, but with complete labeling. ΔproA10 and ΔproA9 denote the difference in observed cleavage rate with and without co-incubation with the specific prodomain inhibitors proADAM9 and proADAM10 (see [166] for greater detail). (B) The clustergram, generated by hierarchical biclustering, presents significant correlations between protein levels and protease activities across the PF samples. Spearman's and Pearson's correlation coefficients were calculated between protease activities (columns) and observed analyte concentrations (rows) across the set of thirteen PF samples, and the more statistically significant result is shown. Significance was determined using an approximation of the exact permutation distributions of correlation for the Spearman's correlation, and using a Student's t distribution for the Pearson correlation. P-values were corrected for multiple hypothesis testing using the Storey false discovery rate, and consequently are reported as q-values [327]. (C-F) Partial least squares - discriminant analysis (PLS-DA) was used to optimally select a minimal number of descriptor variables that would accurately predict disease state. (C-D) Reduced PLS-DA models were generated to classify samples as falling into one of three states demarcated by the three color groups shown in (A), using four descriptor measurements (C) and with >95% cross-validation classification accuracy (D). An additional PLS-DA model (E-F) classifies PF samples as either control or disease, using three descriptor measurements (E) and also exhibiting >95% cross-validation classification accuracy (F).

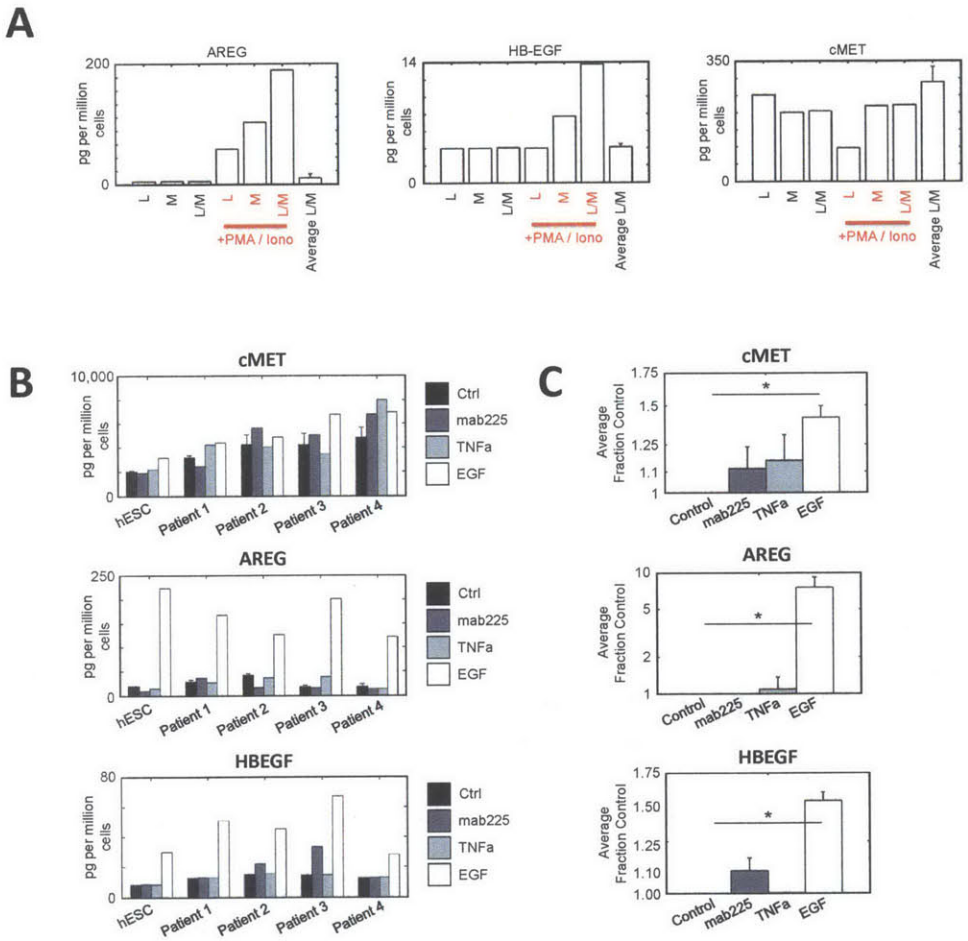

Figure A.17: AREG, HBEGF, and MET shedding in other disease-relevant cell types. (A) Primary PFMCs shed AREG and HBEGF, but not MET, in response to stimulation. Total PFMCs were separated into adherent, mature monocyte populations (M) and non-adherent lymphocyte populations (L). Cells were stimulated with 10 ng mL^{-1} PMA and 1 μg mL^{-1} ionomycin (Iono), supernatant was collected 24 hr later, and was analyzed by ELISA. "Average L/M" describes the average measurements from PFMC across nine separate patient samples, ± standard deviation. Results were normalized to cell count and supernatant volume, and correspond to picogram per million cells per day of analyte release. (B-C) EGF stimulates significant AREG, MET, and HBEGF in endometrial stromal cells. Telomerase-immortalized endometrial stromal cells (tHESC) and primary endometrial stromal cultures from four patients were assayed for ligand and receptor shedding 24 hrs after treatment with either EGF, TNFα, or mab225. Results were normalized to cell count and supernatant volume, and correspond to picogram per million cells per day of analyte release. (C) Shedding induction was calculated relative to basal levels and averaged across all five samples (*$p<0.05$, paired Student's t-test).

Materials and Methods

Growth factors and inhibitors Recombinant growth factors and cytokines were purchased from Peprotech (Rocky Hill, NJ). For all experiments, EGF was used at a final concentration of 100 ng mL^{-1}, NRG1β was used at 80 ng mL^{-1}, and all others were used at 50 ng mL^{-1}. Inhibitors used in this paper, their final concentrations, and vendor source are as follows: BB94 (metalloproteinase inh.; 10 μM; Tocris Bioscience), mAb225 (EGFR blocking mAb; 10 μg mL^{-1}; purified from the ATCC hybridoma), gefitinib (EGFR inh.; 1 μM; LC Labs), lapatinib (EGFR/HER2 inh.; 1 μM; LC Labs), SP600125 (Jnk inh.; 20 μM; LC Labs), TCS-6o (Jnk inh.; 10 μM; Tocris), Jnk-IN-8 (Jnk inh.; 3 μM; generously provided by the Gray Lab, Harvard Medical School), SB203580 (P38 inh.; 20 μM; LC Labs), LY294002 (PI3K inh.; 10 μM; LC Labs), U0126 (Mek inh.; 10 μM; LC Labs), AZD6244 (Mek inh.; 5 μM; Selleck Chem.), PD0325901 (Mek inh.; 10 μM; Tocris), Foretinib (MET inh.; 100 nM; Selleck), α-AREG mAb (AREG inh.; 10 μg mL^{-1}; R&D Systems), pro-ADAM-9 (ADAM-9 inh.; 10 μM; Biozyme, Inc.; Apex, NC), pro-ADAM-10 (ADAM-10 inh.; 4 μM; Biozyme, Inc.).

Tissue culture The 12Z cell line was generously provided by Anna Starzinski-Powitz (University of Frankfurt) by way of Steve Palmer (EMD Serono). Telomerase-immortalized human endometrial fibroblasts (tHESC CRL-4003; ATCC) were cultured according to supplier recommendations. 12Z were routinely cultured in media that consisted of DMEM/F12 supplemented with 100 U/ml penicillin, 100 μg mL^{-1} streptomycin (Invitrogen), along with 10% fetal bovine serum (Atlanta Biologicals; Atlanta, GA) at 37 °C, 5% CO_2. Excluding cell migration assays, 12Z were serum starved for at least 4 hr. before all experiments.

Immunoassays Phospho-protein levels were measured using the following bead-based sandwich immunoassays (Bio-Rad; Hercules, CA): Akt pSer473, cJun pSer63, ERK1/2 pThr202/Tyr204 & pThr185/Tyr187, HSP27 pSer78, Jnk pThr183/Tyr185, P38 pThr180/Tyr182, Src pTyr416, STAT3 pTyr705, GSK3a/b pSer21/Ser9, Tyk2 pTyr1054/Tyr1055, and IRS-1 pSer636/Ser639. Site-specific EGFR pTyr1173 Ab was used in Fig. 3.3B. Other EGFR, HER2, and HER4 phosphorylation levels were measured using a bead-conjugated ectodomain capture Ab and a pan-phosphotyrosine detection Ab (EMD4Biosciences). Supernatant ligand, receptor, MMP, and TIMP measurements were performed using R&D Duo-set ELISA kits (R&D Systems, Minneapolis, MN), Widescreen bead-based ELISAs from EMD4Biosciences (Merck KGaA, Darmstadt, Germany), and Fluorokine MAP Multiplex kits (R&D Systems). p-MET western blots used clone D26 for MET pTyr1234/1235 and clone 130H2 for MET pTyr1349, both from Cell Signaling Technologies (Danvers, MA). ADAM17 western blots used a rabbit polyclonal Ab (Ab2051; Abcam). ADAM10 western blots used a rabbit polyclonal Ab targeting amino acids 732-748 (Sigma). Western blots were imaged using an Odyssey (Li-cor) infrared scanner and dye-conjugated secondary antibodies (Invitrogen). AREG western blots used ectodomain AREG antibodies from the R&D Systems Duo-set. All blot images were processed using standard ImageJ functions for contrast adjustment, background subtraction, and densitometry, in accordance with publication guidelines.

Immunostaining and flow cytometry Immunostaining and flow cytometry were used to assess surface levels of ADAM10, ADAM17, and sheddase substrates. For these measurements, cells were treated with trypsin/EDTA (Gibco) for 15 min, rinsed in 4 °C PBS + 3% FBS, and incubated with primary antibodies at 1:100 dilution for 2 hrs in 4 °C PBS + 3% FBS. Cells were rinsed in 4 °C PBS + 3% FBS, fixed in 2% PFA + PBS overnight, and stained with secondary antibody the following day. Flow cytometry was performed using the BD Biosciences LSR-II. ADAM10 ectodomain mAb (clone 163003) and antibodies from R&D Duo-set kits were used for immunostaining.

ADAM17 Dimerization Confluent 15 cm plates of 12Z cells were starved for 4 hrs and then stimulated for 30 min with the indicated growth factor. After washing with 4 °C PBS, cells were incubated with 0.5 mg mL^{-1}

sulfo-EGS (Pierce) for 30 min, then lysed in 1% NP40 lysis buffer. Lysates were clarified, precleared with agarose resin, and then incubated with protein A/G resin (Pierce) and anti-ADAM17 antibody (R&D Systems Duo-set) overnight. The next day, the resin was washed repeatedly, and then boiled in denaturing lysis buffer to elute protein. Dimerized ADAM17 was identified by western according to size shift, and normalized to the monomer ADAM17 in each sample. Methods roughly follow previously work describing ADAM-17 dimerization [329].

IP/western surface protein measurements Identical numbers of cells were starved in the presence or absence of inhibitor for 4 hrs, and then surface biotinylated with 0.5 mg mL^{-1} S-NHS-biotin (Pierce) for 30 min at 4 °C. Lysate was clarified, precleared with unconjugated sepharose resin for 1 hr (Invitrogen), and incubated with straptavidin-conjugated sepharose resin (Invitrogen) overnight. After washing, the bound fraction was eluted by boiling in denaturing sample buffer.

AREG immunoprecipitation and digestion Four 15 cm plates of 12Z were lysed in 1% NP40 lysis buffer, clarified, and then incubated with protein A/G resin (Pierce) and 10 μg anti-AREG antibody (R&D Systems Duo-set) overnight. After repeated washing, the resin was split into separate samples for digest. Roughly 5 nM active recombinant ADAM-10 and -17 (R&D Systems) were incubated with resin for 4 hr. The reaction was then boiled in denaturing sample buffer, and cleavage products were blotted using ectodomain AREG antibodies from the R&D Systems Duo-set kit. The 55kDa band was detected with the polyclonal goat IgG Ab, while the immunopurification and 19/21 kDa bands were performed using the mouse IgG mAb.

Peritoneal fluid sample and analysis Peritoneal fluid, primary HESC, and PFMC samples were all from patients who provided informed consent in accordance with a protocol approved by the Partners Human Research Committee and the Massachusetts Institute of Technology Committee on the Use of Humans as Experimental Subjects. We limited enrollment to pre-menopausal women with regular cycles (26–32 days), and excluded subjects having received hormone treatment within three months of surgery. Moderate/Severe (Stage III/IV) endometriosis was laparscopically diagnosed based on the revised criteria of the American Society for Reproductive Medicine [330]. Control samples were free of visible endometriosis and typically received laparoscopy for reasons relating to abdominal pain and/or symptomatic uterine fibroids. Peritoneal fluid was aspirated during laparoscopy from the rectouterine pouch, following trocar insertion and before lavage or surgical manipulation. Specimens were immediately clarified within 15 min by centrifugation, aliquoted, and stored at -80°C until further analysis.

Primary and immortalized HESC Endometrial tissue was obtained from pipelle uterine biopsies of normally cycling pre-menopausal women. Isolation and purification of endometrial stromal fibroblasts was performed as previously described [331]. Briefly, tissue was dissected into approximately 1 mm^3 fragments using a sterile scalpel blade, transferred into a tube containing fresh complete media and centrifuged (400×g) to eliminate excess blood and debris. Fragments were resuspended in an enzyme mix containing 0.5% collagenase type IV and 0.02% deoxyribonuclease I, and 2% chicken serum in phenol red-free DMEM-F12. Suspensions were incubated at 37°C for 1 hrs, intermittently aspirated through decreasing sizes of glass pipettes for cell dispersion, and finally filtered through a 100 μm and subsequently 70 μm nylon cell strainer.

PFMC isolation and media conditioning Peritoneal fluid mononuclear cells were isolated from fresh peritoneal aspirates by centrifugation (10 min at 1000×g) and cryopreserved in complete media supplemented with 10% DMSO. Upon thawing, cells were washed and seeded at 10^5 cells/cm^2 in 24-well plates for selective adherence of mature monocytes. Non-adherent populations were removed by gentle washing after three hours of culture, and conditioned media collected following an additional 24 hrs of monocyte-enriched culture. Flow cytometry routinely indicated >99% CD45 expression in fresh PFMC suspensions and >90% lymphocyte depletion in monocyte-enriched preparations.

ADAM17 IP & activity assay ADAM17 was precipitated on an anti-ADAM17 coated 96-well plate and incubated with a FRET-based protease substrate. Increase in fluorescence was tracked over time for 4 hrs The slope of increase was calculated and compared to a standard dilution series according to the manufacturer's instructions (Innozyme TACE activity assay, EMD Millipore, Billerica MA). In all cases, cleavage rates were detected within the dynamic range of the assay according to the standard curve.

Supernatant analysis For quantification of supernatant analytes, cells were plated on polystyrene plates (Corning) at 80% confluency, and stimulated the following day with serum-free media supplemented with growth factors after a 30 min pre-treatment with inhibitor. 12Z were serum starved overnight before treatment. Supernatant was collected 24 hrs after stimulation, clarified by centrifugation (5 min, 300×g), and frozen at -20°C for storage. At the time of supernatant collection, cells were trypsinized and analyzed for cell count and viability using ViCell instrumentation (Beckman Coulter; Brea, CA). Final analyte concentration measurements were normalized to cell count.

siRNA knockdown protocol siRNA treatments used ON-TARGETplus SMARTpool siRNAs (Thermo Scientific), with siGENOME non-targeting siRNA pool-2 as the negative control. 5×10^5 cells were seeded in 10 cm dishes. The following day the cells were transfected using 5 μL Dharmafect 4 and 125 pmol siRNA according to the manufacturer's protocol. One day after transfection, cells were reseeded for knockdown experiments, and 48 hrs after transfection cells were treated and lysed. Experiments for measuring ectodomain shedding and cell migration began with growth-factor stimulation 48 hrs post-transfection, and ended 24 hrs later (48 hrs later, for Fig. 3.7D).

Migration assay computation To interpret live-cell migration experiments, the root-mean-squared cell speed was calculated from position intervals between time points for each cell track, as well as the standard deviation of the mean [59, 132]. In this work, persistence denotes net displacement divided by the total path length. Endpoint migration assays were interpreted using a modified spot finding algorithm [332] in Matlab (Mathworks; Natick, MA). Briefly, confocal z-stacks were first pre-processed using background subtraction to eliminate uneven microscope illumination, followed by top-hat filtering and contrast enhancement. Pre-processed images were segmented using previously described software [332]. Identified nuclei positions were assessed by nearest-neighbor analysis and PCA to infer the well-bottom where the majority of cells reside, and z-positions of the nuclei were determined as a distance from the xy-plane of the well-bottom. Unless otherwise stated, migration metrics were calculated as a fraction of cells that had invaded further than 20 μm from the well-bottom, although this threshold slightly changed depending on day-to-day variability to maximize signal-to-noise and minimize background.

Partial least squares analysis Partial least squares regression (PLSR), partial least squares discriminant analysis (PLS-DA), principal component analysis (PCA), hierarchical biclustering, and all other statistical analyses were performed using Matlab (Mathworks; Natick, MA). Unless otherwise stated, all input and output variables were mean-centered and variance-normalized across the set of environmental stimuli, prior to PLSR, PLS-DA, or PCA. For PLSR and PLS-DA, we implemented a forward-variable selection procedure to heuristically select the minimal combination of input variables that optimally described output variable response. We iteratively added input variables to the PLSR model if they improved model fit as determined by leave-one-out cross validation accuracy. To avoid local optima, we conducted heuristic searches with several cost functions of the cross-validation accuracy, including Q^2 (the R^2 coefficient of determination for prediction accuracy), Spearman rank correlation, Pearson correlation coefficients, and for PLS-DA, area under the R.O.C. curve (AUROC). To avoid over-fitting, we required the added input variables to demonstrate PLSR loadings of greater magnitude than their observed loading standard error. Variable importance in the projection (VIP) statistics were calculated in the usual manner. Standard error for scores, loadings, and VIP were calculated by the jack-knife [142]. Variance of the prediction

values were computed [333]. All results presented in this work with non-zero Q^2 or AUROC accuracy demonstrated a statistical significance ($p<0.05$) as determined by the permutation test. Briefly, we randomly shuffled output variables relative to the model inputs, and ran the variable-selection procedure for each of 1000 random permutations. Shuffled data yielded a lower Q^2 value than that achieved by the actual data-set more than 95% of the time.

Bibliography

1. O'Brien, S. G. *et al.* Imatinib compared with interferon and low-dose cytarabine for newly diagnosed chronic-phase chronic myeloid leukemia. *N Engl J Med* **348,** 994–1004 (Mar. 2003).
2. Lazebnik, Y. What are the hallmarks of cancer? *Nat. Rev. Cancer* **10,** 232–233 (Apr. 2010).
3. Scott, J., Kuhn, P. & Anderson, A. R. A. Unifying metastasis — integrating intravasation, circulation and end-organ colonization. *Nat. Rev. Cancer* **12,** 445–446 (May 2012).
4. Yang, J. *et al.* Twist, a master regulator of morphogenesis, plays an essential role in tumor metastasis. *Cell* **117,** 927–939 (June 2004).
5. Wong, S. G., Levin, W. J. & Ullrich, A. Human breast cancer: correlation of relapse and survival with amplification of the HER-2/neu oncogene. *Science* **235,** 177–182 (Jan. 1987).
6. Creighton, C. J. *et al.* Residual breast cancers after conventional therapy display mesenchymal as well as tumor-initiating features. *Proc. Natl. Acad. Sci. USA* **106,** 13820–13825 (Aug. 2009).
7. Tarin, D., Thompson, E. W. & Newgreen, D. F. The fallacy of epithelial mesenchymal transition in neoplasia. *Cancer Res.* **65,** 5996–5991 (July 2005).
8. Wang, Y. *et al.* Gene-expression profiles to predict distant metastasis of lymph-node-negative primary breast cancer. *Lancet* **365,** 671–679 (Feb. 2005).
9. Tsai, J. H., Donaher, J. L., Murphy, D. A., Chau, S. & Yang, J. Spatiotemporal regulation of epithelial-mesenchymal transition is essential for squamous cell carcinoma metastasis. *Cancer Cell* **22,** 725–736 (Dec. 2012).
10. Lacroix, M. & Leclercq, G. Relevance of breast cancer cell lines as models for breast tumours: an update. *Breast Cancer Res Treat* **83,** 249–289 (Feb. 2004).
11. Aktas, B. *et al.* Stem cell and epithelial-mesenchymal transition markers are frequently overexpressed in circulating tumor cells of metastatic breast cancer patients. *Breast Cancer Res.* **11,** R46 (2009).
12. Cristofanilli, M. *et al.* Circulating tumor cells, disease progression, and survival in metastatic breast cancer. *New Engl J Med* **351,** 781–791 (2004).
13. Yu, M. *et al.* RNA sequencing of pancreatic circulating tumour cells implicates WNT signalling in metastasis. *Nature* **487,** 510–513 (Apr. 2013).
14. Armstrong, A. J. *et al.* Circulating tumor cells from patients with advanced prostate and breast cancer display both epithelial and mesenchymal markers. *Molecular Cancer Research* **9,** 997–1007 (Aug. 2011).
15. Yu, M. *et al.* Circulating Breast Tumor Cells Exhibit Dynamic Changes in Epithelial and Mesenchymal Composition. *Science* **339,** 580–584 (Jan. 2013).
16. Labelle, M., Begum, S. & Hynes, R. O. Direct Signaling between Platelets and Cancer Cells Induces an Epithelial-Mesenchymal-Like Transition and Promotes Metastasis. *Cancer Cell* **20,** 576–590 (Nov. 2011).

17. Murtaza, M. *et al.* Non-invasive analysis of acquired resistance to cancer therapy by sequencing of plasma DNA. *Nature* **497**, 108–112 (Apr. 2014).

18. Navin, N. *et al.* Tumour evolution inferred by single-cell sequencing. *Nature* **472**, 90–94 (Dec. 2011).

19. Gupta, P. B. *et al.* Identification of Selective Inhibitors of Cancer Stem Cellsby High-Throughput Screening. *Cell* **138**, 645–659 (Aug. 2009).

20. Krimpenfort, P. *et al.* Deleted in colorectal carcinoma suppresses metastasis in p53-deficient mammary tumours. *Nature* **482**, 538–541 (Feb. 2012).

21. Gjerdrum, C. *et al.* AXL is an essential epithelial-to-mesenchymal transition-induced regulator of breast cancer metastasis and patient survival. *Proc. Natl. Acad. Sci. USA* **107**, 1124 (2010).

22. Gupta, P. B. *et al.* Stochastic State Transitions Give Rise to Phenotypic Equilibrium in Populations of Cancer Cells. *Cell* **146**, 633–644 (Aug. 2011).

23. Mitchell, M. J., Wayne, E., Rana, K., Schaffer, C. B. & King, M. R. TRAIL-coated leukocytes that kill cancer cells in the circulation. *Proc. Natl. Acad. Sci. U.S.A.* **111**, 930–935 (Jan. 2014).

24. Lu, X. *et al.* VCAM-1 Promotes Osteolytic Expansion of Indolent Bone Micrometastasis of Breast Cancer by Engaging $\alpha 4\beta 1$-Positive Osteoclast Progenitors. *Cancer Cell* **20**, 701–714 (Dec. 2011).

25. Leder, K. *et al.* Mathematical Modeling of PDGF-Driven Glioblastoma Reveals Optimized Radiation Dosing Schedules. *Cell* **156**, 603–616 (Jan. 2014).

26. Friedl, P. & Alexander, S. Cancer Invasion and the Microenvironment: Plasticity and Reciprocity. *Cell* **147**, 992–1009 (Nov. 2011).

27. Petrie, R. J., Gavara, N., Chadwick, R. S. & Yamada, K. M. Nonpolarized signaling reveals two distinct modes of 3D cell migration. *J Cell Biol* **197**, 439–455 (Apr. 2012).

28. Poincloux, R. *et al.* Contractility of the cell rear drives invasion of breast tumor cells in 3D Matrigel. *Proc. Natl. Acad. Sci. USA* **108**, 1943–1948 (Feb. 2011).

29. Cheung, K. J., Gabrielson, E., Werb, Z. & Ewald, A. J. Collective invasion in breast cancer requires a conserved basal epithelial program. *Cell* **155**, 1639–1651 (Dec. 2013).

30. Liu, Y. & Friedl, P. Multi-step pericellular proteolysis controls the transition from individual to collective cancer cell invasion. *Nat Cell Biol* **9**, 893–904 (Aug. 2007).

31. Truong, H. H. *et al.* $\beta 1$ Integrin Inhibition Elicits a Prometastatic Switch Through the TGFβ-miR-200-ZEB Network in E-Cadherin-Positive Triple-Negative Breast Cancer. *Sci Signal* **7**, ra15–ra15 (2014).

32. Giampieri, S. *et al.* Localized and reversible TGFβ signalling switches breast cancer cells from cohesive to single cell motility. *Nat Cell Biol* **11**, 1287–1296 (Nov. 2009).

33. Philippar, U. *et al.* A Mena invasion isoform potentiates EGF-induced carcinoma cell invasion and metastasis. *Dev Cell* **15**, 813–828 (Dec. 2008).

34. Tan, W. *et al.* Tumour-infiltrating regulatory T cells stimulate mammary cancer metastasis through RANKL-RANK signalling. *Nature* **470**, 548–553 (Dec. 2011).

35. Guiet, R. *et al.* The process of macrophage migration promotes matrix metalloproteinase-independent invasion by tumor cells. *The Journal of Immunology* **187**, 3806–3814 (Oct. 2011).

36. Goetz, J. G. *et al.* Biomechanical Remodeling of the Microenvironment by Stromal Caveolin-1 Favors Tumor Invasion and Metastasis. *Cell* **146**, 148–163 (July 2011).

37. Calvo, F. *et al.* Mechanotransduction and YAP-dependent matrixremodelling is required for the generation andmaintenance of cancer-associated fibroblasts. *Nat Cell Biol* **15**, 637–646 (May 2013).

38. Mouneimne, G. *et al.* Phospholipase C and cofilin are required for carcinoma cell directionality in response to EGF stimulation. *J Cell Biol* **166**, 697–708 (Aug. 2004).

39. Chen, J. *et al.* CCL18 from Tumor-Associated Macrophages Promotes Breast Cancer Metastasis via PITPNM3. *Cancer Cell* **19**, 541–555 (Dec. 2011).

40. Niederst, M. J. & Engelman, J. A. Bypass mechanisms of resistance to receptor tyrosine kinase inhibition in lung cancer. *Sci Signal* **6**, re6–re6 (Sept. 2013).

41. Ercan, D. *et al.* Amplification of EGFR T790M causes resistance to an irreversible EGFR inhibitor. *Oncogene* **29**, 2346–2356 (Apr. 2010).

42. Johannessen, C. M. *et al.* COT drives resistance to RAF inhibition through MAP kinase pathway reactivation. *Nature* **468**, 968–972 (Dec. 2010).

43. Wilson, T. R. *et al.* Widespread potential for growth-factor-driven resistance to anticancer kinase inhibitors. *Nature* **487**, 505–509 (July 2012).

44. Johannessen, C. M. *et al.* A melanocyte lineage program confers resistance to MAP kinase pathway inhibition. *Nature* **504**, 138–142 (Apr. 2014).

45. Niepel, M. *et al.* Profiles of Basal and Stimulated Receptor Signaling Networks Predict Drug Response in Breast Cancer Lines. *Sci Signal* **6**, ra84–ra84 (Sept. 2013).

46. Computational Modeling of ERBB2-Amplified Breast Cancer Identifies Combined ErbB2/3 Blockade as Superior to the Combination of MEK and AKT Inhibitors. *Sci Signal* **6**, ra68–ra68 (Aug. 2013).

47. Tozluoğlu, M. *et al.* Matrix geometry determines optimal cancer cell migration strategy and modulates response to interventions. *Nat Cell Biol* **15**, 751–762 (June 2013).

48. Wilson, J. L., Hemann, M. T., Fraenkel, E. & Lauffenburger, D. A. Integrated network analyses for functional genomic studies in cancer. *Semin Cancer Biol* **23**, 213–218 (Aug. 2013).

49. Allen, B. Evolutionary dynamics of cancer in response to targeted combination therapy. *eLife* **2**, e00747–e00747 (Jan. 2013).

50. Fraley, S. I. *et al.* A distinctive role for focal adhesion proteins in three-dimensional cell motility. *Nat Cell Biol* **12**, 598–604 (June 2010).

51. Png, K. J., Halberg, N., Yoshida, M. & Tavazoie, S. F. A microRNA regulon that mediates endothelial recruitment and metastasis by cancer cells. *Nature* **481**, 190–194 (Dec. 2011).

52. Fisher, K. E. *et al.* MT1-MMP- and Cdc42-dependent signaling co-regulate cell invasion and tunnel formation in 3D collagen matrices. *J Cell Sci* **122**, 4558–4569 (Dec. 2009).

53. Leung, C. T. & Brugge, J. S. Outgrowth of single oncogene-expressing cells from suppressive epithelial environments. *Nature* **482**, 410–413 (Feb. 2012).

54. Eke, I. *et al.* β1 Integrin/FAK/cortactin signaling is essential for human head and neck cancer resistance to radiotherapy. *J Clin Invest* **122**, 1529–1540 (Apr. 2012).

55. Malanchi, I. *et al.* Interactions between cancer stem cells and their niche govern metastatic colonization. *Nature* **481**, 85–89 (Dec. 2011).

56. Hakkinen, K. M., Harunaga, J. S., Doyle, A. D. & Yamada, K. M. Direct Comparisons of the Morphology, Migration, Cell Adhesions, and Actin Cytoskeleton of Fibroblasts in Four Different Three-Dimensional Extracellular Matrices. *Tissue Engineering Part A* **17**, 713–724 (Mar. 2011).

57. Loessner, D. *et al.* Bioengineered 3D platform to explore cell-ECM interactions and drug resistance of epithelial ovarian cancer cells. *Biomaterials* **31**, 8494–8506 (Nov. 2010).

58. Gupton, S. & Waterman-Storer, C. Spatiotemporal feedback between actomyosin and focal-adhesion systems optimizes rapid cell migration. *Cell* **125,** 1361–1374 (2006).

59. Meyer, A. S. *et al.* 2D protrusion but not motility predicts growth factor-induced cancer cell migration in 3D collagen. *J Cell Biol* **197,** 721–729 (June 2012).

60. Chiu, C.-L., Digman, M. A. & Gratton, E. Measuring Actin Flow in 3D Cell Protrusions. *Biophys J* **105,** 1746–1755 (Oct. 2013).

61. Eckert, M. A. *et al.* Twist1-Induced Invadopodia Formation Promotes Tumor Metastasis. *Cancer Cell* **19,** 372–386 (Aug. 2011).

62. Perentes, J. Y. *et al.* Cancer Cell-Associated MT1-MMP Promotes Blood Vessel Invasion and Distant Metastasis in Triple-Negative Mammary Tumors. *Cancer Res.* **71,** 4527–4538 (June 2011).

63. Bendell, J. C. *et al.* Central nervous system metastases in women who receive trastuzumab-based therapy for metastatic breast carcinoma. *Cancer* **97,** 2972–2977 (June 2003).

64. Pallasch, C. P. *et al.* Sensitizing Protective Tumor Microenvironments to Antibody-Mediated Therapy. *Cell* **156,** 590–602 (Jan. 2014).

65. Ghajar, C. M. *et al.* The perivascular niche regulates breast tumour dormancy. *Nat Cell Biol* **15,** 807–817 (June 2013).

66. Lindsay, C. R. *et al.* P-Rex1 is required for efficient melanoblast migration and melanoma metastasis. *Nature Communications* **2,** 555–9 (2011).

67. Ebi, H. *et al.* PI3K regulates MEK/ERK signaling in breast cancer via the Rac-GEF, P-Rex1. *Proc. Natl. Acad. Sci. U.S.A.* **110,** 21124–21129 (Dec. 2013).

68. Sosa, M. S. *et al.* Identification of the Rac-GEF P-Rex1 as an Essential Mediator of ErbB Signaling in Breast Cancer. *Mol. Cell* **40,** 877–892 (Dec. 2010).

69. Maquoi, E., Assent, D., Detilleux, J., Pequeux, C. & l, A. N. e. MT1-MMP protects breast carcinoma cells against type I collagen-induced apoptosis. **31,** 480–493 (June 2011).

70. Ota, I., Li, X.-Y., Hu, Y. & Weiss, S. J. Induction of a MT1-MMP and MT2-MMP-dependent basement membrane transmigration program in cancer cells by Snail1. *Proc. Natl. Acad. Sci. USA* **106,** 20318–20323 (2009).

71. Levental, K. R. *et al.* Matrix crosslinking forces tumor progression by enhancing integrin signaling. *Cell* **139,** 891–906 (Nov. 2009).

72. Salt, M. B., Bandyopadhyay, S. & McCormick, F. Epithelial-to-Mesenchymal Transition Rewires the Molecular Path to PI3K-Dependent Proliferation. *Cancer Discovery* **4,** 186–199 (Feb. 2014).

73. Reticker-Flynn, N. E. *et al.* A combinatorial extracellular matrix platform identifies cell-extracellular matrix interactions that correlate with metastasis. *Nature Communications* **3,** 1122–12 (Sept. 2012).

74. Zhang, X. H.-F. *et al.* Selection of Bone Metastasis Seeds by Mesenchymal Signalsin the Primary Tumor Stroma. *Cell* **154,** 1060–1073 (Aug. 2013).

75. Linger, R. M. A., Keating, A. K., Earp, H. S. & Graham, D. K. TAM receptor tyrosine kinases: biologic functions, signaling, and potential therapeutic targeting in human cancer. *Adv. Cancer Res.* **100,** 35–83 (2008).

76. Stitt, T. N. *et al.* The anticoagulation factor protein S and its relative, Gas6, are ligands for the Tyro 3/Axl family of receptor tyrosine kinases. *Cell* **80,** 661–670 (Feb. 1995).

77. Lemke, G. Biology of the TAM Receptors. *Cold Spring Harbor Perspectives in Biology* **5,** a009076–a009076 (Nov. 2013).

78. Burstyn-Cohen, T. *et al.* Genetic Dissection of TAM Receptor-Ligand Interaction in Retinal Pigment Epithelial Cell Phagocytosis. *Neuron* **76,** 1123–1132 (Dec. 2012).

79. Sasaki, T. *et al.* Structural basis for Gas6-Axl signalling. *EMBO J* **25,** 80–87 (Jan. 2006).

80. Sasaki, T. *et al.* Crystal structure of a C-terminal fragment of growth arrest-specific protein Gas6. Receptor tyrosine kinase activation by laminin G-like domains. *J Biol Chem* **277,** 44164–44170 (Nov. 2002).

81. Kulman, J. D. *et al.* Vitamin K-dependent proteins in Ciona intestinalis, a basal chordate lacking a blood coagulation cascade. *Proc. Natl. Acad. Sci. USA* **103,** 15794–15799 (Oct. 2006).

82. Carrera Silva, E. A. *et al.* T cell-derived protein S engages TAM receptor signaling in dendritic cells to control the magnitude of the immune response. *Immunity* **39,** 160–170 (July 2013).

83. Paolino, M. *et al.* The E3 ligase Cbl-b and TAM receptors regulate cancer metastasis via natural killer cells. *Nature* (Feb. 2014).

84. Cook, R. S. *et al.* MerTK inhibition in tumor leukocytes decreases tumor growth and metastasis. *J Clin Invest* **123,** 3231–3242 (July 2013).

85. Thomson, S. *et al.* A systems view of epithelial-mesenchymal transition signaling states. *Clin. Exp. Metastas.* **28,** 137–155 (Feb. 2011).

86. Lee-Sherick, A. B. *et al.* Aberrant Mer receptor tyrosine kinase expression contributes to leukemogenesis in acute myeloid leukemia. *Oncogene* **32,** 5359–5368 (Nov. 2013).

87. Graham, D. K., Dawson, T. L., Mullaney, D. L., Snodgrass, H. R. & Earp, H. S. Cloning and mRNA expression analysis of a novel human protooncogene, c-mer. *Cell Growth Differ.* **5,** 647–657 (June 1994).

88. Graham, D. K. *et al.* Ectopic expression of the proto-oncogene Mer in pediatric T-cell acute lymphoblastic leukemia. *Clin. Cancer Res.* **12,** 2662–2669 (May 2006).

89. Lemke, G. & Rothlin, C. V. Immunobiology of the TAM receptors. *Nat Rev Immunol* **8,** 327–336 (May 2008).

90. Scott, R. S. *et al.* Phagocytosis and clearance of apoptotic cells is mediated by MER. *Nature* **411,** 207–211 (May 2001).

91. Wan, E. *et al.* Enhanced efferocytosis of apoptotic cardiomyocytes through myeloid-epithelial-reproductive tyrosine kinase links acute inflammation resolution to cardiac repair after infarction. *Circ Res* **113,** 1004–1012 (Sept. 2013).

92. Rothlin, C. V., Ghosh, S., Zuniga, E. I., Oldstone, M. B. A. & Lemke, G. TAM Receptors Are Pleiotropic Inhibitors of the Innate Immune Response. *Cell* **131,** 1124–1136 (Dec. 2007).

93. Lu, Q. & Lemke, G. Homeostatic regulation of the immune system by receptor tyrosine kinases of the Tyro 3 family. *Science* **293,** 306–311 (July 2001).

94. Bhattacharyya, S. *et al.* Enveloped Viruses Disable Innate Immune Responses in Dendritic Cells by Direct Activation of TAM Receptors. *Cell Host and Microbe* **14,** 136–147 (Aug. 2013).

95. Bosurgi, L. *et al.* Paradoxical role of the proto-oncogene Axl and Mer receptor tyrosine kinases in colon cancer. *Proc. Natl. Acad. Sci. U.S.A.* (July 2013).

96. Lu, Q. *et al.* Tyro-3 family receptors are essential regulators of mammalian spermatogenesis. *Nature* **398,** 723–728 (Apr. 1999).

97. Goruppi, S., Ruaro, E., Varnum, B. & Schneider, C. Gas6-mediated survival in NIH3T3 cells activates stress signalling cascade and is independent of Ras. *Oncogene* **18,** 4224–4236 (July 1999).

98. Ji, R. *et al.* TAM Receptors Affect Adult Brain Neurogenesis by Negative Regulation of Microglial Cell Activation. *The Journal of Immunology* (Nov. 2013).

99. Gely-Pernot, A. *et al.* An endogenous vitamin K-dependent mechanism regulates cell proliferation in the brain subventricular stem cell niche. *Stem Cells* **30,** 719–731 (Apr. 2012).

100. Systemic Autoimmunity in TAM Triple Knockout Mice Causes Inflammatory Brain Damage and Cell Death. *PLoS ONE* **8,** e64812 (June 2013).

101. Yachida, S. *et al.* Distant metastasis occurs late during the genetic evolution of pancreatic cancer. *Nature* **467,** 1114–1117 (Oct. 2010).

102. Campbell, P. J. *et al.* The patterns and dynamics of genomic instability in metastatic pancreatic cancer. *Nature* **467,** 1109–1113 (Oct. 2010).

103. Scott, K. L. *et al.* Proinvasion Metastasis Drivers in Early-Stage Melanoma Are Oncogenes. *Cancer Cell* **20,** 92–103 (July 2011).

104. Johnson, B. E. *et al.* Mutational analysis reveals the origin and therapy-driven evolution of recurrent glioma. *Science* **343,** 189–193 (Jan. 2014).

105. Lauffenburger, D. A. & Horwitz, A. F. Cell Migration: A Physically Integrated Molecular Process. *Cell* **84,** 359–369 (Jan. 1996).

106. Friedl, P. & Wolf, K. Proteolytic interstitial cell migration: a five-step process. *Cancer Metast Rev* **28,** 129–135 (2009).

107. Wolf, K. & Friedl, P. Mapping proteolytic cancer cell-extracellular matrix interfaces. *Clin. Exp. Metastas.* **26,** 289–298 (2009).

108. Doyle, A. D., Wang, F. W., Matsumoto, K. & Yamada, K. M. One-dimensional topography underlies three-dimensional fibrillar cell migration. *J Cell Biol* **184,** 481–490 (Feb. 2009).

109. Zaman, M. H. *et al.* Migration of tumor cells in 3D matrices is governed by matrix stiffness along with cell-matrix adhesion and proteolysis. *Proc. Natl. Acad. Sci. USA* **103,** 10889–10894 (July 2006).

110. Lara, R. *et al.* An siRNA screen identifies RSK1 as a key modulator of lung cancer metastasis. *Oncogene,* 1–9 (Jan. 2011).

111. Simpson, K. J. *et al.* Identification of genes that regulate epithelial cell migration using an siRNA screening approach. *Nat Cell Biol* **10,** 1027–1038 (2008).

112. Yarrow, J. C., Totsukawa, G., Charras, G. T. & Mitchison, T. J. Screening for cell migration inhibitors via automated microscopy reveals a Rho-kinase inhibitor. *Chem Biol* **12,** 385–395 (Mar. 2005).

113. Wolf-Yadlin, A. *et al.* Effects of HER2 overexpression on cell signaling networks governing proliferation and migration. *Mol Syst Biol* **2** (2006).

114. Rusnak, D. W. *et al.* Assessment of epidermal growth factor receptor (EGFR, ErbB1) and HER2 (ErbB2) protein expression levels and response to lapatinib (Tykerb, GW572016) in an expanded panel of human normal and tumour cell lines. *Cell Prolif.* **40,** 580–594 (Aug. 2007).

115. Nieman, M. T., Prudoff, R. S., Johnson, K. R. & Wheelock, M. J. N-cadherin promotes motility in human breast cancer cells regardless of their E-cadherin expression. *J Cell Biol* **147,** 631–644 (Nov. 1999).

116. Neve, R. M. *et al.* A collection of breast cancer cell lines for the study of functionally distinct cancer subtypes. *Cancer Cell* **10,** 515–527 (Dec. 2006).

117. Hollestelle, A. *et al.* Distinct gene mutation profiles among luminal-type and basal-type breast cancer cell lines. *Breast Cancer Res Treat* **121,** 53–64 (May 2010).

118. Pishvaian, M. J. *et al.* Cadherin-11 is expressed in invasive breast cancer cell lines. *Cancer Res.* **59,** 947–952 (Feb. 1999).

119. Goswami, S. *et al.* Macrophages promote the invasion of breast carcinoma cells via a colony-stimulating factor-1/epidermal growth factor paracrine loop. *Cancer Res.* **65,** 5278–5283 (June 2005).

120. Cheng, N. *et al.* Loss of TGF-beta type II receptor in fibroblasts promotes mammary carcinoma growth and invasion through upregulation of TGF-alpha-, MSP- and HGF-mediated signaling networks. *Oncogene* **24,** 5053–5068 (July 2005).

121. Cheng, N., Chytil, A., Shyr, Y., Joly, A. & Moses, H. L. Transforming growth factor-beta signaling-deficient fibroblasts enhance hepatocyte growth factor signaling in mammary carcinoma cells to promote scattering and invasion. *Mol. Cancer Res.* **6,** 1521–1533 (Oct. 2008).

122. Hankinson, S. E. *et al.* Circulating concentrations of insulin-like growth factor-I and risk of breast cancer. *Lancet* **351,** 1393–1396 (May 1998).

123. Pasanisi, P. *et al.* Serum insulin-like growth factor-I and platelet-derived growth factor as biomarkers of breast cancer prognosis. *Cancer Epidemiol. Biomarkers Prev.* **17,** 1719–1722 (July 2008).

124. Tyan, S.-W. *et al.* Breast cancer cells induce cancer-associated fibroblasts to secrete hepatocyte growth factor to enhance breast tumorigenesis. *PLoS ONE* **6,** e15313 (2011).

125. Mograbi, B. *et al.* Human monocytes express amphiregulin and heregulin growth factors upon activation. *Eur. Cytokine Netw.* **8,** 73–81 (Mar. 1997).

126. Wilson, T. R., Lee, D. Y., Berry, L., Shames, D. S. & Settleman, J. Neuregulin-1-mediated autocrine signaling underlies sensitivity to HER2 kinase inhibitors in a subset of human cancers. *Cancer Cell* **20,** 158–172 (Aug. 2011).

127. Hutcheson, I. R. *et al.* Heregulin beta1 drives gefitinib-resistant growth and invasion in tamoxifen-resistant MCF-7 breast cancer cells. *Breast Cancer Res.* **9,** R50 (2007).

128. McIntyre, E., Blackburn, E., Brown, P. J., Johnson, C. G. & Gullick, W. J. The complete family of epidermal growth factor receptors and their ligands are co-ordinately expressed in breast cancer. *Breast Cancer Res Treat* **122,** 105–110 (Sept. 2009).

129. Dunn, M. *et al.* Co-expression of neuregulins 1, 2, 3 and 4 in human breast cancer. *J Pathol* **203,** 672–680 (June 2004).

130. Kipper, M. J., Kleinman, H. K. & Wang, F. W. New method for modeling connective-tissue cell migration: improved accuracy on motility parameters. *Biophys J* **93,** 1797–1808 (Sept. 2007).

131. Wolf, K. *et al.* Collagen-based cell migration models *in vitro* and *in vivo*. *Semin Cell Dev Biol* **20,** 931–941 (Oct. 2009).

132. Wells, A. Epidermal growth factor-induced enhancement of glioblastoma cell migration in 3D arises from an intrinsic increase in speed but an extrinsic matrix-and proteolysis-dependent increase in persistence. *Mol Biol Cell* **19,** 4249–4259 (2008).

133. Weigelt, B., Peterse, J. L. & van't Veer, L. J. Breast cancer metastasis: markers and models. *Nat. Rev. Cancer* **5,** 591–602 (Aug. 2005).

134. Al-Hajj, M., Wicha, M., Benito-Hernandez, A., Morrison, S. & Clarke, M. Prospective identification of tumorigenic breast cancer cells. *Proc. Natl. Acad. Sci. USA* **100,** 3983–3988 (2003).

135. Bernards, R. & Weinberg, R. Metastasis genes: A progression puzzle. *Nature* **418,** 823–823 (2002).

136. Jin, Q. & Esteva, F. J. Cross-talk between the ErbB/HER family and the type I insulin-like growth factor receptor signaling pathway in breast cancer. *J Mammary Gland Biol Neoplasia* **13,** 485–498 (Dec. 2008).

137. Charafe-Jauffret, E. *et al.* Gene expression profiling of breast cell lines identifies potential new basal markers. *Oncogene* **25,** 2273–2284 (2005).

138. Mader, C. C., Magalhaes, M. A. O., Bravo-Cordero, J. J., Koleske, A. J. & Gil-Henn, H. An EGFR-Src-Arg-Cortactin Pathway Mediates Functional Maturation of Invadopodia and Breast Cancer Cell Invasion. *Cancer Res.* 1–34 (Jan. 2011).

139. Balsamo, M. *et al.* Mena invasive (MenaINV) promotes multicellular streaming motility and transendothelial migration in a mouse model of breast cancer. *J Cell Sci* **124,** 2120–2131 (June 2011).

140. Kim, H.-D. *et al.* Signaling network state predicts twist-mediated effects on breast cell migration across diverse growth factor contexts. *Mol. Cell. Proteomics* **10,** M111.008433 (Nov. 2011).

141. Bear, J. E. *et al.* Antagonism between Ena/VASP proteins and actin filament capping regulates fibroblast motility. *Cell* **109,** 509–521 (May 2002).

142. Efron, B. & Gong, G. A leisurely look at the bootstrap, the jackknife, and cross-validation. *Am Stat* **37,** 36–48 (1983).

143. Blobel, C. P. ADAMs: key components in EGFR signalling and development. *Nat Rev Mol Cell Bio* **6,** 32–43 (Jan. 2005).

144. Morrison, C. J., Butler, G. S., Rodríguez, D. & Overall, C. M. Matrix metalloproteinase proteomics: substrates, targets, and therapy. *Current Opinion in Cell Biology* **21,** 645–653 (Oct. 2009).

145. Fingleton, B. MMPs as therapeutic targets—Still a viable option? *Semin Cell Dev Biol* **19,** 61–68 (Jan. 2008).

146. Melin, A., Sparén, P. & Bergqvist, A. The risk of cancer and the role of parity among women with endometriosis. *Hum Reprod* **22,** 3021–3026 (Nov. 2007).

147. Ozkan, S., Murk, W. & Arici, A. Endometriosis and infertility: epidemiology and evidence-based treatments. *Annals of the New York Academy of Sciences* **1127,** 92–100 (Apr. 2008).

148. Vercellini, P. *et al.* Post-operative endometriosis recurrence: a plea for prevention based on pathogenetic, epidemiological and clinical evidence. *Reproductive BioMedicine Online* **21,** 259–265 (Aug. 2010).

149. Uzan, C. *et al.* Status of HER1 and HER2 in peritoneal, ovarian and colorectal endometriosis and ovarian endometrioid adenocarcinoma. *Virchows Arch.* **454,** 525–529 (May 2009).

150. Inagaki, M. *et al.* Association study between epidermal growth factor receptor and epidermal growth factor polymorphisms and endometriosis in a Japanese population. *Gynecol. Endocrinol.* **23,** 474–478 (2007).

151. Ngô, C. *et al.* Protein kinase inhibitors can control the progression of endometriosis in vitro and in vivo. *J Pathol* **222,** 148–157 (Oct. 2010).

152. Hoeflich, K. P. *et al.* In vivo antitumor activity of MEK and phosphatidylinositol 3-kinase inhibitors in basal-like breast cancer models. *Clin. Cancer Res.* **15,** 4649–4664 (July 2009).

153. Yoshino, O. *et al.* FR 167653, a p38 mitogen-activated protein kinase inhibitor, suppresses the development of endometriosis in a murine model. *J. Reprod. Immunol.* **72,** 85–93 (Dec. 2006).

154. Turke, A. B. *et al.* Preexistence and Clonal Selectionof MET Amplification in EGFR Mutant NSCLC. *Cancer Cell* **17,** 77–88 (Jan. 2010).

155. Muranen, T. *et al.* Inhibition of PI3K/mTOR leads to adaptive resistance in matrix-attached cancer cells. *Cancer Cell* **21,** 227–239 (Feb. 2012).

156. Lee, M. J. *et al.* Sequential application of anticancer drugs enhances cell death by rewiring apoptotic signaling networks. *Cell* **149,** 780–794 (May 2012).

157. Miller-Jensen, K., Janes, K. A., Brugge, J. S. & Lauffenburger, D. A. Common effector processing mediates cell-specific responses to stimuli. *Nature* **448,** 604–608 (Aug. 2007).

158. Baumann, R. & Starzinski-Powitz, A. Identification of an invasive, N-cadherin-expressing epithelial cell type in endometriosis using a new cell culture model. *Am J Pathol* **159,** 1839–1852 (Nov. 2001).

159. Miller, M. A. *et al.* Proteolytic Activity Matrix Analysis (PrAMA) for simultaneous determination of multiple protease activities. *Integr. Biol.* **3,** 422–438 (Apr. 2011).

160. Xu, P. & Derynck, R. Direct activation of TACE-mediated ectodomain shedding by p38 MAP kinase regulates EGF receptor-dependent cell proliferation. *Mol. Cell* **37,** 551–566 (Feb. 2010).

161. Dang, M. *et al.* Epidermal growth factor (EGF) ligand release by substrate-specific a disintegrin and metalloproteases (ADAMs) involves different protein kinase C (PKC) isoenzymes depending on the stimulus. *J Biol Chem* **286,** 17704–17713 (May 2011).

162. Shoyab, M., Plowman, G. D., McDonald, V. L., Bradley, J. G. & Todaro, G. J. Structure and function of human amphiregulin: a member of the epidermal growth factor family. *Science* **243,** 1074–1076 (Feb. 1989).

163. Joslin, E. J. *et al.* Structure of the EGF receptor transactivation circuit integrates multiple signals with cell context. *Molecular BioSystems* **6,** 1293–1306 (July 2010).

164. Dang, M. *et al.* Regulated ADAM17-dependent EGF family ligand release by substrate-selecting signaling pathways. *Proc. Natl. Acad. Sci. U.S.A.* **110,** 9776–9781 (June 2013).

165. Maretzky, T. *et al.* Migration of growth factor-stimulated epithelial and endothelial cells depends on EGFR transactivation by ADAM17. *Nature Communications* **2,** 229 (2011).

166. Chen, C.-H. *et al.* Multiplexed protease activity assay for low-volume clinical samples using droplet-based microfluidics and its application to endometriosis. *J. Am. Chem. Soc.* **135,** 1645–1648 (Feb. 2013).

167. Amour, A. *et al.* The enzymatic activity of ADAM8 and ADAM9 is not regulated by TIMPs. *FEBS letters* **524,** 154–158 (July 2002).

168. Yoshida, S. *et al.* Hepatocyte growth factor/Met system promotes endometrial and endometriotic stromal cell invasion via autocrine and paracrine pathways. *J. Clin. Endocrinol. Metab.* **89,** 823–832 (Feb. 2004).

169. Butler, G. S., Dean, R. A., Morrison, C. J. & Overall, C. M. Identification of cellular MMP substrates using quantitative proteomics: isotope-coded affinity tags (ICAT) and isobaric tags for relative and absolute quantification (iTRAQ). *Methods Mol. Biol.* **622,** 451–470 (2010).

170. ADAM9 inhibition increases membrane activity of ADAM10 and controls α-secretase processing of amyloid precursor protein. *J Biol Chem* **286,** 40443–40451 (Nov. 2011).

171. Le Gall, S. M. *et al.* ADAMs 10 and 17 represent differentially regulated components of a general shedding machinery for membrane proteins such as transforming growth factor alpha, L-selectin, and tumor necrosis factor alpha. *Mol Biol Cell* **20,** 1785–1794 (Mar. 2009).

172. Xia, W., Liu, L.-H., Ho, P. & Spector, N. L. Truncated ErbB2 receptor (p95ErbB2) is regulated by heregulin through heterodimer formation with ErbB3 yet remains sensitive to the dual EGFR/ErbB2 kinase inhibitor GW572016. *Oncogene* **23,** 646–653 (Jan. 2004).

173. Ghedini, G. C. *et al.* Shed HER2 extracellular domain in HER2-mediated tumor growth and in trastuzumab susceptibility. *J. Cell. Physiol.* **225,** 256–265 (Oct. 2010).

174. Naresh, A. *et al.* The ERBB4/HER4 intracellular domain 4ICD is a BH3-only protein promoting apoptosis of breast cancer cells. *Cancer Res.* **66,** 6412–6420 (June 2006).

175. Foveau, B. *et al.* Down-regulation of the met receptor tyrosine kinase by presenilin-dependent regulated intramembrane proteolysis. *Mol Biol Cell* **20,** 2495–2507 (May 2009).

176. Schelter, F. *et al.* Tumor cell-derived Timp-1 is necessary for maintaining metastasis-promoting Met-signaling via inhibition of Adam-10. *Clin. Exp. Metastas.* **28,** 793–802 (July 2011).

177. Yoshino, O. *et al.* Possible pathophysiological roles of mitogen-activated protein kinases (MAPKs) in endometriosis. **52,** 306–311 (Nov. 2004).

178. Wagner, E. F. & Nebreda, A. R. Signal integration by JNK and p38 MAPK pathways in cancer development. *Nat. Rev. Cancer* **9,** 537–549 (Aug. 2009).

179. Huang, C., Rajfur, Z., Borchers, C., Schaller, M. D. & Jacobson, K. JNK phosphorylates paxillin and regulates cell migration. *Nature* **424,** 219–223 (July 2003).

180. Duncan, J. S. *et al.* Dynamic reprogramming of the kinome in response to targeted MEK inhibition in triple-negative breast cancer. *Cell* **149,** 307–321 (Apr. 2012).

181. Bruner, K. L., Matrisian, L. M., Rodgers, W. H., Gorstein, F. & Osteen, K. G. Suppression of matrix metalloproteinases inhibits establishment of ectopic lesions by human endometrium in nude mice. *J Clin Invest* **99,** 2851–2857 (June 1997).

182. Pines, G. The ERBB network: at last, cancer therapy meets systems biology. *Nat. Rev. Cancer* **12,** 553–563 (July 2012).

183. Hynes, N. & Lane, H. ERBB receptors and cancer: The complexity of targeted inhibitors. *Nat. Rev. Cancer* **5,** 341–354 (2005).

184. Harbinski, F. *et al.* Rescue screens with secreted proteins reveal compensatory potential of receptor tyrosine kinases in driving cancer growth. *Cancer Discovery* **2,** 948–959 (Oct. 2012).

185. Tannock, I. F., Lee, C. M., Tunggal, J. K., Cowan, D. S. M. & Egorin, M. J. Limited penetration of anticancer drugs through tumor tissue: a potential cause of resistance of solid tumors to chemotherapy. *Clin. Cancer Res.* **8,** 878–884 (Mar. 2002).

186. Thiery, J., Acloque, H., Huang, R. & Nieto, M. Epithelial-mesenchymal transitions in development and disease. *Cell* **139,** 871–890 (2009).

187. Herschkowitz, J. I. *et al.* Core epithelial-to-mesenchymal transition interactome gene-expression signature is associated with claudin-low and metaplastic breast cancer subtypes. *Proc. Natl. Acad. Sci. U.S.A.* **107,** 15449–15454 (Aug. 2010).

188. Frederick, B. A. *et al.* Epithelial to mesenchymal transition predicts gefitinib resistance in cell lines of head and neck squamous cell carcinoma and non-small cell lung carcinoma. *Mol. Cancer Ther.* **6,** 1683–1691 (June 2007).

189. Byers, L. A. *et al.* An epithelial-mesenchymal transition (EMT) gene signature predicts resistance to EGFR and PI3K inhibitors and identifies AXL as a therapeutic target for overcoming EGFR inhibitor resistance. *Clin. Cancer Res.* (Oct. 2012).

190. Kinase switching in mesenchymal-like non-small cell lung cancer lines contributes to EGFR inhibitor resistance through pathway redundancy. *Clin. Exp. Metastas.* **25,** 843–854 (2008).

191. Arumugam, T. *et al.* Epithelial to mesenchymal transition contributes to drug resistance in pancreatic cancer. *Cancer Res.* **69,** 5820–5828 (July 2009).

192. Li, Q. Q. *et al.* Twist1-mediated adriamycin-induced epithelial-mesenchymal transition relates to multidrug resistance and invasive potential in breast cancer cells. *Clin. Cancer Res.* **15,** 2657–2665 (Apr. 2009).

193. Mercado, P. *et al.* A systems view of epithelial–mesenchymal transition signaling states. *Clin. Exp. Metastas.* **28,** 137–155 (Dec. 2010).

194. Condeelis, J. S. & Gertler, F. B. An EMT-driven alternative splicing program occurs in human breast cancer and modulates cellular phenotype. *PLoS Genet.* **7**, e1002218 (Aug. 2011).

195. Lapuk, A. *et al.* Exon-level microarray analyses identify alternative splicing programs in breast cancer. *Molecular Cancer Research* **8**, 961–974 (July 2010).

196. Craven, R. J. *et al.* Receptor tyrosine kinases expressed in metastatic colon cancer. *Int. J. Cancer* **60**, 791–797 (Mar. 1995).

197. Nemoto, T., Ohashi, K., Akashi, T., Johnson, J. D. & Hirokawa, K. Overexpression of protein tyrosine kinases in human esophageal cancer. *Pathobiology* **65**, 195–203 (1997).

198. Ito, M. *et al.* Expression of receptor-type tyrosine kinase, Axl, and its ligand, Gas6, in pediatric thyroid carcinomas around chernobyl. *Thyroid* **12**, 971–975 (Nov. 2002).

199. Berclaz, G. *et al.* Estrogen dependent expression of the receptor tyrosine kinase AXL in normal and malignant human breast. *Ann. Oncol.* **12**, 819–824 (June 2001).

200. Shieh, Y.-S. *et al.* Expression of axl in lung adenocarcinoma and correlation with tumor progression. *Neoplasia* **7**, 1058–1064 (Dec. 2005).

201. Hutterer, M. *et al.* AXL and growth arrest-specific gene 6 are frequently overexpressed in human gliomas and predict poor prognosis in patients with glioblastoma multiforme. *Clin. Cancer Res.* **14**, 130–138 (Jan. 2008).

202. Ikram, M. *et al.* Overexpression of the AXL tyrosine kinase receptor in cutaneous SCC-derived cell lines and tumours. *Br. J. Cancer* **94**, 1446–1451 (Apr. 2006).

203. Koorstra, J.-B. M. *et al.* The Axl receptor tyrosine kinase confers an adverse prognostic influence in pancreatic cancer and represents a new therapeutic target. *Cancer Biol. Ther.* **8**, 618–626 (Apr. 2009).

204. Liu, L. *et al.* Novel mechanism of lapatinib resistance in HER2-positive breast tumor cells: activation of AXL. *Cancer Res.* **69**, 6871–6878 (Sept. 2009).

205. Shiozawa, Y. *et al.* Gas6/AXL axis regulates prostate cancer invasion, proliferation, and survival in the bone marrow niche. *Neoplasia* **12**, 116–127 (Feb. 2010).

206. Vuoriluoto, K. *et al.* Vimentin regulates EMT induction by Slug and oncogenic H-Ras and migration by governing Axl expression in breast cancer. *Oncogene* **30**, 1436–1448 (Nov. 2010).

207. Zhang, Z. *et al.* Activation of the AXL kinase causes resistance to EGFR-targeted therapy in lung cancer. *Nat. Genet.* 1–11 (July 2012).

208. Tai, K.-Y., Shieh, Y.-S., Lee, C.-S., Shiah, S.-G. & Wu, C.-W. Axl promotes cell invasion by inducing MMP-9 activity through activation of NF-kappaB and Brg-1. *Oncogene* **27**, 4044–4055 (July 2008).

209. McCloskey, P., Pierce, J., Koski, R. A., Varnum, B. & Liu, E. T. Activation of the AXL receptor tyrosine kinase induces mitogenesis and transformation in 32D cells. *Cell Growth Differ.* **5**, 1105–1117 (Oct. 1994).

210. Hafizi, S., Alindri, F., Karlsson, R. & Dahlbäck, B. Interaction of Axl receptor tyrosine kinase with C1-TEN, a novel C1 domain-containing protein with homology to tensin. *Biochem. Biophys. Res. Commun.* **299**, 793–800 (Dec. 2002).

211. Huang, P. H. *et al.* Quantitative analysis of EGFRvIII cellular signaling networks reveals a combinatorial therapeutic strategy for glioblastoma. *Proc. Natl. Acad. Sci. USA* **104**, 12867–12872 (May 2007).

212. Barretina, J. *et al.* The Cancer Cell Line Encyclopedia enables predictive modelling of anticancer drug sensitivity. *Nature* **483**, 603–607 (Mar. 2012).

213. Bishop, C. M. *Pattern recognition and machine learning* (Springer, New York, 2006).

214. Cancer Genome Atlas Network. Comprehensive molecular portraits of human breast tumours. *Nature* **490,** 61–70 (Oct. 2012).

215. Zhuang, G. *et al.* Elevation of Receptor Tyrosine Kinase EphA2 Mediates Resistance to Trastuzumab Therapy. *Cancer Res.* **70,** 299–308 (Jan. 2010).

216. Nagane, M., Levitzki, A., Gazit, A., Cavenee, W. K. & Huang, H. J. Drug resistance of human glioblastoma cells conferred by a tumor-specific mutant epidermal growth factor receptor through modulation of Bcl-XL and caspase-3-like proteases. *Proc. Natl. Acad. Sci. USA* **95,** 5724–5729 (May 1998).

217. Li, Y. *et al.* Axl as a potential therapeutic target in cancer: role of Axl in tumor growth, metastasis and angiogenesis. *Oncogene* **28,** 3442–3455 (July 2009).

218. Mark, M. R., Chen, J., Hammonds, R. G., Sadick, M. & Godowsk, P. J. Characterization of Gas6, a member of the superfamily of G domain-containing proteins, as a ligand for Rse and Axl. *J Biol Chem* **271,** 9785–9789 (Apr. 1996).

219. Hasanbasic, I., Rajotte, I. & Blostein, M. The role of gamma-carboxylation in the anti-apoptotic function of gas6. *J. Thromb. Haemost.* **3,** 2790–2797 (Dec. 2005).

220. Hurvich, C. M. & Tsai, C. L. Bias of the corrected AIC criterion for underfitted regression and time series models. **78,** 499–509 (1991).

221. Gusenbauer, S., Vlaicu, P. & Ullrich, A. HGF induces novel EGFR functions involved in resistance formation to tyrosine kinase inhibitors. *Oncogene,* 1–11 (Oct. 2012).

222. Cerchia, L. *et al.* Targeting AXL with an high-affinity inhibitory aptamer. *Mol. Ther.* **20,** 1–13 (Nov. 2009).

223. Ye, X. *et al.* An anti-AXL monoclonal antibody attenuates xenograft tumor growth and enhances the effect of multiple anticancer therapies. *Oncogene* **29,** 5254–5264 (Sept. 2010).

224. Martens, T. *et al.* A novel one-armed anti-c-Met antibody inhibits glioblastoma growth in vivo. *Clin. Cancer Res.* **12,** 6144–6152 (Oct. 2006).

225. Jin, H. *et al.* MetMAb, the one-armed 5D5 anti-c-Met antibody, inhibits orthotopic pancreatic tumor growth and improves survival. *Cancer Res.* **68,** 4360–4368 (June 2008).

226. Holland, S., Pan, A., Franci, C., Hu, Y. & Chang, B. R428, a Selective Small Molecule Inhibitor of Axl Kinase, Blocks Tumor Spread and Prolongs Survival in Models of Metastatic Breast Cancer. *Cancer Res.* (2010).

227. Zhao, B. *et al.* Prospective assessment of discontinuation and reinitiation of erlotinib or gefitinib in patients with acquired resistance to erlotinib or gefitinib followed by the addition of everolimus. *Clin. Cancer Res.* **13,** 5150–5155 (2007).

228. Chaft, J. E. *et al.* Disease flare after tyrosine kinase inhibitor discontinuation in patients with EGFR-mutant lung cancer and acquired resistance to erlotinib or gefitinib: implications for clinical trial design. *Clin. Cancer Res.* **17,** 6298–6303 (Oct. 2011).

229. Pop, O., Pirvu, A. & Toffart, A. C. Disease flare after treatment discontinuation in a patient with EML4-ALK lung cancer and acquired resistance to crizotinib. *J. Thorac. Oncol.* 7, e1–e2 (2012).

230. Yeh, C.-Y. *et al.* Transcriptional activation of the AXL and PDGFR-α by c-Met through a ras- and Src-independent mechanism in human bladder cancer. *BMC Cancer* **11,** 139 (Apr. 2011).

231. Greco, W. R., Bravo, G. & Parsons, J. C. The search for synergy: a critical review from a response surface perspective. *Pharmacol. Rev.* 47, 331–385 (June 1995).

232. Milo, R., Jorgensen, P., Moran, U., Weber, G. & Springer, M. BioNumbers—the database of key numbers in molecular and cell biology. *Nucleic Acids Research* **38**, D750–D753 (2010).

233. Meyer, A. S., Miller, M. A., Gertler, F. B. & Lauffenburger, D. A. The receptor AXL diversifies EGFR signaling and limits the response to EGFR-targeted inhibitors in triple-negative breast cancer cells. *Sci Signal* **6**, ra66 (Aug. 2013).

234. Mercer, J. & Aebersold, R. Direct identification of ligand-receptor interactions on living cells and tissues. *Nature Biotechnol*, 1–7 (Sept. 2012).

235. Morizono, K. *et al.* The Soluble Serum Protein Gas6 Bridges Virion Envelope Phosphatidylserine to the TAM Receptor Tyrosine Kinase Axl to Mediate Viral Entry. *Cell Host and Microbe* **9**, 286–298 (Jan. 2011).

236. Song, X. *et al.* Overexpression of receptor tyrosine kinase Axl promotes tumor cell invasion and survival in pancreatic ductal adenocarcinoma. *Cancer* **117**, 734–743 (Oct. 2010).

237. Shankar, S. L. *et al.* Gas6/Axl signaling activates the phosphatidylinositol 3-kinase/Akt1 survival pathway to protect oligodendrocytes from tumor necrosis factor alpha-induced apoptosis. *J. Neurosci.* **26**, 5638–5648 (May 2006).

238. Mishra, A. *et al.* Hypoxia stabilizes Gas6/AXL signaling in metastatic prostate cancer. *Molecular Cancer Research* (Apr. 2012).

239. Fridell, Y., Villa, J., Attar, E. C. & Liu, E. GAS6 induces Axl-mediated chemotaxis of vascular smooth muscle cells. *J Biol Chem* (1998).

240. Ammoun, S. *et al.* Axl/Gas6/NFκB signalling in schwannoma pathological proliferation, adhesion and survival. *Oncogene*, pages (Jan. 2013).

241. Dormady, S. P., Zhang, X. M. & Basch, R. S. Hematopoietic progenitor cells grow on 3T3 fibroblast monolayers that overexpress growth arrest-specific gene-6 (GAS6). *Proc. Natl. Acad. Sci. USA* **97**, 12260–12265 (Oct. 2000).

242. Gould, W., Baxi, S. & Schroeder, R. Gas6 receptors Axl, Sky and Mer enhance platelet activation and regulate thrombotic responses. ... *of Thrombosis and* ... (2005).

243. Nakano, T. *et al.* Requirement of gamma-carboxyglutamic acid residues for the biological activity of Gas6: contribution of endogenous Gas6 to the proliferation of vascular smooth muscle cells. *Biochem J* **323 (Pt 2)**, 387–392 (Apr. 1997).

244. Yanagita, M. *et al.* Mechanism of inhibitory effect of warfarin on mesangial cell proliferation. *J. Am. Soc. Nephrol.* **10**, 2503–2509 (Dec. 1999).

245. Haugh, J. M. Mathematical model of human growth hormone (hGH)-stimulated cell proliferation explains the efficacy of hGH variants as receptor agonists or antagonists. *Biotechnol Prog* **20**, 1337–1344 (2004).

246. Monast, C. S., Furcht, C. M. & Lazzara, M. J. Computational Analysis of the Regulation of EGFR by Protein Tyrosine Phosphatases. *Biophys J* (2012).

247. French, A. R. & Lauffenburger, D. A. Controlling receptor/ligand trafficking: Effects of cellular and molecular properties on endosomal sorting. *Ann Biomed Eng* **25**, 690–707 (July 1997).

248. Kleiman, L. B., Maiwald, T., Conzelmann, H., Lauffenburger, D. A. & Sorger, P. K. Rapid phospho-turnover by receptor tyrosine kinases impacts downstream signaling and drug binding. *Mol. Cell* **43**, 723–737 (Sept. 2011).

249. Chen, W. W. *et al.* Input–output behavior of ErbB signaling pathways as revealed by a mass action model trained against dynamic data. *Mol Syst Biol* **5**, 1–19 (Jan. 2009).

250. Nakano, T. Cell Adhesion to Phosphatidylserine Mediated by a Product of Growth Arrest-specific Gene 6. *J Biol Chem* **272**, 29411–29414 (Nov. 1997).

251. Cosemans, J. M. E. M. *et al.* Potentiating role of Gas6 and Tyro3, Axl and Mer (TAM) receptors in human and murine platelet activation and thrombus stabilization. *J. Thromb. Haemost.* **8**, 1797–1808 (Aug. 2010).

252. Balogh, I., Hafizi, S., Stenhoff, J., Hansson, K. & Dahlbäck, B. Analysis of Gas6 in human platelets and plasma. *Arteriosclerosis, Thrombosis, and Vascular Biology* **25**, 1280–1286 (June 2005).

253. Angelillo-Scherrer, A. *et al.* Deficiency or inhibition of Gas6 causes platelet dysfunction and protects mice against thrombosis. *Nat Med* **7**, 215–221 (Feb. 2001).

254. Uehara, H. & Shacter, E. Auto-oxidation and oligomerization of protein S on the apoptotic cell surface is required for Mer tyrosine kinase-mediated phagocytosis of apoptotic cells. *J Immunol* **180**, 2522–2530 (Feb. 2008).

255. Rajotte, I., Hasanbasic, I. & Blostein, M. Gas6-mediated signaling is dependent on the engagement of its gamma-carboxyglutamic acid domain with phosphatidylserine. *Biochem. Biophys. Res. Commun.* **376**, 70–73 (Nov. 2008).

256. Stenhoff, J., Dahlbäck, B. & Hafizi, S. Vitamin K-dependent Gas6 activates ERK kinase and stimulates growth of cardiac fibroblasts. *Biochem. Biophys. Res. Commun.* **319**, 871–878 (July 2004).

257. Tanabe, K. *et al.* Roles of γ-carboxylation and a sex hormone-binding globulin-like domain in receptor-binding and in biological activities of Gas6. *FEBS letters* **408**, 5–5 (May 1997).

258. Hall, M. O., Obin, M. S., Prieto, A. L., Burgess, B. L. & Abrams, T. A. Gas6 Binding to Photoreceptor Outer Segments Requires γ-Carboxyglutamic Acid (Gla) and Ca2+ and is Required for OS Phagocytosis by RPE Cells in vitro. *Experimental Eye Research* **75**, 391–400 (Oct. 2002).

259. Casaletto, J. B. & McClatchey, A. I. Spatial regulation of receptor tyrosine kinases in development and cancer. *Nat. Rev. Cancer* **12**, 387–400 (June 2012).

260. Maiwald, T. & Timmer, J. Dynamical modeling and multi-experiment fitting with PottersWheel. *Bioinformatics* **24**, 2037–2043 (Sept. 2008).

261. Hindmarsh, A. C. *et al.* SUNDIALS. *ACM Trans. Math. Softw.* **31**, 363–396 (Sept. 2005).

262. Schlegel, J. *et al.* MERTK receptor tyrosine kinase is a therapeutic target in melanoma. *J. Clin. Invest.* **123**, 2257–2267 (May 2013).

263. Camenisch, T. D., Koller, B. H., Earp2, H. S. & Matsushima, G. K. A Novel Receptor Tyrosine Kinase, Mer, Inhibits TNF-α Production and Lipopolysaccharide-Induced Endotoxic Shock. *The Journal of Immunology* **162**, 3498–3503 (Mar. 1999).

264. Prasad, D. *et al.* TAM receptor function in the retinal pigment epithelium. *Mol. Cell. Neurosci.* **33**, 96–108 (Sept. 2006).

265. Barton, W. A. *et al.* Crystal structures of the Tie2 receptor ectodomain and the angiopoietin-2-Tie2 complex. *Nat Struct Mol Biol* **13**, 524–532 (June 2006).

266. Yu, X. *et al.* Structural basis for angiopoietin-1-mediated signaling initiation. *Proc. Natl. Acad. Sci. U.S.A.* **110**, 7205–7210 (Apr. 2013).

267. Lema Tomé, C. M. *et al.* Structural and functional characterization of monomeric EphrinA1 binding site to EphA2 receptor. *J Biol Chem* **287**, 14012–14022 (Apr. 2012).

268. Jones, R. B., Gordus, A., Krall, J. A. & MacBeath, G. A quantitative protein interaction network for the ErbB receptors using protein microarrays. *Nature* **439**, 168–174 (Jan. 2006).

269. Lopez, C. F., Muhlich, J. L., Bachman, J. A. & Sorger, P. K. Programming biological models in Python using PySB. *Mol Syst Biol* **9**, 646 (2013).

270. Eyles, J. *et al.* Tumor cells disseminate early, but immunosurveillance limits metastatic outgrowth, in a mouse model of melanoma. *J. Clin. Invest.* **120**, 2030–2039 (June 2010).

271. Balic, M. *et al.* Most early disseminated cancer cells detected in bone marrow of breast cancer patients have a putative breast cancer stem cell phenotype. *Clin. Cancer Res.* **12**, 5615–5621 (Oct. 2006).

272. Pantel, K. *et al.* Detection and clinical implications of early systemic tumor cell dissemination in breast cancer. *Clin. Cancer Res.* **9**, 6326–6334 (Dec. 2003).

273. Blick, T. *et al.* Epithelial mesenchymal transition traits in human breast cancer cell lines. *Clin. Exp. Metastas.* **25**, 629–642 (2008).

274. Bergert, M., Chandradoss, S. D., Desai, R. A. & Paluch, E. Cell mechanics control rapid transitions between blebs and lamellipodia during migration. *Proc. Natl. Acad. Sci. U.S.A.* **109**, 14434–14439 (Sept. 2012).

275. Pritchard, J. R. *et al.* Defining principles of combination drug mechanisms of action. *Proc. Natl. Acad. Sci. U.S.A.* **110**, E170–9 (Jan. 2013).

276. Lamar, J. M., Stern, P., Schindler, J. W., Jiang, Z. G. & Hynes, R. O. The Hippo pathway target, YAP, promotes metastasis through its TEAD-interaction domain. *Proc. Natl. Acad. Sci. USA* **109**, E2441–E2450 (2012).

277. Cordenonsi, M. *et al.* The Hippo Transducer TAZ Confers Cancer Stem Cell-Related Traits on Breast Cancer Cells. *Cell* **147**, 759–772 (Nov. 2011).

278. Kyama, C. M. *et al.* Increased peritoneal and endometrial gene expression of biologically relevant cytokines and growth factors during the menstrual phase in women with endometriosis. *Fertility and Sterility* **85**, 1667–1675 (June 2006).

279. Bedaiwy, M. A. *et al.* Prediction of endometriosis with serum and peritoneal fluid markers: a prospective controlled trial. *Hum Reprod* **17**, 426–431 (Feb. 2002).

280. Overton, C., Fernandez-Shaw, S., Hicks, B., Barlow, D. & Starkey, P. Peritoneal fluid cytokines and the relationship with endometriosis and pain. *Hum Reprod* **11**, 380–386 (Feb. 1996).

281. Xavier, P. *et al.* Serum levels of VEGF and TNF-alpha and their association with C-reactive protein in patients with endometriosis. *Archives of gynecology and obstetrics* **273**, 227–231 (Jan. 2006).

282. Pizzo, A. *et al.* Behaviour of cytokine levels in serum and peritoneal fluid of women with endometriosis. *Gynecologic and obstetric investigation* **54**, 82–87 (2002).

283. De Leon, F. D. *et al.* Peritoneal fluid volume, estrogen, progesterone, prostaglandin, and epidermal growth factor concentrations in patients with and without endometriosis. *Obstet Gynecol* **68**, 189–194 (Aug. 1986).

284. Huang, J. C., Papasakelariou, C. & Dawood, M. Y. Epidermal growth factor and basic fibroblast growth factor in peritoneal fluid of women with endometriosis. *Fertility and Sterility* **65**, 931–934 (May 1996).

285. Simms, J. S., Chegini, N., Williams, R. S., Rossi, A. M. & Dunn, W. A. Identification of epidermal growth factor, transforming growth factor-alpha, and epidermal growth factor receptor in surgically induced endometriosis in rats. *Obstet Gynecol* **78**, 850–857 (Nov. 1991).

286. Sheng, Q. *et al.* An activated ErbB3/NRG1 autocrine loop supports in vivo proliferation in ovarian cancer cells. *Cancer Cell* **17**, 298–310 (Mar. 2010).

287. Kalu, E. *et al.* Cytokine profiles in serum and peritoneal fluid from infertile women with and without endometriosis. *J Obstet Gynaecol Res* **33**, 490–495 (Aug. 2007).

288. Osuga, Y. *et al.* Hepatocyte growth factor concentrations are elevated in peritoneal fluid of women with endometriosis. *Hum Reprod* **14**, 1611–1613 (June 1999).

289. Matalliotakis, I. M. *et al.* Serum concentrations of growth factors in women with and without endometriosis: the action of anti-endometriosis medicines. *Int. Immunopharmacol.* **3**, 81–89 (Jan. 2003).

290. Steff, A.-M. *et al.* Serum concentrations of insulin-like growth factor-1, soluble tumor necrosis factor receptor-1 and angiogenin in endometriosis patients. *Am. J. Reprod. Immunol.* **51**, 166–173 (Feb. 2004).

291. Gurgan, T., Bukulmez, O., Yarali, H., Tanir, M. & Akyildiz, S. Serum and peritoneal fluid levels of IGF I and II and insulinlike growth binding protein-3 in endometriosis. *J Reprod Med* **44**, 450–454 (May 1999).

292. Zhou, W.-D. *et al.* SB203580, a p38 mitogen-activated protein kinase inhibitor, suppresses the development of endometriosis by down-regulating proinflammatory cytokines and proteolytic factors in a mouse model. *Hum Reprod* **25**, 3110–3116 (Dec. 2010).

293. Murk, W. *et al.* Extracellularly signal-regulated kinase activity in the human endometrium: possible roles in the pathogenesis of endometriosis. *J. Clin. Endocrinol. Metab.* **93**, 3532–3540 (Sept. 2008).

294. Honda, H., Barrueto, F. F., Gogusev, J., Im, D. D. & Morin, P. J. Serial analysis of gene expression reveals differential expression between endometriosis and normal endometrium. Possible roles for AXL and SHC1 in the pathogenesis of endometriosis. *Reprod. Biol. Endocrinol.* **6**, 59 (2008).

295. Uz, Y. H. *et al.* Increased c-Jun N-terminal kinase activation in human endometriotic endothelial cells. *Histochem. Cell Biol.* **135**, 83–91 (Jan. 2011).

296. Yousef, M. H. M., Chai, D. C., Mwenda, J. M. & D'Hooghe, T. M. The effect of JNK-inhibitors on endometriosis in baboons with induced disease: a placebo-controlled randomized study. *Fertility and Sterility* **92**, S11 (Sept. 2009).

297. Matsuzaki, S. *et al.* DNA microarray analysis of gene expression profiles in deep endometriosis using laser capture microdissection. *Molecular Human Reproduction* **10**, 719–728 (Oct. 2004).

298. El-Ghobashy, A. A., Shaaban, A. M., Innes, J., Prime, W. & Herrington, C. S. Upregulation of heat shock protein 27 in metaplastic and neoplastic lesions of the endocervix. *Int. J. Gynecol. Cancer* **15**, 503–509 (May 2005).

299. Shazand, K. *et al.* FOXO1 and c-jun transcription factors mRNA are modulated in endometriosis. *Molecular Human Reproduction* **10**, 871–877 (Dec. 2004).

300. Ohlsson Teague, E. M. C. *et al.* MicroRNA-regulated pathways associated with endometriosis. *Molecular Endocrinology* **23**, 265–275 (Feb. 2009).

301. Cinar, O. *et al.* Differential regulation of Akt phosphorylation in endometriosis. *Reproductive BioMedicine Online* **19**, 864–871 (Dec. 2009).

302. Laudanski, P. *et al.* Expression of selected tumor suppressor and oncogenes in endometrium of women with endometriosis. *Hum Reprod* **24**, 1880–1890 (Aug. 2009).

303. Itoh, F. *et al.* Possible involvement of signal transducer and activator of transcription-3 in cell-cell interactions of peritoneal macrophages and endometrial stromal cells in human endometriosis. *Fertility and Sterility* **99**, 1705–1713 (May 2013).

304. Lee, J., Banu, S. K., Burghardt, R. C., Starzinski-Powitz, A. & Arosh, J. A. Selective inhibition of prostaglandin E2 receptors EP2 and EP4 inhibits adhesion of human endometriotic epithelial and stromal cells through suppression of integrin-mediated mechanisms. *Biol. Reprod.* **88**, 77–77 (Mar. 2013).

305. Lee, J., Banu, S. K., Subbarao, T., Starzinski-Powitz, A. & Arosh, J. A. Selective inhibition of prostaglandin E2 receptors EP2 and EP4 inhibits invasion of human immortalized endometriotic epithelial and stromal cells through suppression of metalloproteinases. *Mol. Cell. Endocrinol.* **332,** 306–313 (Jan. 2011).

306. Cayan, F. *et al.* Association of G1057D variant of insulin receptor substrate-2 with endometriosis. *Fertility and Sterility* **94,** 1622–1626 (Oct. 2010).

307. Peluso, C. *et al.* TYK2 rs34536443 polymorphism is associated with a decreased susceptibility to endometriosis-related infertility. *Hum. Immunol.* **74,** 93–97 (Jan. 2013).

308. Ejskjaer, K. *et al.* Expression of the epidermal growth factor system in eutopic endometrium from women with endometriosis differs from that in endometrium from healthy women. *Gynecologic and obstetric investigation* **67,** 118–126 (2009).

309. Koga, K. *et al.* Increased concentrations of soluble tumour necrosis factor receptor (sTNFR) I and II in peritoneal fluid from women with endometriosis. *Molecular Human Reproduction* **6,** 929–933 (Oct. 2000).

310. Khan, K. N. *et al.* Immunoexpression of hepatocyte growth factor and c-Met receptor in the eutopic endometrium predicts the activity of ectopic endometrium. *Fertility and Sterility* **79,** 173–181 (Jan. 2003).

311. Prefumo, F., Venturini, P. L. & Fulcheri, E. Analysis of p53 and c-erbB-2 expression in ovarian endometrioid carcinomas arising in endometriosis. *Int. J. Gynecol. Pathol.* **22,** 83–88 (Jan. 2003).

312. Philippoussis, F., Gagné, D., Hugo, P. & Gosselin, D. Concentrations of alpha-fetoprotein, insulin-like growth factor binding protein-3, c-erbB-2, and epidermal growth factor in serum of patients with endometriosis. *J. Soc. Gynecol. Investig.* **11,** 175–181 (Apr. 2004).

313. Aghajanova, L. *et al.* Unique transcriptome, pathways, and networks in the human endometrial fibroblast response to progesterone in endometriosis. *Biol. Reprod.* **84,** 801–815 (Apr. 2011).

314. Chung, H. W. *et al.* Matrix metalloproteinase-2, membranous type 1 matrix metalloproteinase, and tissue inhibitor of metalloproteinase-2 expression in ectopic and eutopic endometrium. *Fertility and Sterility* **78,** 787–795 (Oct. 2002).

315. Huang, H.-F., Hong, L.-H., Tan, Y. & Sheng, J.-Z. Matrix metalloproteinase 2 is associated with changes in steroid hormones in the sera and peritoneal fluid of patients with endometriosis. *Fertility and Sterility* **81,** 1235–1239 (May 2004).

316. Ramón, L. *et al.* mRNA analysis of several components of the plasminogen activator and matrix metalloproteinase systems in endometriosis using a real-time quantitative RT-PCR assay. *Hum Reprod* **20,** 272–278 (Jan. 2005).

317. Bruner-Tran, K. L. *et al.* Steroid and cytokine regulation of matrix metalloproteinase expression in endometriosis and the establishment of experimental endometriosis in nude mice. *J. Clin. Endocrinol. Metab.* **87,** 4782–4791 (Oct. 2002).

318. Saito, T. *et al.* Expression of MMP-3 and TIMP-1 in the endometriosis and the influence of danazol. *Nihon Sanka Fujinka Gakkai Zasshi* **47,** 495–496 (May 1995).

319. Shan, K. *et al.* Polymorphisms in the promoter regions of the matrix metalloproteinases-7, -9 and the risk of endometriosis and adenomyosis in China. *Molecular Human Reproduction* **12,** 35–39 (Jan. 2006).

320. Chung, H. W. *et al.* Matrix metalloproteinase-9 and tissue inhibitor of metalloproteinase-3 mRNA expression in ectopic and eutopic endometrium in women with endometriosis: a rationale for endometriotic invasiveness. *Fertility and Sterility* **75,** 152–159 (Jan. 2001).

321. Collette, T., Maheux, R., Mailloux, J. & Akoum, A. Increased expression of matrix metalloproteinase-9 in the eutopic endometrial tissue of women with endometriosis. *Hum Reprod* **21,** 3059–3067 (Dec. 2006).

322. Szamatowicz, J., Laudanski, P. & Tomaszewska, I. Matrix metalloproteinase-9 and tissue inhibitor of matrix metalloproteinase-1: a possible role in the pathogenesis of endometriosis. *Hum Reprod* **17,** 284–288 (Feb. 2002).

323. Sharpe-Timms, K. L., Keisler, L. W., McIntush, E. W. & Keisler, D. H. Tissue inhibitor of metalloproteinase-1 concentrations are attenuated in peritoneal fluid and sera of women with endometriosis and restored in sera by gonadotropin-releasing hormone agonist therapy. *Fertility and Sterility* **69,** 1128–1134 (June 1998).

324. Gottschalk, C. *et al.* Matrix metalloproteinases and TACE play a role in the pathogenesis of endometriosis. *Adv. Exp. Med. Biol.* **477,** 483–486 (2000).

325. Finas, D. *et al.* L1 cell adhesion molecule (L1CAM) as a pathogenetic factor in endometriosis. *Hum Reprod* **23,** 1053–1062 (May 2008).

326. Herrlich, A., Klinman, E., Fu, J., Sadegh, C. & Lodish, H. Ectodomain cleavage of the EGF ligands HB-EGF, neuregulin1-beta, and TGF-alpha is specifically triggered by different stimuli and involves different PKC isoenzymes. *Faseb J* **22,** 4281–4295 (Dec. 2008).

327. Storey, J. D. A direct approach to false discovery rates. *Journal of the Royal Statistical Society: Series B (Statistical Methodology)* **64,** 479–498 (2002).

328. Brown, C. L., Meise, K. S., Plowman, G. D., Coffey, R. J. & Dempsey, P. J. Cell surface ectodomain cleavage of human amphiregulin precursor is sensitive to a metalloprotease inhibitor. Release of a predominant N-glycosylated 43-kDa soluble form. *J Biol Chem* **273,** 17258–17268 (July 1998).

329. Xu, P., Liu, J., Sakaki-Yumoto, M. & Derynck, R. TACE activation by MAPK-mediated regulation of cell surface dimerization and TIMP3 association. *Sci Signal* **5,** ra34–ra34 (May 2012).

330. Revised American Society for Reproductive Medicine classification of endometriosis: 1996. *Fertility and Sterility* **67,** 817–821 (May 1997).

331. Osteen, K. G., Hill, G. A., Hargrove, J. T. & Gorstein, F. Development of a method to isolate and culture highly purified populations of stromal and epithelial cells from human endometrial biopsy specimens. *Fertility and Sterility* **52,** 965–972 (Dec. 1989).

332. Santella, A., Du, Z., Nowotschin, S., Hadjantonakis, A.-K. & Bao, Z. A hybrid blob-slice model for accurate and efficient detection of fluorescence labeled nuclei in 3D. *BMC Bioinformatics* **11,** 580 (2010).

333. Höskuldsson, A. PLS regression methods. *Journal of Chemometrics* **2,** 211–228 (1988).